

# 学位論文

$^8\text{B}$  solar neutrino spectrum measurement using  
Super-Kamiokande IV  
(Super-Kamiokande IV を用いた  
 $^8\text{B}$  太陽ニュートリノスペクトラム測定)

平成 27 年 12 月博士 (理学) 申請

東京大学大学院 理学系研究科  
物理学専攻

中野 佑樹



## Abstract

The results of solar neutrino measurement using the fourth phase of the Super-Kamiokande detector, SK-IV, are presented. The main motivation of this thesis is to observe the matter effect of solar neutrinos oscillations. For this purpose, the “up-turn” of the energy spectrum and day/night asymmetry measurements are performed.

The data for this thesis were taken from September 2008 to April 2015. The livetime of the data sample is 2055.5 days. With the improvements of water circulation system, calibration methods and reduction cuts, the energy threshold for the analysis was lowered to 3.5 MeV in kinetic energy in SK-IV.

Systematic uncertainties for the flux and spectrum measurements are re-evaluated precisely. Finally, the total systematic uncertainty on the  $^8\text{B}$  solar neutrino flux is obtained as  $\pm 1.7\%$ , which is the lowest among all SK phases.

Using the all events above 3.5 MeV, the  $^8\text{B}$  solar neutrino flux in SK-IV is obtained as  $\Phi_{^8\text{B},\text{SK4}} = 2.314 \pm 0.018(\text{stat.}) \pm 0.039(\text{syst.}) \times 10^6/\text{cm}^2/\text{sec}$ , which is consistent with those of other phases. In the 3.5 – 4.0 MeV region, the number of the extracted solar neutrino signal is  $1299_{-154}^{+156}(\text{stat.})_{-64}^{+66}(\text{syst.})$ , which is the most precise (statistically significant) measurement among the all solar neutrino experiments.

Combining the measurements of all SK phases, the  $^8\text{B}$  solar neutrino flux is  $\Phi_{^8\text{B},\text{SK}} = 2.341 \pm 0.044(\text{stat.} + \text{syst.}) \times 10^6/\text{cm}^2/\text{sec}$ . The  $^8\text{B}$  solar neutrino fluxes during daytime and nighttime are compared and the day/night flux asymmetry is calculated as  $A_{\text{DN}} = -3.3 \pm 1.1(\text{stat.}) \pm 0.8(\text{syst.})\%$ , which is  $2.4\sigma$  away from zero.

The  $\chi^2$  values of energy spectrum fit to all SK data with a general quadratic fit, flat shape, solar global and solar plus KamLAND oscillation parameters are obtained to be 71.25, 71.42, 72.47 and 74.79 with d.o.f of 80, respectively. The flat shape is favored by  $1.1 - 1.9\sigma$  level compared with the MSW prediction with best fit oscillation parameters. Although this result is not statistically significant, with the improvement of the detection efficiency and the reducing the radon background in the solar analysis, the “up-turn” of the energy spectrum is expected to be observed at  $\sim 3\sigma$  level within about 6 years.

## Acknowledgements

First of all, I would like to express my sincere gratitude to my adviser, Prof. M. Nakahata giving me the opportunity of studying the solar neutrino. I have learned many things under his excellent guidance. He always supported me throughout this work.

I never forget those who worked with me on the solar analysis, Prof. Y. Takeuchi, Dr. M. Smy, Prof. Y. Koshio, Dr. L. Marti, Dr. M. Ikeda, Dr. T. Yokozawa, Dr. G. Caminati, Dr. A. Renshaw, P. Weatherly, and Dr. E. Muhammad. Without their works, this thesis was never completed.

I would like to thank Prof. S. Tasaka. He gave me useful advice related with the Rn measurement. Discussions with him was very useful.

I would like to thank Prof. J. Sato. He suggested to me that I go in the experimental field. His suggestion changed my fate.

I would like to thank Prof. H. Sekiya. He gave me many detailed and practical advice including the solar analysis and the Rn study in many occasions. He was always there when I needed him.

I would like to thank Dr. T. Tomura for giving me many useful advice on analysis and always listening to my complain during stay in Kamioka.

I am grateful to those who worked with me as Water/Radon team, Prof. R. A. Wendell, Prof. M. Matsubara, Dr. T. Nakamura, M. Miwa, K. Iwamoto, A. Orii, R. Akutsu, D. Fukuda, K. Watanabe, H. Nagao and K. Ito. Without their support, the Rn measurement study is never completed.

I thank to S. Tobayama and Y. Suda for working with me on the dark noise study.

I thank to K. Hosokawa for working with me on the Rn detector study.

I would like to thank to all other Super-Kamiokande collaborators, especially, Prof. Y. Suzuki, Prof. T. Kajita, Prof. Y. Itow, Prof. M. Shiozawa, Prof. S. Moriyama, Prof. Y. Hayato, Prof. Y. Kishimoto, Prof. M. Yokoyama, Prof. M. Vagins, Prof. K. Martens, Dr. M. Miura, Dr. S. Mine, Dr. S. Nakayama, Dr. H. Tanaka, Dr. Y. Nishimura and Dr. T. Yano.

Many thanks to the (previous, current) members of the Kamioka observatory, especially, Dr. B. Yang, Dr. K. Ichimura, M. Kanazawa, Dr. N. Okazaki, and M. Kobayashi.

Finally, I thank my friends who understand me very well, C. Kudo, C. Imai, K. Katami, T. Masunaga, T. Kuwahara, K. Yamada, T. Maruchi, Y. Mishima and T. Fujisaki.

# Contents

<b>1</b>	<b>Introduction</b>	<b>1</b>
1.1	Brief history of Neutrino . . . . .	1
1.2	Theoretical Background of Neutrino . . . . .	2
1.2.1	Neutrino Oscillation in vacuum . . . . .	2
1.2.2	Matter enhanced oscillation . . . . .	5
1.3	Current status of Neutrino properties . . . . .	7
1.3.1	Generation of Neutrino . . . . .	7
1.3.2	Oscillation parameters . . . . .	7
<b>2</b>	<b>Solar neutrino physics</b>	<b>9</b>
2.1	The Sun . . . . .	9
2.1.1	Standard Solar Model . . . . .	9
2.1.2	Properties of the Sun . . . . .	9
2.1.3	Solar Neutrino . . . . .	12
2.1.4	Solar activity . . . . .	13
2.2	Solar Neutrino Experiment . . . . .	14
2.2.1	Homestake Chlorine Experiment . . . . .	14
2.2.2	Kamiokande . . . . .	16
2.2.3	Gallium Experiments . . . . .	17
2.2.4	Super-Kamiokande . . . . .	19
2.2.5	SNO Experiment . . . . .	19
2.2.6	Borexino Experiment . . . . .	21
2.2.7	KamLAND experiment . . . . .	23
2.2.8	Summary of solar neutrino experimental results . . . . .	24
2.3	Physics motivation of this thesis . . . . .	25
2.3.1	Solar neutrino flavor oscillation . . . . .	25
2.3.2	Analysis target . . . . .	26
<b>3</b>	<b>Super-Kamiokande detector</b>	<b>29</b>
3.1	Overview of Super-Kamiokande . . . . .	29
3.2	The structure of detector . . . . .	30
3.2.1	Inner detector and Outer detector . . . . .	30
3.2.2	20-inch PMT for ID and PMT cover . . . . .	31
3.2.3	8-inch PMT for OD . . . . .	32
3.2.4	Helmholtz coils . . . . .	32

3.3	Data acquisition system . . . . .	34
3.3.1	Data acquisition system for SK-I to SK-III . . . . .	35
3.3.2	Hardware trigger . . . . .	35
3.3.3	Data acquisition system for SK-IV . . . . .	35
3.3.4	Software trigger . . . . .	39
3.4	Water circulation system . . . . .	40
3.4.1	Water purification system . . . . .	40
3.4.2	Rn free air system . . . . .	42
3.5	Detector simulation . . . . .	45
3.5.1	Cherenkov photon production . . . . .	45
3.5.2	Water transparency . . . . .	46
3.5.3	Detector response . . . . .	47
<b>4</b>	<b>Event reconstruction</b> . . . . .	<b>49</b>
4.1	Vertex reconstruction . . . . .	49
4.2	Direction reconstruction . . . . .	51
4.3	Energy reconstruction . . . . .	51
<b>5</b>	<b>Detector calibration method</b> . . . . .	<b>56</b>
5.1	PMT calibration . . . . .	56
5.1.1	Absolute gain calibration . . . . .	56
5.1.2	Relative gain calibration . . . . .	58
5.1.3	PMT quantum efficiency measurement . . . . .	58
5.1.4	PMT timing calibration . . . . .	61
5.2	Water transparency measurement . . . . .	63
5.2.1	Measurement of water transparency with laser light injection . . . . .	64
5.2.2	Measurement of water transparency with Decay electron . . . . .	66
5.2.3	Top bottom asymmetry . . . . .	67
5.3	Absolute energy scale calibration . . . . .	69
5.3.1	LINAC calibration . . . . .	69
5.3.2	DT generator . . . . .	73
5.3.3	Systematic uncertainty of absolute energy scale . . . . .	75
<b>6</b>	<b>Data reduction</b> . . . . .	<b>77</b>
6.1	Run selection . . . . .	77
6.2	Pre-reduction . . . . .	77
6.2.1	Vertex position cut . . . . .	78
6.2.2	Low or high energy cut . . . . .	78
6.2.3	Loose external cut . . . . .	78
6.2.4	Loose event quality cut . . . . .	78
6.2.5	Summary of pre-reduction . . . . .	79
6.3	Solar neutrino analysis . . . . .	80
6.3.1	Bad channel cut . . . . .	80
6.3.2	Muon rate . . . . .	81
6.3.3	Total number of hit PMT . . . . .	83
6.3.4	Calibration trigger/source cut . . . . .	83

6.3.5	Flasher cut . . . . .	83
6.3.6	Time difference cut . . . . .	83
6.3.7	OD event cut . . . . .	84
6.3.8	Event quality cut . . . . .	84
6.3.9	Spallation cut . . . . .	85
6.3.10	Hit patten cut . . . . .	90
6.3.11	$^{16}\text{N}$ cut . . . . .	91
6.3.12	External cut . . . . .	91
6.3.13	Small hit cluster event cut . . . . .	91
6.3.14	Tight fiducial volume cut . . . . .	92
6.4	Summary of the reduction step . . . . .	93
6.5	Multiple scattering goodness . . . . .	94
<b>7</b>	<b>Trigger efficiency of low energy event</b>	<b>97</b>
7.1	Motivation and History . . . . .	97
7.2	Special Ni calibration . . . . .	97
7.3	Result of the position dependence . . . . .	99
7.4	The efficiency in the low energy region . . . . .	100
7.5	Time variation of the detection efficiency . . . . .	103
7.6	Summary of this chapter . . . . .	104
<b>8</b>	<b>Background study for low energy region</b>	<b>105</b>
8.1	Rn in SK water . . . . .	105
8.1.1	Motivation and History . . . . .	105
8.1.2	Direct Rn measurements in SK water and their results . . . . .	106
8.1.3	Supply water problem . . . . .	107
8.2	Rn injection analysis . . . . .	109
8.2.1	Motivation and history . . . . .	109
8.2.2	Rn rich water production technique . . . . .	109
8.2.3	Analysis method . . . . .	109
8.2.4	Result . . . . .	111
8.3	Event rate analysis . . . . .	112
8.3.1	Motivation . . . . .	112
8.3.2	Analysis method . . . . .	112
8.3.3	Result . . . . .	113
8.3.4	Position dependence . . . . .	114
8.4	Future prospect . . . . .	116
8.4.1	Solar neutrino observation . . . . .	116
8.4.2	Refurbishment of the membrane degasifier . . . . .	118
8.5	Summary of this chapter . . . . .	119
<b>9</b>	<b>Signal extraction method</b>	<b>121</b>
9.1	Extended likelihood function . . . . .	121
9.2	The expected fraction of signal events ( $Y_i$ ) . . . . .	122
9.2.1	Step 1: Calculation of the recoil electron spectrum . . . . .	122
9.2.2	Step 2 and Step 3: Detector Simulation and the comparison . . . . .	127

<b>10 Systematic uncertainty</b>	<b>129</b>
10.1 Systematic uncertainty on the total flux	129
10.1.1 Energy scale	129
10.1.2 Energy resolution	129
10.1.3 $^8\text{B}$ spectrum	131
10.1.4 Background shape	132
10.1.5 Signal extraction method	133
10.1.6 Cross section	133
10.1.7 Angular resolution	133
10.1.8 Vertex shift	134
10.1.9 Event quality cut	135
10.1.10 Hit pattern cut	135
10.1.11 Spallation cut	136
10.1.12 External cut	137
10.1.13 Small hit cluster cut	137
10.1.14 Trigger efficiency	138
10.2 Summary of systematic uncertainties	138
10.3 Spectrum systematic uncertainty	138
10.3.1 Energy correlated uncertainty	138
10.3.2 Energy uncorrelated uncertainty	139
<b>11 Solar neutrino analysis using SK-IV data</b>	<b>142</b>
11.1 $^8\text{B}$ solar neutrino flux measurement	142
11.2 Day/Night flux asymmetry	143
11.3 Energy spectrum	144
11.4 Low energy region	152
<b>12 Combined analysis result</b>	<b>153</b>
12.1 $^8\text{B}$ solar neutrino flux measurement	153
12.1.1 Extracted signal	153
12.1.2 Combined result of $^8\text{B}$ solar neutrino flux measurement	153
12.1.3 Yearly variation of the $^8\text{B}$ solar neutrino flux	156
12.2 Energy spectrum	158
12.3 Oscillation Analysis	159
12.3.1 Spectrum shape prediction	159
12.3.2 $\chi^2$ definition for the spectrum shape	160
12.3.3 Time variation analysis	162
12.3.4 Flux constraint	163
12.3.5 Oscillation analysis result	164
<b>13 Discussion</b>	<b>166</b>
13.1 Comparison with other solar neutrino experiments	166
13.2 Combined energy spectrum	168
13.3 Future prospect	170
13.3.1 “Up-turn” observation	170
13.3.2 Day/Night flux asymmetry	174

<b>14 Conclusion</b>	<b>175</b>
<b>A Rn measurement system</b>	<b>178</b>
A.1 Development of Rn extraction system . . . . .	178
A.1.1 Mechanical structure . . . . .	178
A.1.2 Extraction efficiency . . . . .	179
A.1.3 Calibration setup . . . . .	179
A.1.4 Calibration method . . . . .	179
A.1.5 Systematic uncertainties . . . . .	181
A.1.6 Calibration result . . . . .	181
A.2 Measurement system and method . . . . .	181
A.2.1 Absorption and desorption with activated charcoal . . . . .	181
A.2.2 Measurement setup . . . . .	182
A.2.3 Measurement method . . . . .	182
A.2.4 Analysis method . . . . .	185

# Chapter 1

## Introduction

In this chapter, properties of neutrinos are described. The main topic is the neutrino oscillation.

### 1.1 Brief history of Neutrino

Neutrinos are members of the elementary particle in the standard model of elementary particle physics. They are categorized in lepton sector and are subject to only the weak interaction<sup>1</sup>. So far, there have been many theoretical and experimental achievements in the neutrino physics.

Neutrinos were firstly introduced by Pauli [1] in 1930. He tried to explain the energy conservation law in the beta decay process. More than twenty years after the Pauli's postulation, F. Reines and C. L. Cowan discovered the electron-anti-neutrino from a nuclear reactor in 1956 [2, 3]. The second type neutrino, muon-neutrino  $\nu_\mu$ , was discovered by Lederman, Schwartz and Steinberger *et al.* in 1962 [4]. The third type neutrino, tau-neutrino  $\nu_\tau$ , has assumed to exist after the discovery of tau-lepton in 1975, and it was discovered in 2000 by Niwa *et al.* [5]. The helicity of the neutrino was measured by Goldhaber *et al.* [6].

It had been believed that neutrinos do not have masses and actually in the standard model it is assumed that they are massless. Now we know that neutrinos have masses and they oscillate.

The first indication of the neutrino oscillation was found in a solar neutrino measurement. R. Davis *et al.* measured solar neutrino fluxes using the Homestake detector since 1968 [7] and the measured flux was a factor of 3 – 4 smaller than the expectation from the standard solar model, known as “Solar neutrino problem”. A similar deficit was observed by Kamiokande experiment in 1989 [8]. Another indication was found using atmospheric neutrino by Kamiokande [9] and IMB [10] in 1988.

The evidence for the neutrino oscillations was reported by Super-Kamiokande experiment in 1998 using the up/down asymmetry of the atmospheric neutrinos [11]. In 2001, the solar neutrino problem was solved in terms of neutrino oscillation by comparing the  $^8\text{B}$  solar neutrino flux measured by Super-Kamiokande experiment [12] and the SNO experiment [13]. It was further strengthened a neutral current (NC) measurement by SNO [13].

---

<sup>1</sup>Of course, neutrino is subject to the gravity but it is negligible because of its tiny mass.

## 1.2 Theoretical Background of Neutrino

### 1.2.1 Neutrino Oscillation in vacuum

Neutrino oscillations are the transitions between the different types of neutrinos, hence one type of neutrino transforms into another type of neutrino distinguished by the different lepton numbers. A theoretical idea of neutrino oscillations was proposed by Pontecorvo for neutrino-antineutrino oscillation in 1957 [14, 15]. In 1962, Maki *et al.* [16] formulated the current neutrino framework, i.e. taking into account mixing of neutrinos.

Since the neutrino mass eigenstates can be different from the weak interaction eigenstates (flavor eigenstate), the flavor eigenstates are constructed by a combination of different mass eigenstates. The flavor eigenstates  $|\nu_\alpha\rangle$ , where  $\alpha = e, \mu, \tau$ , can be expressed as the superposition of the mass eigenstates  $|\nu_i\rangle$  with mass  $m_i$  ( $i = 1, 2, 3$ )

$$|\nu_\alpha\rangle = \sum_{i=1}^N U_{\alpha i}^* |\nu_i\rangle, \quad (1.2.1)$$

where  $U$  is an unitary matrix. If this matrix is not diagonal, each flavor state will be a mixture of the mass states. The unitary matrix is often called the Pontecorvo-Maki-Nakagawa-Sakata matrix (PMNS or MNSP matrix). This matrix is characterized by four independent parameters<sup>2</sup>:

$$\begin{aligned} U_{3\times 3} &= \begin{pmatrix} 1 & 0 & 0 \\ 0 & c_{23} & s_{23} \\ 0 & -s_{23} & c_{23} \end{pmatrix} \begin{pmatrix} c_{13} & 0 & s_{13}e^{-i\delta} \\ 0 & 1 & 0 \\ -s_{13}e^{\delta} & 0 & c_{13} \end{pmatrix} \begin{pmatrix} c_{12} & s_{12} & 0 \\ -s_{12} & c_{12} & 0 \\ 0 & 0 & 1 \end{pmatrix} \\ &= \begin{pmatrix} s_{12}c_{12} & s_{12}c_{13} & s_{13}e^{-i\delta} \\ -s_{12}c_{23} - c_{12}s_{13}s_{23}e^{i\delta} & c_{12}s_{23} - s_{12}s_{13}s_{23}e^{i\delta} & c_{13}s_{23} \\ s_{12}s_{23} - c_{12}s_{13}c_{23}e^{i\delta} & -c_{12}s_{23} - s_{12}s_{13}c_{23}e^{i\delta} & c_{13}c_{23} \end{pmatrix}, \end{aligned} \quad (1.2.2)$$

where  $s_{ij} = \sin \theta_{ij}$ ,  $c_{ij} = \cos \theta_{ij}$ . The angle  $\theta_{ij}$  represents the mixing between the state  $i$  and  $j$ . The  $\delta$  is a charge-parity (CP) violating phase. If  $\delta \neq 0$ , CP among neutrinos is violating.

The time evolution of the mass eigenstates is governed by the Schrödinger equation as

$$i \frac{\partial}{\partial t} |\nu_i\rangle = E_i |\nu_i\rangle.$$

This equation can be solved if it assumes the propagation of particle through vacuum as

$$|\nu_i(t)\rangle = e^{-iE_i t} |\nu_i(0)\rangle. \quad (1.2.3)$$

However, the time evolution of each mass eigenstate is different from one another if their masses are different. Thus, it is convenient to re-write the neutrino flavor states at time  $t$  using the mass eigenstates as

$$|\nu_\alpha(t)\rangle = \sum_i U_{\alpha i}^* e^{-iE_i t} |\nu_i\rangle.$$

---

<sup>2</sup>Majorana phases could be included in the unitary matrix but since they do not affect neutrino oscillation, they are not shown here.

The amplitude of detecting neutrino as a flavor eigenstate  $\nu_\beta$  at time  $t$  starting from  $\nu_\alpha$  at  $t = 0$  is expressed as

$$\begin{aligned} A_{\nu_\alpha \rightarrow \nu_\beta}(t) &= \langle \nu_\beta | \nu_\alpha(t) \rangle = e^{-itH} \sum_i U_{\alpha i}^* \langle \nu_\beta | \nu_i \rangle \\ &= \sum_i \sum_j e^{-iE_i t} U_{\alpha i}^* U_{\beta j} \langle \nu_j | \nu_i \rangle \\ &= \sum_i e^{-iE_i t} U_{\alpha i}^* U_{\beta i}. \end{aligned}$$

The transition probability can be expressed as

$$\begin{aligned} P_{\nu_\alpha \rightarrow \nu_\beta} &= |A_{\nu_\alpha \rightarrow \nu_\beta}(t)|^2 \\ &= \sum_i \sum_j U_{\alpha i}^* U_{\beta i} U_{\alpha j} U_{\beta j}^* e^{-i(E_i - E_j)t}. \end{aligned}$$

The relationship between the energy and the mass can be approximated as follows, if neutrinos are relativistic

$$E_i = \sqrt{p^2 + m_i^2} \sim p + \frac{m_i^2}{2E}.$$

Then, the transition probability is written as

$$P_{\nu_\alpha \rightarrow \nu_\beta} = \sum_i \sum_j U_{\alpha i}^* U_{\beta i} U_{\alpha j} U_{\beta j}^* \exp\left(-i \frac{\Delta m_{ij}^2}{2E} t\right),$$

where  $\Delta m_{ij}^2 = m_i^2 - m_j^2$  represents the mass difference between the mass states  $i$  and  $j$ . If  $m_i \neq m_j$ , the oscillation is expected. It is useful to use the traveling distance  $L$  instead of the time  $t$

$$\begin{aligned} P_{\nu_\alpha \rightarrow \nu_\beta} &= \sum_i \sum_j U_{\alpha i}^* U_{\beta i} U_{\alpha j} U_{\beta j}^* \exp\left(-i \frac{\Delta m_{ij}^2}{2E} t\right) \\ &= \delta_{\alpha\beta} - 4 \sum_{i>j} \text{Re}(U_{\alpha i}^* U_{\beta i} U_{\alpha j} U_{\beta j}^*) \sin\left(\frac{\Delta m_{ij}^2 L}{2E}\right) \\ &\quad + 2 \sum_{i>j} \text{Im}(U_{\alpha i}^* U_{\beta i} U_{\alpha j} U_{\beta j}^*) \sin\left(\frac{\Delta m_{ij}^2 L}{2E}\right). \end{aligned} \tag{1.2.4}$$

In order to understand experimental effect of neutrino oscillations, a transition probability is shown for two flavor case. In the case of the two flavor oscillation, the unitary matrix is written as

$$U_{2 \times 2} = \begin{pmatrix} \cos \theta & \sin \theta \\ -\sin \theta & \cos \theta \end{pmatrix}. \tag{1.2.5}$$

Using this approximation, the transition probability becomes

$$\begin{aligned}
 P(\nu_\alpha \rightarrow \nu_\beta) &= \sin^2 2\theta \sin^2 \left( \frac{\Delta m^2 L}{4E} \right) \\
 &= \sin^2 2\theta \sin^2 \left( \frac{1.27 \Delta m^2 [\text{eV}^2] L [\text{m}]}{E [\text{MeV}]} \right),
 \end{aligned}
 \tag{1.2.6}$$

where the index of the mass states are omitted because there is only one mass difference in the two flavor case. Since the mixing angle  $\theta$  is the constant, it affects the amplitude of the transition probability. In contrast, the mass difference  $\Delta m^2$  contributes the oscillatory effect in the transition probability. Thus, neutrino oscillation experiments can measure mixing angle by measuring amplitude of the oscillation, and  $\Delta m^2$  by looking at energy ( $E$ ) and length ( $L$ ) dependence of the oscillation<sup>3</sup>.

The sensitivity of oscillation experiments depends on both the neutrino energy and its traveling length. To understand the sensitivity, the survival probability is re-written as

$$P_{\nu_\alpha \rightarrow \nu_\beta} = \sin^2 2\theta \sin^2 \left( \frac{\pi L}{L_0} \right),
 \tag{1.2.7}$$

where  $L_0 = 4\pi E / \Delta m^2$  is called oscillation length. If the oscillation length is much longer than the traveling length,  $L_0 \gg L$ , the oscillation period become large and oscillation effect is hard to detect. However, if the oscillation length is much shorter than the traveling length,  $L_0 \ll L$ , the frequency of the oscillation becomes too high and averaged probability, which reflects mixing angle, is observed. Table 1.1 shows the typical energy and the traveling length as well as the sensitivity to the mass difference for the various neutrino sources.

Table 1.1: The typical traveling length and the energy of neutrino for various neutrino sources.

Source	Traveling length ( $L$ ) [km]	Energy ( $E$ ) [MeV]	Mass difference ( $\Delta m^2$ ) [ $\text{eV}^2$ ]
Short baseline reactor	1	$\sim 3$	$10^{-3}$
Long baseline reactor	$10^2$	$\sim 3$	$10^{-5}$
Long baseline accelerator	250 – 1000	600 – several 1000	$10^{-3}$
Atmospheric	$10^4$	$10^3$	$10^{-4}$
Solar	$10^8$	1 – 10	$10^{-11}$

In the case of the solar neutrino observation, it is convenient to define the survival probability that a neutrino created as an electron neutrino will be observed as an electron neutrino. It is written as

$$P_{\nu_e \rightarrow \nu_e} = 1 - P_{\nu_e \rightarrow \nu_x} = 1 - \sin^2 2\theta \sin^2 \left( \frac{\Delta m^2 L}{4E} \right).
 \tag{1.2.8}$$

---

<sup>3</sup>The CP violating phase  $\delta$  is also including the goal of the neutrino oscillation experiments. However, it is hard to measure.

## 1.2.2 Matter enhanced oscillation

The neutrino oscillation framework discussed above assumes that neutrinos travel in vacuum. When neutrinos travel through the matter, they may undergo coherent forward scattering on electrons, protons and neutrons. All neutrinos flavors can interact with matter via a neutral current  $Z$  boson exchange interaction while only  $\nu_e$  can interact with electrons in matter via a charged current  $W^\pm$  boson exchange interaction. The charged current interaction affects the oscillation transition due to the additional contribution to the Hamiltonian. The effective potentials of the different neutrino flavors are written as

$$V_e = V_{CC} + V_{NC}, \quad V_{\mu/\tau} = V_{VC}, \quad (1.2.9)$$

where NC represents the neutral current and CC represents the charged current interactions. They are expressed as

$$V_{CC} = \sqrt{2}G_F N_e, \quad V_{NC} = -\frac{\sqrt{2}}{2}G_F N_n, \quad (1.2.10)$$

where  $G_F$  is the weak coupling constant and  $N_{e/n}$  are the number density of electrons or neutrons in matter<sup>4</sup>. For the two flavor mixing case, the time evolution of the mass eigenstates is governed by

$$i\frac{d}{dt} \begin{pmatrix} \nu_1 \\ \nu_2 \end{pmatrix} = \begin{pmatrix} E_1 & 0 \\ 0 & E_2 \end{pmatrix} \begin{pmatrix} \nu_1 \\ \nu_2 \end{pmatrix}. \quad (1.2.11)$$

Then, it is converted into the flavor basis as

$$i\frac{d}{dt} \begin{pmatrix} \nu_e \\ \nu_\mu \end{pmatrix} = U \begin{pmatrix} E_1 & 0 \\ 0 & E_2 \end{pmatrix} U^\dagger \begin{pmatrix} \nu_e \\ \nu_\mu \end{pmatrix} \quad (1.2.12)$$

$$= \begin{pmatrix} -\frac{\Delta m^2}{4E} \cos 2\theta & \frac{\Delta m^2}{4E} \sin 2\theta \\ \frac{\Delta m^2}{4E} \sin 2\theta & \frac{\Delta m^2}{4E} \cos 2\theta \end{pmatrix} \begin{pmatrix} \nu_e \\ \nu_\mu \end{pmatrix}. \quad (1.2.13)$$

The additional contribution from the charged current interaction is put into the (1, 1) element of the matrix, hence it is expressed as

$$i\frac{d}{dt} \begin{pmatrix} \nu_e \\ \nu_\mu \end{pmatrix} = \begin{pmatrix} -\frac{\Delta m^2}{4E} \cos 2\theta + \sqrt{2}G_F N_e & \frac{\Delta m^2}{4E} \sin 2\theta \\ \frac{\Delta m^2}{4E} \sin 2\theta & \frac{\Delta m^2}{4E} \cos 2\theta \end{pmatrix} \begin{pmatrix} \nu_e \\ \nu_\mu \end{pmatrix}. \quad (1.2.14)$$

In order to diagonalize the matrix, the mixing matrix in matter,  $U_M$ , with the effective mixing angle in matter,  $\theta_M$ , is newly defined as

$$U_M = \begin{pmatrix} \cos \theta_M & \sin \theta_M \\ -\sin \theta_M & \cos \theta_M \end{pmatrix}, \quad (1.2.15)$$

where the effective mixing angle is give by

$$\tan 2\theta_M = \frac{\frac{\Delta m^2}{2E} \sin 2\theta}{\frac{\Delta m^2}{2E} \cos 2\theta - \sqrt{2}G_F N_e}. \quad (1.2.16)$$

---

<sup>4</sup>In the case of anti neutrino case, the potentials are replaced  $V_{CC} \rightarrow -V_{CC}$  and  $V_{NC} \rightarrow -V_{NC}$

The effective mixing mass difference becomes

$$\Delta m_M^2 = \Delta m^2 \sqrt{(\cos 2\theta - A)^2 + \sin^2 2\theta} \quad (1.2.17)$$

where

$$A = \frac{2\sqrt{2}G_F N_e E}{\Delta m^2}. \quad (1.2.18)$$

The form can extract the vacuum oscillation case if  $N_e \rightarrow 0$  ( $A \rightarrow 0$ ). If the parameter  $A$  satisfies the following condition

$$N_{e,\text{cirt}} = \frac{\Delta m^2}{2\sqrt{2}G_F E} \cos 2\theta, \quad (1.2.19)$$

the maximal mixing occurs. The survival probability of  $\nu_e$  propagating through a matter of constant electron density  $N_e$  can be written using the effective mixing angle and the effective mass difference as

$$P_{\nu_e \rightarrow \nu_e} = 1 - \sin^2 2\theta_M \sin^2 \left( \frac{\Delta m_M^2 L}{4E} \right). \quad (1.2.20)$$

When neutrinos travel through the matter of the Sun or the Earth, neutrino oscillation can be affected due to their high electron density. The matter effect was introduced by Wolfenstein [17, 18], then the resonance effect was applied by Mikheyev and Smirnov [19]. The probability for the flavor transition can be significantly increased even though the oscillation effect is small in vacuum.

In the high electron density condition, the mixing angle and the mass difference are converted into the effective mixing angle and the effective mass difference given by equation (1.2.16) and (1.2.17). Then the survival probability is calculated by equation (1.2.20).

Using the effective mixing angle and the effective mass difference, flavor eigenstates are expressed as

$$\nu_e = \nu_{M_1} \cos \theta_M + \nu_{M_2} \sin \theta_M, \quad (1.2.21)$$

$$\nu_x = -\nu_{M_1} \sin \theta_M + \nu_{M_2} \cos \theta_M, \quad (1.2.22)$$

where it is assumed that  $M_1 > M_2$ .

If the electron density is small ( $N_e \ll N_{e,\text{cirt}}$ ), the electron neutrino  $\nu_e$  mainly coincides with the low mass eigenstate  $\nu_{M_1}$  while the other flavor neutrino  $\nu_x$  coincides with the other mass eigenstate  $\nu_{M_2}$ . For example, inside of the core of the Sun, where the electron density is large ( $N_e \gg N_{e,\text{cirt}}$ ),  $\nu_{M_2}$  of  $\nu_e$  varies with the electron density (proportion to  $N_e$ ) while  $\nu_{M_1}$  of  $\nu_x$  is not affected. Thus, the electron neutrino created in the solar interior,  $\nu_e$  is mostly  $\nu_{M_2}$ , while  $\nu_1$  is unchanged. If the electron density changes at a slow rate, no transition occurs between the mass eigenstates, hence the electron neutrino remains  $\nu_{M_2}$  and then change to the other flavor  $\nu_x$  at the surface of the Sun, because of the small (zero) electron density. Figure 1.1 shows the two eigenvalues of  $m_\nu^2$  as a function of the electron density.

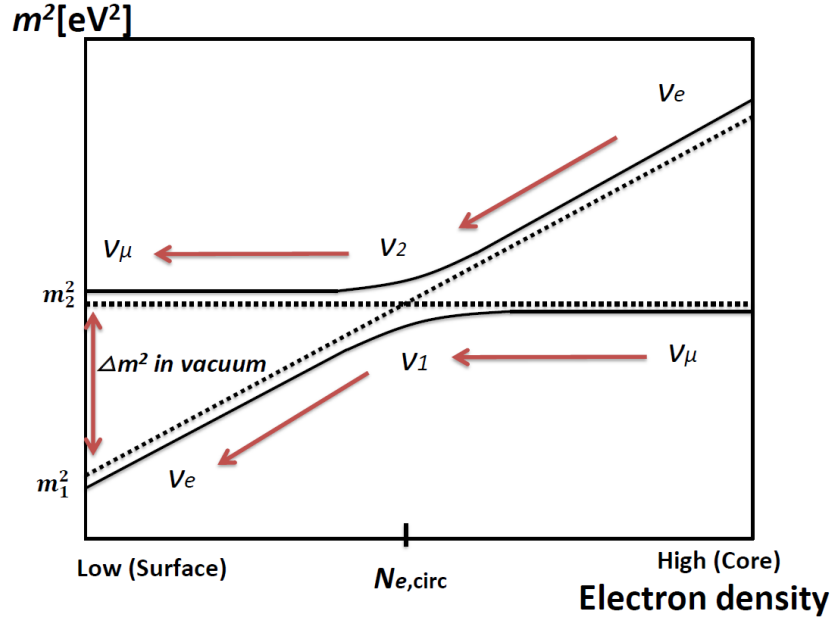


Figure 1.1: A visual explanation of the neutrino mass eigenstates in matter. The horizontal axis shows the electron density and the vertical axis shows the mass difference. The original figure was drawn by Bethe in 1986 [20].

## 1.3 Current status of Neutrino properties

### 1.3.1 Generation of Neutrino

The generation of neutrinos has not been determined yet. However, it is known that there are at least three generations,  $\nu_e$ ,  $\nu_\mu$  and  $\nu_\tau$ . The LEP experiment measured the total width of the  $Z^0$  resonance and gives the number of light neutrino generations below 45 GeV. According to the combined result reported in [21], the number of light neutrino species is determined to be

$$N_{\text{eff}} = 2.9840 \pm 0.0082(\text{stat.} + \text{syst.}). \quad (1.3.1)$$

The left of Figure 1.2 shows the measurement result which favors the three generation of the light neutrinos.

Furthermore, the Planck satellite released the cosmological constrain on the generation of neutrinos. The right of Figure 1.2 shows the experimental result in 2013 [22]. The Planck result shows that

$$N_{\text{eff}} = 3.52_{-0.45}^{+0.48}(95\% \text{ C.L.}). \quad (1.3.2)$$

### 1.3.2 Oscillation parameters

Currently, all mixing angles ( $\theta_{12}$ ,  $\theta_{23}$  and  $\theta_{13}$ ) are experimentally measured. All of them are non-zero values. Both mass differences of  $\Delta m_{21}^2$  and  $\Delta m_{31}^2$  are also measured. Sign of  $\Delta m_{21}^2$  is determined to be positive but the sign of  $\Delta m_{31}^2$  has not been determined yet.

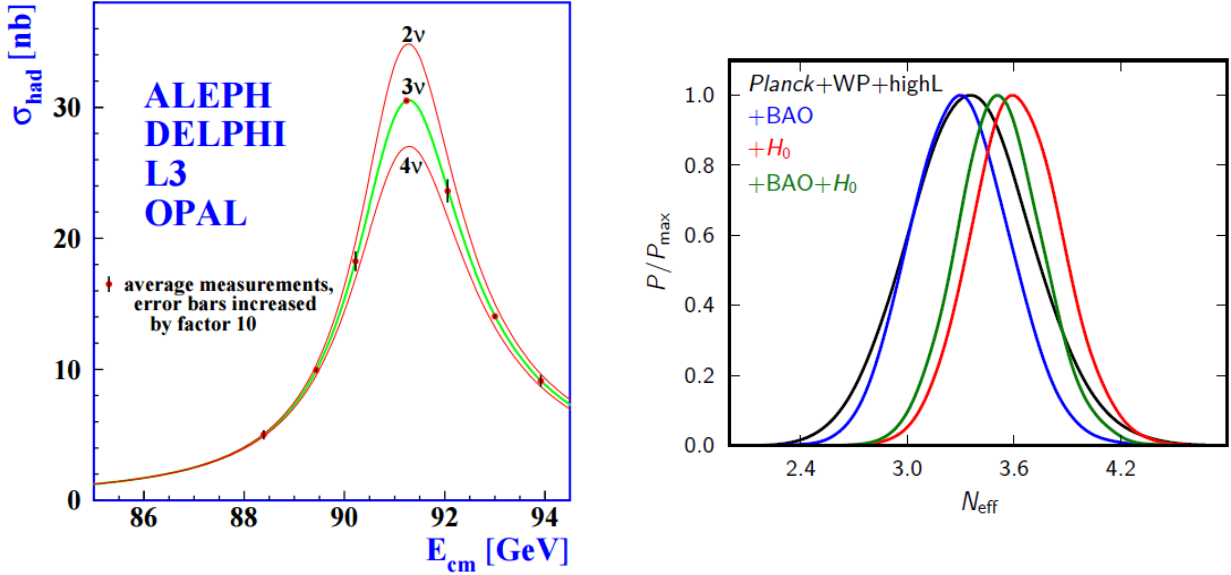


Figure 1.2: Left: The resonance of the  $Z^0$  boson measured at LEP in CERN [21]. Right: The distribution of  $N_{\text{eff}}$  for Planck+WP+highL (black) and additionally BAO (blue), the  $H_0$  measurement (red), and both BAO and  $H_0$  (green) [22].

The first angle  $\theta_{12}$  is basically measured by the solar neutrino experiments and the KamLAND experiment [23, 24]. The detail of these measurements are described in the next chapter. Atmospheric neutrino and long baseline neutrino experiments are sensitive to the second angle  $\theta_{23}$ . So far, Super-Kamiokande [11, 25], K2K (KEK to Kamioka)[26], MINOS [27, 28, 29, 30] and T2K (Tokai to Kamioka) [31, 32] experiments have contributed to measure  $\theta_{23}$ . The first indication of the finite  $\theta_{13}$  was given by the T2K experiment by the discovery of  $\nu_e$  appearance from the  $\nu_\mu$  beam [33]. Now  $\theta_{13}$  is measured precisely by Daya Bay [34, 35, 36], RENO [37] and Double Chooz [38, 39] experiments.

Because of the very precise determination of the mixing angle  $\theta_{13}$  by the reactor experiments, the CP phase can be discussed at the T2K experiment [40]. The recent best fit parameters are summarized in Table 1.2 [41].

Table 1.2: The best fit values after Neutrino 2014 [41]. There are two possibility of the mass hierarchy, i.e. Normal hierarchy or Inverted hierarchy.

Parameter	Best fit result ( $1\sigma$ ) [ NH (IH)]
$\Delta m_{21}^2$ [ $10^{-5}$ eV $^2$ ]	$7.60^{+0.19}_{-0.18}$
$ \Delta m_{31}^2 $ [ $10^{-3}$ eV $^2$ ]	$2.48^{+0.05}_{-0.07}$ ( $2.38^{+0.05}_{-0.06}$ )
$\sin^2 \theta_{12}$	$0.323 \pm 0.016$
$\sin^2 \theta_{23}$	$0.567^{+0.032}_{-0.124}$ ( $0.573^{+0.025}_{-0.039}$ )
$\sin^2 \theta_{13}$	$0.0226 \pm 0.0012$ ( $0.0229 \pm 0.0012$ )
$\delta/\pi$	$1.41^{+0.55}_{-0.40}$ ( $1.48 \pm 0.31$ )

# Chapter 2

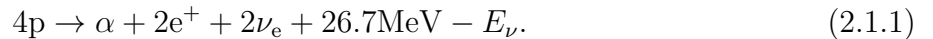
## Solar neutrino physics

### 2.1 The Sun

#### 2.1.1 Standard Solar Model

The Standard Solar Model (SSM) is the well-established theoretical model which has been constructed to explain the stellar evolution of the Sun [42]. It predicts the expected solar neutrino fluxes which are produced via various nuclear fusion reactions in the core of the Sun. This model has been revised several times<sup>1</sup> based on the updated of input parameters and etc.

The Sun has been generating its energy for a long time via nuclear fusion reactions. The process to generate the energy is the net thermonuclear reaction in the core, i.e. the fusion of four protons into a  ${}^4\text{He}$ , two positrons and two electron neutrinos. This process is written as



This reaction actually proceeds via two different chains, the one is the pp-chain and the other is the Carbon-Nitrogen-Oxygen (CNO) cycle as shown in Figure 2.1. According to the SSM, 98.4% of the total solar luminosity is produced by the pp-chain process while the rest of 1.6% is produced by the CNO cycle. The detail of these reactions are described in subsection 2.1.3.

#### 2.1.2 Properties of the Sun

Based on the SSM, various properties of the interior of the Sun are predicted. The Sun is assumed to be in hydrostatic equilibrium, so the radiation and the pressure should balance the gravity of matter inside the Sun. Figure 2.2 shows the distributions of the luminosity and the pressure. According to the left of Figure 2.2, one half (95%) of the photon luminosity is produced within  $\leq 0.09R_\odot$  ( $\leq 0.2R_\odot$ ). The luminosity information is sensitive to the solar neutrino flux because both are produced by the nuclear fusion reactions in the deep interior.

The chemical component of the Sun is important because it is sensitive to the nuclear fusion reactions. In addition, its fractional abundances are important to determined the stellar opacity. The local abundances of the isotopes are predicted as shown in the left of Figure 2.3. It is assumed that the  ${}^1\text{H}$  fraction is the highest in the interior of the Sun. The abundance of

---

<sup>1</sup>For example, BP98 [43], BP 2000 [44], BP2004 [45] and so on.

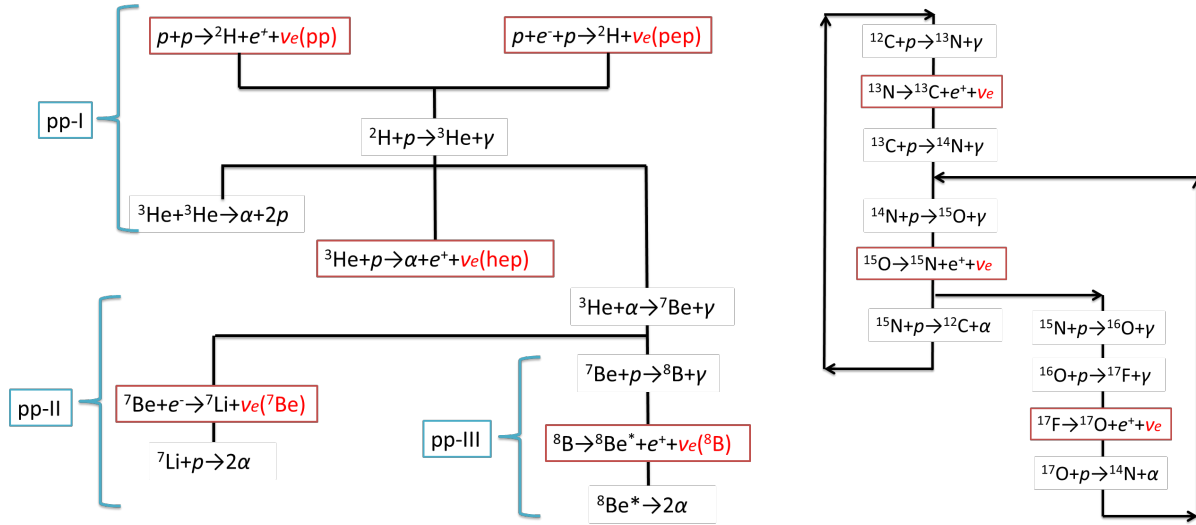


Figure 2.1: The schematic view of the pp-chain (left) and the CNO cycle (right).

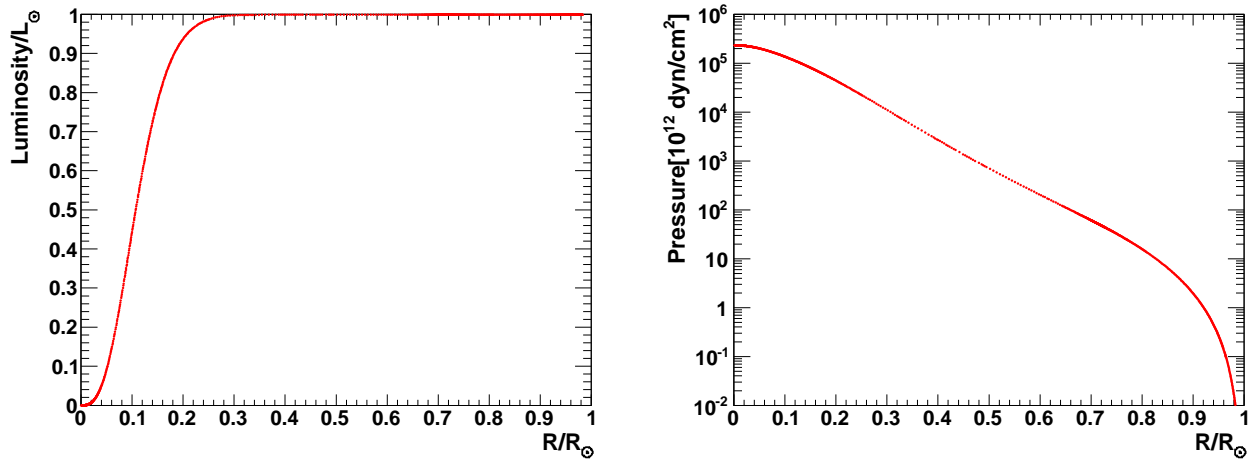


Figure 2.2: The distribution of the luminosity (left) and the pressure (right) as a function of  $R/R_\odot$ . The values were taken from the web site of John Bahcall's [46, 47].

$^4\text{He}$  increases with the nuclear fusion of  $^1\text{H}$  in the solar interior. Furthermore,  $^3\text{He}$  has a strong peak around  $R_\odot = 0.3$  because  $^3\text{He}$  is used for the reaction rapidly within  $\leq 0.3R_\odot$ . The left of Figure 2.3 shows the fraction of the mass in the Sun.

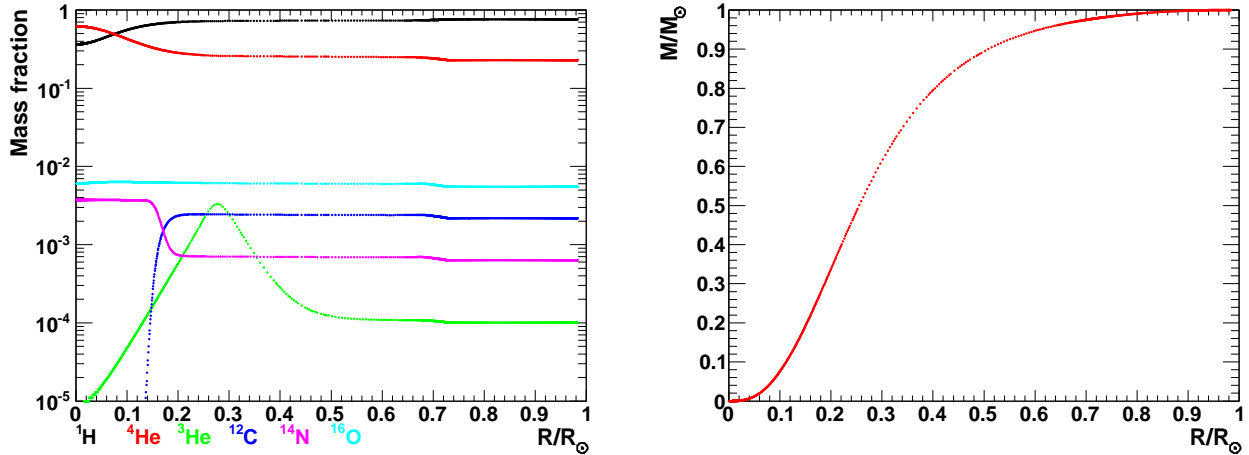


Figure 2.3: The distribution of the chemical abundance of each isotope (left) and the mass fraction (right) as a function of  $R/R_\odot$ . The values were taken from the web site of John Bahcall's [46, 47].

The electron density and the temperature in the Sun are also predicted as shown in Figure 2.4. The electron density decreases much more rapidly than the temperature. The temperature contributes to the production rate of the solar neutrinos. Especially, the flux of  $^8\text{B}$  solar neutrinos is significantly affected by the profile of the temperature. The electron density in the Sun is sensitive to the MSW effect of neutrino oscillations.

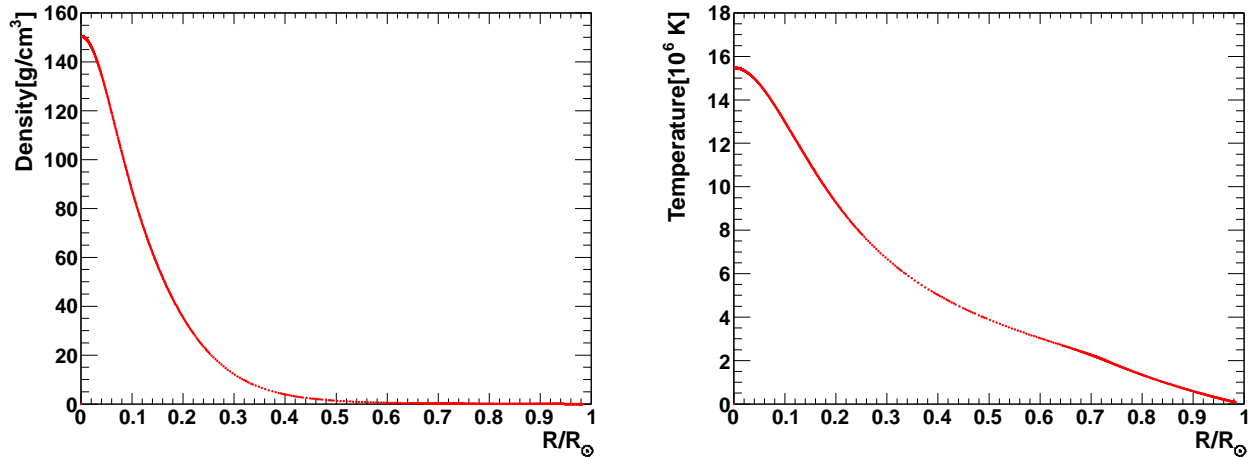


Figure 2.4: The distribution of the electron density (left) and the temperature (right) as a function of  $R/R_\odot$ . The values were taken from the web site of John Bahcall's [46, 47].

### 2.1.3 Solar Neutrino

As described in section 2.1, the energy is produced by the pp-chain and the CNO cycle. The pp-chain proceeds via five reactions while the CNO cycle proceeds via multiple branches.

The five reactions within the pp-chain produce neutrinos. They are described as

$$p + p \rightarrow {}^2\text{H} + e^+ + \nu_e (\leq 0.420 \text{ MeV}), \quad (2.1.2)$$

$$p + e^- + p \rightarrow {}^2\text{H} + \nu_e (1.442 \text{ MeV}), \quad (2.1.3)$$

$${}^7\text{Be} + e^- \rightarrow {}^7\text{Li} + \nu_e (0.861 \text{ MeV}(90\%), 0.383 \text{ MeV}(10\%)), \quad (2.1.4)$$

$${}^8\text{B} \rightarrow {}^8\text{Be}^* + e^+ + \nu_e (\leq 14.06 \text{ MeV}), \quad (2.1.5)$$

$${}^3\text{He} + p \rightarrow {}^4\text{He} + e^+ + \nu_e (\leq 18.77 \text{ MeV}), \quad (2.1.6)$$

which are called, *pp*, *pep*,  ${}^7\text{Be}$ ,  ${}^8\text{B}$  and *hep* solar neutrinos in order. The *pep* and  ${}^7\text{Be}$  solar neutrinos are mono-energetic while *pp*,  ${}^8\text{B}$  and *hep* solar neutrinos distribute below their own maximum energy.

The CNO cycle is a complex reaction cycle as shown in the right of Figure 2.1. Electron neutrinos are produced by the following three reactions:

$${}^{13}\text{N} \rightarrow {}^{13}\text{C} + e^+ + \nu_e (\leq 1.27 \text{ MeV}), \quad (2.1.7)$$

$${}^{15}\text{O} \rightarrow {}^{15}\text{C} + e^+ + \nu_e (\leq 1.73 \text{ MeV}), \quad (2.1.8)$$

$${}^{17}\text{F} \rightarrow {}^{17}\text{O} + e^+ + \nu_e (\leq 1.74 \text{ MeV}). \quad (2.1.9)$$

The left of Figure 2.5 shows the solar neutrino energy spectrum at the Earth predicted by the SSM [46]. In addition, the right of Figure 2.5 shows the fraction of the production rate as a function of the radius inside the Sun. The difference of the production position is caused by the composition of atoms, temperature and gravity. Due to the strong temperature dependence of  ${}^8\text{B}$  solar neutrinos, their production occur in the small region below  $\sim 0.1R_\odot$ . The production of  ${}^7\text{Be}$  occurs in the region between the  ${}^8\text{B}$  and *pp*. The *hep* solar neutrino distributes relatively in the wide region below  $0.3R_\odot$ .

Table 2.1 summarizes the solar neutrino fluxes predicted by the BP 2004 SSM [45].

Table 2.1: The predicted solar neutrino fluxes [45].

Type	BP 2004 flux [ $\text{cm}^2/\text{sec}$ ]
<i>pp</i>	$5.94(1 \pm 0.01) \times 10^{10}$
<i>pep</i>	$1.4(1 \pm 0.02) \times 10^8$
${}^7\text{Be}$	$4.86(1 \pm 0.12) \times 10^9$
${}^8\text{B}$	$5.79(1 \pm 0.23) \times 10^6$
<i>hep</i>	$7.88(1 \pm 0.16) \times 10^3$
${}^{13}\text{N}$	$5.71(1^{+0.37}_{-0.35}) \times 10^8$
${}^{15}\text{O}$	$5.03(1^{+0.43}_{-0.39}) \times 10^8$
${}^{17}\text{F}$	$5.91(1 \pm 0.44) \times 10^6$

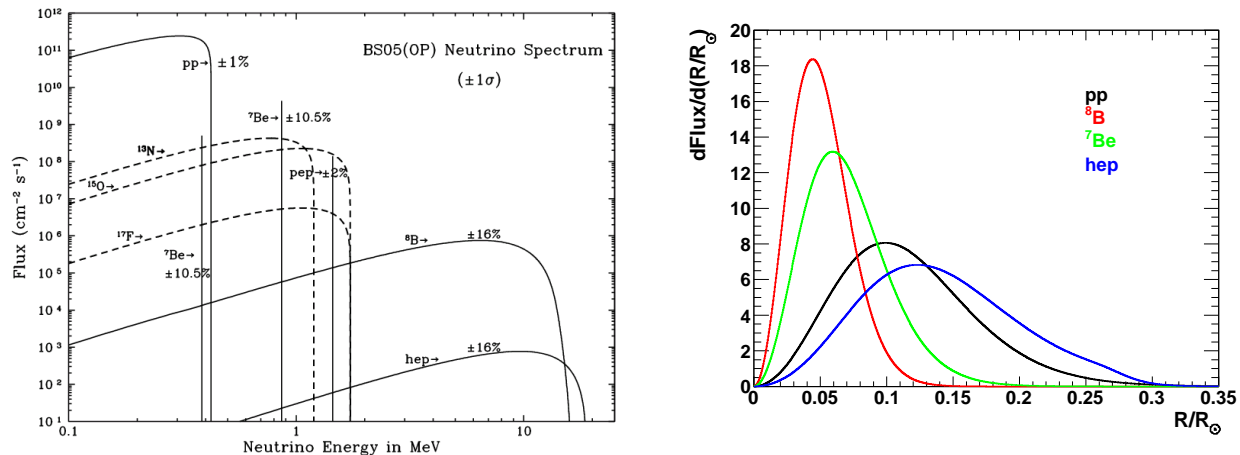


Figure 2.5: Left: The solar neutrino energy spectrum predicted by the BP05 (OP) [46]. The horizontal axis shows the neutrino energy [MeV] and the vertical axis shows the expected flux at the earth [ $1/\text{cm}^2/\text{sec}$ ]. Right: The local production rate of the  $pp$ ,  $^7\text{Be}$ ,  $^8\text{B}$  and  $hep$  solar neutrinos. The horizontal axis shows the radius of the sun and the vertical axis shows the fraction of the production rate. The values are taken from the web site of John Bahcall’s homepage [46, 47].

## 2.1.4 Solar activity

The solar activity influences the environments of the Earth. It is known that the solar activity has a periodic cycle, i.e. the 11 years modulation. The solar activity has been measured using the sunspot number (Wolf number) introduced by R. Wolf [48]<sup>2</sup>. The sunspot number has been recorded for more than 300 years. The sunspot which is releasing the magnetic flux appears at the surface of the Sun. When the solar activity is in an active phase, the sunspot number becomes large. Thus, its appearance is strongly correlated with the solar activity cycle. Figure 2.6 shows the time variation of the sunspot number from around 1750.

The magnetic field of the Sun has been measured by the Wilcox Solar Observatory at the surface of the Earth. It started the measurement in 1975. Figure 2.7 shows the time variation of the sunspot number during the cycle 21 through 24 as well as the time variation of the mean magnetic field and the magnetic field at the pole of the Sun. Recently, the solar cycle 24 is not active compared with other cycles as indicated by the smaller sunspot number at the maximum. When the sunspot number is large, the mean magnetic field is also large while the magnetic field at the pole is small. The reversal of the magnetic field at the pole happens when the solar activity is at the maximum. According to these measurements, it is obvious that the solar activity is strongly correlated with the magnetic field of the Sun.

It is interesting to check whether the solar neutrino flux is correlated with the solar activity

<sup>2</sup> It is globally used to measure or estimate the solar activity. It is defined as

$$R = k(10g + f), \quad (2.1.10)$$

where the parameter  $g$  is the number of the sunspot groups on the Sun,  $f$  is the total number of all sunspot in these groups at the time of the observation and  $k$  is “reduction factor” to convert the counts of other observations onto a uniform scale.  $k$  depends on various things, for example atmospheric condition, instrument of the measurement devices and so on.

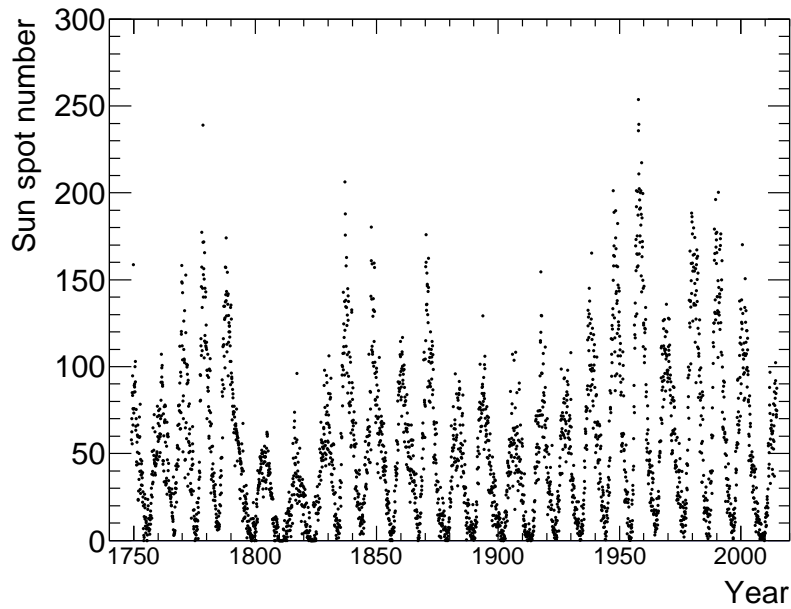


Figure 2.6: The time variation of sun spot number. The plots shows the monthly average of the sunspot. These numbers are taken from the web site of NASA [49].

cycle or not. Because the solar neutrinos are produced in the core of the Sun as shown in the right of Figure 2.5 while the appearance of the sunspot is the phenomenon at the surface of the Sun.

## 2.2 Solar Neutrino Experiment

### 2.2.1 Homestake Chlorine Experiment

The first solar neutrino experiment was the Homestake experiment which used 615 tons of tetrachloroethylene,  $C_2Cl_4$ , for the target of neutrinos [7]. The detector was constructed in the Homestake gold mine at South Dakota in the U.S. It was located 1478 m below the surface, which corresponds to  $\sim 4200$  m water equivalent. The Homestake experiment had already finished data taking in 1994 and had taken the data for about 25 years.

The detection method for solar neutrinos is the absorption on chlorine



The energy threshold is 0.814 MeV and it is sensitive to  ${}^7\text{Be}$ ,  ${}^8\text{B}$ ,  $pep$  and CNO solar neutrinos. The appearance of argon atom in the detector indicates the absorption interaction of a solar neutrino in a chlorine atom.

To count the rate of the interactions, the detector was exposed for 1 – 3 months and then the generated argons were extracted by purging the tank with He gas. After collecting argon atoms,  ${}^{37}\text{Ar}$  decays, whose half-life is 35.0 days, were counted by a low background proportional counter.

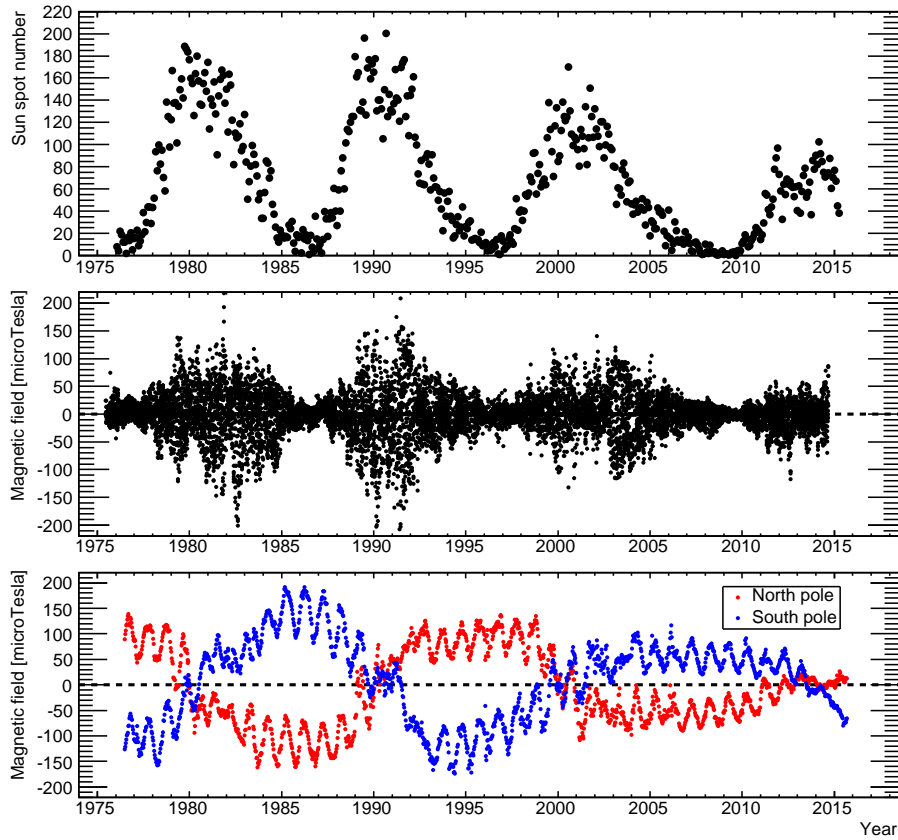


Figure 2.7: The time variation of sunspot number and the magnetic fields observed by Wilcox Solar Observatory. The corresponding period is from the cycle 21 through the cycle 24. The sunspot number (top panel) is taken from the web site of NASA [49]. The mean magnetic field is taken from the web site of The Wilcox Solar Observatory [50]. The magnetic fields at the solar poles are also taken from the web site of the Wilcox Solar Observatory [51].

The average of the measured capture rate over 25 years is

$$R_{Cl} = 2.56 \pm 0.16(\text{stat.}) \pm 0.16(\text{syst.}) \text{ SNU}, \quad (2.2.2)$$

where SNU (Solar Neutrino Unit) is the number of the interactions per  $10^{36}$  target atoms per second. However, this capture rate is significantly lower than the prediction of the SSM, which is  $9.30^{+1.2}_{-1.4}$  SNU. This discrepancy had been called “the solar neutrino problem”. The left of Figure 2.8 shows the result of the yearly neutrino capture (Argon production) rate from 1970 to 1994 [52].

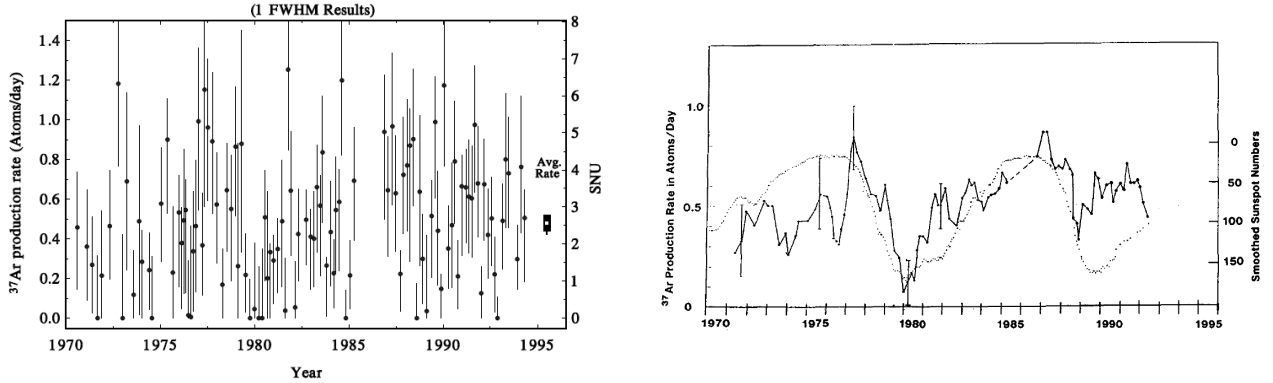


Figure 2.8: Left: The  $^{37}\text{Ar}$  production rate as a function of time [52]. The horizontal axis shows the data from 1970 to 1994 and the vertical axis shows the production rate. Right: The correlation between the production rate and the sunspot numbers [53]. The horizontal axis shows the date. The horizontal axis shows the production rate as well as the inverse of the sunspot number.

Since Homestake experiment had taken the data for about 25 years, this long operation period spanned the solar cycle 20, 21 and 22. The right of Figure 2.8 also shows the time variation of the production rate vs. the inverse of the sunspot number. It seems that the production rate is anti-correlated with the sunspot number (solar activity) but its statistical significance was not high (61% significance level) [54].

## 2.2.2 Kamiokande

The solar neutrino measurement at the Kamioka Nucleon Decay Experiment (Kamioka-NDE) began in 1987 and data was taken until 1995 [55, 56]. Its detector was constructed in the Ikenoyama mountain at Gifu prefecture in Japan. It was located  $\sim 1000$  m below the top of the mountain, which corresponds to  $\sim 2700$  m water equivalent. The detector was a cylindrical tank whose diameter was 15.6 m and height was 16.1 m. It hold 680 tons of ultra pure water in the fiducial volume ( $> 2$  m from the wall).

The detection method for solar neutrinos is the elastic scattering of electrons [8]. The elastic scattering provides with the directional information of neutrinos. Because of this detection method, the Kamiokande detector observed solar neutrinos in real-time for the first time in the world. The left of Figure 2.9 shows the solar angle distribution observed by Kamiokande-III. The solar neutrino signals are clearly seen around  $\cos\theta_{\text{sun}} = 1$ , thus this detector confirmed

signals really comes from the Sun. In addition, the recoil electron spectrum was measured as shown in the right of Figure 2.9.

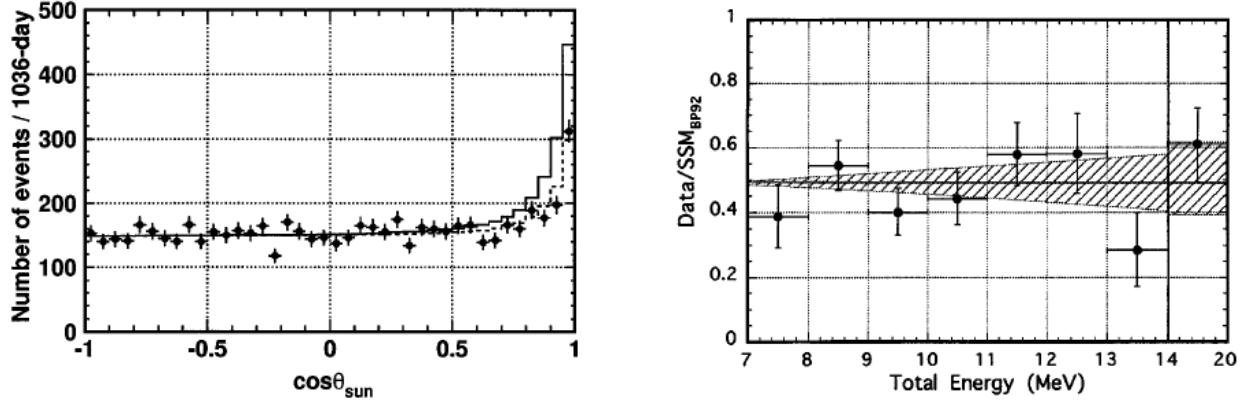


Figure 2.9: Left: The solar angle ( $\cos \theta_{\text{sun}}$ ) distribution using 1036 days data of Kamiokande-III [57]. The horizontal axis shows the solar angle  $\cos \theta_{\text{sun}}$  and the vertical axis shows the number of the events per 1036 days. The clear peak around  $\cos \theta_{\text{sun}} = 1$  indicated the solar neutrino signal. The black solid histograms illustrate the prediction of the SSM and the dashed ones illustrate the best fit result. Right: The ratio of the observed energy spectrum to the prediction of SSM above 7.0 MeV. The horizontal axis shows the total energy [MeV] and the vertical axis shows the ratio [57].

The flux of  $^8\text{B}$  solar neutrinos was measured using the combined 2079 days data [57] as

$$\Phi_{^8\text{B},\text{Kamiokande}} = 2.80 \pm 0.19(\text{stat.}) \pm 0.33(\text{syst.}) \times 10^6/\text{cm}^2/\text{sec}. \quad (2.2.3)$$

Compared with the prediction of the SSM, the ratio of the flux to the prediction is

$$\frac{\Phi_{^8\text{B},\text{Kamiokande}}}{\text{SSM}} = 0.492^{+0.034}_{-0.033}(\text{stat.}) \pm 0.058(\text{syst.}). \quad (2.2.4)$$

Kamiokande also confirmed the deficit of the solar neutrino flux.

Kamiokande observed the solar neutrinos for about 12 years, this period covered the solar cycle 22. The left (right) of Figure 2.10 shows the time variation of the measured  $^8\text{B}$  solar neutrino flux (the number of the sunspot number). According to the experimental result, there was no statistically significant correlation between them.

### 2.2.3 Gallium Experiments

There were two experiments using gallium since 1990. One was the Soviet American Gallium Experiment (SAGE) in Russia, which used 50 tons of metallic gallium [59]. The other was GALLEX experiment in Gran Sasso in Italy, which used 30.3 tons of gallium in form of  $\text{GaCl}_3 - \text{HCl}$  [60]. After the end of the GALLEX experiment, Gallium Neutrino Observatory (GNO) started data taking in 1998 [61].

The detection method for solar neutrinos is the absorption on gallium



and then the produced  ${}^{71}\text{Ge}$  was extracted and counted. The energy threshold of this reaction is 0.233 keV, thus it is mainly sensitive to  $pp$  neutrinos.

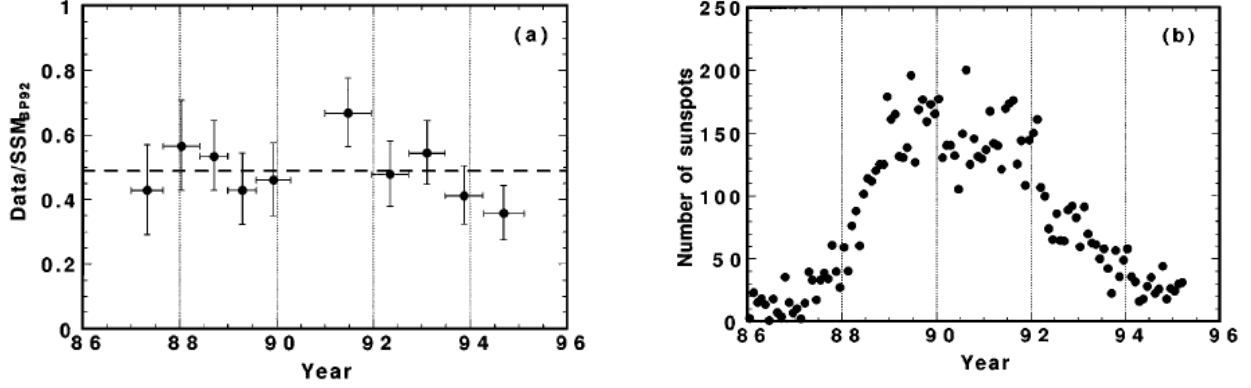


Figure 2.10: The  $^8\text{B}$  solar neutrino flux measured by Kamiokande vs the sunspot number [57]. The horizontal axis shows the date during the operation of Kamiokande. The vertical axis in the left (right) panel shows the ratio of the measured flux to the prediction of the SSM (the number of the sunspot number in the cycle 22).

## SAGE

The SAGE experiment had taken data from 1990. Its detector was located at the Baksan Neutrino Observatory in Russia. It used 55 tons of liquid metal  $^{71}\text{Ga}$  as the target. The detector was exposed for 3 weeks, then the produced Ge atoms were extracted. The  $^{71}\text{Ge}$  decays which occur only by the electron capture to the ground state of  $^{71}\text{Ga}$  were counted by a low background proportional counter.

After the 12-year observation, the average capture rate of the solar neutrino [62] is

$$R_{\text{SAGE}} = 70.8^{+5.3}_{-5.2}(\text{stat.})^{+3.7}_{-3.2}(\text{syst.}) \text{ SNU}. \quad (2.2.6)$$

This result was also inconsistent with the prediction of the SSM, which is  $128^{+9}_{-7}$  SNU. The left of Figure 2.11 shows the capture rate measured by the SAGE experiment.

## GALLEX/GNO

The GALLEX experiment had taken data from 1991 to 1997 and then the GNO experiment followed data taking from 1998 to 2003. Their detectors were located at the Gran Sasso Underground Laboratory in Italy. They exposed for 4 – 6 weeks, then the produced  $^{71}\text{Ge}$  atoms were extracted and counted. The GNO result and the combined GALLEX+GNO result [63] are

$$R_{\text{GNO}} = 62.9^{+6.0}_{-5.9}(\text{stat.} + \text{syst.}) \text{ SNU}, \quad (2.2.7)$$

$$R_{\text{GALLEX+GNO}} = 69.3 \pm 4.1(\text{stat.}) \pm 3.6(\text{syst.}) \text{ SNU}. \quad (2.2.8)$$

The two results are consistent with the one from SAGE. The right of Figure 2.11 shows the capture rate measured by GALLEX and GNO experiments. In addition, the ratio of the measured capture rate to the prediction was  $0.556 \pm 0.047(\text{stat.}) \pm 0.036(\text{syst.})$ .

Combining SAGE and GALLEX/GNO results, the gallium capture rate [64] is

$$R_{\text{Ga}} = 66.1 \pm 3.1(\text{stat.} + \text{syst.}) \text{ SNU}. \quad (2.2.9)$$

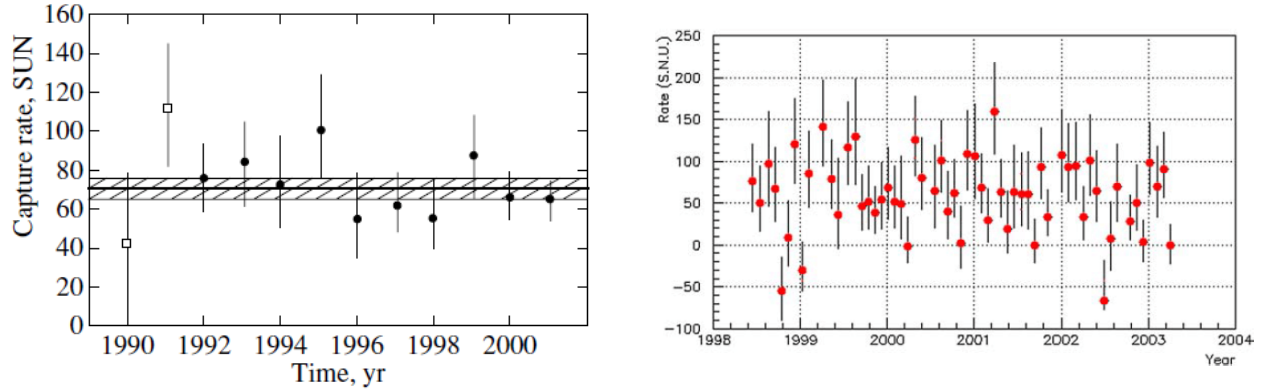


Figure 2.11: Left: The capture rate of the solar neutrino measured by SAGE experiment [62]. The horizontal axis shows the time in year and the vertical axis shows the measured rate. Right: The combined result from GALEX and GNO experiments [63]. The horizontal axis shows the time in year and the vertical axis shows the capture rate (after subtracting the side reaction described in [61]).

This is about half the prediction value, thus the gallium experiment also confirmed the solar neutrino problem.

## 2.2.4 Super-Kamiokande

The Super-Kamiokande experiment [58] is the largest water Cherenkov detector all over the world. SK has four phases, SK-I, SK-II, SK-III and SK-IV. Currently, SK-IV is running. Because of the large detector size, SK has a statistical advantage for the neutrino observation. SK can measure neutrino energy spectrum and the day night effect. Since these are the main topic of this thesis, the details of the detector and analysis will be explained in following the chapters.

## 2.2.5 SNO Experiment

The Sudbury Neutrino Observatory (SNO) experiment began in 1999. The detector was constructed in the Creighton mine near Sudbury in Canada [65]. It was located 2039 m below the surface, which corresponds to approximately  $\sim 6000$  m water equivalent. The detector holds 1000 tons of heavy water,  $D_2O$ , as the neutrino target. The merit of using heavy water was that neutrinos can be detected through the following three reactions:

$$\begin{aligned}
 \nu_e + d &\rightarrow p + p + e^-, & \text{Charged Current,} \\
 \nu_x + d &\rightarrow p + n + \nu_x, & \text{Neutral Current,} \\
 \nu_x + e^- &\rightarrow \nu_x + e^-, & \text{Elastic Scattering,}
 \end{aligned}
 \tag{2.2.10}$$

where  $\nu_x$  is any active flavor neutrinos, d is a deuteron and p is a proton. The first reaction, the charged current reaction (CC), is sensitive only to  $\nu_e$ . This reaction is observed by Cherenkov radiation of the produced electrons. Using this channel, the electron flavor solar neutrino flux can be determined. The second reaction, the neutral current reaction (NC), is the disintegration of a deuteron by a neutrino. This reaction is sensitive to the all active flavor neutrinos. This

reaction provides with the total  $^8\text{B}$  solar neutrino flux independently from active neutrino flavor oscillations. The NC reaction is identified by detecting the produced neutrons. SNO had been operated three different phases and they had different detection methods discussed later. The third reaction, the elastic scattering reaction (ES), is the same as in SK. This reaction is mainly sensitive to  $\nu_e$  with a factor of 1/6 contributions from  $\nu_{\mu/\tau}$ .

The phase I of SNO started data taking in 1999 and it used pure  $\text{D}_2\text{O}$ . The detection method of the neutrons is the absorption on deuteron



where t is a tritium. In addition, the produced neutron is sometimes absorbed on proton. Thus, in the phase I, 6.25 MeV events are detected.

The  $^8\text{B}$  solar neutrino flux is measured using the CC and ES data [66] as

$$\Phi_{^8\text{B,SNO,CC}} = 1.75 \pm 0.07(\text{stat.})_{-0.11}^{+0.12}(\text{syst.}) \times 10^6/\text{cm}^2/\text{sec}, \quad (2.2.12)$$

$$\Phi_{^8\text{B,SNO,ES}} = 2.39 \pm 0.34(\text{stat.})_{-0.14}^{+0.16}(\text{syst.}) \times 10^6/\text{cm}^2/\text{sec}. \quad (2.2.13)$$

The left of Figure 2.12 shows the first result of the SNO CC measurement. It was obvious that the NC rate measured by SNO was lower than the ES rate measured by SK. The difference between the SNO CC and the SK ES is  $(0.57 \pm 0.17) \times 10^6 / \text{cm}^2/\text{sec}$ , which is equivalent to  $3.3\sigma$  away from 0. From this discrepancy, it was clearly found that the solar neutrinos changed their flavor traveling to the Earth. The measurement result of the CC reaction provided with the information of  $\nu_e$  component in the total flux. Using the CC rate and the ES rate, other components ( $\nu_{\mu}, \nu_{\tau}$ ) are determined as

$$\Phi_{^8\text{B,SNO}}(\nu_{\mu/\tau}) = 3.69 \pm 1.13 \times 10^6/\text{cm}^2/\text{sec}, \quad (2.2.14)$$

$$\Phi_{^8\text{B,SNO}}(\nu_x) = 5.44 \pm 0.99 \times 10^6/\text{cm}^2/\text{sec}. \quad (2.2.15)$$

The total  $^8\text{B}$  flux is consistent with the prediction of the SSM. Then SNO collaboration reported the NC reaction result in 2002 [13]. In this paper, the results of the CC and NC reactions were updated:

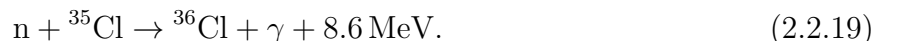
$$\Phi_{^8\text{B,SNO,CC}} = 1.76_{-0.05}^{+0.06}(\text{stat.}) \pm 0.09(\text{syst.}) \times 10^6/\text{cm}^2/\text{sec}, \quad (2.2.16)$$

$$\Phi_{^8\text{B,SNO,ES}} = 2.39_{-0.23}^{+0.24}(\text{stat.}) \pm 0.12(\text{syst.}) \times 10^6/\text{cm}^2/\text{sec}, \quad (2.2.17)$$

$$\Phi_{^8\text{B,SNO,NC}} = 5.09_{-0.43}^{+0.44}(\text{stat.})_{-0.43}^{+0.46}(\text{syst.}) \times 10^6/\text{cm}^2/\text{sec}. \quad (2.2.18)$$

The NC flux measurement result was higher than CC flux, hence this results showed the strong evidence of the solar neutrino oscillation because the NC reaction is sensitive to the all active flavor neutrinos while the CC reaction is sensitive only to the electron type neutrino. The right of Figure 2.12 shows the possible flavor components of the active neutrinos.

The phase II (Salt phase) began in 2001 [67]. In this phase, more than 2 tons of NaCl was dissolved to the detector to improve the detection efficiency of the NC reaction. The neutron captured on Cl releases a  $\gamma$  cascade whose energy is  $\sim 8.6$  MeV as



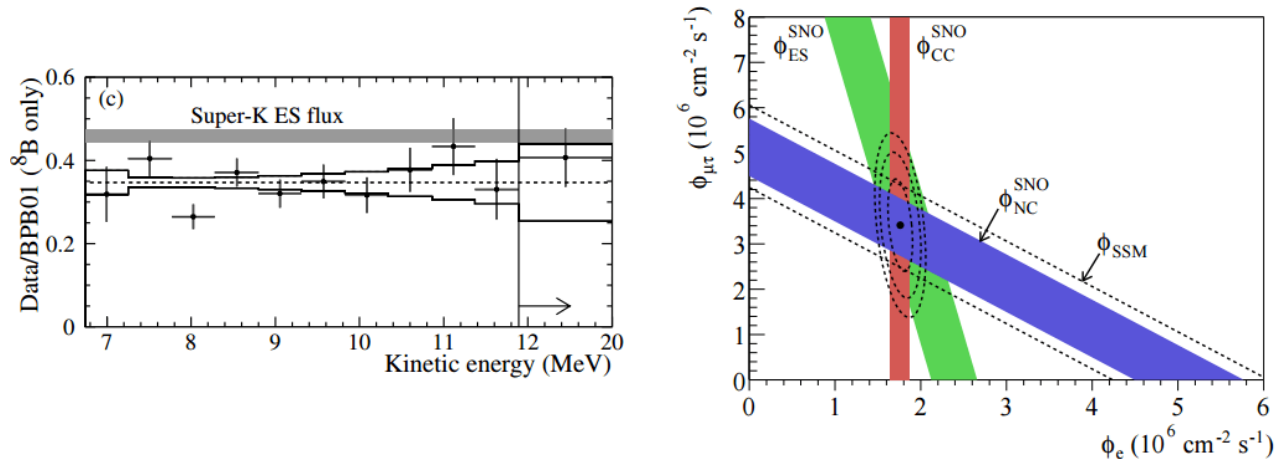


Figure 2.12: Left: The CC measurement result by SNO [66]. The horizontal axis shows the electron kinetic energy and the vertical axis shows the ratio of the CC reaction to the SSM (BPB01) prediction. The gray band illustrates the SK ES rate. Right: The measurement of the <sup>8</sup>B solar neutrino flux using the three different reactions by SNO [13]. The horizontal axis shows the flux of electron flavor neutrino and the vertical axis shows the flux of the other type of flavor ( $\mu/\tau$ ) in unit of  $[\times 10^6/\text{cm}^2/\text{sec}]$ . The brown, blue and green bands shows the CC, NC and ES result by SNO, respectively.

The measured <sup>8</sup>B solar neutrino flux of phase II [68] is

$$\Phi_{\text{sB,SNO,NC}} = 4.94 \pm 0.21(\text{stat.})_{-0.34}^{+0.38}(\text{syst.}) \times 10^6/\text{cm}^2/\text{sec}, \quad (2.2.20)$$

which is consistent with the result of phase I.

The phase III (NCD array phase) started data taking in 2004 [69]. In this phase, the salt was removed, while 36 strings of <sup>3</sup>He proportional counters were installed in the detector. Due to <sup>3</sup>He's large cross section for thermal neutrons, the detection efficiency for the NC reaction was improved. The reaction is described as



The measured <sup>8</sup>B solar neutrino flux of phase III [70] is

$$\Phi_{\text{sB,SNO,NC}} = 5.54_{-0.31}^{+0.33}(\text{stat.})_{-0.34}^{+0.36}(\text{syst.}) \times 10^6/\text{cm}^2/\text{sec}, \quad (2.2.22)$$

This result was also consistent with the other phases.

Combining the NC results of all phases, <sup>8</sup>B solar neutrino flux is reported as [71]

$$\Phi_{\text{sB,SNO,NC}} = 5.25 \pm 0.16(\text{stat.})_{-0.13}^{+0.11}(\text{syst.}) \times 10^6/\text{cm}^2/\text{sec}. \quad (2.2.23)$$

## 2.2.6 Borexino Experiment

The Borexino experiment started data taking in 2007 [72]. It is located in Gran Sasso underground laboratory, Italy. It used low background liquid scintillator which allowed to measure

solar neutrinos below 2.0 MeV region in real-time. The first target of the Borexino experiment was  ${}^7\text{Be}$  solar neutrino whose energy is 0.862 MeV.

The LMA solution predicts a transition of the survival probability of  $\nu_e$  over the energy range of solar neutrinos. It is expected that the transition from matter enhanced oscillation around  ${}^8\text{B}$  energy range to vacuum oscillation below a few MeV including  ${}^7\text{Be}$ . Due to the transition, the survival probability increases from  $\sim 0.3$  in the high energy region to  $\sim 0.6$  in the low energy region. Therefore, the measurement of the  ${}^7\text{Be}$  solar neutrino rate can test the predicted increase in the survival probability.

The first experimental result on  ${}^7\text{Be}$  solar neutrinos was reported in 2008 [73, 74]. The latest  ${}^7\text{Be}$  solar neutrino flux [75, 76] is

$$R_{{}^7\text{Be},\text{Borexino}} = 46.0 \pm 1.5(\text{stat.})_{-1.6}^{+1.5}(\text{syst.}) \text{ counts}/(\text{day} \cdot 100\text{ton}), \quad (2.2.24)$$

$$\Phi_{{}^7\text{Be},\text{Borexino}} = 2.78 \pm 0.13(\text{stat.} + \text{syst.}) \times 10^9/\text{cm}^2/\text{sec}. \quad (2.2.25)$$

The Borexino is the first experiment which measured  ${}^7\text{Be}$  solar neutrinos.

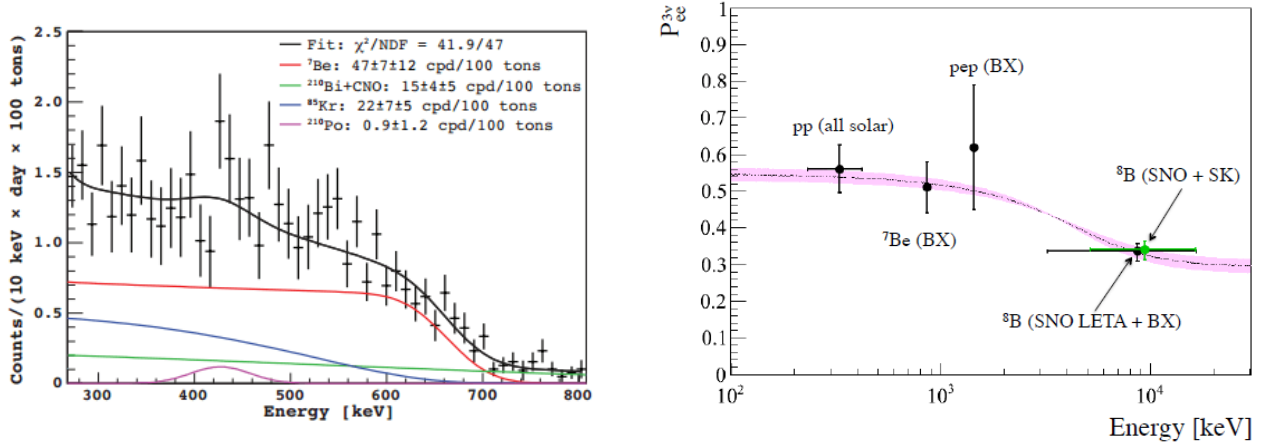


Figure 2.13: Left : The result of the  ${}^7\text{Be}$  solar neutrino rate measured by Borexino [73]. The horizontal axis shows the energy [keV] and the horizontal axis shows the count rate [counts/(10 keV $\times$ day $\times$ 100 tons)]. The black points shows the measured data and the black curve show the best fit result. Right: The survival probability of  $\nu_e$  measured by all solar neutrino experiments [76]. The horizontal axis shows the energy [keV] and the vertical axis shows the survival probability.

The  ${}^8\text{B}$  flux was also measured using the data above 3.0 MeV [77] as

$$\Phi_{{}^8\text{B},\text{Borexino}} = 2.4 \pm 0.4(\text{stat.}) \pm 0.1(\text{syst.}) \times 10^6/\text{cm}^2/\text{sec}. \quad (2.2.26)$$

Since the energy threshold of the Borexino detector is low, it can search for solar neutrinos in the wider energy range, hence it is sensitive to the  $pep$  and CNO cycle solar neutrinos. They reported on the observation of  $pep$  neutrinos [78] and set upper limit on the CNO flux [76]

$$R_{pep,\text{Borexino}} = 3.1 \pm 0.6(\text{stat.}) \pm 0.3(\text{syst.}) \text{ counts}/(\text{day} \cdot 100\text{ton}), \quad (2.2.27)$$

$$\Phi_{pep,\text{Borexino}} = 1.6 \pm 0.3(\text{stat.} + \text{syst.}) \times 10^8/\text{cm}^2/\text{sec}, \quad (2.2.28)$$

$$R_{\text{CNO},\text{Borexino}} < 7.9 \text{ counts}/(\text{day} \cdot 100\text{ton}), \quad (2.2.29)$$

$$\Phi_{\text{CNO},\text{Borexino}} < 7.7 \times 10^8/\text{cm}^2/\text{sec}, \text{ (95\% C.L.)}. \quad (2.2.30)$$

The right of the Figure 2.13 shows the survival probability as a function of the neutrino energy. Recently, they also claimed measurement of primary  $pp$  neutrinos by subtracting background from  $^{14}\text{C}$  [79].

## 2.2.7 KamLAND experiment

The KamLAND experiment started data taking from 2002 [80]. Its detector is located at the Kamiokande site in the Ikenoyama Mountain, Japan. It uses organic ultra-pure liquid scintillator in order to detect reactor neutrino  $\bar{\nu}_e$  coming from many nuclear power plants in Japan. Kamioka is a very good site for the long baseline reactor experiment because major high power reactors are located about 140 – 210 km from Kamioka. Electron-anti-neutrinos are detected by the inverse  $\beta$  decay interaction as

$$\bar{\nu}_e + p \rightarrow e^+ + n. \quad (2.2.31)$$

The prompt scintillation light is emitted from the produced position, while the produced neutron is captured by the proton and then emits  $\gamma$ -ray whose energy is 2.2 MeV with a lifetime of 200  $\mu\text{sec}$ . This delayed coincidence detection method can reduce the background event against the  $\bar{\nu}_e$  measurement. The KamLAND experiment can determine a precise value of the neutrino oscillation parameter of  $\Delta m_{21}^2$  by observing the oscillation pattern of the reactor anti-neutrino's energy spectrum. The left of Figure 2.14 shows the observed energy spectrum by KamLAND.

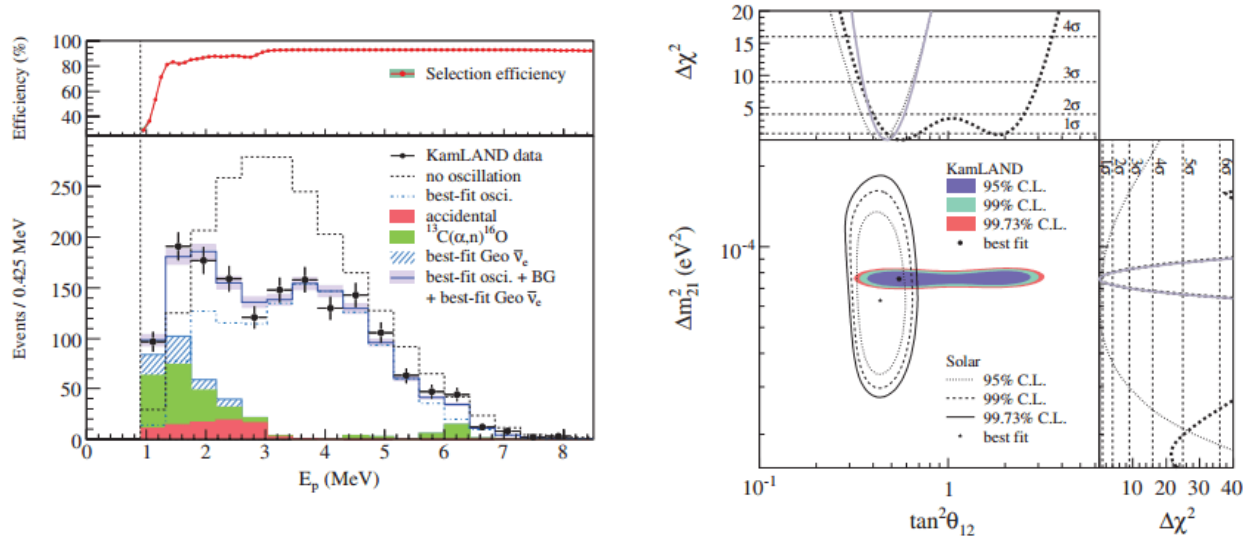


Figure 2.14: Left: Energy spectrum of prompt events of reactor neutrino events at KamLAND [80]. The horizontal axis shows the energy of the prompt signal and the vertical axis shows the event rate [Event/0.425 MeV]. Right: The oscillation parameters measured by KamLAND [80]. The horizontal axis shows  $\tan^2 \theta_{12}$  and the vertical axis shows  $\Delta m_{21}^2$  [eV $^2$ ]. The color contours are the experimental result from KamLAND, while the back lines are the result from the solar neutrino experiments.

Assuming the CPT invariance neutrino disappearance and anti-neutrino disappearance should be governed by the same oscillation parameters. So, the KamLAND reactor anti-neutrino result

can be directly compared with the solar neutrino results. The right of Figure 2.14 shows the allowed region for the neutrino oscillation parameters from KamLAND and the solar neutrino experiments.

### 2.2.8 Summary of solar neutrino experimental results

Figure 2.15 summarizes the theoretical prediction of solar neutrino flux [46] and the experimental results from solar neutrino experiments except for Borexino [81]. When the neutrino oscillation is considered, the SSM flux and the experimental results agrees very well.

**Total Rates: Standard Model vs. Experiment**  
Bahcall–Serenelli 2005 [BS05(OP)]

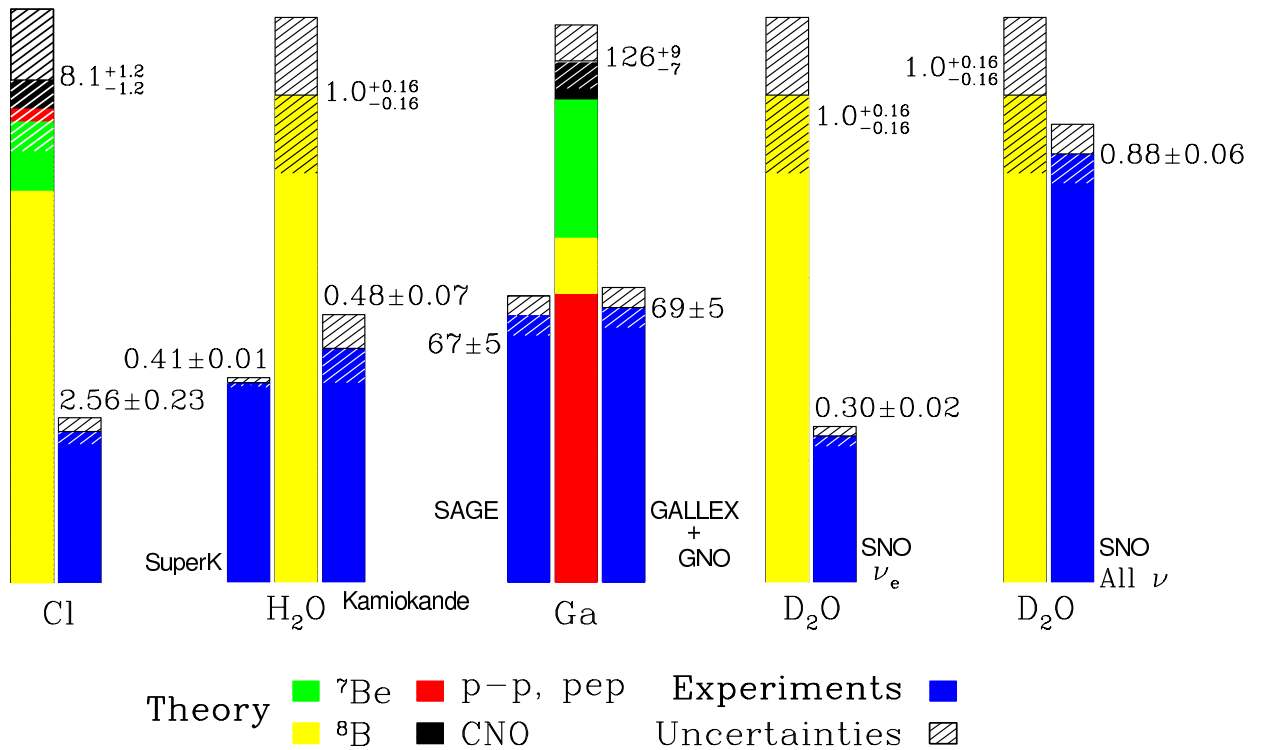


Figure 2.15: The solar neutrino flux prediction vs the experimental results [81]. The unit for Cl and Ga is SNU, while the unit for H<sub>2</sub>O and D<sub>2</sub>O is the ratio of the experimental rate over the prediction.

## 2.3 Physics motivation of this thesis

### 2.3.1 Solar neutrino flavor oscillation

The solar neutrinos are originally created as electron-neutrinos and they travel to the Earth. The survival probability in vacuum oscillation is calculated by equation (1.2.8).

The matter enhanced oscillation also happens when a neutrino travels through the Earth. In this situation, some of  $\nu_\mu$  are converted back to  $\nu_e$ . Thus, the regeneration of electron neutrinos occur. This regeneration leads to the day/night flux asymmetry.

Since the MSW effect depends on the neutrino energy, the survival probability varies with the energy. Thus, the observed energy spectrum should be distorted due to the MSW effect in the Sun. Using the solar oscillation parameters measured so far, the MSW resonance in the Sun should occur around  $\sim 3$  MeV. This resonance leads to distortion of the observed energy spectrum in SK. Figure 2.16 shows the expected survival probability of solar neutrinos, assuming that current best fit neutrino oscillation parameters obtained in subsection 13.1 in this thesis. Since the energy spectrum measurement of  $^8\text{B}$  solar neutrino reflects the survival probability, the “up-turn” in the energy spectrum of  $^8\text{B}$  solar neutrino events will be expected below  $\sim 6$  MeV.

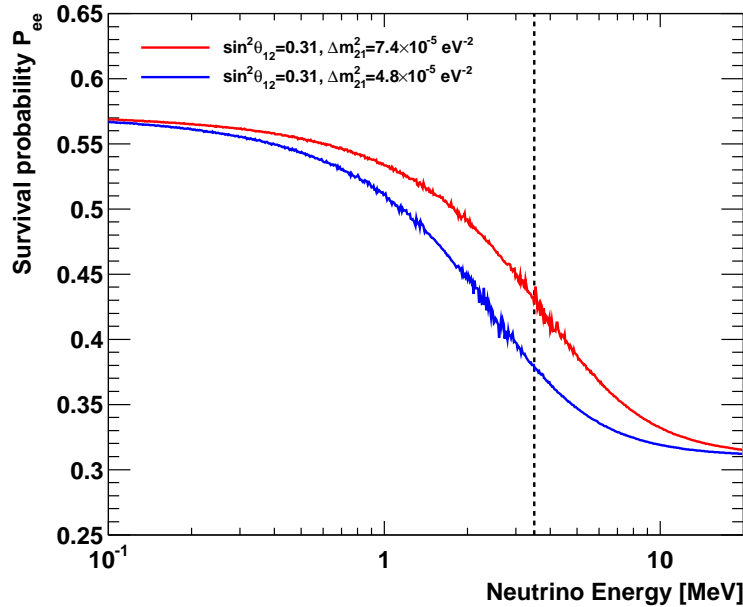


Figure 2.16: The expected survival probability of solar neutrinos. The red line shows the expectation assuming  $(\sin^2 \theta_{12}, \Delta m_{21}^2) = (0.31, 7.4 \times 10^{-5})$  while the blue line shows the expectation assuming  $(\sin^2 \theta_{12}, \Delta m_{21}^2) = (0.31, 4.8 \times 10^{-5})$ . The dotted line indicates 3.5 MeV of neutrino energy.

### 2.3.2 Analysis target

The main physics target of this thesis is to observe the matter effect. The two methods are conceivable to observe it. The one is the energy spectrum measurement and the other is the day/night flux asymmetry measurement.

In addition, current interest in the field of neutrino physics is to measure the CP phase in the lepton sector by long baseline neutrino experiments [82, 40]. Since a neutrino beam travels in the matter between a neutrino source and a neutrino detector, it undergoes the matter effect in the Earth. Accordingly, the measurement of the CP phase in the lepton sector is affected by the matter effect in the Earth [83]. Therefore, it is very important to measure the matter effect independently of the long baseline CP phase neutrino experiments.

#### Energy spectrum measurement

The “up-turn” in the survival probability of electron neutrinos is expected assuming the MSW effect. SK can search for the “up-turn” by measuring the recoil electron spectrum because it reflects the survival probability of the electron neutrino.

So far, the vacuum oscillation dominant region below 1.0 MeV and the matter oscillation dominant region above 4.0 MeV have been measured by many solar neutrino experiments as shown in the right of Figure 2.13. However, the transition region, i.e. between 1.0 and 4.0 MeV, has not been measured precisely yet.

The ways to measure the solar neutrino in the transition region with SK are as follows:

1. Reduce the background: It is required to lower the energy threshold because the energy spectrum distortion is expected in the lower energy region. Therefore, it is important to understand the origin of the background event in the solar neutrino analysis in SK because the energy threshold depends on the background level of the detector. If the number of the background events is reduced, the statistical error is expected to become smaller.
2. Reduce the systematic errors: The large uncertainty in the spectrum analysis is caused by the systematic uncertainties in the detector performance. It is important to tune up the detector simulation based on the careful calibrations.

#### Day/Night flux asymmetry

Due to the matter effect in the Earth, the electron flavor neutrinos are regenerated as shown in the left of Figure 2.17. This regeneration is depends on the electron density of the Earth. The profile of the matter density is shown in the right of Figure 2.17. It is expected that the night flux is larger than the day flux by about a few % level depending on the oscillation parameters as shown in Figure 2.18. Using the recent best fit oscillation parameters, the day/night flux asymmetry is expected to be  $\sim 1.7\%$  level.

The day/night flux difference is defined as

$$A_{\text{DN}} = \frac{\Phi_{\text{Day}} - \Phi_{\text{Night}}}{(\Phi_{\text{Day}} + \Phi_{\text{Night}})/2}, \quad (2.3.1)$$

where  $\Phi_{\text{Day}}$  is the flux measured during daytime and  $\Phi_{\text{Night}}$  is that during nighttime. To observe the matter effect in the Earth, it is required to reduce the uncertainty for the solar neutrino

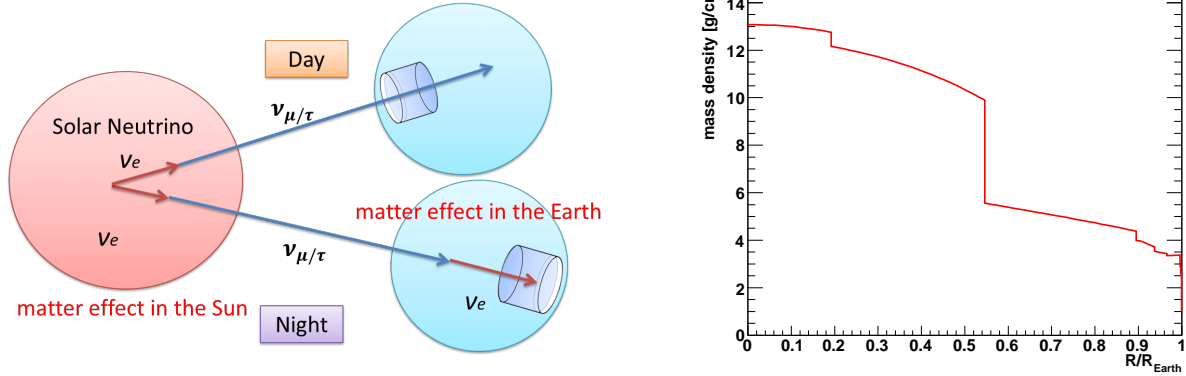


Figure 2.17: Left: The visual explanations of the day/night flux asymmetry. Right: The profile of the mass density of the Earth (PREM model) [84].

flux as much as possible. So far, SK has measured the day/night flux asymmetry and reported the indication of the terrestrial matter effect [85]. In this thesis, update of the day/night flux asymmetry is presented.

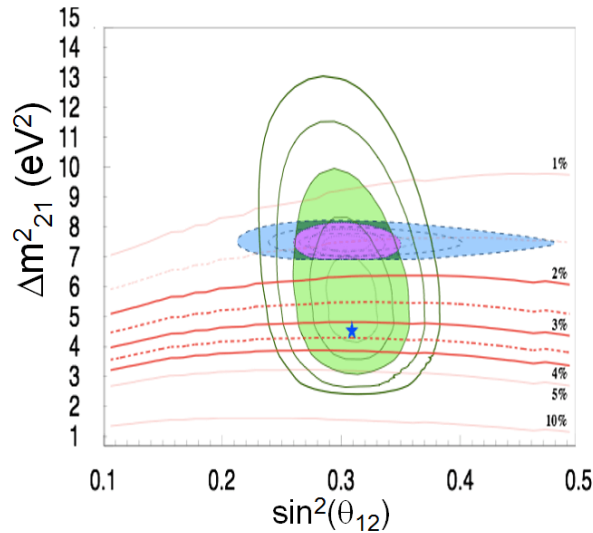


Figure 2.18: The expectation of the value of the day/night flux asymmetry. The horizontal axis shows  $\sin^2 \theta_{12}$  and the vertical axis shows  $\Delta m^2_{21}$ . The region filled in green (blue) shows the allowed region obtained by the solar neutrino experiments (KamLAND experiment). The region filled in purple shows the combined allowed region. The red lines shows the expected values of the day/night flux asymmetry.

### Time variation of the solar neutrino flux

This topic is not related with the matter effect, but it is related with the solar activity. As already mentioned, the Homestake experiment reported the anti-correlation between the solar

neutrino flux and the sunspot number as shown in the right of Figure 2.8. On the other hand, the Kamiokande experiment reported the no-correlation between the  $^8\text{B}$  solar neutrino flux and the sunspot number as shown in Figure 2.10.

To explain the anti-correlation reported by the Homestake experiment, several theoretical models were proposed [86, 87]. Because of the correlation between the magnetic field of the Sun and the solar activity as shown in Figure 2.7, these models introduce the neutrino conversion with its magnetic moment, such as spin-flip conversion. This idea requires that the neutrino magnetic moment is  $\sim 1.0 \times 10^{-10} \mu_B$ , where  $\mu_B$  is the Bohr magneton. However, current upper limit reported by the GEMMA experiment [88] is  $2.9 \times 10^{-11} \mu_B$ . Therefore, these theoretical models have already excluded.

In this thesis, about 18 years data taken by SK is presented. This data set covers the solar activity 23 and 24. So, it is possible to discuss whether the solar neutrino flux is correlated with the solar activity or not.

# Chapter 3

## Super-Kamiokande detector

This chapter describes the details of components of this detector, for example, its structure, photomultiplier tubes, data acquisition system, a water circulation system, etc.

### 3.1 Overview of Super-Kamiokande

The Super-Kamiokande (SK) detector is a ring imaging water Cherenkov detector with ultra pure water [58]. SK is located 1000 m underground at Ikenoyama, Kamioka, Gifu, Japan. The construction of the detector started in March 1991, and was completed in March 1996. SK started the data taking on April 1st, 1996. SK observes Cherenkov lights emitted from relativistic charged particles traveling in water by photomultiplier tubes (PMTs).

The Super-Kamiokande, whose name originally stands for “Super-Kamioka Nucleon Decay Experiment”, conducts researches for many physics targets, for example, proton decay, atmospheric neutrino, solar neutrino and so on. So far, SK has contributed a lot to neutrino physics for 19 years.

After the construction, the operation started in April 1996 as SK-I. SK-I was continuously operated for 5 years and finished taking data in July 2001 to replace some dead PMTs. However, an accident happened during the water refilling in November 2001. Due to the accident, a half of the PMTs were lost by a chain reaction of shock wave. Using the roughly 5,000 surviving PMTs, the detector was recovered temporarily. In order to avoid such kind of accident, a FRP (Fiber Reinforced Plastic) and an acrylic cover were newly installed to the PMTs in the inner detector. Then, SK resumed data taking in October 2002 with 19% photo-coverage as SK-II. In October 2005, SK-II finished taking data and then the full reconstruction work started. After the work, SK resumed data taking in July 2006 as SK-III. In September 2008, SK-III finished data taking to upgrade front-end electronics modules. In September 2008, SK resumed data taking as SK-IV and has continued data taking since then. Table 3.1 summarizes the characteristics of each SK phase. The energy threshold in SK-IV was set to 4.0 MeV in kinetic energy [108, 110] till 2013. After 2013, when the study to enhance the neutrino detection efficiency and to lower background level made a progress, the energy threshold was successfully lowered down to 3.5 MeV in kinetic energy. It is the lowest energy threshold among the all SK phase. The details of the study on the detection efficiency and the background will be described in Chapter 7 and Chapter 8.

Table 3.1: The summary of characteristics of each SK phase. The livetime means the total livetime of the data set for the solar analysis. Energy threshold is the recoil electron kinetic energy, adopted for the analysis. In this thesis the data until April 30, 2015 is used.

Phase	SK-I	SK-II	SK-III	SK-IV
Period (from to)	April 1996 July 2001	October 2002 October 2005	July 2006 August 2008	September 2008 running
Livetime [day]	1496	791	548	2055
ID PMT	11146	5182	11129	11129
OD PMT	1885	1885	1885	1885
PMT coverage	40%	19%	40%	40%
Electronics	ATM	ATM	ATM	QBEE
Energy threshold [MeV]	4.5 MeV	6.5 MeV	4.0 MeV	3.5 MeV

## 3.2 The structure of detector

### 3.2.1 Inner detector and Outer detector

SK is a cylindrical stainless tank structure which holds 50,000 tons of ultra pure water. Figure.3.1 shows the schematic view of the SK detector. The diameter of the detector is 39.3 m and the height is 41.4 m. Figure.3.2 shows a development view of SK and definitions for the position variables used in SK analyses, i.e. the height of SK is denoted by  $z$ , and the radius is denoted by  $r$ . SK is divided into two regions, one is an inner detector (ID) and the other is an outer detector (OD).

The ID is also a cylindrical structure, its diameter is 33.8 m and its height is 36.2 m. The ID contains 32,000 tons of ultra pure water. The ID is surrounded by 11129 20-inch PMTs which cover 40% of the surface of ID<sup>1</sup>. This coverage corresponds to 1 PMT per 0.5 m<sup>3</sup>. The remaining surface area is covered with black polyethylene terephthalate sheets in order to avoid the reflection of Cherenkov light and the leakage of light from and to the OD region.

The OD has a 2.75 m thickness in the side and 2.6 m thickness in the top and the bottom regions. The OD contains 17,500 tons of ultra pure water. The OD is surrounded by 1885 8-inch PMTs. The remaining area is covered with the white Tyvek sheets in order to increase reflectivity. The purpose of OD is to tag and veto any charged particles entering the ID region from the outside of SK, for example, cosmic ray muons, and charged particles or  $\gamma$  rays emitted from the radioactive sources existing in the rock surrounding the SK detector.

The structure which divides SK into two regions is a stainless module called super-module as shown in Figure.3.3. This module also supports twelve 20-inch PMTs for ID and two 8-inch PMTs for OD.

---

<sup>1</sup>Originally, the number of the ID PMTs were 11149 in SK-I as shown in Table 3.1. However, the number of ID PMTs was changed after the reconstruction for SK-III. It is because some PMTs could not be mounted geometrically at the edge of the top (bottom) region because of the installation of the FRP and the acrylic cases.

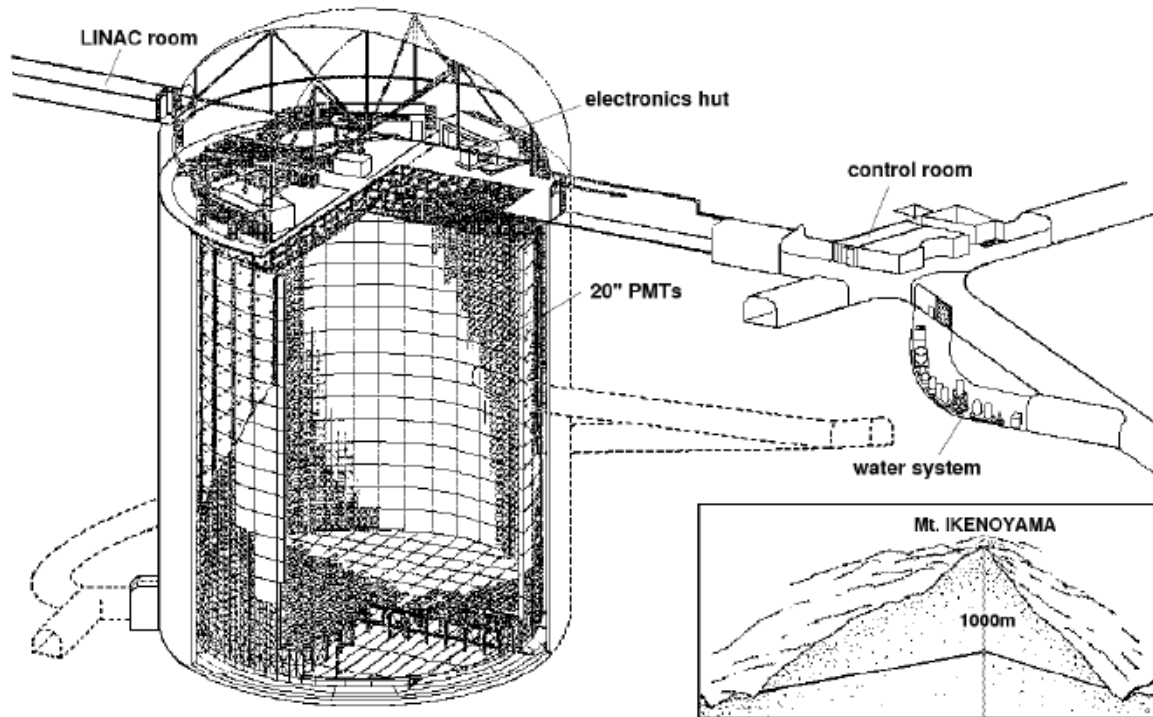


Figure 3.1: The Super Kamiokande detector [58].

### 3.2.2 20-inch PMT for ID and PMT cover

The 20-inch photomultiplier tube (PMT) was originally developed with Hamamatsu Photonics K.K. in collaboration with some researchers in Kamiokande [90]. Then, some items were optimized for Super Kamiokande [91] and the PMT used in SK ID is shown in Figure 3.4. Table 3.2 summarizes the properties of this PMT. The photo-sensitive surface of the glass is 50 cm in diameter and its thickness is 5 mm. The inner surface of the glass is a photo-cathode made of bialkali (Sb-K-Cs). The neck of the PMTs is covered with a silver reflector to avoid entering light. The 11-stage Venetian blind dynodes are used and it multiplies the photoelectrons by a factor of  $10^7$ , which is called the gain of the PMT.

This PMT is sensitive to wavelength between 280 and 660 nm. The quantum efficiency of the PMT depends on the wavelength and its peak is about 21% for 360 – 400 nm as shown in the left of Figure 3.5. The transit time spread is about  $\sim 2.2$  nsec as shown in the middle of Figure 3.5. The one photoelectron peak is clearly found as shown in the right of Figure 3.5.

After the accident in 2001, a combination of an acrylic and a FRP (Fiber Reinforced Plastic) cases were installed to each ID PMT in order to avoid the chain reaction of implusions. The PMT is covered with a 12 mm thick UV-transparent acrylic dome as shown in the right of Figure 3.4. The transparency of the acrylic case is more than 96% above 350 nm. The rear side of the PMT is covered with a FRP case. The combination of the acrylic and FRP cases prevent shock wave generation even if the PMT is imploded. There are some holes on its surface so that water fill inside of the case. It is necessary to prevent total reflection of Cherenkov light.

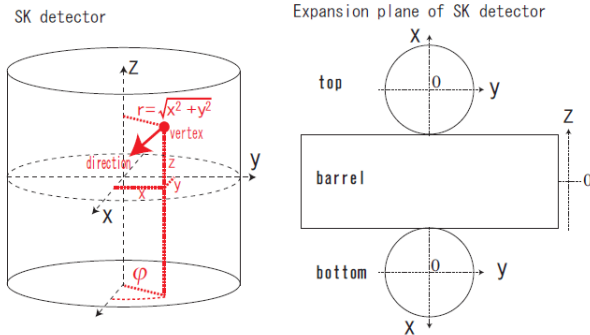


Figure 3.2: Basic variable definitions used in our analysis [99].

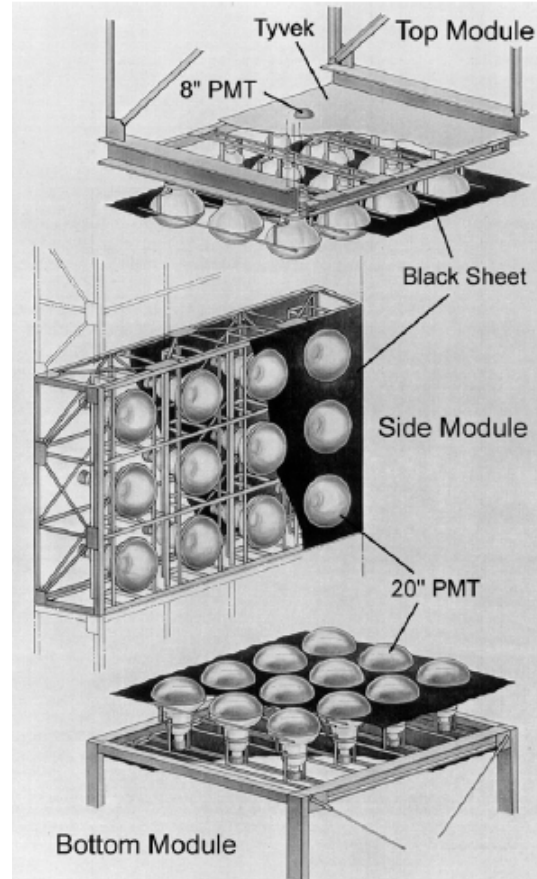


Figure 3.3: The schematic view of one unit of the PMT support structure. The thickness is about 55 cm. This support module holds twelve 20-inch PMTs for ID and two 8-inch PMTs for OD [58].

### 3.2.3 8-inch PMT for OD

The PMTs used in the outer detector are 8-inch PMTs. When SK-I was constructed, R1408 PMTs developed by Hamamatsu Photonics were mounted. PMTs had been originally used in the IMB experiment. After the accident in 2001, newly installed PMTs were R5912. Now, 591 R1408 and 1293 R5912 PMTs are used in the OD.

An 60 cm  $\times$  60 cm square acrylic plate is attached to each PMT as a wavelength shifter to improve the light detection efficiency.

### 3.2.4 Helmholtz coils

Since photoelectrons produced on the photo-cathode are collected to the first anode using an applied electrical field, the geomagnetic field affects the collection efficiency for the photoelectrons. To reduce the geomagnetic field, 26 sets of Helmholtz coils are arranged surrounding the water tank as shown in Figure 3.6 [92].

Table 3.2: The characteristic of 20-inch PMT.

Product Name	R3600
Photocathode area	50 cm diameter
Photocathode material	Bialkali(Sb-K-Cs)
Collection efficiency	70%
Dynode	11 stage Venetian bind type
Quantum efficiency	about 21% (360 – 400 nm)
Gain	$10^7$ (1700 – 2000 V)
Dark Noise Rate	4.5 kHz
Timing resolution	2.2 ns RMS(1p.e.)
Drift time	$\sim 100$ ns
Weight	13 kg
Pressure tolerance	6 kg/cm <sup>2</sup> water proof

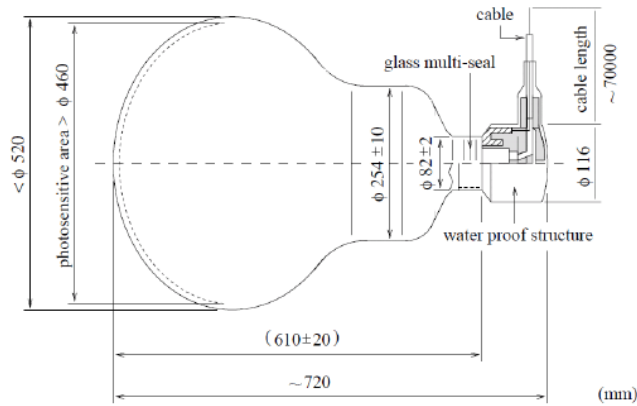


Figure 3.4: Left: The schematic view of the 20-inch PMT [58]. Right: The picture of the FRP and the acrylic case for PMT.

The electric current value in each coil is listed in Table 3.3. The currents of the coils are monitored by the real-time monitoring system. The original magnetic field was measured before filling the water in SK-I and its value was about 450 mG [58]. Then, the average magnetic field intensity was measured under the Helmholtz coil operation and the measured value was 32 mG on average [93]. The effect of the residual magnetic field for the collection efficiency of the PMTs was estimated to be about 1  $\sim$  2% level [93].

Table 3.3: The values of the current for each Helmholtz coil surrounding the tank [92].

Coil	A	B	C	D	E	F	G
Current [mA]	31.35	31.35	31.35	28.20	30.10	28.60	30.10

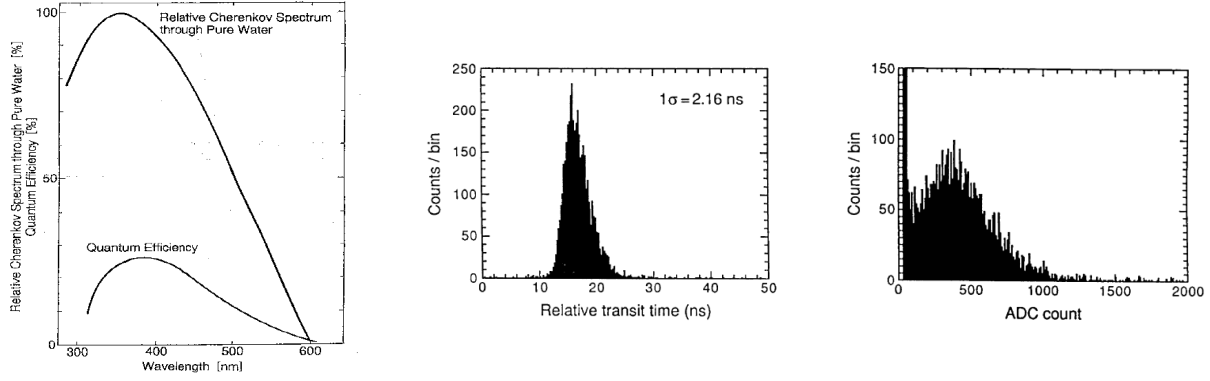


Figure 3.5: Left: The quantum efficiency of the ID PMT and the Cherenkov spectrum as a function of the wavelength [58]. Middle: The typical relative transit time distribution for 410 nm photon [58]. Right: The typical distribution for single photoelectron [58].

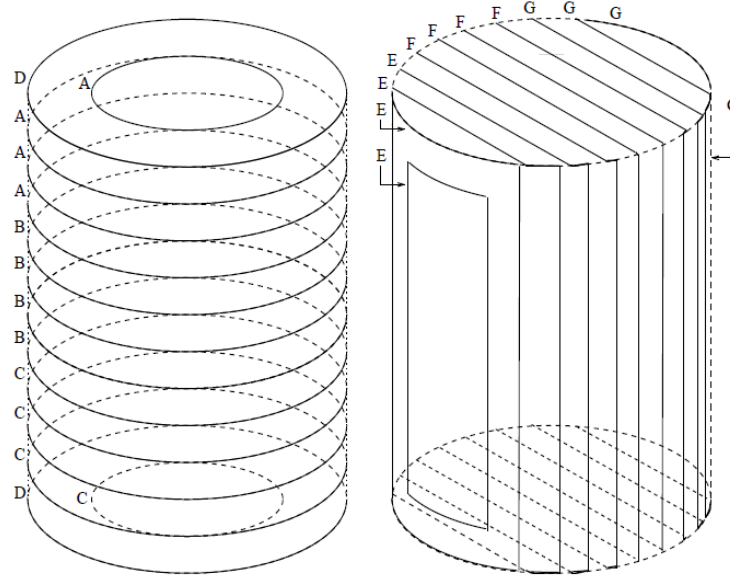


Figure 3.6: The schematic view of Helmholtz coils surrounding the water tank to eliminate the effects of the geomagnetic field [92].

### 3.3 Data acquisition system

There are two kinds of the data acquisition systems used in SK. The difference between them is the front-end electronics; the ATM (Analog Timing Module) [94, 95] based on TKO (Tristan KEK Online) standards [96] was used in SK-I through SK-III, and the QBEE (QTC-Based Electronics with Ethernet) [97] has been used in SK-IV .

There are 5 huts on the top of the SK tank, called “Central hut” and four “Electronics huts”. In the electronics huts, HV power supplies and the electronics system are placed; the former supplies high voltage to ID and OD PMTs and the latter digitizes the analog signal from the PMTs. In the central hut, the trigger system and the control electronics are placed and the

signals digitalized in the four Electronics huts are merged.

### 3.3.1 Data acquisition system for SK-I to SK-III

The schematic view of the data acquisition system used in SK-I to SK-III is illustrated in Figure 3.7. The front-end electronic ATM integrates the charge and timing information and then digitalizes both information by an ADC (Analog to Digital Converter) module on its board. One ATM board connects to 12 ID PMTs and about 1000 ATM modules were used in total.

Figure 3.8 shows the schematic view of the input and output channels of the ATM module. The input signal from a PMT is amplified by a factor of 100 and divided into four signals by the hybrid integral circuit (IC). The first of the divided signals is sent to a discriminator whose threshold was set to 100 mV ( $\sim 0.32$  photoelectrons). If this first signal exceeds the threshold, two pulses are generated.

1. The first pulse has 200 nsec timing width and its pulse height is  $-15$  mV. The pulses from the input 12 PMTs channels are summed and then the output pulse is generated as HITSUM. The HITSUM pulse is used to generate a global trigger which is used for determining whether or not to save the obtained event. The details of the global trigger will be described in next subsection.
2. The second pulse has 900 nsec timing width and its height is  $-15$  mV. This pulse is called as self-gate signal, which is used as a trigger to start the QAC (charge to analog converter) and TAC (time to analog converter) integration.

The second and third of the divided signals are sent to QAC and to TAC. The QAC integrates the charge for 400 nsec and then TAC generates the hit timing. If a global trigger is generated within  $1.3 \mu\text{sec}$ , the integrated QAC and TAC information are digitized by an ADC.

The fourth of the divided signals is generated as a PMTSUM signal which is the sum of the input PMTs signals for one ATM board. The PMTSUM is sent to a Flash ADC which records the waveform information.

### 3.3.2 Hardware trigger

The HITSUM signals from the ATM boards are eventually summed at the central hut and the global trigger is generated. The global trigger generation is illustrated in Figure 3.9.

There are three kind of global triggers, Super Low Energy (SLE), Low Energy (LE) and High Energy (HE). These triggers have different threshold levels and they are summarized in Table 3.4. When the summed HITSUM exceeds the threshold, the trigger type is determined.

The data acquisition capacity depends on the event rate. In general, the data acquisition rate is expected to be larger when the threshold level becomes lower. In the case of SLE, its threshold was changed many times (7 times in SK-I [98], 3 times in SK-III [99]) depending on the background condition.

### 3.3.3 Data acquisition system for SK-IV

In order to achieve more stable observation and to improve the detector performance, the new front-end electronics QBEE was installed at the beginning of the SK-IV. Figure 3.10 illustrates

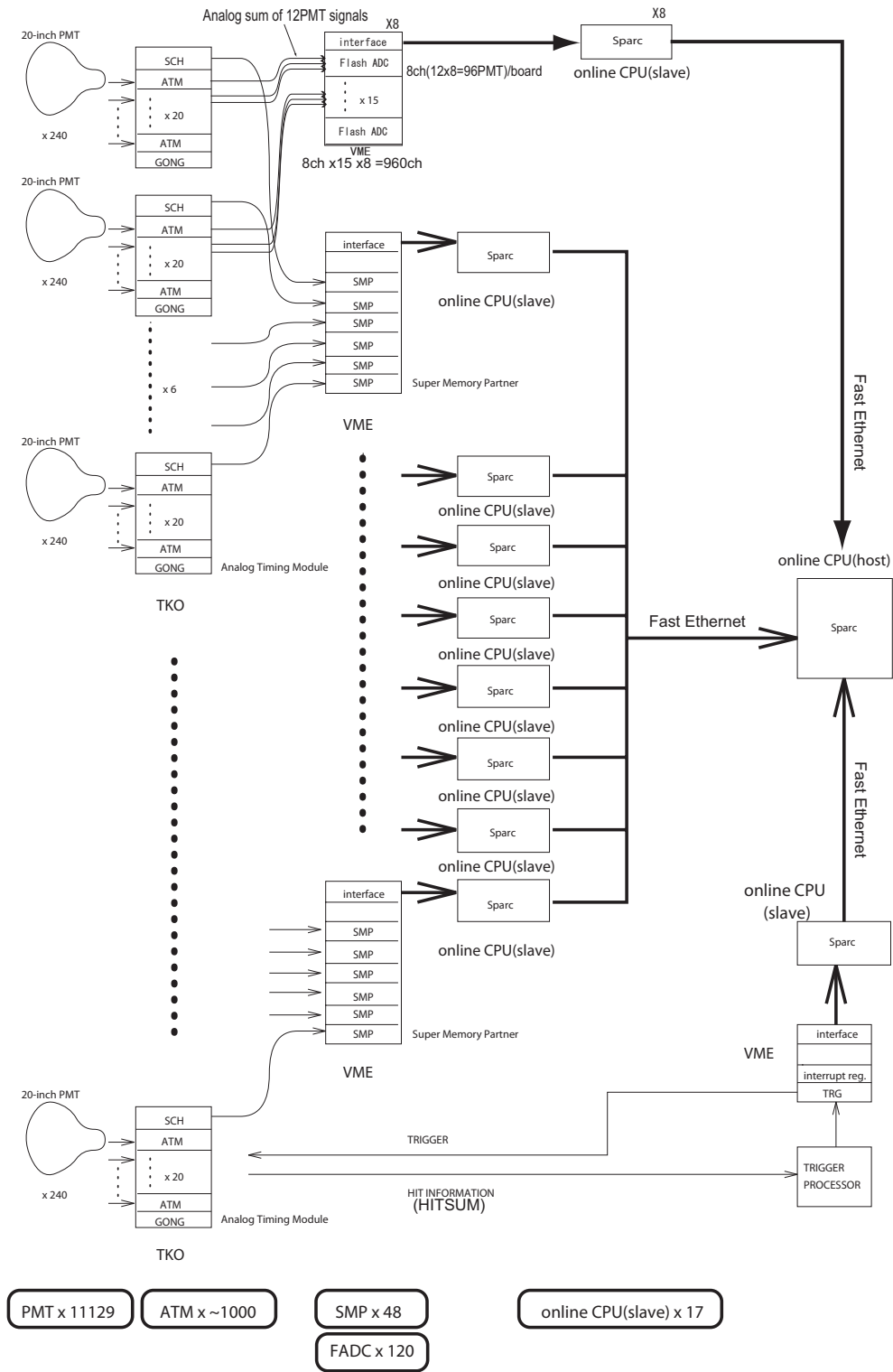


Figure 3.7: The layout of the ID DAQ used in SK-I through SK-III [92].

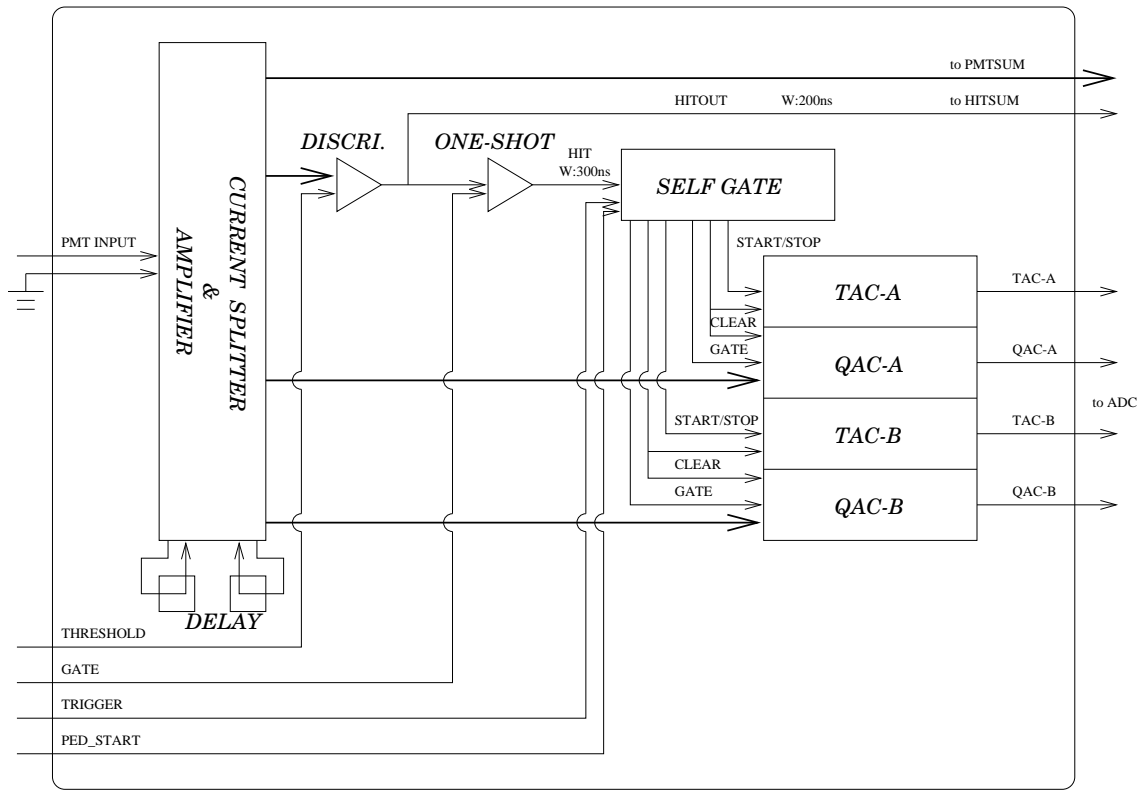


Figure 3.8: The schematic view of the input and output channel of the ATM module.

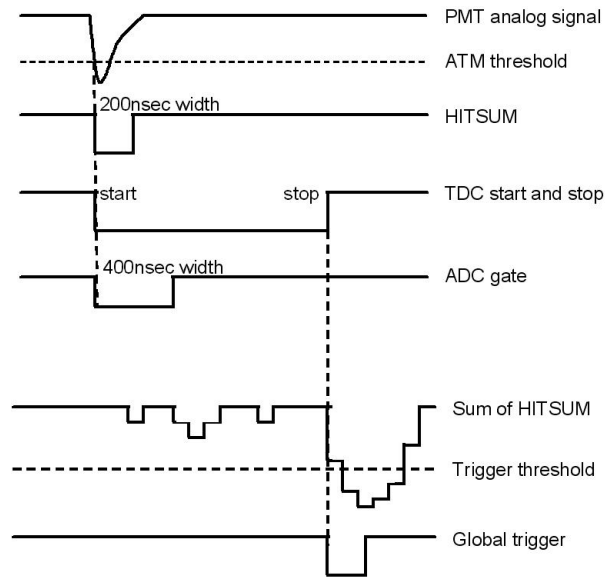


Figure 3.9: The timing chart for the signal and the generation of the global trigger.

the schematic view of the data acquisition system used in SK-IV. Due to the different electronics, the readout scheme is completely changed.

Table 3.4: The global trigger threshold in each SK phase. In the SK-I and SK-III, the SLE trigger threshold was changed many times according to the background level. Therefore, the initial value and the last value were written.

	SK-I	SK-II	SK-III
SLE	-260 → -186 mV	-110 mV	-212 → -186 mV
LE	-110 mV	-152 mV	-302 mV
HE	-340 mV	-180 mV	-320 mV

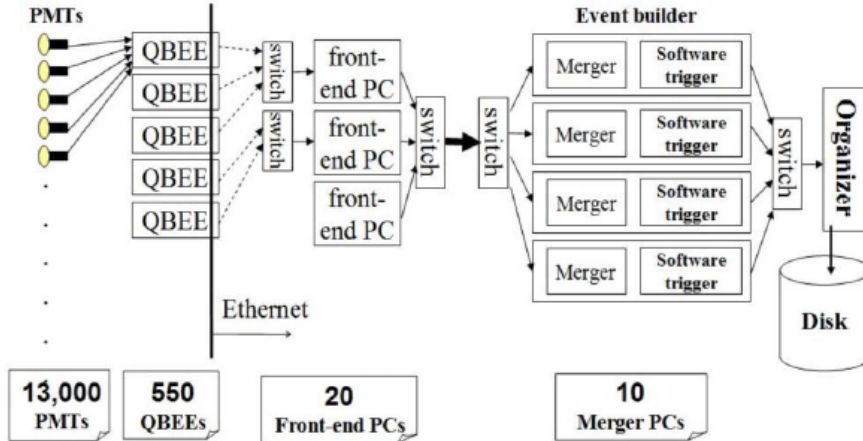


Figure 3.10: The schematic view of the DAQ system used in SK-IV [97].

## QBEE

The left of Figure 3.11 illustrates the picture of the new front end electronics and the right of Figure 3.11 illustrates the block diagram of the signal processing in the QBEE. One QBEE module connects to 24 PMTs, so about 550 modules were used in total as shown in Figure 3.10.

The main parts of QBEE module are the QTC (charge to time converter) ASIC and the TDC (time multi-hit time-to-digital) [100]. There are 8 QTC on the QBEE board and one QTC processes 3 PMTs. When the QTC detects the analog signals from the PMTs and if the pulse height exceeds  $-0.69$  mV, it creates an output timing pulse whose width represents the integrated charge of the PMT signal within 400 nsec time window. Three kinds of dynamic ranges were prepared to keep better charge resolution at a few p.e. level. The three dynamic ranges select the gain depending on the observed charge and they are summarized in Table 3.5. The overall charge dynamic range is 0.2 to 2,500 pC and this range was about 5 times wider than that of the ATMs.

## Readout scheme

The output pulse from the QTC is sent to a multi-hit TDC which measures the width of the QTC output pulse by detecting the leading and trailing edges of the pulse. A FPGA (Field

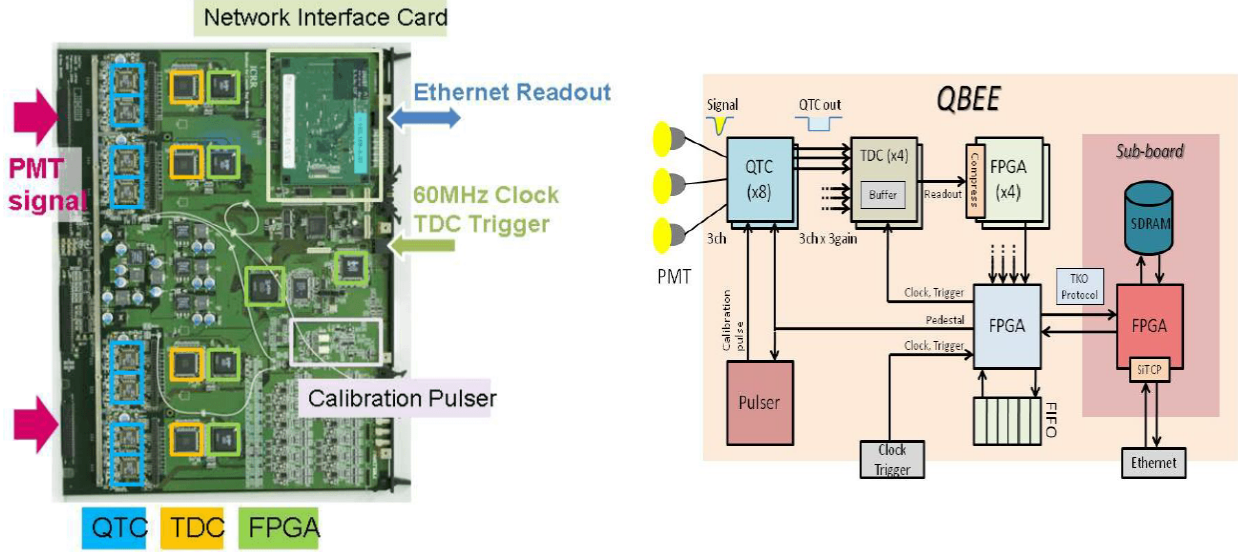


Figure 3.11: Left: The picture of the new front end electronics QBEE. Right: The block diagram of the signal processing in the QBEE.

Table 3.5: The characteristics of each input channel.

Type	Gain Range [pC]	Resolution
Small	0 ~ 51	0.1 pC/count (0.05 p.e./count)
Medium	0 ~ 357	0.7 pC/count (0.35 p.e./count)
Large	0 ~ 2500	4.9 pC/count (2.5 p.e./count)

Programmable Gate Array) reads and processes the data stored in the TDC. There are 4 TDC and 4 FPGA on the QBEE board. The width information is digitized into charge information and arrival timing information is digitized into the timing information. Both digitalized information are sent to the front-end PCs via ethernet. The front-end PC sorts the received data by time order and then sends it to a merger PC. At the stage of the merger PC, a software trigger program is run to extract events from the hit data. The triggered event is collected by an organizer PC and then finally recorded onto disk.

### 3.3.4 Software trigger

Thanks to the achievement of the higher speed signal digitalization, every hit PMT information can be collected at the merger PC located in the central hut. The software trigger searches for the events by sliding the 200 nsec time window. The number of the hit PMTs within 200 nsec is defined as  $N_{200}$ . When  $N_{200}$  exceeds the threshold as shown in Table 3.6, the trigger signal is issued. The software trigger can select the timing width depending on the trigger type. Table 3.6 summarizes the threshold of  $N_{200}$  and the timing width for the each trigger type.

For the trigger of LE, HE and SHE, the event timing width is set to 40  $\mu$ sec and this width is wider than that of the old trigger system (1.3  $\mu$ sec). Because of this wider timing width, some

other physical events within 200 nsec can be searched for. For example, a prompt gamma-ray from the excited oxygen molecule as a pre-activity and a muon decay as a post-activity. For the SLE trigger, the timing width is set to  $1.5 \mu\text{sec}$  due to the high rate from the background events. It is required that the data size should be reduced.

On May 1st 2015, the threshold of the SLE trigger was lowered to 31 hits to improve the sensitivity for low energy solar neutrino events.

Table 3.6: The threshold for each trigger and its event time width.

Trigger Type	Threshold for $N_{200}$ [hit PMTs]	Event timing width [ $\mu\text{s}$ ]
SLE	34 $\rightarrow$ 31 (After May 2015)	1.5 ( $-0.5 \sim +1.0$ )
LE	47	40 ( $-5 \sim +35$ )
HE	50	40 ( $-5 \sim +35$ )
SHE	70 $\rightarrow$ 58 (After September 2011)	40 ( $-5 \sim +35$ )
OD	22 in OD	40 ( $-5 \sim +35$ )

## 3.4 Water circulation system

### 3.4.1 Water purification system

The water filled in the SK tank is one of the most important element in the experiment because its quality (transparency) affects the propagation of the Cherenkov light traveling in water. It is required to remove the contaminants as they may be radioactive (for example Radon  $^{222}\text{Rn}$ ). The water is originally supplied from the two streams inside the Kamioka mine, which are sourced by the natural seepage of rain and snow melt through the mountain rock. Before filling the tank, the water is pumped through a water purification system to remove contaminants and make it ultra-pure. Figure 3.12 illustrates the schematic view of the water purification system.

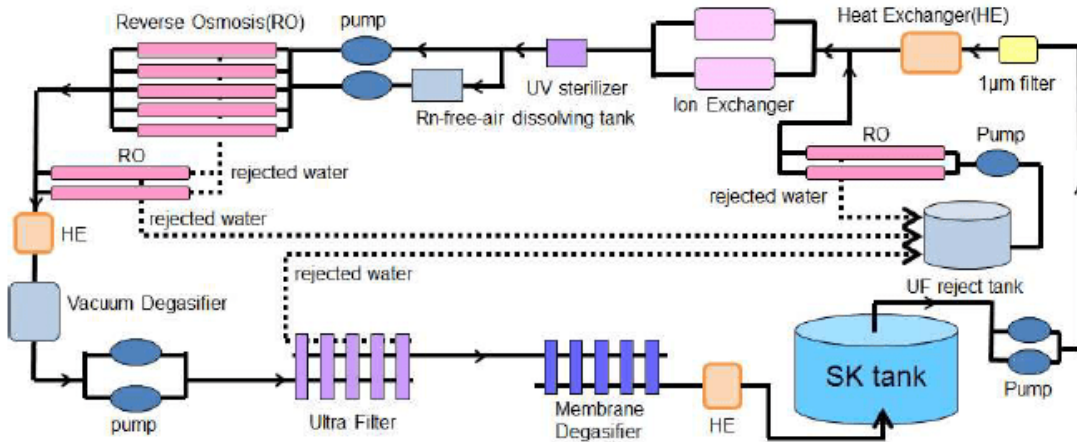


Figure 3.12: The schematic view of the water circulation system.

The main components of the water purification system are as follows:

1.  $1\ \mu\text{m}$  filters: They are located at the first stage of the water purification system. They are series of the mesh filters which can remove the dust larger than  $1\ \mu\text{m}$  in size and the radioactive contaminations in water.
2. Heat exchanger (HE): The water temperature increases due to the heat generated by drain pumps, PMTs, the surrounding rock and so on. There are three sets of heat exchangers in the water purification system to control the water temperature. The most important one is located at the final stage of the water purification system, i.e. in front of the tank. The temperature of the supply water is controlled with an accuracy of  $0.01\ ^\circ\text{C}$  to suppress convection inside the tank.
3. Ion exchanger : Resin to remove high molecular and heavy ions including the radioactive contaminations. This resin eliminates ions such as  $\text{Na}^+$ ,  $\text{Cl}^-$ ,  $\text{Ca}^{2+}$  and others.
4. UV sterilizer : Since bacterias sometimes survive in water and they affects the water transparency, it is required to kill them. This device radiates ultraviolet light to water.
5. Rn free air dissolving system: This system mixes water with Radon free air in order to increase the efficiency of a vacuum degasifier (VD). Rn free air is produced in the Rn free air system which will be described in next subsection 3.4.2.
6. Reverse Osmosis (RO) membranes: They were newly installed to remove the contaminants heavier than 1,000 molecular in weight since SK-III.
7. Vacuum Degasifier (VD) : This system removes gas components dissolved in water. The main targets are radon gas and oxygen, its removal efficiencies are  $\sim 96\%$  for Radon and  $\sim 99\%$  for oxygen.
8. Ultra filter (UF) : These filters remove particles larger than 10 nm.
9. Membrane Degasifier : This system was installed at the end of SK-I. It removes radon gas in water with the efficiency of  $\sim 83\%$ . On May 22, 2014, this system was bypassed because the Rn concentration in water increased when passed through this system. The detail would be described in Chapter 8.

The purified water is continuously circulated through the water purification system with a flow rate of 60 ton/hour to keep the water quality. In addition, the water flow is well tuned in order to keep the uniformity of the water quality.

The left of Figure 3.13 shows the schematic view of the water flow piping lines for the supply and the drain in SK-IV. Based on study of the water flow, the water is supplied from the bottom and drained mainly from the top.

Since the water flow in the SK tank is sensitive to the water temperature difference in the tank, it is important to understand its position dependence. The right of Figure 3.13 shows the position dependence of the water temperature. It was found that water is always convecting below  $z = -11\ \text{m}$  as can be seen by the uniform temperature profile. Above the convection zone, there is  $0.2\ ^\circ\text{C}$  difference between the top of the ID and the convection zone. The low temperature entire in the detector prevents bacteria growing.

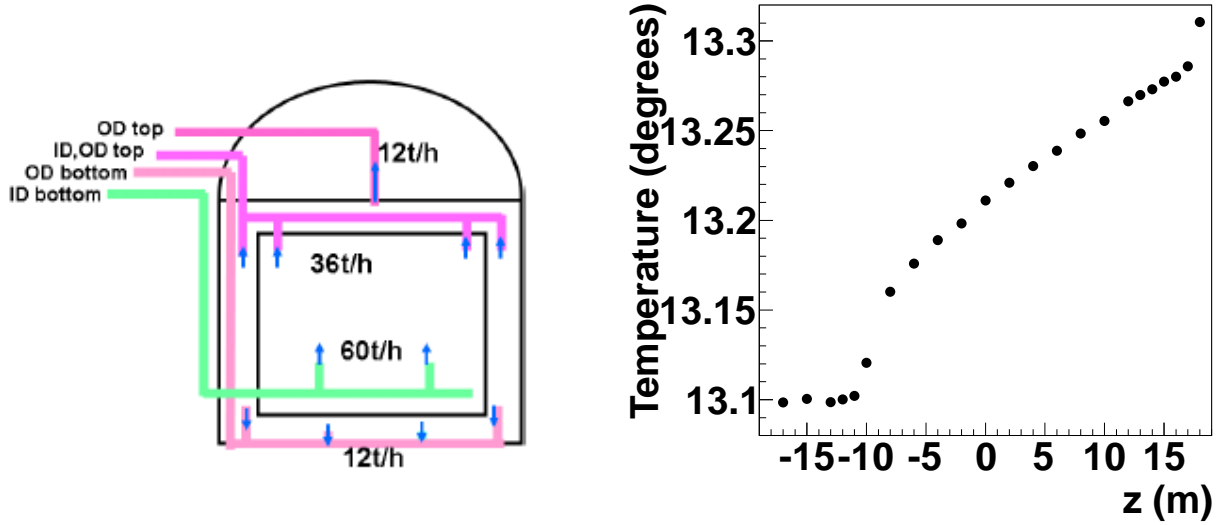


Figure 3.13: Left: The diagram of the water pipes for the supply and the drawn [93]. Right: The monitored water temperature [93]. The horizontal axis shows the depth of the tank and the horizontal axis shows the water temperature. Below  $-11$  m, the water is always convecting. Above this level, water is layered and the temperature gradually increases.

After passing through the water purification system, the Rn concentration in the supply water is  $1.83 \pm 0.31$  mBq/m<sup>3</sup>. The detail of the Rn concentration in SK water will be explained in Chapter 8.

### 3.4.2 Rn free air system

#### Fresh air supply system

The air in the mine was dirty due to the dust and the rich Rn gas emanating from the surrounding rocks. The Rn concentration in summer is  $\sim 1500$  Bq/m<sup>3</sup> while in winter it is  $\sim 30$  Bq/m<sup>3</sup> because of the different air flow pattern in the mine.

The special air supply system was installed for the purpose of keeping clean environment. This system consists of a large air blower, air filters and a heat exchanger and it is located at the entrance of the mine. This system can supply the outside “fresh” air into the SK experimental area in the mine with a rate of 70 m<sup>3</sup>/min. As a result, the Rn concentration in the SK experimental area is kept at approximately  $\sim 50$  Bq/m<sup>3</sup>.

#### Rn free air system

There is a 60 cm air layer between the surface of the SK water and the top of the SK tank in order to prevent from breaking the tank by sloshing in case of earthquake. The volume of this air layer is 753.6 m<sup>3</sup>. It is required to supply air into the air layer to keep its pressure at +0.3 kPa relative to atmospheric pressure. In addition, this air purging is necessary because the top of the SK tank is exposed to dome of the tank to which fresh air is supplied, i.e. Rn level of  $\sim 50$  Bq/m<sup>3</sup>.

This Rn concentration in the dome air is still too high. In order to keep low Rn concentration in the tank, a special Radon free air system was developed to reduce the Rn concentration as much as possible. The Rn free air system is illustrated in Figure 3.14 and its main components are as follows:

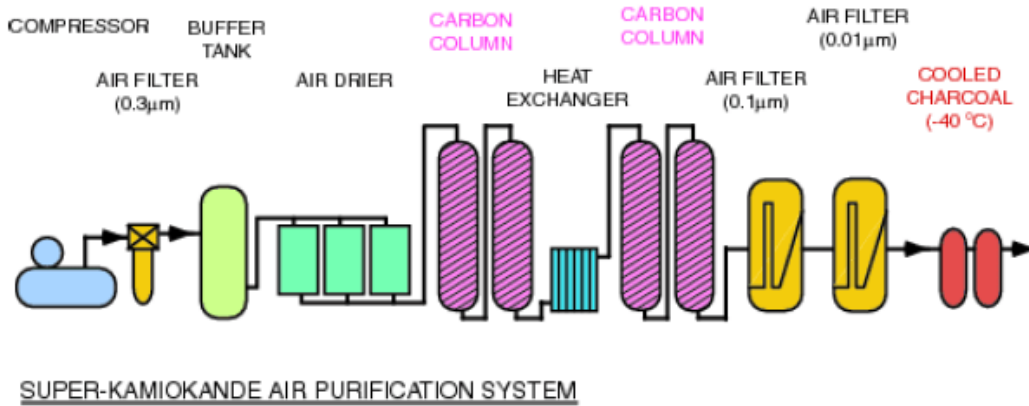


Figure 3.14: The schematic view of the Rn free air system [58].

1. Air compressor: This system compresses the air to 7.5 ~ 8 atm.
2. Mesh filters: 0.3, 0.1 and 0.01  $\mu\text{m}$  filters are used to remove dusts in the compressed air. The 0.3  $\mu\text{m}$  one is located after the compressor. The air passing through it is stored in a buffer tank temporarily. The other filters are located after room temperature carbon columns.
3. Air drier: This system removes water in the air.
4. Carbon columns: This system removes Rn in the air because the activated charcoal absorbs Rn [101]. There are two types of carbon columns. One is located after the air drier and it is operated under room temperature. The other is located at the last stage of the Rn free air system and it is operated with a cooling system. The original cooling system could chill the carbon column at  $-40\text{ }^\circ\text{C}$  [58]. In order to further improve the Rn removal efficiency, the cooling system for the last carbon column was upgraded in March 2013. Finally, the temperature was achieved below  $-60\text{ }^\circ\text{C}$ . At this temperature, the removal efficiency is  $\sim 100\%$ .

In order to monitor the Rn concentration in the Rn free air, a 80 L Rn detector was developed [102]. Three Rn detectors were put on the SK area as shown in Figure 3.15. The first one monitors the Rn concentration just after the production in the Rn free air system. The second one monitors the supply air and the third one monitors the air in the air layer of the SK tank.

The result of the monitoring is shown in Figure 3.16. The Rn concentration in the air passing through the Rn free air system is  $0.06 \pm 0.05\text{ mBq/m}^3$  after the upgrade of the cooling system.

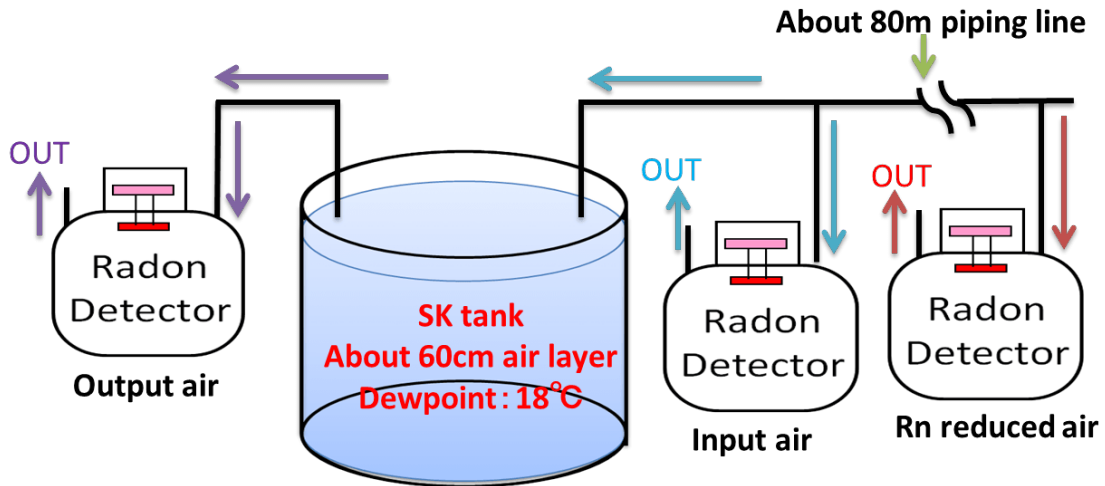


Figure 3.15: The schematic view of the Rn concentration monitoring system for Rn water.

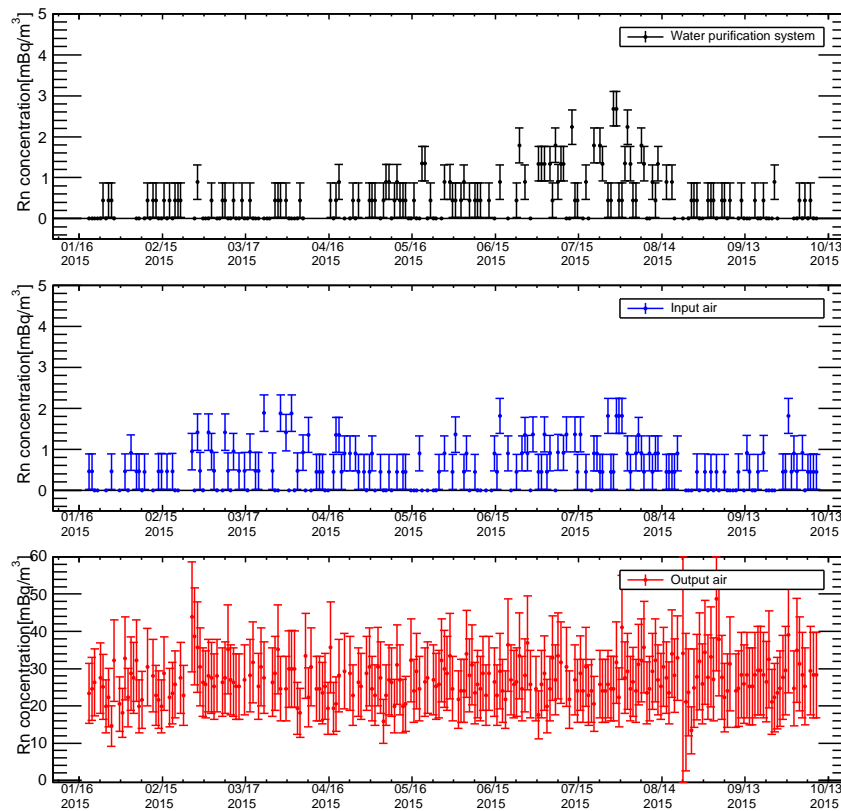


Figure 3.16: The time variation of the Rn concentration for the water purification system (black), the supplied Rn free air (blue) and the air layer (red). The horizontal axis is the dates from January 8th 2015 to November 8th 2015. The vertical axis shows the measured Rn concentration. in unit of  $\text{mBq}/\text{m}^3$

## 3.5 Detector simulation

In order to understand the detector response, the behavior of recoil electrons traveling in water, the emission of Cherenkov light and its propagation should be simulated. The MC simulation was developed by SK working group based on GEANT 3.21. GEANT 3 package simulates most of physics processes. However, since some physics processes such as the production and the propagation of Cherenkov light and the light attenuation in water could not be precisely simulated in the original GEANT 3, so the simulations for such processes were newly developed by a SK working group.

### 3.5.1 Cherenkov photon production

The number of the Cherenkov photons (in wave length  $d\lambda$ ) is represented as

$$d^2 N = \frac{2\pi\alpha}{n(\lambda)\lambda^2} \left(1 - \frac{1}{n^2\beta^2}\right) dx d\lambda, \quad (3.5.1)$$

where  $n$  is the refractive index for water,  $\alpha$  is the fine structure constant,  $\beta$  is the velocity of the photon traveling in water in unit of the light velocity in vacuum and  $dx$  is the traveling length. Since the refractive index  $n$  depends on the wavelength, the water temperature, the water pressure and so on [103], not only the wavelength but also these environmental values are taken into account in the simulation.

The Cherenkov opening angle  $\theta$  is represented as

$$\cos \theta = \frac{1}{n\beta}. \quad (3.5.2)$$

Based on the above formula, the Cherenkov light emission is simulated in the SK simulation. The threshold of the Cherenkov light emission is calculated as

$$E_{\text{thr}} = \frac{nm}{\sqrt{n^2 - 1}}, \quad (3.5.3)$$

where  $m$  is the mass of a charged particle. Table 3.7 illustrates the threshold of the Cherenkov emission for typical charged particles.

Table 3.7: Threshold of the Cherenkov radiation for typical charged particles.

Particle type	Energy threshold [MeV]
$e^\pm$	0.767
$\mu^\pm$	157.4
$\pi^\pm$	207.9

## 3.5.2 Water transparency

### Simulation of the water attenuation

The water transparency is the most important thing in the simulation because it significantly affects the propagation of the Cherenkov light. It is considered that the photon is reflected or absorbed by the impurity in the water or that the energy of the photon is sometimes transformed to the other type of the energy, for example as heat. So, It is complicated to simulate the absorption and scattering in water.

The intensity of the light traveling in water exponentially decreases as

$$I(x) = I_0(\lambda) \exp(-x/L(\lambda)) \quad (3.5.4)$$

where  $x$  is the traveling length,  $L(\lambda)$  is the total attenuation length and  $I_0(\lambda)$  is the initial light intensity. The total attenuation length (water transparency) is characterized using three scattering coefficients which depend on the wavelength of the photon traveling in water. The coefficients are Absorption part  $\alpha_{\text{Abs}}$ , Rayleigh scattering part  $\alpha_{\text{Ray}}$  and Mie scattering part  $\alpha_{\text{Mie}}$ . However, it is very difficult to separate the part of Mie scattering from the attenuation length by the scattering process.

The angular distribution of Rayleigh scattering is symmetric, namely its intensity is the same in the forward and backward direction. But, the angular distribution of Mie scattering is asymmetric and it tends to favor the forward direction. The total attenuation length in the MC simulation was newly defined as

$$L_{\text{MC}}(\lambda) = \frac{1}{\alpha_{\text{abs}} + \alpha_{\text{sym}} + \alpha_{\text{asym}}}, \quad (3.5.5)$$

where  $\alpha_{\text{abs}}$ ,  $\alpha_{\text{sym}}$  and  $\alpha_{\text{asym}}$  were absorption, symmetric scattering and asymmetric scattering coefficients respectively. The symmetric scattering coefficient consist of Rayleigh and symmetric Mie scattering and the asymmetric scattering coefficient consist of forward Mie scattering as shown in Figure 3.17.

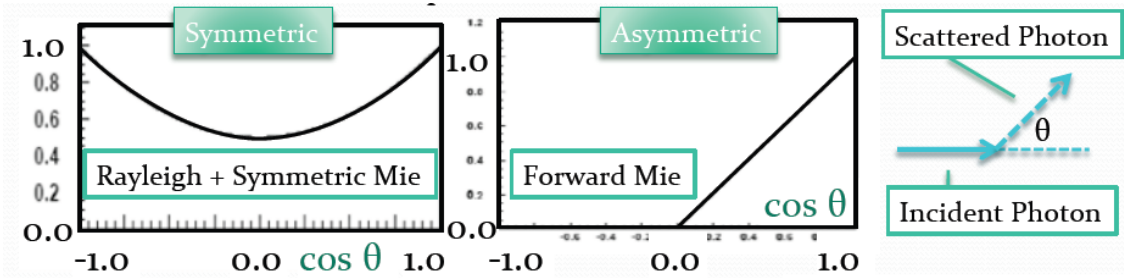


Figure 3.17: A position dependence of the PMT hit rate.

They are empirical functions used in the SK simulation and are defined as

$$\alpha_{\text{abs}}(\lambda) = P_0 \times \frac{P_1}{\lambda^4} + C, \quad (3.5.6)$$

$$\alpha_{\text{sym}}(\lambda) = \frac{P_4}{\lambda^4} \times \left( 1.0 + \frac{P_5}{\lambda^2} \right), \quad (3.5.7)$$

$$\alpha_{\text{asym}}(\lambda) = P_6 \times \left( 1.0 + \frac{P_7}{\lambda^4} \times (\lambda - P_8)^2 \right), \quad (3.5.8)$$

where  $P_0 \sim P_8$  are the fitting parameters. In the absorption part, the parameter  $C$  is the amplitude based on the experimental data obtained in [104] for  $\lambda \geq 464$  nm while  $C = P_0 \times P_2 \times (\lambda/500)^{P_3}$  is used for  $\lambda < 464$  nm.  $P_0 \sim P_8$  were tuned by the calibration data. Using these parameters, the water attenuation could be simulated approximately, but they did not exactly represent the real physics properties.

### Position dependence of the water transparency

As mentioned in subsection 3.4.1, the convection occurs in the tank below  $z = -11$  m. This convection affects the uniformity of the water transparency because of its nonuniform water flow.

The position dependence of the water transparency is continuously monitored using two calibration sources. The one is the auto Xenon light and the another is the Ni-Cf calibration source. These calibration methods will be described in Chapter 5.

The hit rate difference between the top PMTs and the bottom PMTs can be used to evaluate the position dependence of the water transparency. The difference called as TBA (Top-Bottom Asymmetry) is defined as

$$TBA = \frac{\langle \text{top} \rangle - \langle \text{bottom} \rangle}{\langle \text{barrel} \rangle}, \quad (3.5.9)$$

where  $\langle \text{region} \rangle$  illustrates the mean hit rate of PMTs for each region. In order to take into account the position dependence of the water transparency, the absorption coefficient is modified as

$$\alpha_{\text{abs}}(\lambda, z) = \begin{cases} \alpha_{\text{abs}}(\lambda) \times (1.0 + \beta z) & (z \geq -11 \text{ m}), \\ \alpha_{\text{abs}}(\lambda) \times (1.0 - 1100\beta) & (z < -11 \text{ m}), \end{cases} \quad (3.5.10)$$

where the parameter  $\beta$  is determined by the calibration. Using the parameter  $\beta$ , the SK simulation is tuned to match the calibration data and the simulation.

## 3.5.3 Detector response

### PMT and electronics response

In order to simulate the detector response, the PMT and the electronics should be taken into account. In the SK simulation, three kinds of the responses of the PMT are considered; the first is the absorption by the photo-cathode, the second is the reflection on the PMT surface

and the third is the transmission through the PMT. The photoelectron generation occurs when the absorption response is selected. The left of the Figure 3.18 illustrates the response of the PMT when the photon reaches the surface of the PMT in the SK simulation. These responses depend on the incident angle of the photon and this dependence is also taken into account as shown in the right of Figure 3.18.

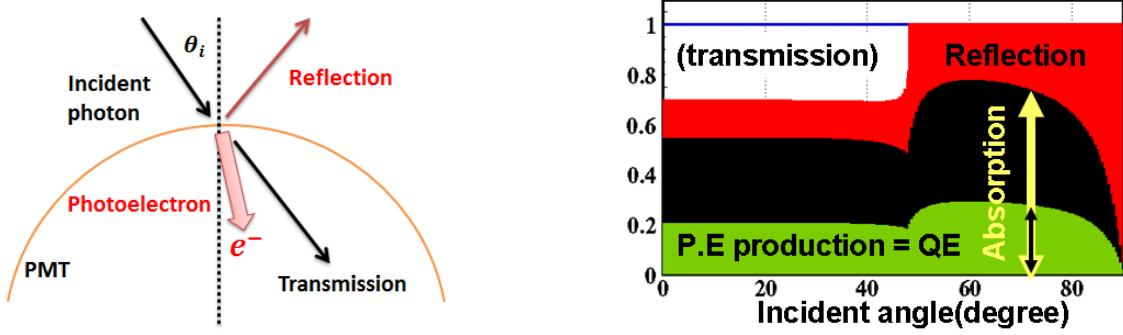


Figure 3.18: Left: The schematic view of the PMT response for the incident photon in the simulation. Right: PMT response for the 420 nm using the unpolarized light. The black area means that the photons are absorbed into the PMT surface and the photoelectron is not generated.

The probability of the PMTs to produce the one photoelectron when the generated photon reaches its surface is defined as

$$Prob(\lambda, i) = QE(\lambda) \times Prob_{obs}(\lambda, \theta_i) \times COREPMT \times getable(i), \quad (3.5.11)$$

where the introduced parameters are:

1.  $QE(\lambda)$ : The quantum efficiency of the 20-inch PMT. It depends on the wavelength of the incident photon as shown in the left of Figure 3.5.
2.  $Prob_{obs}(\lambda, \theta_i)$ : The probability of selecting either the PMT responses of the absorption or the photoelectron generation.
3.  $COREPMT$ : A common parameter used for all PMT to correct the average quantum efficiency. This parameter was tuned using a LINAC calibration described in subsection 5.3.1.
4.  $getable(i)$ : A relative quantum efficiency for the  $i$ -th PMT measured by Ni calibration source described in subsection 5.1.3.

Finally, when photoelectrons are generated, the output charge is simulated. When it exceeds the threshold of the electronics, the photon is detected by the PMT in the simulation.

### Reflection by the detector structure

The Cherenkov photons are reflected by the detector structure such as the surface of PMT, the black sheet and so on. Since the reflectivity of them was also measured by the some calibration devices [58, 93], these effects are also taken into account in the SK simulation.

# Chapter 4

## Event reconstruction

In this chapter, the event reconstruction method is described. The SK detector has many physics targets, thus there are many analysis tools to reconstruct events. Since this thesis focuses on the solar neutrino observation, the reconstruction method for low energy charged particles is explained.

### 4.1 Vertex reconstruction

Low energy charged particles, such as electrons scattered by solar neutrinos travel only  $\sim 10$  cm in water. Due to the large size of the detector and the timing resolution of the PMTs, position resolution is not as good as the track length. Therefore, the tracks of electrons are treated as point-like sources.

In order to reconstruct the vertex position, a maximum likelihood fit to the timing of Cherenkov signal is used. This maximum likelihood fitting program is called BONSAI (Branch Optimization Navigating Successive Annealing Interactions) [105]. This program uses the timing information. The timing residual of each PMT hit is defined as  $t - t_{\text{tof}} - t_0$ , where  $t$  is the hit timing,  $t_{\text{tof}}$  is the time of flight from the vertex position of the interaction to hit PMT and  $t_0$  is the time of the interaction. Using the timing residual information, the likelihood function is defined as

$$\mathcal{L}(\vec{x}, t_0) = \sum_{i=1}^{N_{\text{hit}}} \log(P(t - t_{\text{tof}} - t_0)), \quad (4.1.1)$$

where  $\mathbf{x}$  is the testing vertex position and  $P(t - t_{\text{tof}} - t_0)$  is the probability density function of the timing residual for a single photoelectron signal as shown in Figure 4.1.

$P(t - t_{\text{tof}} - t_0)$  is extracted by the LINAC calibration along with the vertex resolution. The vertex resolution is the distance which involves 68% of the reconstructed LINAC events and its energy dependence is shown in Figure 4.2. The worse vertex resolution in the lower energy region is due to the smaller number of emitted photons. The vertex resolution at SK-IV is slightly better than that at SK-III because of the installation of the new front-end electronics and the improvement of its timing calibration.

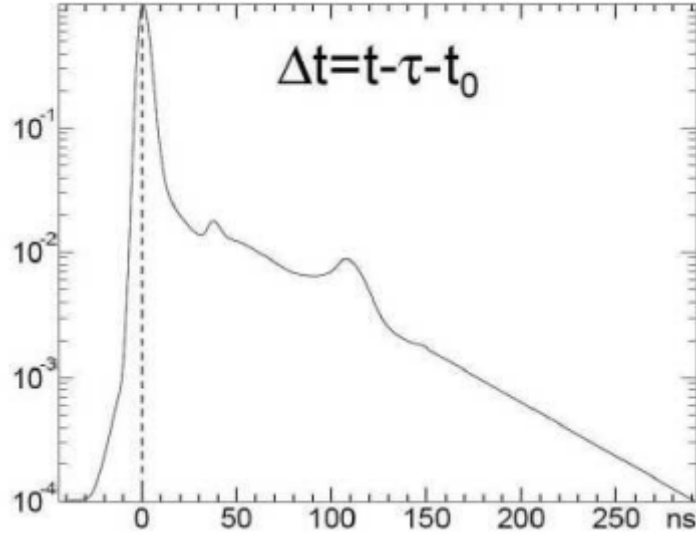


Figure 4.1: The probability density function of the timing residuals used for the vertex reconstruction maximum likelihood fit. The second and third peaks around 30 nsec and 100 nsec are caused by the PMT's after pulses.

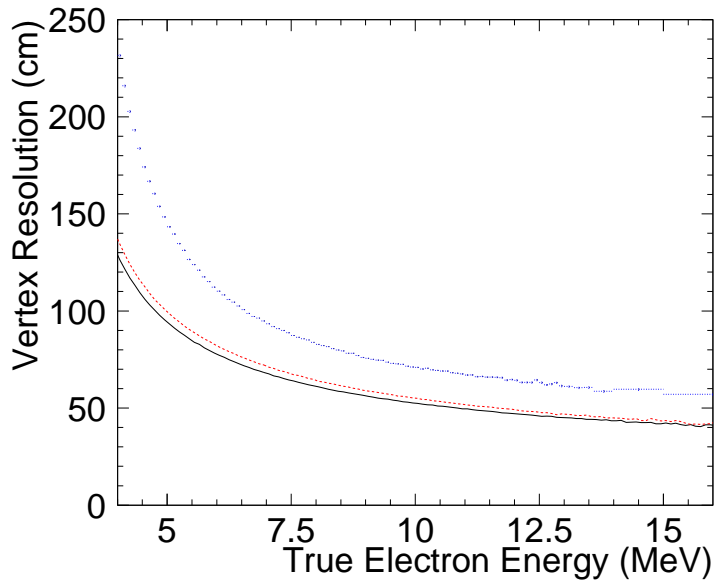


Figure 4.2: The vertex resolutions for SK-I (Blue), SK-III (Red) and SK-IV (Black) [110]. The horizontal axis shows the true electron kinetic energy [MeV]. The vertex resolution is defined as the point which contains 68% of events in the distance distribution between the real vertex and the reconstructed vertex.

## 4.2 Direction reconstruction

Sine the Cherenkov light makes a ring-like pattern of photons, it is possible to reconstruct the direction of the event. The direction reconstruction uses a maximum likelihood function which is defined as

$$\mathcal{L}(\vec{d}) = \sum_i^{N_{20}} \log (f(\cos \theta_i, E)) \times \frac{\cos \theta_i}{a(\theta_i)}. \quad (4.2.1)$$

The variables used in this likelihood function are the following:

1.  $N_{20}$ : The number of the hit PMTs within 20 nsec around  $t - t_{\text{tof}} - t_0 = 0$ .
2.  $f(\cos \theta_i)$ : The expected distribution of the opening angle between the direction of the particle and the direction of the observed photon from the vertex position.  $f(\cos \theta_i, E)$  depends on the energy because a particle traveling in the water scatters via multiple Coulomb scatterings. In order to take into account this effect, its energy dependence is evaluated using the MC simulation of mono-energetic electrons and it is shown in Figure 4.3.
3.  $\cos \theta_i/a(\theta_i)$ : The correction factor coming from PMT acceptance. The angle  $\theta_i$  is defined as the vector from the reconstructed vertex position to the  $i$ -th hit PMT and the vector normal to the PMT surface.  $a(\theta_i)$  is the correction factor of PMT acceptance, which depends on the incident angle of Cherenkov light as shown in Figure 5.4.

In order to maximize the likelihood function, the direction is scanned and the best-fit direction is determined.

## 4.3 Energy reconstruction

The energy reconstruction is the most important item for the detector performance because the solar neutrino energy spectrum measurement requires the precise energy determination. Generally speaking, the number of emitted Cherenkov photons are approximately proportional to the recoil electron energy.

In the low energy reconstruction, the effective number of hits,  $N_{\text{eff}}$ , is used.  $N_{\text{eff}}$  is calculated from the number of the hit PMTs within 50 nsec time window with some corrections.  $N_{\text{eff}}$  is represented as

$$N_{\text{eff}} = \sum_i^{N_{\text{hit}}} \left[ (X_i + \varepsilon_{\text{tail}} - \varepsilon_{\text{dark}}) \times \frac{N_{\text{all}}}{N_{\text{alive}}} \times \frac{1.0}{S(\theta_i, \phi_i)} \times \exp\left(\frac{r_i}{\lambda_{\text{eff}}}\right) \times \frac{1}{QE_i(t)} \right]. \quad (4.3.1)$$

The parameters used in equation (4.3.1) are the following:

1. Occupancy ( $X_i$ ): When the event happens near the wall (or a higher energy particle), a hit PMT detects multiple photons. If this situation occurs, it is likely that many surrounding PMTs also detect signals. The effect of the multiple p.e.'s for each hit PMT should be

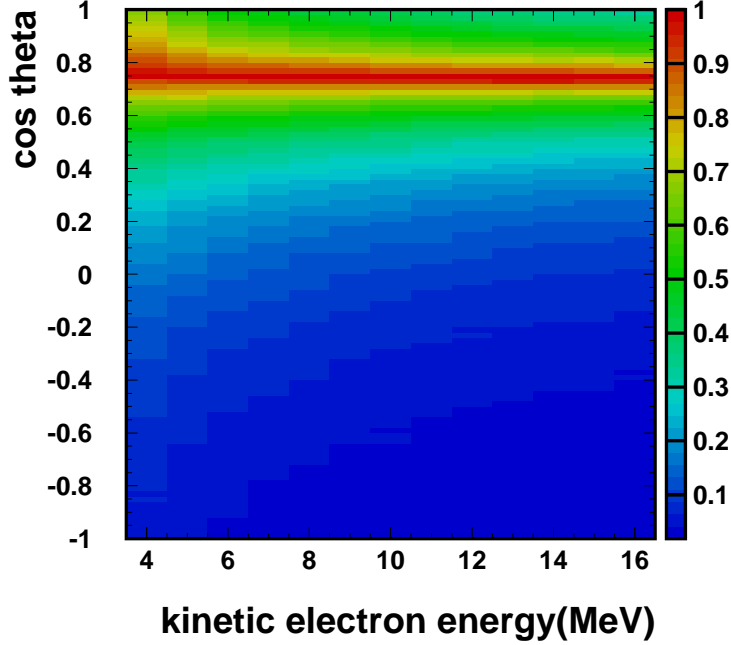


Figure 4.3: The energy dependence of the angular likelihood function used in the direction reconstruction [99].

considered. In order to correct the fraction of the  $i$ -th hit PMT which observes more than a single photon, the occupancy correction is used. The correction factor is defined as

$$X_i = \begin{cases} \frac{\log[1/(1-x_i)]}{x_i} & x_i < 1, \\ 3.0 & x_i = 1, \end{cases} \quad (4.3.2)$$

where  $x_i$  is the fraction of the hit PMT in a  $3 \times 3$  patch around the  $i$ -th hit PMT.

2. Late hits ( $\varepsilon_{\text{tail}}$ ): Some of the emitted Cherenkov photons can be scattered or reflected during traveling in the water. Such photons are not detected within the 50 nsec timing window. In order to correct these late signals, the late hits should be added for the correction. The correction factor is defined as

$$\varepsilon_{\text{tail}} = \frac{N_{100} - N_{50} - N_{\text{alive}} \times R_{\text{dark}} \times 50 \text{ nsec}}{N_{50}}, \quad (4.3.3)$$

where  $N_{100}$  is the maximum number of the hits in a 100 nsec timing window,  $N_{\text{alive}}$  is the number of the functioning PMTs and  $R_{\text{dark}}$  is the average of the dark rate. The dark rate is measured for each run and it varies in time as shown in Figure 4.4.

3. Dark noise ( $\varepsilon_{\text{dark}}$ ): The dark noise hits accidentally enter the 50 nsec time window. Such contaminations should be subtracted when  $N_{\text{eff}}$  is calculated. The dark noise correction

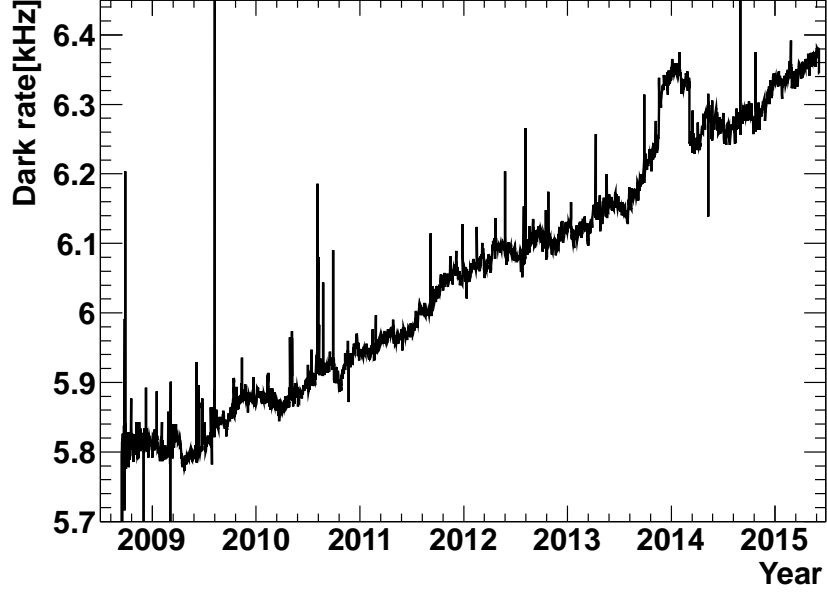


Figure 4.4: The time variation of the average of the dark rate of PMTs. The jump around August 2013 was caused by the replacement of the HV power supply for ID PMTs.

is defined as

$$\varepsilon_{\text{dark}} = \frac{N_{\text{alive}} \times R_{\text{dark}} \times 50 \text{ nsec}}{N_{50}}. \quad (4.3.4)$$

4. Dead PMTs ( $N_{\text{all}}/N_{\text{alive}}$ ): The number of the ID PMTs are considered. In order to account for the dead PMTs, the scaling factor is used.  $N_{\text{all}}$  is the total number of the PMTs, which is 11,129 in SK-IV.  $N_{\text{alive}}$  is the number of alive PMTs.
5. Photo-cathode coverage ( $S(\theta_i, \phi_i)$ ): The photo-cathode area affects the directional dependence for the detection efficiency. The effective photo-cathode area of the  $i$ -th PMT is defined as  $S(\theta_i, \phi_i)$ . The angles  $\theta_i$  (the incident angle to the  $i$ -th PMT) and  $\phi_i$  (azimuth angle) are illustrated in the left of Figure 4.5. This correction factor as function of these angles is shown in the right of Figure 4.5.
6. Water transparency ( $\lambda_{\text{eff}}$ ): Since the emitted photons are absorbed or scattered in the water, this effect should be corrected. The water transparency is measured using muon-decay electrons as described in section 5.2. In the term of  $\exp(r_i/\lambda_{\text{eff}})$ ,  $r_i$  is the distance between the reconstructed vertex and the position of the  $i$ -th PMT and  $\lambda_{\text{eff}}$  is the measured water transparency.
7.  $QE_i$ : Quantum efficiency of each PMT is corrected.

After all above corrections, the total (kinetic and mass) electron energy is determined as a function of  $N_{\text{eff}}$ . Figure 4.6 shows the relationship between the  $N_{\text{eff}}$  and the reconstructed

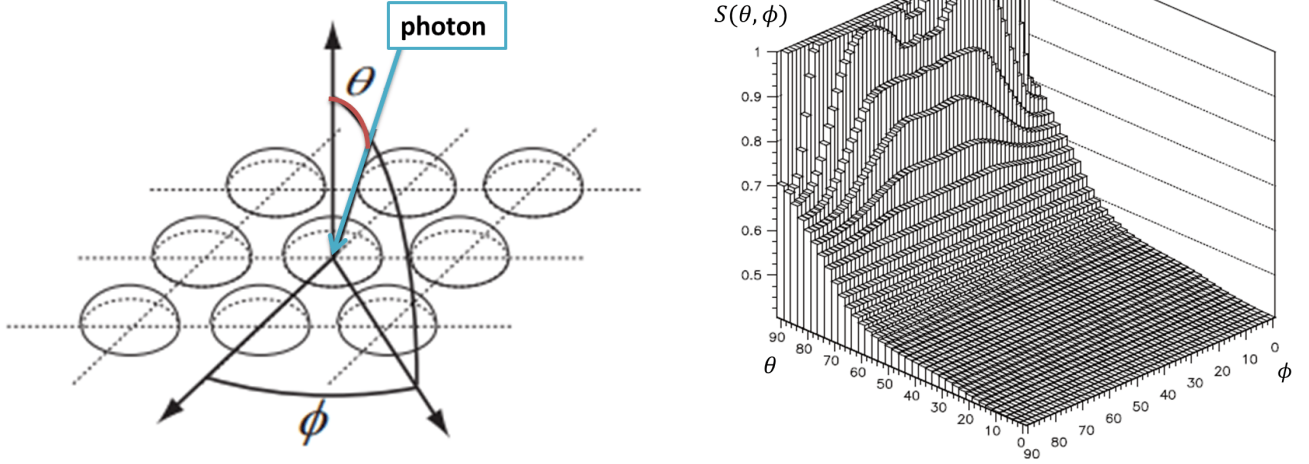


Figure 4.5: Left: The definition of the angles  $(\theta_i, \phi_i)$  for the  $i$ -th hit PMT. Right: The effective PMT photo-cathode coverage correction factor  $S(\theta, \phi)$  as a function of  $(\theta, \phi)$  [99].

energy extracted by LINAC calibration data and MC simulation. In the case of  $N_{\text{eff}} < 189.8$  ( $\sim 25$  MeV), the following function is used

$$E_{\text{rec}} = \sum_{i=0}^4 a_i (N_{\text{eff}})^i, \quad (4.3.5)$$

where  $a_0 = 0.82$ ,  $a_1 = 0.13$ ,  $a_2 = -1.11 \times 10^{-4}$ ,  $a_3 = 1.25 \times 10^{-6}$  and  $a_4 = -3.42 \times 10^{-9}$  respectively. Since above 25 MeV, the proportionality is better than that below  $\sim 25$  MeV, the first order polynomial fit is used as,

$$E_{\text{rec}} = 25.00 + 0.138(N_{\text{eff}} - 189.8). \quad (4.3.6)$$

This reconstruction method is applied to electrons and positrons not for muons and pions.

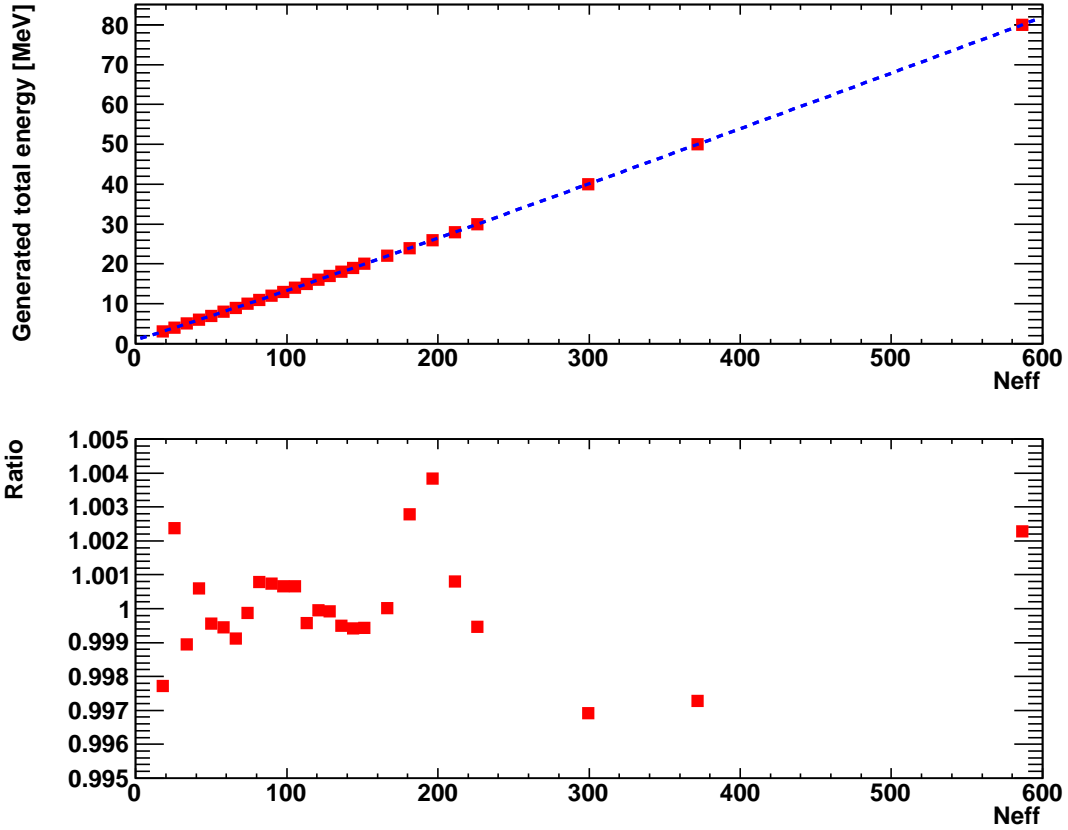


Figure 4.6: The upper panel shows the relationship between  $N_{\text{eff}}$  and the generated electron total energy [MeV]. The lower panel shows the difference between the MC simulate energy and the fitting function.

# Chapter 5

## Detector calibration method

In this chapter, the methods of the detector calibration are described. There are 4 phases of SK and their detector performances are not exactly same because of the difference in the detector structure and the electronics. The calibration methods used in SK-I was reported in [58].

Since this thesis focuses on SK-IV, the calibration methods used in SK-III and SK-IV are explained, because the important (pre-)calibration was performed at the beginning of SK-III after the recovery of the PMTs. Because the difference between SK-III and SK-IV is the installation of the new front-end electronics, the difference in the detector performance between SK-III and SK-IV is caused by the difference in the electronics performance.

### 5.1 PMT calibration

Since the timing behavior of PMTs depends on the charge of the measured pulse, it is useful to define the two factors related with the charge calibration. The one is a conversion factor from the number of photoelectrons to charge in units of pC, which is called “gain”. It is divided into 2 parts, the absolute gain and the relative gain. The other is called “QE” which is the product of the quantum efficiency and the collection efficiency of photoelectrons onto the first dynode of the PMT. Since each PMT may have different QE, it is required to calibrate for each individual PMT. In this section, the calibration methods for the absolute gain, the relative gain and the individual PMT QEs are described.

#### 5.1.1 Absolute gain calibration

The absolute gain is commonly applied to all PMTs. According to this factor, the number of the photoelectrons is converted to the output charge in pC. Since the absolute gain depends on the supplied HV value, the supplied HV values for each PMT were determined at the beginning of the SK-III using a Xe light source.<sup>1</sup>

---

<sup>1</sup>The Xe light source consists of a Xe lamp, an UV fiber and a scintillator ball. The Xe lamp was produced by Hamamatsu Photonics, and it is located on the SK tank. Light released from the Xe lamp passes through a UV filter and then simultaneously injects into two optical fibers. The one fiber connect to the scintillator ball which is installed at the near the center position of the SK tank at  $(x, y, z) = (353.5, -70.7, 0.0)$  cm. The other fiber is connected to a monitoring system to measure the light intensity of the Xe lamp.

In order to evaluate the observed charge for each PMT, it is useful to define a charge response ( $Q_{\text{obs}}$ ) for each PMT

$$Q_{\text{obs}} \propto N_{\text{photon}}(i) \times QE(i) \times A(i), \quad (5.1.1)$$

where  $N_{\text{photon}}(i)$  is the number of the photons which hit the photocathode on the  $i$ -th PMT,  $QE(i)$  is ‘‘QE’’ of the  $i$ -th PMT and  $A(i)$  is the gain of  $i$ -th PMT. After evaluating each  $Q_{\text{obs}}(i)$ , the supplied HV values were determined to produce the same  $Q_{\text{obs}}$  value.

After setting the value of supplied HV for each PMT, the absolute gain was determined using a Ni-Cf calibration source. The absolute gain was determined to measure the output charge distribution of the one photoelectron hits. Figure 5.1 shows the typical charge distribution of the single photoelectron using Ni source calibration data in SK-III.

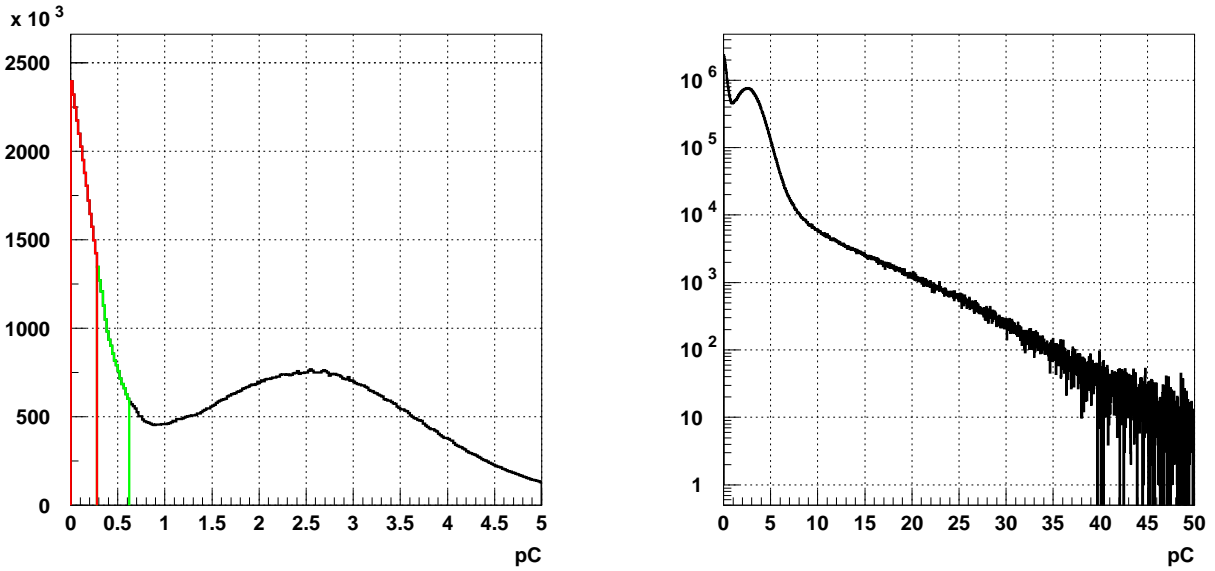


Figure 5.1: The typical charge distribution of the single photoelectron using Ni calibration source [93]. The left (right) figure illustrates the histograms in liner (logarithmic) scale. In the left figure, the black histograms indicate the result with the normal PMT gain, the green histograms indicate the result with the double gain and half threshold and the red histograms indicate the linear extrapolation.

According to this calibration result, the absolute gain for SK-III was determined as 2.243 pC/p.e. After the installation of the new front-end electronics, the same calibration was performed at the begging of SK-IV and the its value was determined as 2.645 pC/p.e. Table 5.1 summarizes the absolute gain for each SK phase.

The difference between SK-II and SK-III is caused by the installation of the newly produced PMTs. The new PMTs have a lower gain compared with the PMTs used in SK-II and this difference makes the absolute gain in SK-III to be lower than that of SK-II. The difference between SK-III and SK-IV is caused by a long-term increase of the PMT gain, which equivalent to 2 ~ 3% per year, and by the different performance of the electronics.

Table 5.1: The values of the absolute gain for each SK phase.

SK phase	Absolute gain [pC/p.e.]
SK-I	2.055
SK-II	2.297
SK-III	2.243
SK-IV	2.645

### 5.1.2 Relative gain calibration

The relative gain adjusted for the relative difference among PMTs to insure that all PMTs produce an uniform response for the output charge. In order to evaluate the relative gain of each individual PMT, a laser calibration system was developed. This laser system could inject high and low intensity light. In the case of the high (low) output, each PMT detects  $\sim 50$  p.e. (1 p.e.). The observed charge in the  $i$ -th PMT in the high intensity data is defined as

$$Q_{\text{obs}}(i) = I_{\text{high}}(i) \times QE(i) \times G_{\text{rel}}(i) \quad (5.1.2)$$

where  $I_{\text{high}}(i)$  is the light intensity seen by the  $i$ -th PMT and  $G_{\text{rel}}(i)$  is the relative gain of the  $i$ -th PMT. Using the low intensity data, the number of hits,  $N_{\text{hit}}(i)$  is counted when the  $i$ -th PMT records a charge which is greater than the threshold value.

The ratio between  $Q_{\text{obs}}(i)$  to  $N_{\text{hit}}(i)$  provides the relative gain  $G_{\text{rel}}(i)$  because  $Q_{\text{obs}}(i)$  is proportional to  $QE(i)$  and  $G_{\text{rel}}(i)$ , while  $N_{\text{hit}}(i)$  is proportional only to  $QE(i)$

$$\frac{Q_{\text{obs}}(i)}{N_{\text{hit}}(i)} \propto G_{\text{rel}}(i). \quad (5.1.3)$$

Figure 5.2 shows the result of the relative gain measurement. The  $1\sigma$  in this distribution is within  $\sim 6\%$ . This measurement method can remove the effect from the water transparency and the geomagnetic field variations, because the common effects are canceled out when the ratio is taken.

After the determination of the absolute and the relative gain of each PMT, these parameters are used to covert the output charge from the PMT to the number of the photoelectrons.

### 5.1.3 PMT quantum efficiency measurement

In order to measure the individual QE for each PMT, the hit rate of each PMT is evaluated using the Ni calibration source because the hit probability should be proportional to the value of QE of each PMT when low intensity light is injected.

Since the dark noise hits or the radioactive background enter the event timing window during a Ni calibration, they should be removed from the calibration data to measure the QE. In order to remove these background hits, the timing window is divided into two regions, one is “on-time” and the other is “off-time” as shown in Figure 5.3. When the timing distribution is made, the time of flight is subtracted, because the hit timing depends on the calibration source position. The “on-time window” is set with a 300 nsec around the peak position of the timing distribution. The “off-time window” is set with a 300 nsec window starting at 150 nsec after

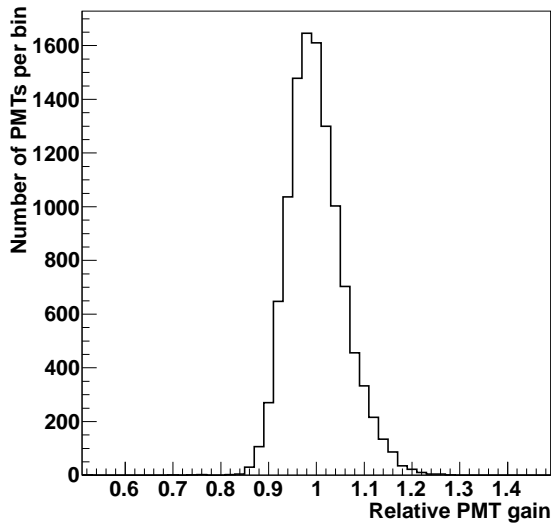


Figure 5.2: The relative gain measured using the laser calibration data [93].

the end of the “on-time window”. The hits within these timing windows are called “on-time hit” and “off-time hit”, respectively.

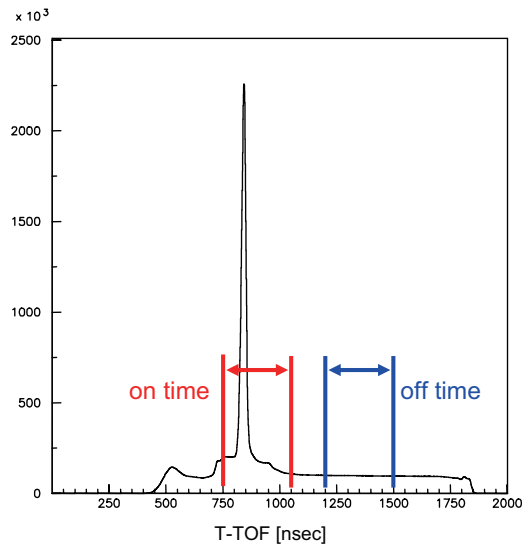


Figure 5.3: A typical hit timing distribution of the Ni calibration [108]. The on-time (off-time) window is set to 750 – 1050 nsec (1200 – 1500 nsec).

To obtain the number of true hits, the number of the hit within the “off-time window” is subtracted from that of the “on-timing window”. Since the hit rate depends on both geometrical location of a PMT and the Ni calibration source position, the corrected hit rate for the  $i$ -th PMT is defined as

$$h_{\text{corr}}(i) = \frac{h_i \times r_i^2}{a(\theta_i)} \quad (5.1.4)$$

where  $h_i$  is the hit rate for the  $i$ -th PMT,  $r_i$  is the distance between the  $i$ -th PMT and the calibration source position and  $a(\theta_i)$  is the PMT acceptance which is extracted by the MC simulation as shown in Figure 5.4. This acceptance depends on the geometry of the PMT and the acrylic case. After the installation of the acrylic case in SK-II, its value was changed<sup>2</sup>. The PMT angular dependence of the PMT acceptance was represented as

$$a(\theta_i) = 0.205 + 0.524 \cos \theta_i + 0.390 \cos^2 \theta_i - 0.132 \cos^3 \theta_i. \quad (5.1.6)$$

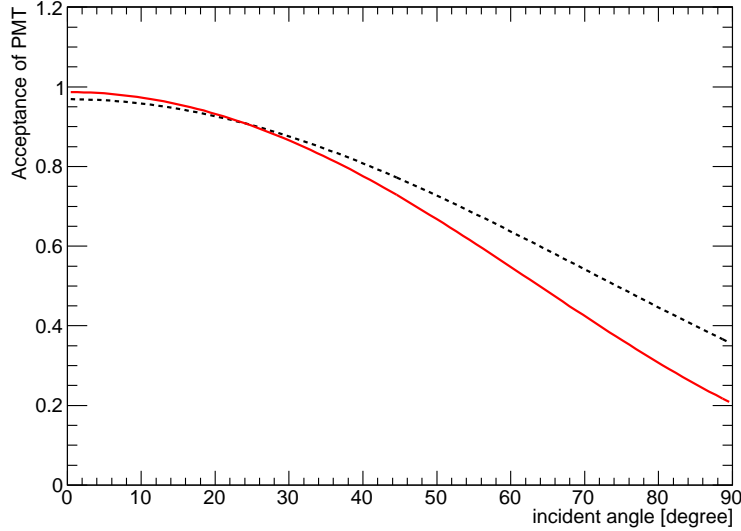


Figure 5.4: The incident angle dependence of the PMT acceptance. The black dotted curve indicates the acceptance without the acrylic case. The red curve indicates the acceptance with the acrylic case used in SK-II, SK-III and SK-IV. The difference of acceptance above  $40^\circ$  is caused by the combination of the geometry of the PMT and the acrylic case.

Finally, the hit rate is normalized to obtain the hit probability as

$$P_h(i) = \frac{h_{\text{corr}}(i)}{\sum h_{\text{corr}}(i)/N_{\text{all}}}, \quad (5.1.7)$$

<sup>2</sup> Before the installation of the acrylic case when SK-I, the angular dependence of the PMT acceptance was described as

$$a(\theta_i) = 0.354 + 0.510 \cos \theta_i + 0.116 \cos^2 \theta_i - 0.012 \cos^3 \theta_i. \quad (5.1.5)$$

where  $N_{\text{all}}$  is the total number of the PMTs in the detector. Figure 5.5 shows the result of the hit rate probability for the barrel, top and bottom regions. According to Figure 5.5, there remains a position dependence in the hit probability  $P_h(i)$ . It is caused by the photon scattering and absorption in water and by the reflection on the surface of the neighboring PMTs or the black sheets.

In order to evaluate this position dependence, a MC simulation is prepared which considered the absorption and the scattering in water, and the reflection from the surface of the PMTs and the black sheets. When the MC simulation is generated, the value of QE for each PMT is set to the same value. The result from the MC simulation is also shown in Figure 5.5 and the same tendency of position dependence is seen and it is well modeled. However, there is a few % level difference between the data and the MC simulation.

Taking the ratio between the data and the MC simulation, the value of QE for individual PMT in the MC simulation is determined. These QE values are listed as ‘getable’ as already described in equation (3.5.11). In the SK simulation, this table is used for weighting the photoelectron production.

#### 5.1.4 PMT timing calibration

The detail of the calibration method for obtaining the timing resolution is described in [93]. The brief explanation is given in this subsection.

The PMT timing information is the most important item for the reconstruction of the vertex position. Since the difference in length of the cable and the variation in response of the electronics, the timing response would not be same among PMTs. Due to the property of the signal of the PMT, the time-walk occurs when the different amount of charge is observed. Figure 5.6 shows the example of the time-walk, when the small charge signal or the large charge signal is observed. If the large charge signal is observed, the pulse height exceeds the TDC discriminator threshold earlier than in the small charge signal case.

In order to calibrate the PMT timing response for various charges, the relation between the timing and the charge is evaluated using a laser calibration device. The relation is called ‘‘TQ-map’’, which is the timing as a function of the pulse height. This map is fitted by various polynomial functions depending on its charge range. Then, the fitted parameters are used to correct the time response for each PMT as a function of the observed charge.

To calibrate the TQ-map, a laser calibration device is used, because a fast rise time light pulse and an easy control of intensity are needed. At the beginning of the SK-IV, a calibration was made using the USHO laser calibration system as shown in the left of Figure 5.7.

In order to calibrate the TQ-map for each channel, the timing distribution for each PMT is made subtracting the time of flight from the source position to each PMT. The selected laser hits of each readout channel are divided into 180 bins of charge, which are called ‘‘ $Q_{\text{Bin}}$ ’’. Each  $Q_{\text{Bin}}$  is defined as the amount of charge in pC; It is defined on a linear scale from 0 to 10 pC and on a logarithmic scale from 10 to 3981 pC.

After dividing into the 180  $Q_{\text{Bin}}$ s, timing distributions are made for each  $Q_{\text{Bin}}$ . Since the timing distribution does not have a symmetric shape due to the late hits by the reflection and the scattering. In order to take into account this asymmetric effect in the timing distribution, the timing distributions are fitted by an asymmetric Gaussian function. Finally, the timing peak and the standard deviation for respective charges are fitted by various polynomial functions.

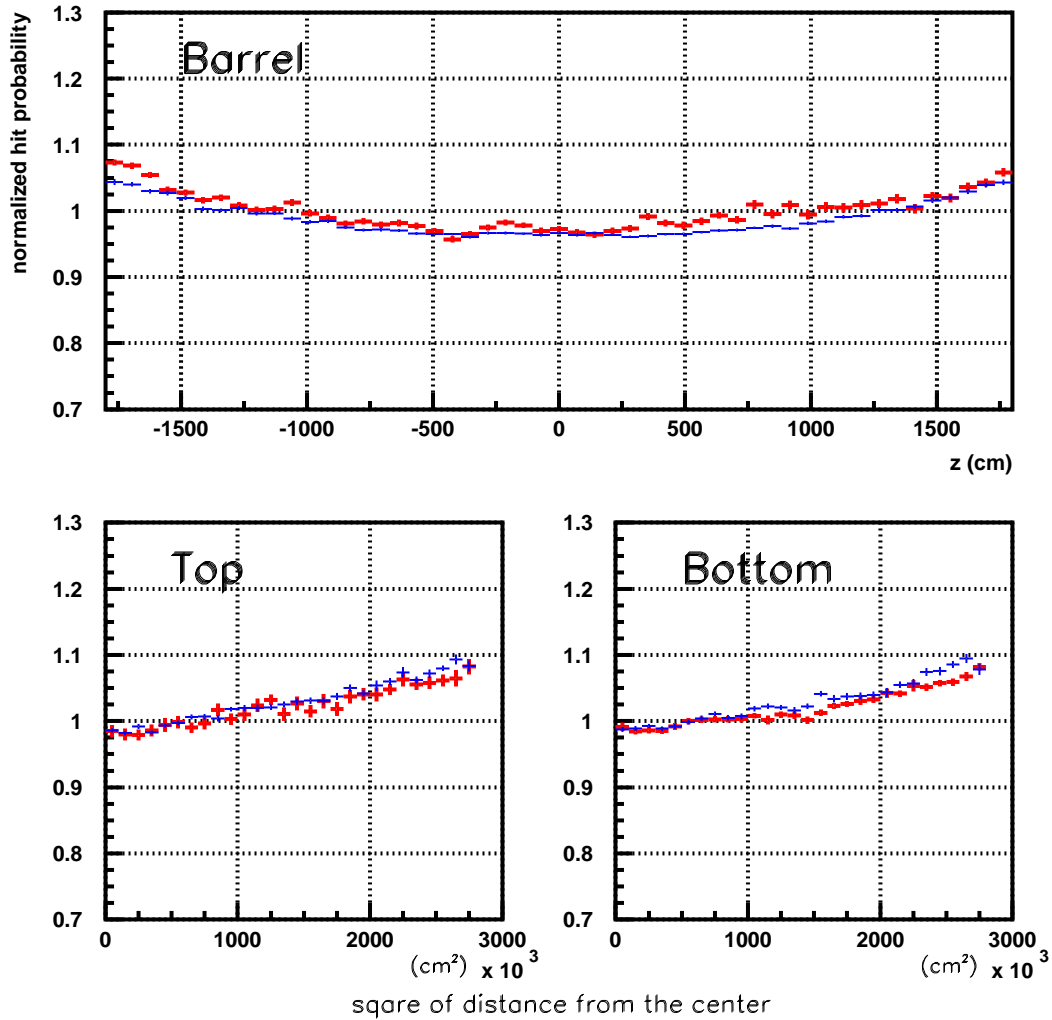


Figure 5.5: A position dependence of the normalized hit probability [93]. The red and blue points show the result from the calibration data and that of MC simulation, respectively. The upper panel shows a plot for the barrel PMTs where the horizontal axis is the  $z$  position of PMTs. The lower figure shows top (left) and the bottom (right) PMTs, where the horizontal axis is the square of the distance from the center position.

The timing resolution is evaluated for each  $Q_{\text{bin}}$  by taking the average fitted time resolutions of all PMTs. The right of Figure 5.8 shows the results of the timing resolution for SK-I, SK-III and SK-IV. At the single photoelectron level, the timing resolution in SK-IV is 2.1 nsec. The better timing resolution in SK-IV is due to the better timing performance of the front-end electronics.

During normal data taking, the stability of the timing response is monitored using a nitrogen laser which fires at  $\sim 0.03$  Hz. The stability of the timing resolution keeps within  $\pm 0.1$  ns for a few years [93].

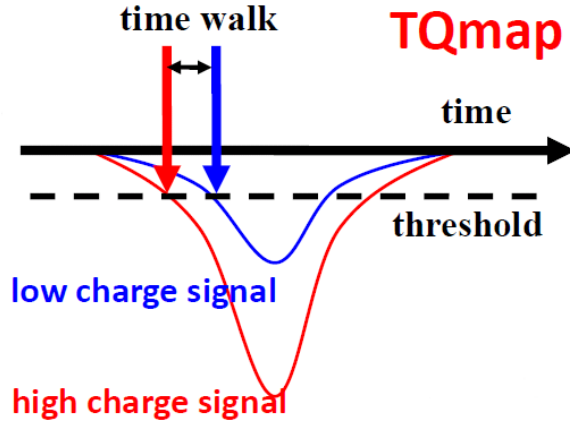


Figure 5.6: The visual explanation of the time-walk effect [108]. The red (blue) curve indicates the large (small) charge signal and the dashed line indicates the TDC discriminator threshold. When the large charge signal is observed, the pulse height exceeds the threshold earlier than in the case of the small charge signal.

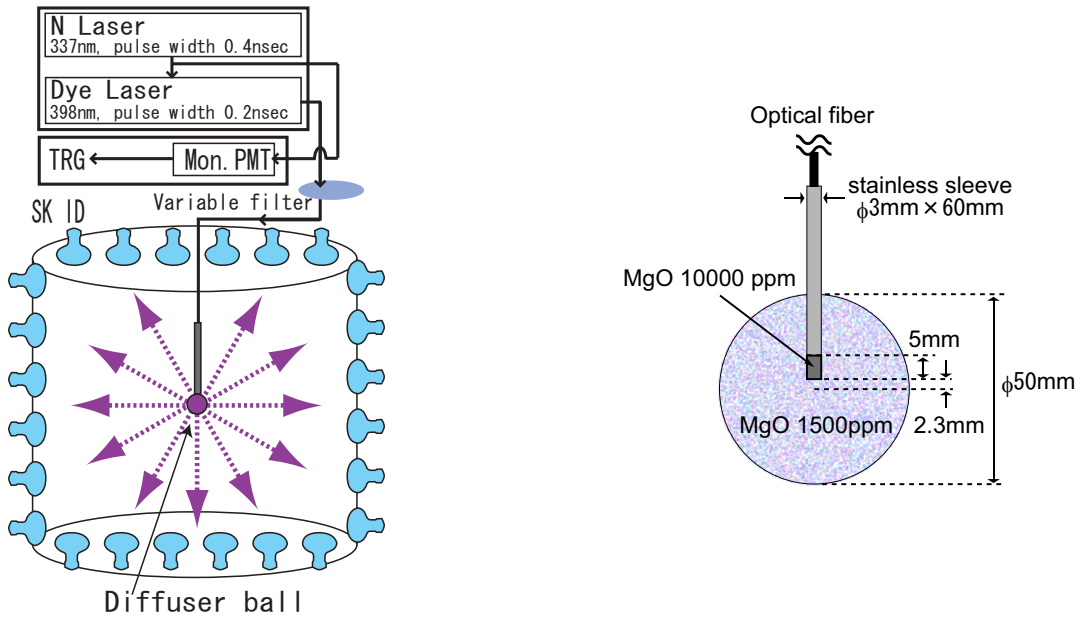


Figure 5.7: Left: A schematic view of the USHO laser light calibration system [93]. Right: The cross section of the diffuser ball [93].

## 5.2 Water transparency measurement

Transparency of pure water in the tank is an important parameter to characterize the response of the detector to the solar neutrino events, since it determines the number of detected Cherenkov photons.

In this section, two methods to measure water transparency are described. One is using  $N_2$  laser light injected in the tank and the other using decay electrons from stopping cosmic ray

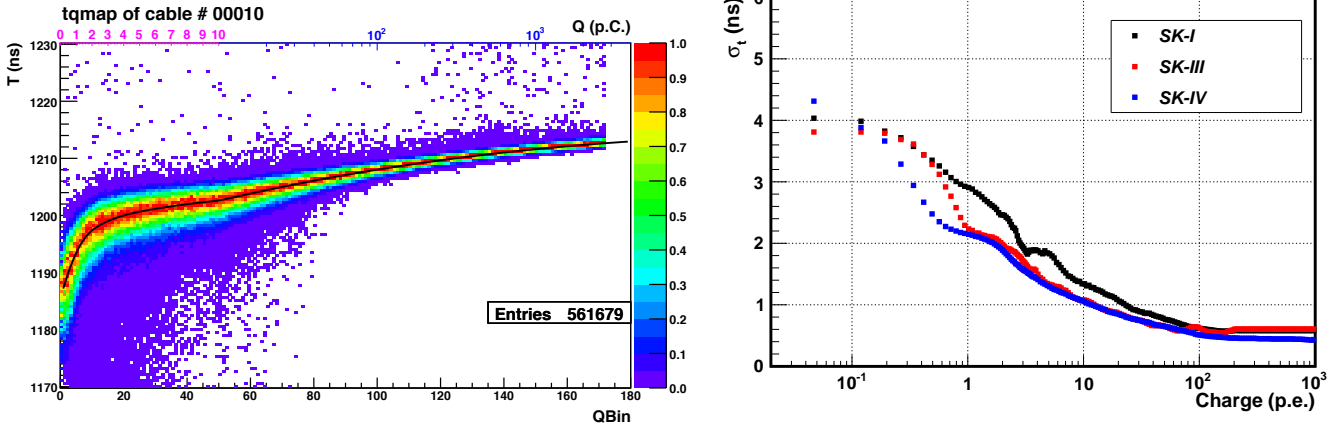


Figure 5.8: Left: Typical scatter plot for the timing and charge distribution for a readout channel in SK-IV [93]. The horizontal axis is charge of each hit (QBin), and the vertical axis is time [ns] after subtracting the time of flight [93]. Right: The timing resolution after correcting by TQ-map. The black, red and blue points show the timing resolution in SK-I, SK-III and SK-IV, respectively. The improvement in SK-IV was due to the better timing performance of the front-end electronics.

muons. The former is important for the SK simulation in the step of the Cherenkov photon propagation and the later is used for correcting for energy as the water attenuation length in the solar neutrino analysis.

### 5.2.1 Measurement of water transparency with laser light injection

As described in the subsection 3.5.2, the water attenuation length is characterized by using the three coefficients  $\alpha_{\text{abs}}$ ,  $\alpha_{\text{sym}}$  and  $\alpha_{\text{asym}}$  in the SK simulation. These coefficients are measured using light injectors N<sub>2</sub> laser (337 nm) or the laser diodes (375 nm, 405 nm, 445 nm and 473 nm). Figure 5.9 illustrates the laser light injection system to measure three coefficients for the water transparency [93].

The light is injected every one minute and the hit rate in the different region of the SK ID are monitored. The measurement methods are as following:

1. The detector is divided into 6 regions, top and barrel (B1 ~ B5) according to the left of Figure 5.9.
2. The scattered hit rate and the observed total charge  $Q_{\text{tot}}$  are measured and the ratio of hits and  $Q_{\text{tot}}$  (hits/ $Q_{\text{tot}}$ ) distributions are obtained for each divided region. The observed charges in the bottom PMT are used for the reference to monitor the intensity of the laser light.
3. Several sets of MC simulations are generated with varying the coefficients and the same hits/ $Q_{\text{tot}}$  distributions are prepared. The right of Figure 5.9 shows the typical distribution of hits/ $Q_{\text{tot}}$  in the each region.

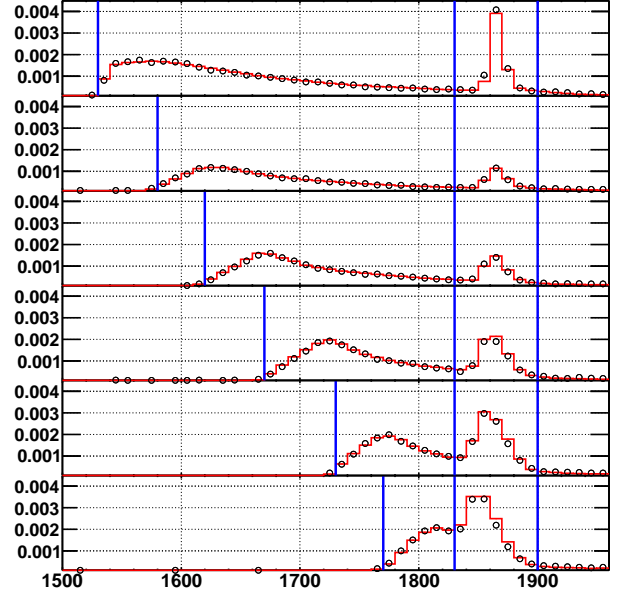
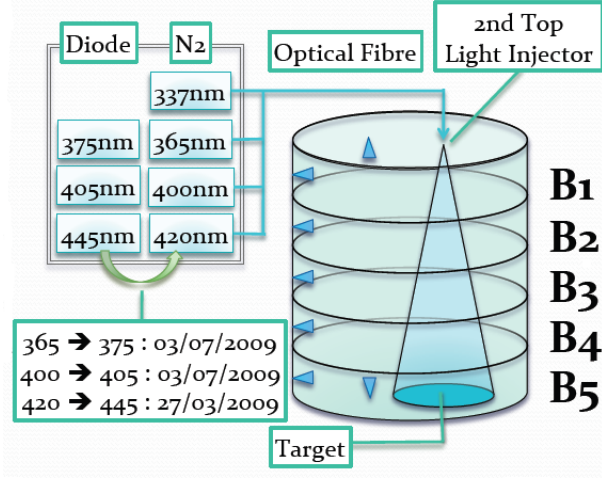


Figure 5.9: Left: The schematic view of the laser injection system for water parameter measurement [93]. Right: The typical hit rate distribution [93]. The horizontal axis shows the time [nsec] after subtracting the time of flight. The vertical axis shows the hit rate. The left broad peak is caused by the scattered light and the right peak is caused by the reflection on the detector structure.

Table 5.2: The summary of the typical water parameters obtained using the calibration data in April 2009 [93].

$P_0$	$P_1$	$P_2$	$P_3$	$P_4$	$P_5$	$P_6$	$P_7$	$P_8$
0.624	$2.96 \times 10^7$	$3.24 \times 10^{-2}$	10.9	$8.51 \times 10^7$	$1.14 \times 10^5$	$1.00 \times 10^{-4}$	$4.62 \times 10^6$	392

- The distributions of the calibration data and the MC simulation are compared using the  $\chi^2$  defined as

$$\chi^2 = \sum_{\text{region}} \frac{(\text{Data} - \text{MC})^2}{\sigma_{\text{Data}}^2 + \sigma_{\text{MC}}^2}, \quad (5.2.1)$$

where Data (MC) is the peak position of the hits/ $Q_{\text{tot}}$  distribution,  $\sigma_{\text{Data}}$  ( $\sigma_{\text{MC}}$ ) is the standard variation of the hits/ $Q_{\text{tot}}$  distributions.

- Scanning the water transparency coefficients to minimize the value of  $\chi^2$ . Table 5.2 shows the result of typical water fitting parameters in April 2009.

Obtained coefficients are shown in the left of Figure 5.10. The right of Figure 5.10 shows the time variation of the measured coefficients measured by the laser calibration. According to the right of Figure 5.10,  $\alpha_{\text{sym}}$  is stable within  $\sim 3\%$  from October 2008 to November 2012. However,  $\alpha_{\text{abs}}$  and  $\alpha_{\text{asym}}$  varied, by 20 – 40% for  $\alpha_{\text{abs}}$  and by 20 – 60% for  $\alpha_{\text{asym}}$  over the time period. Since  $\alpha_{\text{abs}}$  is larger than  $\alpha_{\text{asym}}$ , as shown in the left of Figure 5.10, the time variation of the water transparency was mainly caused by the absorption process in water.

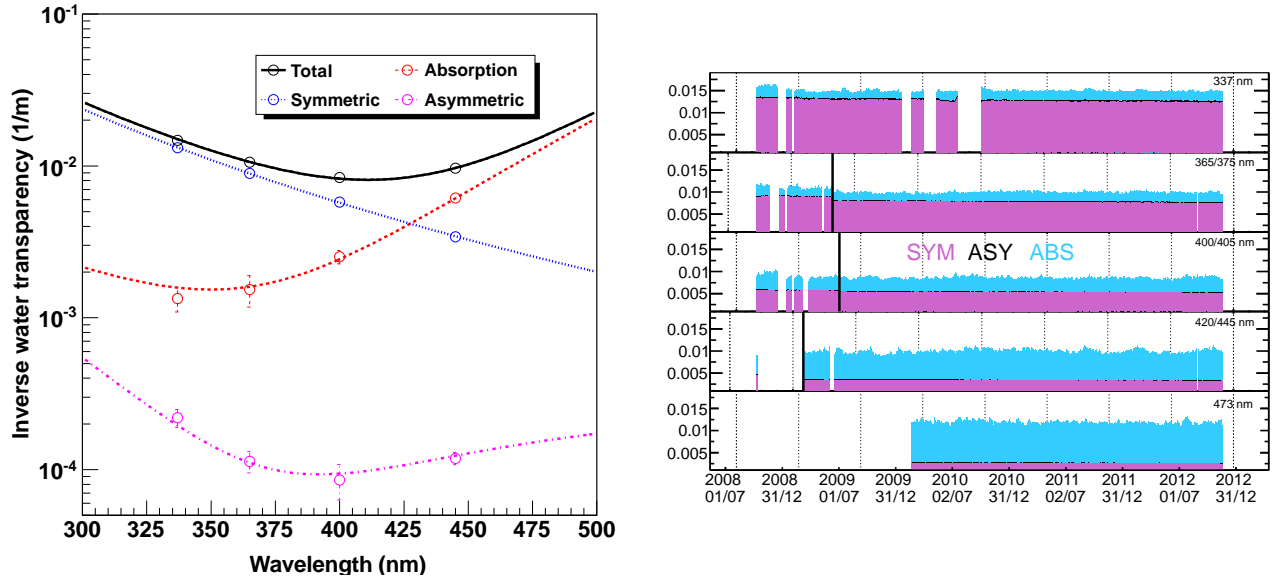


Figure 5.10: Left: Typical observed coefficients of water parameters and fitted functions (dashed lines) which are used in the SK MC simulation [93]. The horizontal axis shows the wavelength and the vertical axis shows the coefficients. The points illustrate the calibration data obtained in April 2009 [93]. Right: The time variation of the coefficients measured by the laser injection system [93]. The horizontal axis shows the date in SK-IV and the vertical axis shows the coefficients stacked in order of SYM (symmetric scattering), ASY (asymmetric scattering) and ABS (absorption).

### 5.2.2 Measurement of water transparency with Decay electron

As described in subsection 3.4.1, the improvements of the water circulation system made the water transparency more stable during SK-IV. However, still there is  $\sim 20\%$  level time variation. In order to precisely monitor this time variation, water transparency is continuously monitored using decay electrons (positrons) from cosmic ray muons, which stop in the SK tank.

The selection criteria of decay electron events are following:

1. The time difference between the parent muon event and the decay electron candidate event, defined as  $\Delta t$ , should be  $3.0 \mu\text{sec} \leq \Delta t \leq 8.0 \mu\text{sec}$ .
2. The reconstructed vertex of the decay electron candidate event is within the 22.5 kton fiducial volume, i.e. 2 m from the ID wall.
3. The distance between the stopping point of cosmic ray muon and decay electron candidate event is within 250 cm.

After selecting the decay electron events, the observed charge ( $Q_{\text{obs},i}$ ) of the  $i$ -th PMT and the distance ( $r$ ) between the  $i$ -th PMT and the decay electron candidate are calculated. Then, mean of the observed charge is evaluated as  $\overline{Q_{\text{obs}}} = \sum Q_{\text{obs},i} / N_{\text{total}}$ , where  $N_{\text{total}}$  is the total number of the hit PMTs. The typical histograms of  $\ln(\overline{Q_{\text{obs}}})$  versus the mean distance  $r$  are shown in the left of Figure 5.11. According to the left of Figure 5.11, the mean observed charge decreases when the distance is more than 10 m.

To obtain the water transparency, the histograms are fitted by a linear fitting function, as shown in the left of Figure 5.11 where the fitting region is selected between 1200 cm and 3500 cm. Since the  $y$ -intercept of the linear fitting function varies with time as shown in the right of Figure 5.11, this calculation method is affected by the PMT gain, because if the PMT gain increases, the observed charge also increases. In the case of the SK-IV analysis, its value is fixed at 1.468 which is equivalent to the average value during SK-III. Finally, the inverse of the slope of the linear fitting function is used as water transparency.

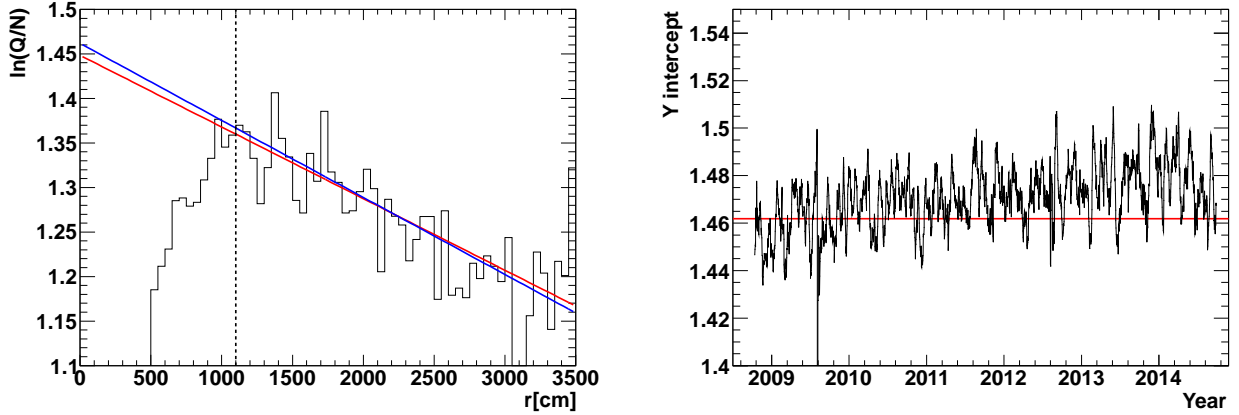


Figure 5.11: The left figure shows the typical hist of  $\ln(\bar{Q}(r))$  vs  $r$ . The blue one was fitted with the fixed value of  $y$ -intercept, 1.486, and the red was fitted with free  $y$ -intercept. The dashed vertical black line corresponds to 1200 cm. The right figure shows the time variation of the  $y$ -intercept of the fitting function. The red line corresponds to the fixed value (1.468), which is used to fit.

From the statistical point of view, the fitting needs to take a  $\pm 7$ -day running average. Figure.5.12 shows the time variation of water transparency during the SK-IV period.

As described in subsection 4.3, the effective hit ( $N_{\text{eff}}$ ) is calculated using the water transparency information. The left of Figure 5.13 shows the time variation of the effective hit distribution of the decay electron events. After the water transparency correction, the mean  $N_{\text{eff}}$  becomes stable within 0.5%, as shown in the right of Figure 5.13.

### 5.2.3 Top bottom asymmetry

As described in the subsection 3.5.2, the top-bottom asymmetry is monitored by using the laser and the Ni-Cf source. Since the top-bottom asymmetry is represented as equation (3.5.9), it is required to calculate the average hit rate in each region ( $\langle region \rangle$ ). The analysis method is almost the same as the QE measurement described in subsection 5.1.3. The difference is that the quantum efficiency of each PMT is added to equation (5.1.4) as

$$h_{\text{corr,tba}}(i) = \frac{h_i \times r_i^2 \times QE(i)}{a(\theta_i)}. \quad (5.2.2)$$

Using  $h_{\text{corr,tba}}(i)$ , the average hit rates in the top, the bottom and the barrel regions are obtained and  $TBA$  which is defined in equation (3.5.9) is evaluated. Figure 5.14 illustrates the

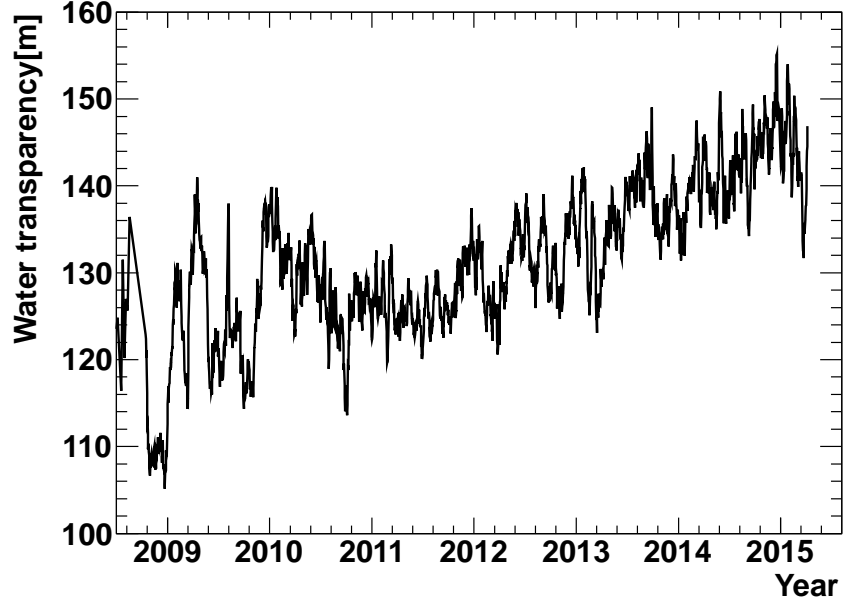


Figure 5.12: The time variation of water transparency with decay electrons samples.

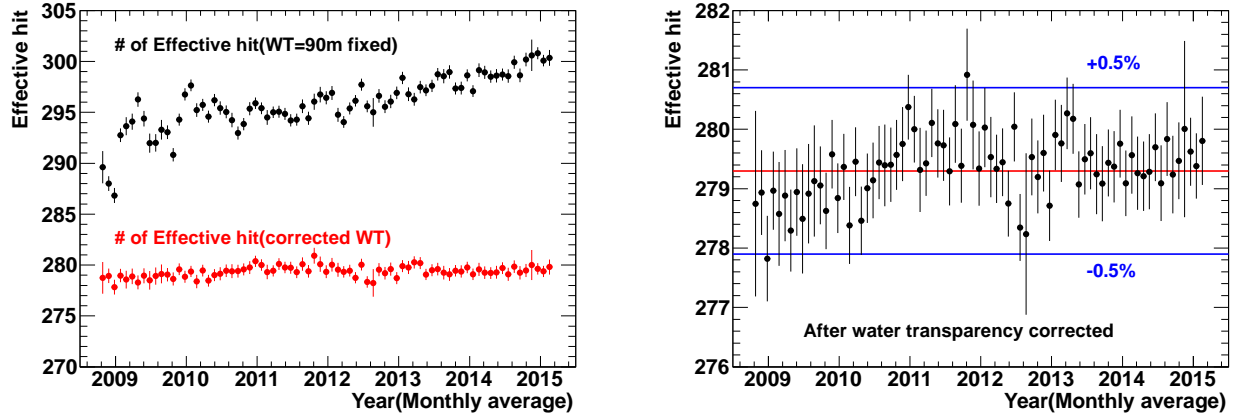


Figure 5.13: Left: The time variation of the effective hits before and after the water transparency correction which are calculated with decay electron. Right: The time variation of the effective hits after the water transparency correction.

result of  $TBA$  by using the laser and the Ni calibration sources. The two calibration results are consistent and the same tendency in the time variation is seen.

In order to obtain the best values of the parameter  $\beta$  in the equation (3.5.10), the Ni MC simulations with various  $\beta$  values are prepared. Then, the MC simulation sample are compared with the Ni calibration data. Finally the parameter  $\beta$  is determined as

$$\beta = (-0.164 \times TBA^2 - 3.676 \times TBA) \times 10^{-3}. \quad (5.2.3)$$

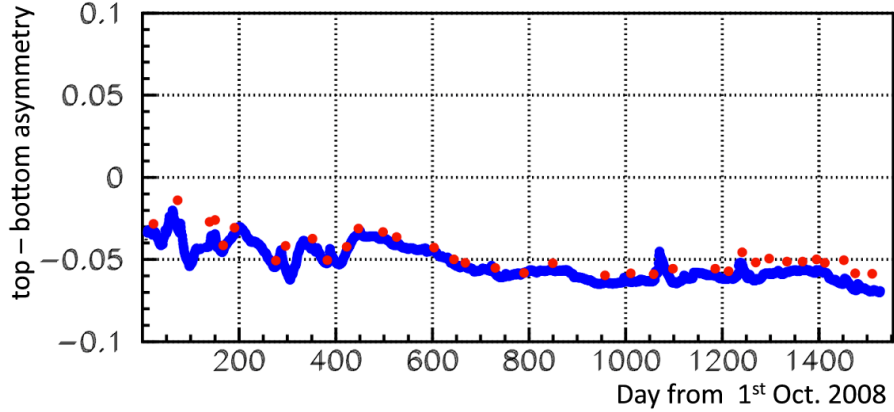


Figure 5.14: The monitoring result of the top-bottom asymmetry [93]. The horizontal axis shows the day from the beginning of the SK-IV, and the vertical axis shows the result of the monitoring. The blue line indicates the laser, and the red points indicate the Ni calibration result.

## 5.3 Absolute energy scale calibration

The calibration for the absolute energy scale is the most important item to measure the energy spectrum of solar neutrinos. In order to determine the absolute energy scale, a LINAC calibration and a DT (deuterium-tritium neutron) calibration are performed. The information of the absolute energy scale is necessary to simulate the detector response. The detector simulation should be tuned using the absolute energy scale. Especially, *COREPMT* in equation (3.5.11) should be tuned, because this factor determines the absolute energy scale in the SK simulation.

### 5.3.1 LINAC calibration

#### Overview

The LINAC calibration is the most important for the low energy data analysis to determine the precise absolute energy scale [106]. Based on this calibration, the correlation between the observed amount of Cherenkov light emitted from a charged particle and its energy is determined. This calibration also provides the information of the position, direction and time dependence of the energy scale.

The used calibration device is Mitsubishi ML15MIII electron linear accelerator (LINAC), which was originally used for medical purposes. It is installed above the SK tank [58]. The LINAC was modified to make it more useful to calibrate single electron events. It consists of a special electron gun, steering magnets and collimators to reduce the number of electrons injected into the SK tank to 0.1 per bunch. The mono-energetic electrons are injected into the tank to the downward direction.

## Data taking and Condition

LINAC calibrations were performed in 2009, 2010 and 2012 during SK-IV period. Since the calibration hole positions are fixed and the length of the beam pipe is also fixed, the calibration data were taken at the fixed 6 points as shown in the left of Figure 5.17. Table 5.3 summarizes the beam positions and the target beam energies in SK-IV. The calibration data taken in 2012 were enough to determine the tuning parameters for the SK simulation, thus the determination of the *COREPMT* was performed using the data in 2012.

During the calibration data taking, the detector was operated with the usual water circulation.

Table 5.3: The summary of the LINAC calibration position and the target beam energy. The adopted calibration data is marked by open circle.

Position	Position [cm]			Target beam energy [MeV]					
	$x$ [cm]	$y$ [cm]	$z$ [cm]	4.4	4.8	7.0	8.8	13.6	18.0
2009									
1	-1237	-70.7	+1197	○	—	—	○	○	○
2	-1237	-70.7	-6	—	○	—	○	○	○
3	-1237	-70.7	-1209	○	—	—	○	○	○
4	-388.9	-70.7	+1197	○	○	—	○	○	○
5	-388.9	-70.7	-6	○	○	—	○	○	○
6	-388.9	-70.7	-1209	○	○	—	○	○	○
2010									
1	-1237	-70.7	+1197	—	—	○	—	○	—
2	-1237	-70.7	-6	—	—	○	—	○	—
3	-1237	-70.7	-1209	—	—	○	—	○	—
4	-388.9	-70.7	+1197	—	—	○	—	○	—
5	-388.9	-70.7	-6	—	—	○	—	○	—
6	-388.9	-70.7	-1209	—	—	○	—	○	—
2012									
1	-1237	-70.7	+1197	○	○	○	○	○	○
2	-1237	-70.7	-6	○	○	○	○	○	○
3	-1237	-70.7	-1209	○	○	○	○	○	○
4	-388.9	-70.7	+1197	○	○	○	○	○	○
5	-388.9	-70.7	-6	—	○	○	○	○	○
6	-388.9	-70.7	-1209	○	○	○	○	○	○

## Beam energy measurement

In order to measure the energy of the single electron generated by the LINAC calibration system, a germanium detector is used. It is commonly known that the energy resolution of the Ge detector is very high (1.92 keV at 1.33 MeV electron) and it is useful to determine the energy of the single electron. The left of Figure 5.15 shows the output charge of the Ge detector as a

function of  $\gamma$ -ray energy. The Ge detector itself was calibrated by 0.662 MeV monochromatic gamma rays from  $^{137}\text{Cs}$  and gamma rays from  $\text{Ni}(n,\gamma)\text{N}$  reaction, e.g. 9.0 MeV. The right of Figure 5.15 shows the difference of the deviation between data and the fitted line. According to Figure 5.15, its difference is within 0.1%.

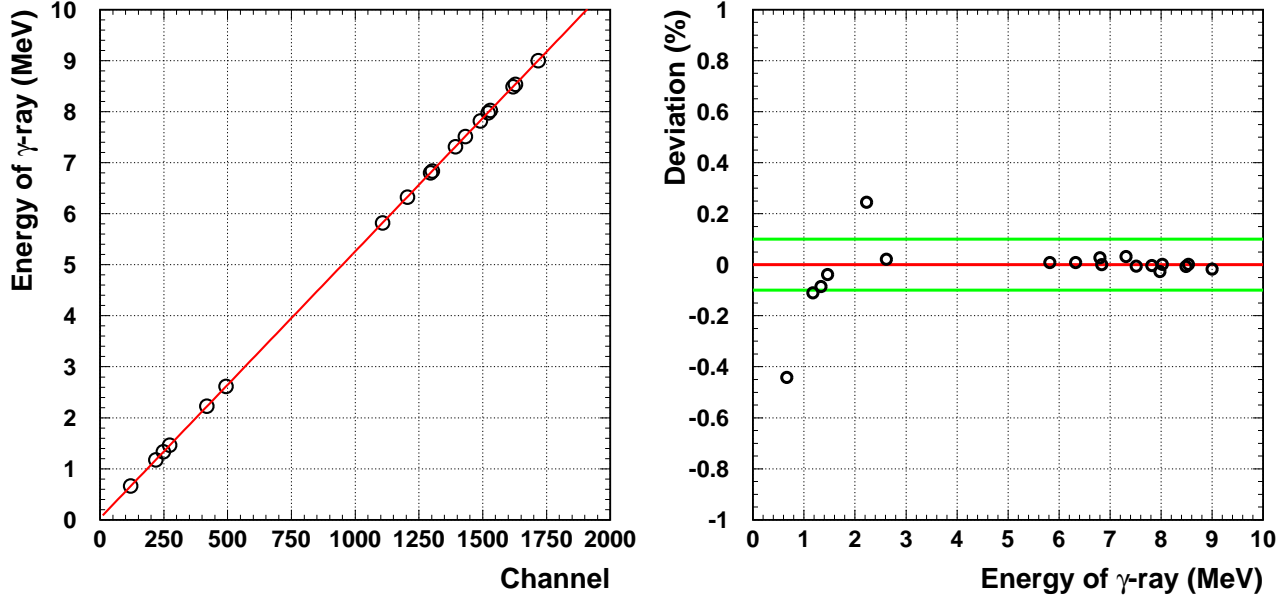


Figure 5.15: Left: The linearity of the germanium detector [108]. The horizontal axis shows the output from the germanium detector [channel] and the vertical axis shows the energy of the calibration  $\gamma$ -ray sources [MeV]. Right: The horizontal axis shows the energy of  $\gamma$ -ray [MeV] and the vertical axis shows the deviation. The open circles show the difference between the data and the fitted line.

## Result

Figure 5.16 shows typical distributions of the LINAC calibration at  $(x, y, z) = (-388.9, -70.7, -6.0)$  cm with 7.0 MeV in total energy.

After the LINAC calibration data is taken, the SK simulation is tuned to match the detector response. Comparing the peak positions in the  $N_{\text{eff}}$  distributions,  $\text{COREPMT}$  is determined as 0.88 for SK-IV. After this value is fixed, the difference of  $N_{\text{eff}}$  between the calibration data and the MC simulation was evaluated. The right of Figure 5.17 shows difference in the energy peak position between the data and MC simulation. The average of the differences in each beam energy mode is summarized in Table 5.4. According to Table 5.4, the average of the difference in each beam energy mode is explained within the systematic uncertainties<sup>3</sup> [106].

<sup>3</sup>This systematic uncertainty is caused by the reflection at the end cap of the beam pipe [106].

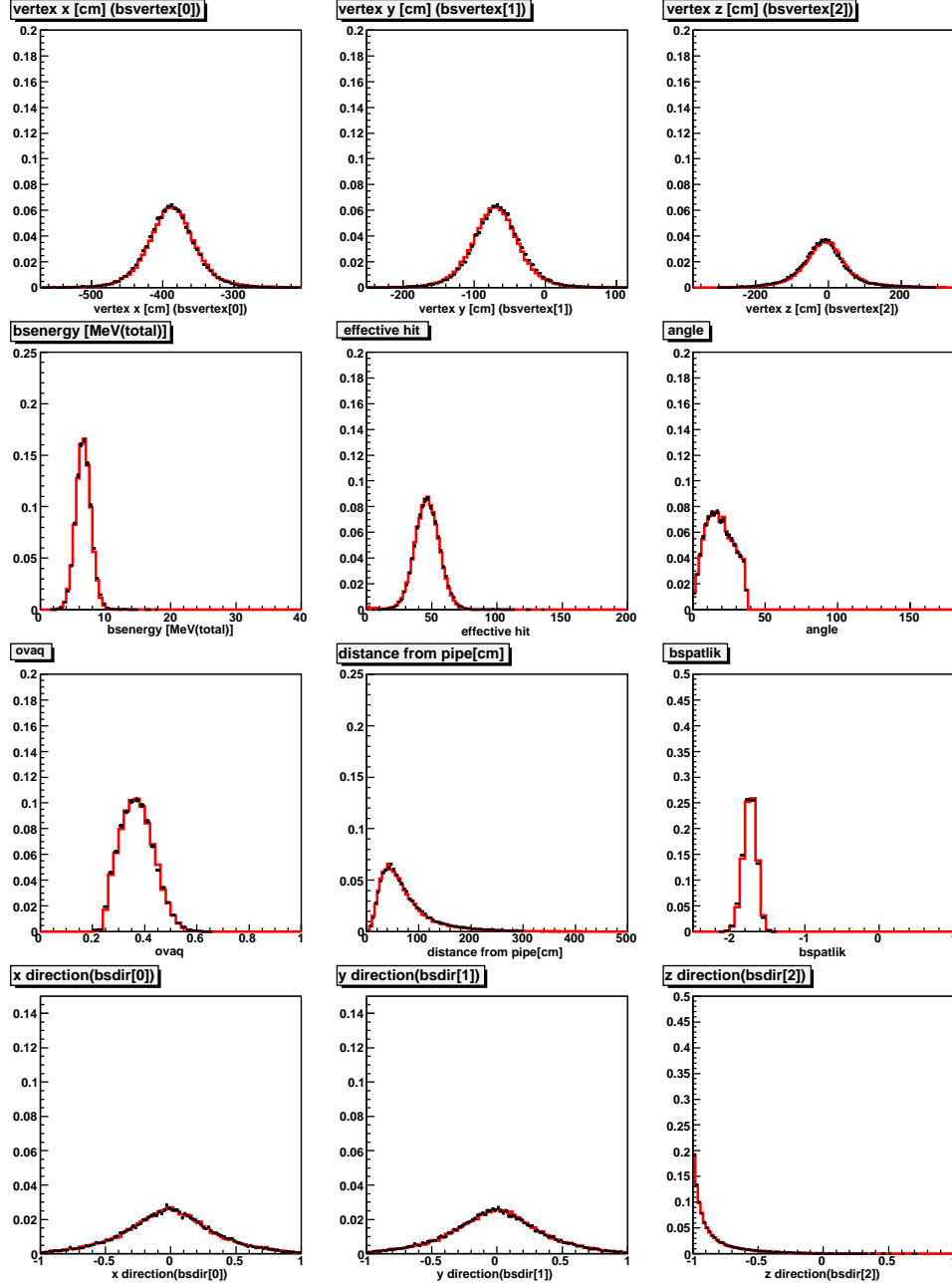


Figure 5.16: The typical distributions of LINAC calibration data. The back points shows the data and the red histograms show the MC. The data was taken at  $(x, y, z) = (-388.9, -70.7, -6.0)$  cm. The energy of the LINAC beam was adjusted at 7.0 MeV in total energy. The top three figures show vertex distributions of  $x$ ,  $y$  and  $z$ , respectively. The 2nd top figures show distributions of the reconstructed total energy, the effective hit ( $N_{\text{eff}}$  and the angle between the injected direction and the reconstructed direction (see the left of Figure 10.4), respectively. The 3rd top figures show distributions of the event quality  $g_V^2 - g_A^2$  (see subsection 6.2.4), the distance between the injection point and the reconstructed vertex and  $\mathcal{L}_{\text{pattern}}$  (see subsection 6.3.10), respectively. The bottom figures show distributions of the reconstructed direction of  $x$ ,  $y$  and  $z$ , respectively.

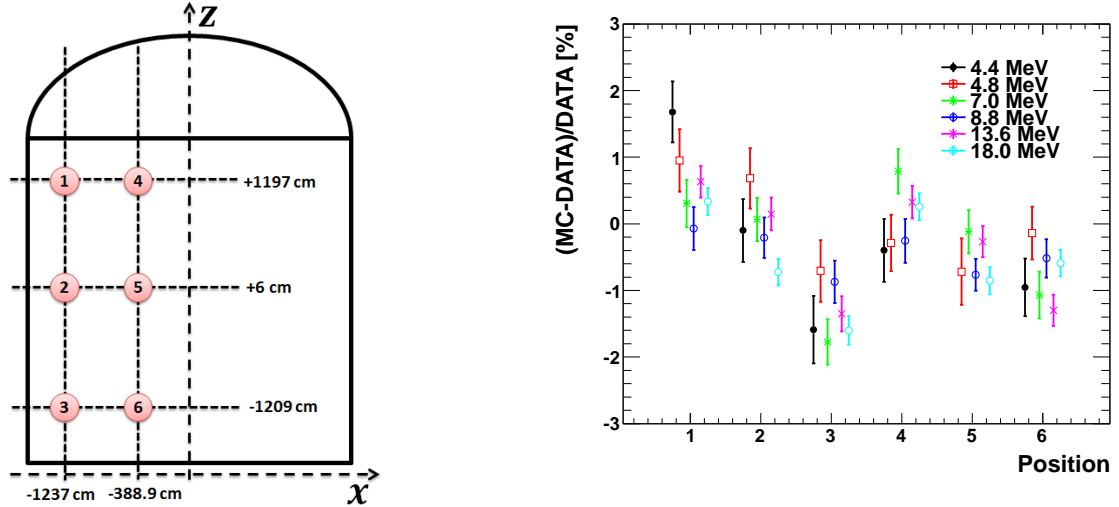


Figure 5.17: Left: The schematic view of the LINAC calibration position. The fixed 6 positions are labeled. Right: The differences of the peak position in the  $N_{\text{eff}}$  distribution at each position. The horizontal axis shows the calibration position and the horizontal axis shows the differences [%].

Table 5.4: The summary of the average for the difference between the data and MC simulation.

Energy [MeV]	4.4	4.8	7.0	8.8	13.6	18.0
Average	-0.89%	-0.04%	-0.30%	-0.45%	-0.30%	-0.53%
Systematic uncertainty [106]	$\pm 0.81\%$	$\pm 0.55\%$	$\pm 0.44\%$	$\pm 0.33\%$	$\pm 0.24\%$	$\pm 0.21\%$

### 5.3.2 DT generator

#### Overview

The DT (deuterium-tritium neutron) generator [107] is a calibration device which emits neutrons via the following reaction



The energy of the generated neutron is 14.2 MeV and this energy is large enough to create  ${}^{16}\text{N}$  in water as



The  ${}^{16}\text{N}$  decays via several channels with its half-life of 7.13 seconds. The main decay channels produce a 6.1 MeV  $\gamma$  ray and a 4.3 MeV  $\beta$  (66%) and a 10.41 MeV  $\beta$  (28%)



Although the beta spectrum is spread and it is not good for absolute energy calibration, there are several advantages of the DT calibration over the LINAC calibration. Since this

calibration system is easy to move and to set the position, the calibration at more positions can be performed. The direction of  $\beta$ 's and  $\gamma$ 's from  $^{16}\text{N}$  decay is uniform while only downward events are available in the LINAC calibration. This provides the directional and the positional dependence of energy scale. The directional and positional dependences are important for the solar neutrino analysis, because the neutrino events point back to the Sun and the events happen uniformly in the detector volume.

### Calibration device and method

Figure 5.18 shows a schematic view of DT calibration method. This calibration is done by the following steps:

1. A crane is used to insert, retract and set the DT generator in the SK tank.
2. DT generator is fired and  $\sim 10^6$  neutrons are created around the DT generator. Then,  $\sim 10^4$   $^{16}\text{N}$  are generated in water.
3. After firing, the crane lifts up the DT generator to prevent from making shadow of the DT generator. During this lift-up time, a short veto time ( $\sim$  few seconds) is applied.
4. After the above step, SK starts to take data of  $^{16}\text{N}$  decay events.
5. The mean reconstructed energy of the  $^{16}\text{N}$  data is compared with that of the MC simulation.

Using the differences between data and MC, the various aspects of energy scales including positional dependence, directional dependence and timing dependence are estimated.

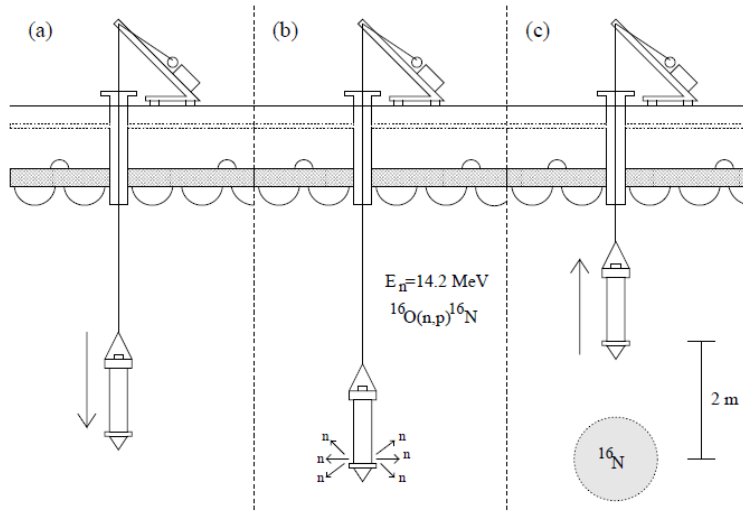


Figure 5.18: The schematic view of DT calibration method [107].

## Results of DT calibration

The left (right) of Figure 5.19 shows the position (directional) dependence of the energy scale. Figure 5.20 shows the stability of effective hit ( $N_{\text{eff}}$ ) during the SK-IV phase. During SK-IV, 20 sets of DT calibrations were performed. The time dependence of effective hit is within 0.3% level during the SK-IV phase. This results show that the energy scale has been stable during the SK-IV phase.

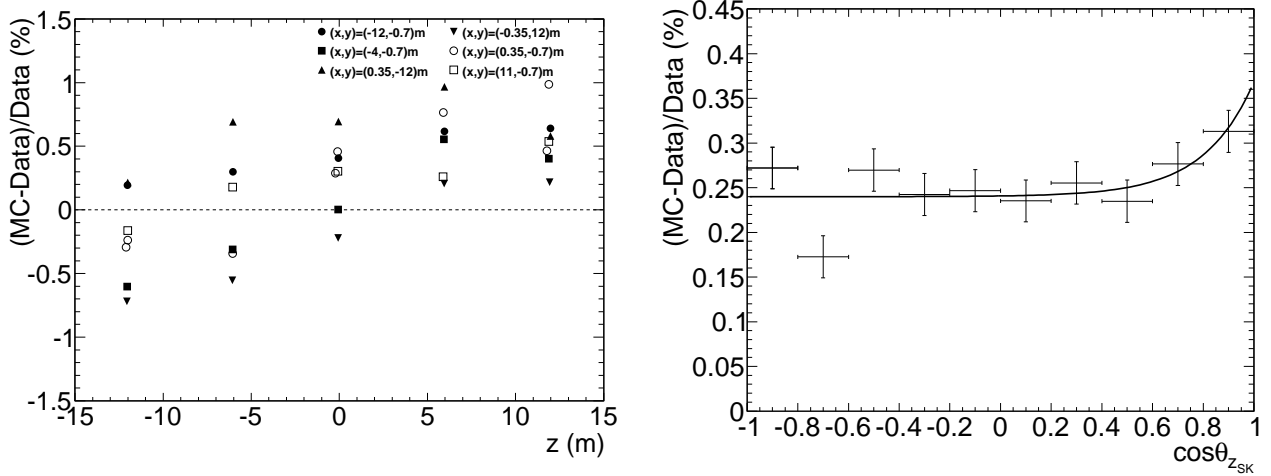


Figure 5.19: Left: The position dependence of the difference of effective hit,  $N_{\text{eff}}$ , peak between the data and MC simulation [110]. The horizontal axis shows the  $z$  position [m] and the vertical axis shows the differences. Right: The directional dependence of DT calibration [110]. The horizontal axis shows the cosine of the zenith angle (see the left of Figure 11.3) and the vertical axis shows the difference of  $N_{\text{eff}}$  peak between the calibration data and the MC simulation.

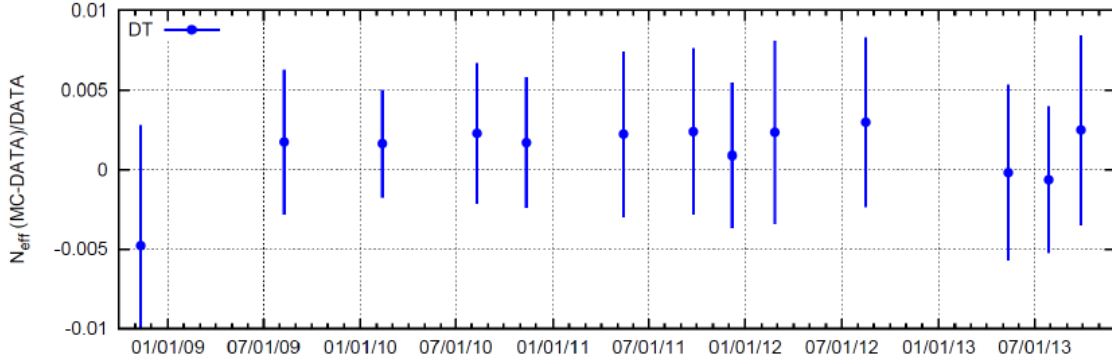


Figure 5.20: The stability of energy scale obtained by the DT calibrations during the SK-IV phase.

### 5.3.3 Systematic uncertainty of absolute energy scale

The uncertainty of the absolute energy scale is estimated taking into account the calibration result.

1. LINAC calibration: As already mentioned, the LINAC beam energy was measured by the Ge detector. The Ge detector was calibrated by the two radioactive sources and the uncertainty in this calibration is estimated to be 0.21%. In addition, the time variation of the water transparency during LINAC calibration should be taken into account in the uncertainty of the energy scale and it is 0.2%.
2. DT calibration: The position and directional dependence shown in Figure 5.19 is considered to estimate the uncertainty of the energy scale. They are 0.1% and 0.44%, respectively.

Combining these errors in quadrature, the total uncertainty of the energy scale is estimated to be 0.54%.

# Chapter 6

## Data reduction

In this chapter, the details of the analysis methods are described. It is noted that the energy is written in the recoil electron kinetic energy.

### 6.1 Run selection

A basic unit of SK dataset is a run which is at most 24 hours long. The run is divided into subruns whose time length are from 45 to 85 seconds depending on the trigger rate.

The quality of data was checked within each run unit and the selection criteria of bad run were as following:

1. The run whose total livetime less is than 5 minutes is removed because there is not enough pedestal data and bad channel monitoring data.
2. If any hardware or software troubles are reported, the correspond subrun is rejected. For example, if DAQ stops at the end of the run, some subruns at the end of the run are removed.
3. If any calibration or detector maintenance are performed, that subrun is rejected. For example, when LED Supernova burst test is done for a training, corresponding subruns are removed.
4. If the run starts after turning the high voltage on, the trigger rate fluctuates because of higher dark noise rate than in the normal case. Therefore, some subruns at the beginning of the run after high voltage on are removed.

### 6.2 Pre-reduction

Although it is expected that about 295 elastic scatterings between solar neutrinos and electrons occur in the entire SK detector each day, the number of the background events is significantly larger than that, which is typically  $\sim 2 \times 10^5$  events per day. If all of data are stored to disk without any cut, the total size of data file becomes more than a few hundred gigabyte ( $\sim 100$

GB) per day. To reduce the file size, the obvious background events are removed by the pre-reduction in the real-time process. The pre-reduction applies very loose cut to eliminate obvious background events and avoids removing true solar neutrino signals.

### 6.2.1 Vertex position cut

The fiducial volume cut is applied to remove the events whose reconstructed vertex position is close to the wall. If the vertex position is close within 200 cm from the wall, that event is removed. Hence, the event whose radial coordinate ( $r$ ) of vertex is  $r > 14.9$  m ( $r^2 > 222.01$  m<sup>2</sup>),  $z < -16.1$  m or  $z > 16.1$  m for  $z$ -axis are removed.

### 6.2.2 Low or high energy cut

If reconstructed energy is less than 2.5 MeV in kinetic energy, the event is removed. On the other hand, in order to remove cosmic ray muons, events more than 2000 p.e. are removed.

### 6.2.3 Loose external cut

External  $\gamma$ -rays and radioactivity coming from the structure of SK including PMTs are major background sources in the solar neutrino analysis. Since the direction of such background events are mostly inward, they are reduced using the distance from the reconstructed vertex position to the wall along with the opposite reconstructed direction,  $d_{\text{eff}}$ , as shown in Figure 6.1.

In the pre-reduction,  $d_{\text{eff}} > 400$  cm is applied for entire energy range and later tighter cut will be applied later described in subsection 6.3.12.

### 6.2.4 Loose event quality cut

Reconstruction goodness parameters are defined in order to test whether the reconstructed vertex is mis-reconstructed or not. One parameter,  $g_V$ , is the vertex goodness, which is defined as

$$g_V = \frac{\sum^{\text{allhit}} e^{-\left(\frac{t_{\text{res},i}(\vec{v})-t_0}{\sqrt{2}w}\right)^2} e^{-\left(\frac{t_{\text{res},i}(\vec{v})-t_0}{\sqrt{2}\sigma}\right)^2}}{\sum^{\text{allhit}} e^{-\left(\frac{t_{\text{res},i}(\vec{v})-t_0}{\sqrt{2}w}\right)^2}}. \quad (6.2.1)$$

where  $t_{\text{res},i}(\vec{v})$  is the  $i$ -th PMT's hit time after subtracting the time of flight,  $t_0$  is the fit peak time of  $t_{\text{res},i}(\vec{v})$  distribution,  $w$  is the resolution of the  $t_{\text{res},i}(\vec{v})$  distribution and  $\sigma$  is the timing resolution of the PMTs. This vertex goodness is the degree of vertex reconstruction quality estimated by hit PMT timing information.

Another parameter,  $g_A$ , is defined as

$$g_A = \frac{\max[\angle_{\text{uniform}}(i) - \angle_{\text{data}}(i)] - \min[\angle_{\text{uniform}}(i) - \angle_{\text{data}}(i)]}{2\pi}. \quad (6.2.2)$$

$\angle_{\text{uniform}}(i)$  is the azimuthal angle of the  $i$ -th hit PMT, assuming that the hit PMTs are uniformly distributed along a Cherenkov cone.  $\angle_{\text{data}}(i)$  is that of the real angle. The range of the two parameters is from 0.0 to 1.0.  $g_V = 1.0$  and  $g_A = 0.0$  are the best quality cases.

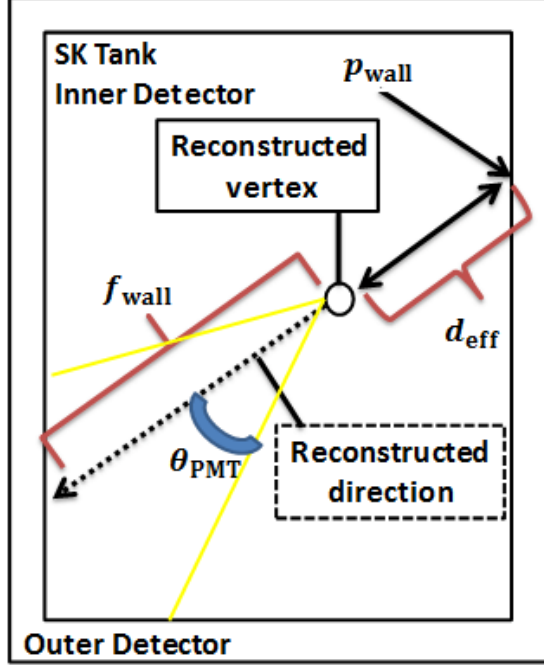


Figure 6.1: The definition of  $d_{\text{eff}}$ ,  $p_{\text{wall}}$ ,  $f_{\text{wall}}$  and  $\theta_{\text{PMT}}$ . The first parameter,  $d_{\text{eff}}$  is defined as the distance from the reconstructed vertex position to the wall along with the opposite reconstructed direction. The second parameter,  $p_{\text{wall}}$  is defined the wall position when tracking back along the reconstructed direction from the vertex. The third parameter,  $f_{\text{wall}}$  is defined the distance between the wall and the reconstructed vertex position. The fourth parameter,  $\theta_{\text{PMT}}$  is defined the angle between the reconstructed direction and the vector from the reconstructed vertex to each hit PMT.

The left (right) of Figure 6.2 shows the correlation between  $g_V^2$  and  $g_A^2$  for a background sample (solar neutrino simulation events). Based on the MC simulation, peaks of the solar neutrino signals appears around  $g_V^2 \sim 0.4$  and  $g_A^2 \sim 0.03$ .

In the pre-reduction,  $g_V^2 - g_A^2 > 0.10$  is applied for the entire energy range and tighter cut will be applied later as described in subsection 6.3.8.

### 6.2.5 Summary of pre-reduction

The number of events after the each step of pre-reduction for a 24 hours run is summarized in Table 6.1. After the pre-reduction, the number of events is reduced by a factor of  $\sim 100$ . The inefficiency for the solar neutrino event is estimated using the solar neutrino MC simulation is shown in the right of Figure 6.18. Signal loss is less than 5% above 5.0 MeV.

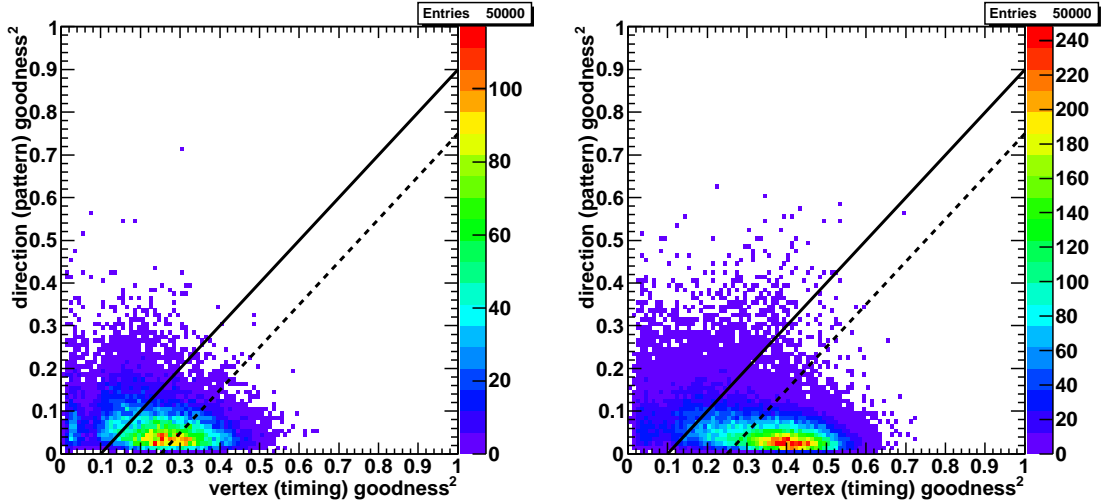


Figure 6.2: Correlation of  $g_V^2$  and  $g_A^2$  for data (left) and solar neutrino MC sample (right). The black solid (dashed) line shows  $g_V^2 - g_A^2 = 0.10$  ( $0.25$ ).

Table 6.1: The example for the reduction efficiencies after each of the pre-reduction steps. The number of events is reduced to  $\sim 1\%$  after the pre-reduction [108].

Pre-reduction step	Number of events	Efficiency [%]
Initial	197,524	100
Fiducial volume cut	28,161	14.2
Loose external cut	14,864	7.5
Low energy cut	6,872	3.5
Loose event quality cut	2,057	1.0

## 6.3 Solar neutrino analysis

### 6.3.1 Bad channel cut

The left of Figure 6.3 (Figure 6.4) illustrates the time variation of the number of ID (OD) bad channels. So far SK-IV continuously has been running for more than 7 years, some of the PMTs were out of order due to long-term use. Currently, there were 140 (160) bad channels for ID (OD), which was equivalent to 1.3% (13.5%) loss of PMTs. The reasons why bad channels fluctuated are followings: (1)When the run time is short, sometimes the number of bad channel becomes small. (2)When a front-end electronics QBEE board has a trouble, the connected 24 PMTs are dead and counted as bad channels.

In order to remove such (sub)runs, additional cut criteria are applied as following:

1. If the number of bad channels is less than 10, the subrun is removed. This situation frequently happens when the total run time is short.
2. A monthly average of ID (OD) bad channel is calculated, if the number of bad channels

is larger than  $(\text{monthly average} + 1.5 \times 24)$ , the (sub)run is removed. For example, Figure 6.5 illustrates that last several subruns are removed in Normal run 65999.

The right of Figure 6.3 (Figure 6.4) shows the number of bad channels after this cut. Around August 2013, corresponding run number is  $\sim 71500$ , the number of ID bad channel decreased because some bad channels caused by the HV for ID were recovered when the HV for ID was replaced.

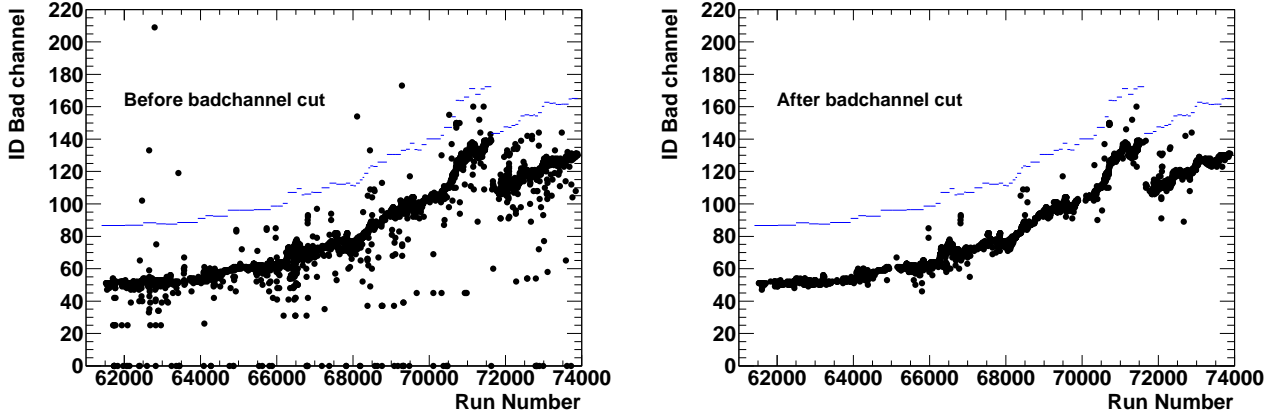


Figure 6.3: The time variation of bad channel of ID. The black dots shows the average of bad channel for each Normal run and the blue lines shows the monthly average of bad channel. Around Run 71500, the number of bad channel decreased because the HV for ID was replaced on August 2013.

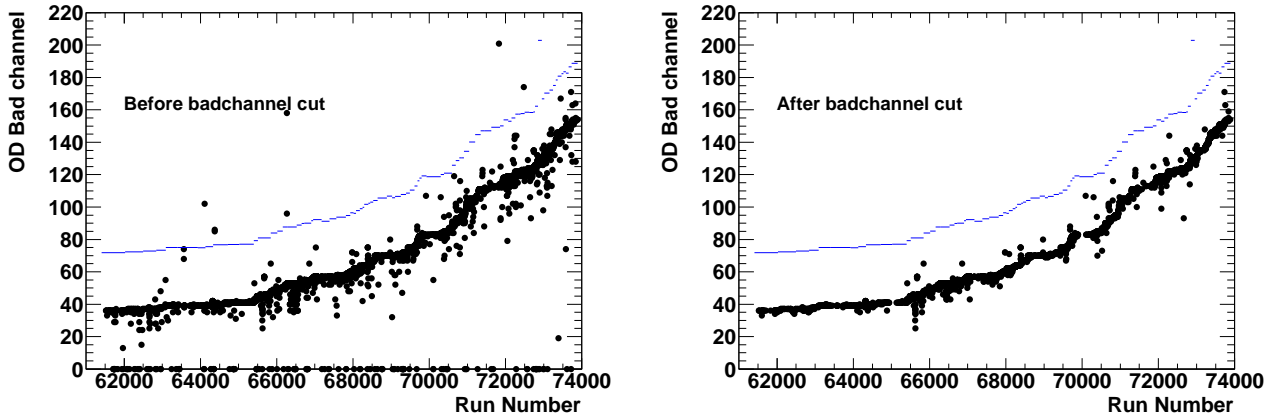


Figure 6.4: The time variation of bad channel of OD. The black dots show the average of bad channel for each Normal run and the blue lines show the monthly cut value of bad channel.

### 6.3.2 Muon rate

Cosmic ray muons rate is monitored for each run. The average muon rate is  $1.954 \pm 0.180$  muon/sec as shown in Figure 6.6.

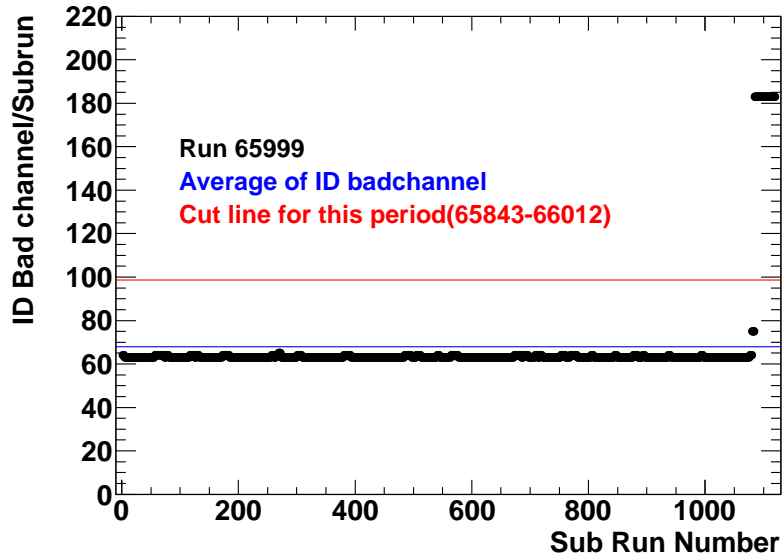


Figure 6.5: An example of an increase in number of bad channels. The black points show the number of ID bad channels for each sub run. The red (blue) line shows the cut value (average value) for this run. At the end of this run, ID bad channel suddenly increased and it was larger than the cut criterion. Hence the last 35 subruns were removed.

The OD trigger rate is sometimes largely fluctuated when OD PMTs become noisy. A cut criterion is set in order to remove such a noisy muon rate (sub)run. If the muon rate is deviated by  $5\sigma$  from the average value, which is equivalent to 2.847 (1.047) muon/sec, that (sub)run is rejected.

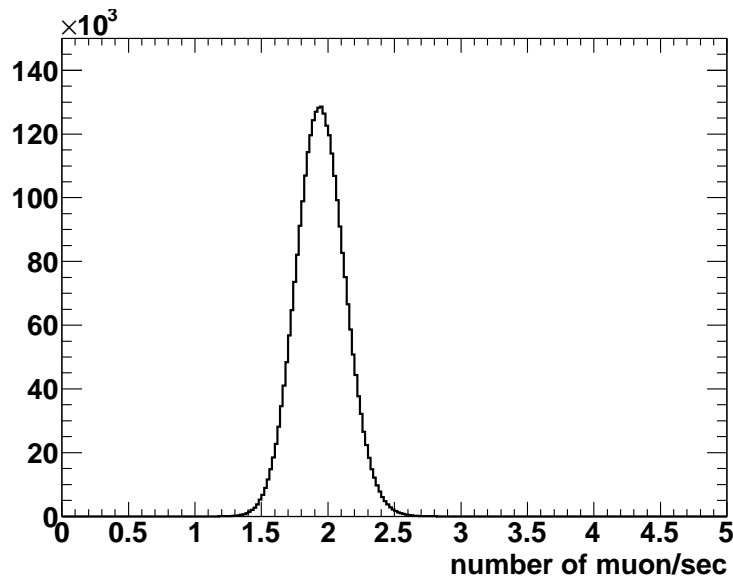


Figure 6.6: The rate of the OD trigger rate.

### 6.3.3 Total number of hit PMT

Since the energy of solar neutrino is distributed from 0 MeV to 20 MeV, the events whose total number of hit PMTs, defined as  $N_{\text{tot}}$ , is larger than 400 are removed.  $N_{\text{tot}} = 400$  corresponds to an energy of  $\sim 60$  MeV for electrons. This cut removes mostly atmospheric neutrinos and cosmic ray muons.

### 6.3.4 Calibration trigger/source cut

Events which are triggered by one of the external calibration triggers and scheduled calibration events are rejected. Table 6.2 summarizes the calibration sources and those positions. The auto-calibration events are automatically triggered during data taking.

Table 6.2: The calibration sources and those positions. There are two positions installing water temperature sensors.

source	$x$ [cm]	$y$ [cm]	$z$ [cm]
Xenon light	353.5	-70.7	0.0
LED light	35.5	-350.0	150.0
TQ diffuser ball	-176.8	-70.7	100.0
LED for Supernova test	-35.3	353.5	100.0
Water temperature sensors (1)	-35.0	1200	-2000
Water temperature sensors (2)	70.7	-777.7	-2000

The events with vertex position closer than 200 cm to the calibration source or 100 cm to the cable of the sources are removed (all cables run along the  $z$ -axis from the top of the tank to the source position).

### 6.3.5 Flasher cut

Sometimes an arc discharge occurs on the dynodes of PMTs during data taking. When it happens, other PMTs also optically get signals. In the case of a typical flasher event, flashing PMT gets large number of photons and many other surrounding PMTs detect signals. If the maximum charge of a single PMT is larger than 50 p.e. and the number of hits of the surrounding 24 PMTs is larger than 3, the event is recognized as a flasher event. This cut criteria and typical good and bad runs are shown in Figure 6.7.

### 6.3.6 Time difference cut

The events occurring within 50  $\mu\text{sec}$  from the previous low energy triggered event are removed in order to reject the following events:

1. A ringing noise event caused by cosmic ray muons.
2. Electrons from the decay of cosmic ray muons (whose life time is 2.2  $\mu\text{sec}$ ).

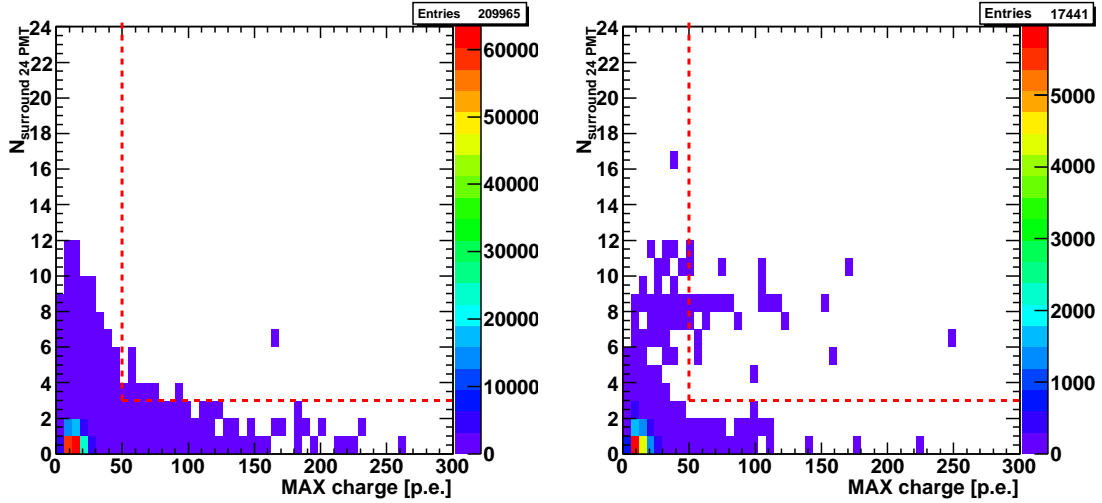


Figure 6.7: The typical scatter plot for max charge [p.e.] vs the number of hit PMTs surrounding PMT with max charge. The red dashed lines show the cut values of flasher cut. The left figure shows good run while the right figure shows bad-flasher run.

### 3. Events caused by after pulses.

Figure 6.8 shows the typical distribution for the time difference between an ID triggered event and the previous event signals. According to Figure 6.8, the main peak around  $15 \mu\text{sec}$  is due to the event caused by after pulses.

## 6.3.7 OD event cut

Since the ID and the OD layers are optically separated, Cherenkov light of solar neutrino events are detected only in the ID detector. As mentioned in section 3.3, the OD trigger is issued if more than 22 (19) OD PMTs hit in SK-IV (SK-III) and it is caused by the charged particle from outside of the detector. In order to reject events occurring in OD, the following cuts are applied:

1. If the OD trigger is fired, the event is rejected.
2. When the event is not tagged by the OD trigger, the total number of hits in OD PMTs is counted between 500 nsec to 1300 nsec (1000 nsec in the case of SLE trigger time window). If it is larger than 20, the event is rejected.

## 6.3.8 Event quality cut

As described in section 6.2.4, the quality of the reconstructed vertex and direction can be described by the 2 goodness parameters,  $g_V$  and  $g_A$ . According to Figure 6.2, the correlation between  $g_V^2$  and  $g_A^2$  is quite different between the background sample and the solar neutrino

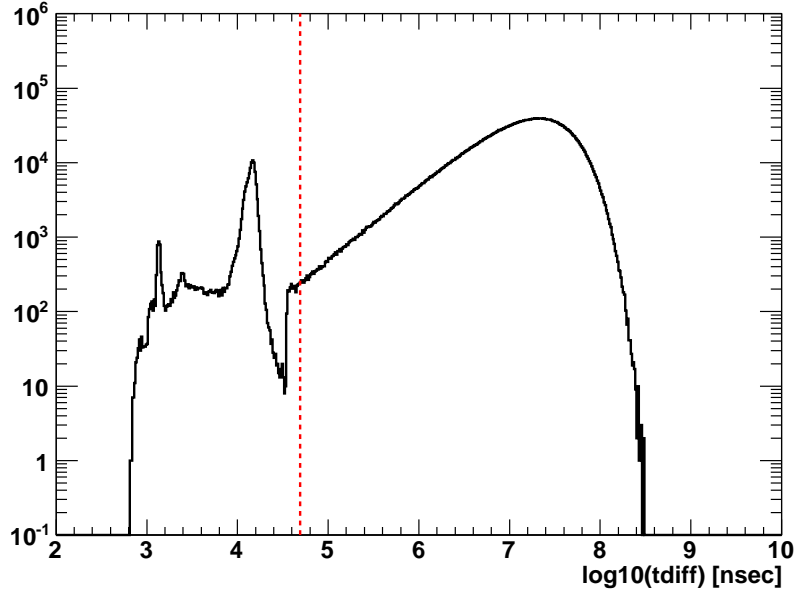


Figure 6.8: The typical distribution of the time difference to previous low energy triggered event. The red dashed line illustrates the 50  $\mu\text{sec}$  and events below this line are removed. The peak around 1  $\mu\text{sec}$  is caused by the ringing event after high energy cosmic ray muons, the another peak around 15  $\mu\text{sec}$  is caused by after pulse events.

MC sample. To maximize the extracting efficiency for the solar neutrino signal, cut criteria are determined using the following significance:

$$\text{significance} = \frac{\text{extracting efficiency for solar neutrino signal}}{\sqrt{\text{background event}}}. \quad (6.3.1)$$

The cut criteria of this cut are following:

$$\begin{aligned} g_V^2 - g_A^2 &> 0.29, \text{ for } 3.5 - 5.0 \text{ MeV} \\ g_V^2 - g_A^2 &> 0.25, \text{ for } 5.0 - 7.0 \text{ MeV} \\ g_V^2 - g_A^2 &> 0.20, \text{ for above } 7.0 \text{ MeV} \end{aligned} \quad (6.3.2)$$

In the low energy region, tighter criteria are required, because the uncertainty in the vertex reconstruction is large due to smaller number of hit PMTs.

### 6.3.9 Spallation cut

When cosmic ray muons enter the SK tank, their subsequent cascade-shower particles interact with  $^{16}\text{O}$  and produce various kind of radioactive elements. Since the subsequent cascade shower by muon interaction with  $^{16}\text{O}$  produce hadrons, such as n, p,  $\pi^\pm$  and so on, these secondary particles are also captured by other  $^{16}\text{O}$  nuclei and result in producing some radioactive nuclei. Possible radioactive nuclei are summarized in Table 6.3. The decays from them often involve  $\gamma$

and  $\beta$  decay and these signals mimic solar neutrino interactions. These  $\beta$  ( $\gamma$ ) events are called “spallation events” in this thesis.

In Table 6.3, the spallation background events which give 6 ~ 20 MeV energy are listed. The analysis method to identify the spallation event has been developed in the SK-I analysis [109] and it is adopted also in the SK-IV analysis.

Table 6.3: The list of Spallation production.

Isotope	$\tau_{1/2}$ [sec]	decay mode	Kinetic Energy [MeV]
${}^8_2\text{He}$	0.119	$\beta^-$ $\beta^-n$	$9.67 + 0.98(\gamma)$ 16%
${}^8_3\text{Li}$	0.838	$\beta^-$	$\sim 13$
${}^8_3\text{B}$	0.77	$\beta^+$	13.9
${}^9_3\text{Li}$	0.178	$\beta^-$ $\beta^-n$	13.6(50.5%) ( $\sim 50\%$ )
${}^9_6\text{C}$	0.127	$\beta^+n$	3 ~ 15
${}^{11}_3\text{Li}$	0.0085	$\beta^-$ $\beta^-n$	16 ~ 20( $\sim 50\%$ ) $\sim 16(\sim 50\%)$
${}^{11}_4\text{Be}$	13.8	$\beta^-$	11.51(54.7%) $9.41 + 2.1(\gamma)(31.4\%)$
${}^{11}_4\text{Be}$	13.8	$\beta^-$	11.71
${}^{12}_5\text{B}$	0.0236	$\beta^-$	13.37
${}^{12}_7\text{N}$	0.0110	$\beta^+$	16.32
${}^{13}_5\text{B}$	0.0174	$\beta^-$	13.44
${}^{13}_8\text{O}$	0.086	$\beta^+$	13.2 or 16.7
${}^{14}_5\text{B}$	0.0138	$\beta^-$	$14.55 + 6.09(\gamma)$
${}^{15}_6\text{C}$	2.449	$\beta^-$	9.77(36.8%) $4.47 + 5.30(\gamma)$
${}^{16}_6\text{C}$	0.747	$\beta^-n$	$\sim 4$
${}^{16}_7\text{N}$	7.13	$\beta^-$	10.42(28.0%) $4.29 + 6.13(\gamma)(66.2\%)$

A likelihood function is introduced as:

$$\mathcal{L}_{\text{spa}} = f(\Delta T) \times f(\Delta L) \times f(Q_{\text{res}}), \quad (6.3.3)$$

where

1.  $\Delta T$ : The time difference between the spallation candidate event and the preceding muon event. The distribution of  $\Delta T$  is shown in the left of Figure 6.9.
2.  $\Delta L$ : The distance between the reconstructed vertex of the spallation candidate event and the reconstructed track of the preceding muon. The distribution of  $\Delta L$  is shown in the right of Figure 6.9

3.  $Q_{\text{res}}$ : The residual charge of the proceeding muon event, which is defined as the difference between the observed charge ( $Q_{\text{obs}}$ ) and the track length ( $L$ ) of the proceeding muon times the expected observed charge per cm from a muon in water ( $Q_{\text{unit}} = 11.4 \text{ p.e./cm}$ ), i.e. it is represented as  $Q_{\text{res}} = Q_{\text{obs}} - Q_{\text{unit}} \times L$ . The left of Figure 6.10 shows the time variation of the observed charge  $Q_{\text{obs}}$  and it has increased with time because of the time variation of the PMT gain. If a muon causes spallation, it releases more charge than expected because of hadronic cascades. The distribution of  $f(Q_{\text{res}})$  is shown in the right of Figure 6.10.

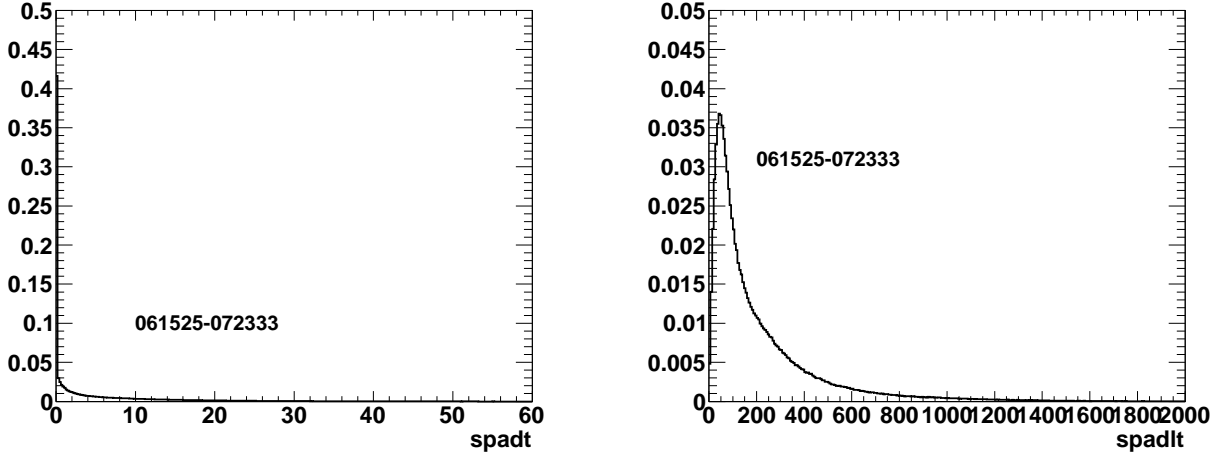


Figure 6.9: The distribution of the variables using in spallation cut. The left figure shows the distribution of  $\Delta T$  and the right figure shows the distribution of  $\Delta L$ .

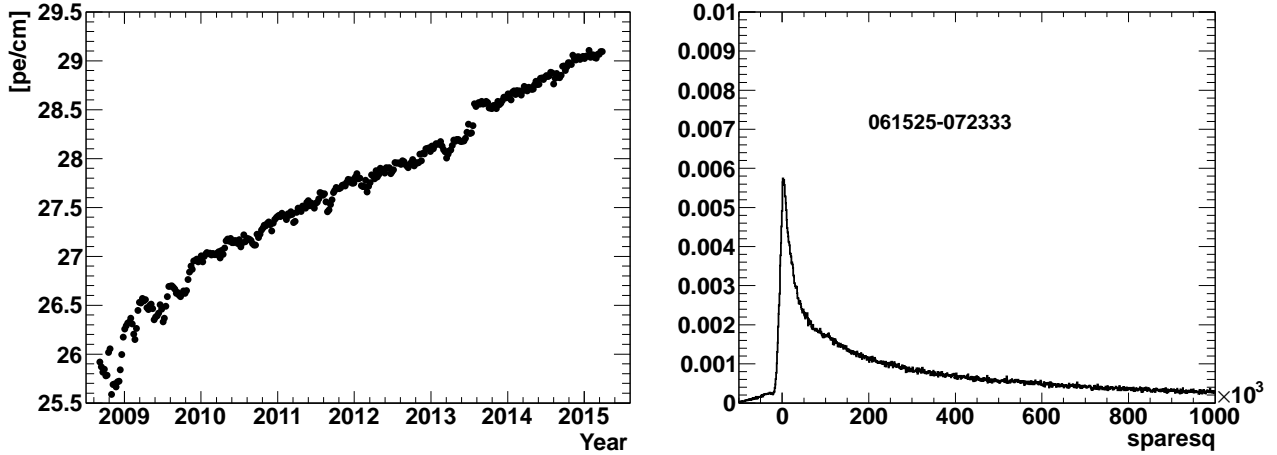


Figure 6.10: Left: The time variation of the observed charge per cm for muon. Right: The distribution of  $f(Q_{\text{res}})$ .

The likelihood function of  $f(\Delta T)$  is generated by considering the lifetime of the produced radioactive elements as shown in Table 6.3, while the others ( $f(\Delta L)$  and  $f(Q_{\text{res}})$ ) are generated using a spallation-like sample and a random sample from real data. These samples are created as follows:

1. Spallation-like sample: This sample is composed of events whose  $\Delta T$  is less than 0.1 sec and  $E$  is larger than 7.5 MeV.
2. Random sample: This sample is composed of events whose  $E$  is less than 4.5 MeV. The time of the events are adopted from real data, while the vertex position is randomly generated to mimic the signal distribution.

Figure 6.11 shows the distribution of  $\log(\mathcal{L}_{\text{spa}})$  for the spallation sample (black) and the random sample (red). The cut value of the spallation likelihood is determined so that the dead time of the random sample is 20%, and the actual  $\log(\mathcal{L}_{\text{spa}}) > 4.52$  in SK-IV.

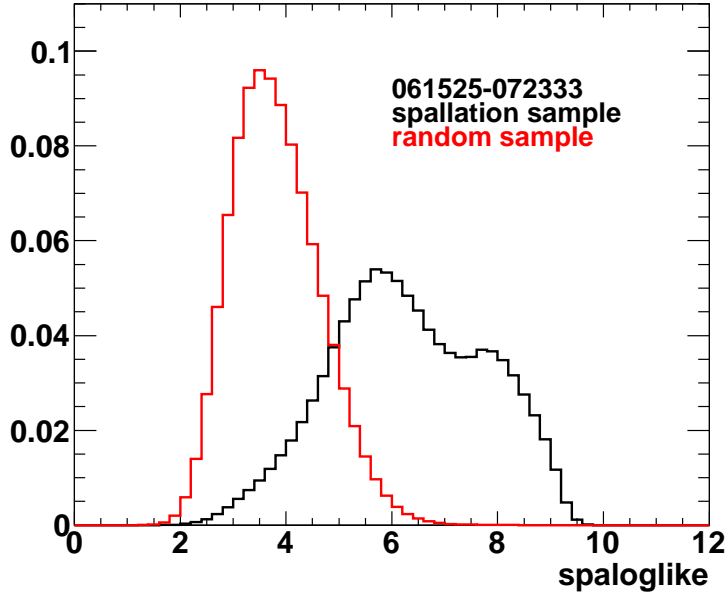


Figure 6.11: The distribution of spalogle like for Random samples and spallation like samples.

Since the spallation cut causes the dead time in the solar neutrino analysis, the position dependence of the dead time is also considered in the MC simulation to calculate the expected number of solar neutrino events.<sup>1</sup>

The left (right) of Figure 6.12 shows the position dependence of the dead time ( $dead_z$  ( $dead_r$ )). According to Figure 6.12, the dead time becomes small when the position is close to the wall.

<sup>1</sup>First of all, the dead time for  $z$ -axis direction,  $dead_z$ , is calculated and the the dead time for the radius  $r^2$  direction,  $dead_r$ , is calculated. Finally the total dead time is calculated by multiplying them and a normalization factor (5.08691) like below.

$$\begin{aligned}
 dead_z &= 1.0 - (0.79143 + (-0.93206 \times 10^{-5})z + (0.98724 \times 10^{-11})z^2 + (-0.30075 \times 10^{-11})z^3 \\
 &\quad + (0.16359 \times 10^{-14})z^4 + (-0.26618 \times 10^{-18})z^5 + (-0.63656 \times 10^{-22})z^6) \\
 dead_r &= 1.0 - (0.77799 + (0.18903 \times 10^{-7})r^2 + (0.22175 \times 10^{-14})r^4) \\
 dead_{\text{total}} &= 5.08691 \times dead_r \times dead_z
 \end{aligned} \tag{6.3.4}$$

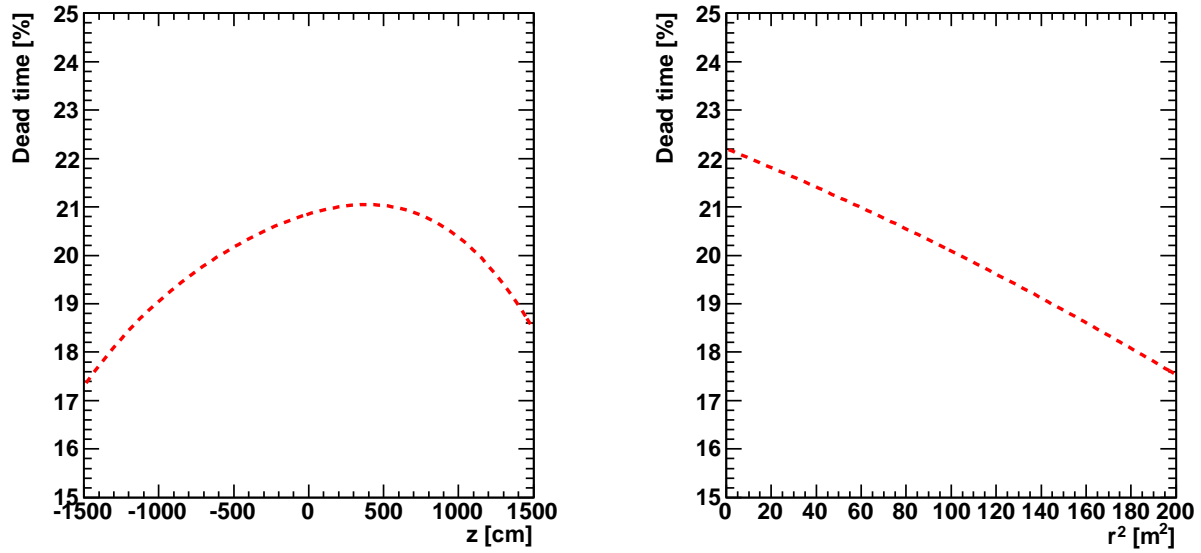


Figure 6.12: The position dependence of the dead time resulting from the spallation cut. The left (right) figure illustrates the dependence of  $z$ -axis [cm] ( $r^2$  [ $m^2$ ]) direction.

The left of Figure 6.13 shows the time variation of the spallation dead time. It is stable within  $\pm 0.3\%$  level for the entire period of SK-IV.

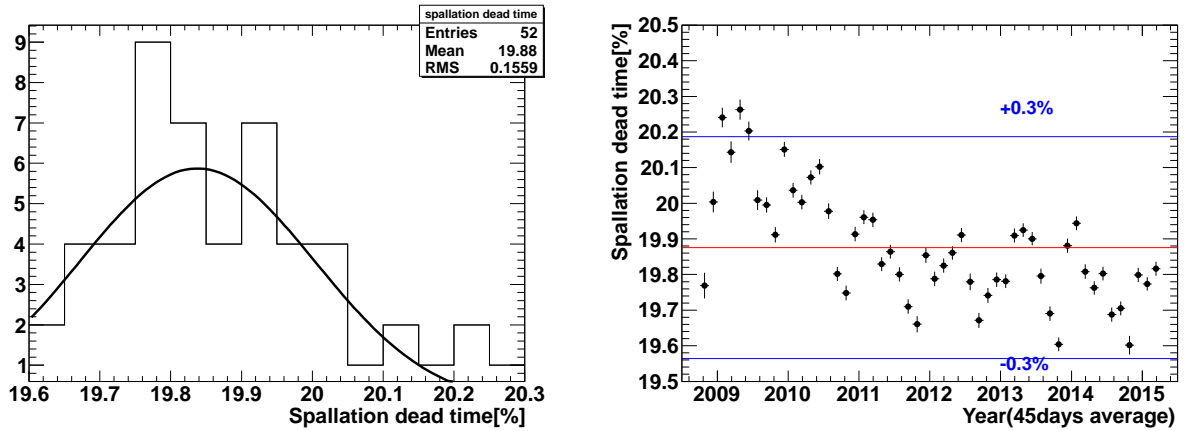


Figure 6.13: The distribution of spallation dead time (left) and its time variation during SK-IV (right).

### 6.3.10 Hit patter cut

Since some spallation products emit multiple  $\gamma$ 's and  $\beta$ 's, their pattern of the Cherenkov light becomes a non-clear ring. In order to distinguish single electron pattern from such background pattern, a likelihood function based on the PMTs hit pattern is used.

The likelihood function is developed as follows:

$$\mathcal{L}_{\text{pattern}}(E, \vec{v}) = \frac{1}{N_{50}} \sum_i^{N_{50}} \log(P_i(E, \cos \theta_{\text{PMT}}, f_{\text{wall}})), \quad (6.3.5)$$

where  $N_{50}$  is the number of hit PMTs within a 50 sec time window,  $E$  is the reconstructed energy of an electron,  $\theta_{\text{PMT}}$  is the angle between the reconstructed direction and the vector from the reconstructed vertex to each hit PMT as shown in Figure 6.1,  $f_{\text{wall}}$  is the distance between the wall and the reconstructed vertex as shown in Figure 6.1, and  $P_i$  is a probability density function (PDF) of hit pattern generated using the single electron MC simulation.

Figure 6.14 shows the hit pattern likelihood for both data and the MC simulation in three different energy range.

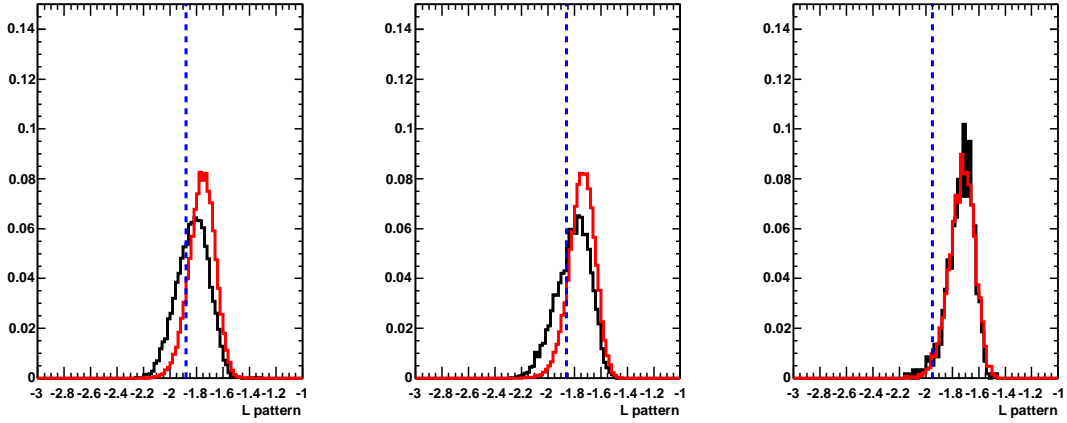


Figure 6.14: The distribution of  $L_{\text{pattern}}$  for data (black) and solar neutrino MC (red), for 5.5 – 7.5 MeV (left), 7.5 – 11.5 MeV (middle) and 11.5 – 19.5 MeV (right) in kinetic energy .

The cut values are determined by evaluating the significance and they are:

$$\begin{aligned} \mathcal{L}_{\text{pattern}} &> -1.88, \text{ for } 6.0 - 7.5 \text{ MeV,} \\ \mathcal{L}_{\text{pattern}} &> -1.86, \text{ for } 7.5 - 11.5 \text{ MeV,} \\ \mathcal{L}_{\text{pattern}} &> -1.95, \text{ above } 11.5 \text{ MeV.} \end{aligned} \quad (6.3.6)$$

Because of the small number of hit PMTs, it is difficult to determine the cut value below 6.0 MeV in kinetic energy. Thus, this cut is applied above 6.0 MeV.

### 6.3.11 $^{16}\text{N}$ cut

A muon can be captured with a nucleus via semileptonic process  $\mu^- Z \rightarrow (Z-1)\nu_\mu^*$ . In the case of SK,  $^{16}\text{N}$  can be produced when a low energy cosmic muon is absorbed by  $^{16}\text{O}$  in water.

As mentioned in subsection 5.3.2,  $^{16}\text{N}$  whose half-life time is 7.13 seconds decays producing  $\gamma$ 's and  $\beta$ 's. Since this half-life time is longer than  $50 \mu\text{sec}$ , this event can not be rejected by the timing difference cut. In order to remove the  $^{16}\text{N}$  background, the events around the captured muon are checked.

1. Stopping muons are picked up by criteria of total p.e.  $> 1000$  p.e. and to ensure no exit position in the tank.
2. Stopping position is calculated from the fitted direction and momentum of the muon.
3. Events whose vertex position is within 250 cm and  $\Delta T < 30$  sec are rejected.

### 6.3.12 External cut

As described in subsection 6.2.3, there are many  $\gamma$ -rays and radioactivities coming from the structure of the SK detector including PMTs. In order to reject such background events, tighter cut is applied.

Above 5.0 MeV, the cut is applied as follows:

$$\begin{aligned} d_{\text{eff}} &> 650 \text{ cm, for } 5.0 - 7.5 \text{ MeV(kin)}, \\ d_{\text{eff}} &> 400 \text{ cm, for above } 7.5 \text{ MeV(kin)}. \end{aligned} \tag{6.3.7}$$

In the low energy region, there are many radioactivities around the edge of the ID and they are not distributed uniformly. It is assumed that those background events come from decays of Rn daughters as discussed in Chapter 8 later.

As discussed in the subsection 6.3.14 later, a tight fiducial volume cut is applied for the low energy event to keep the uniformity of the vertex distribution. Due to this additional vertex position cut, the events occurring near the edge region are not used in the solar neutrino analysis. Therefore, this cut for the low energy event is optimized based on the parameter  $p_{\text{wall}}$ , which is defined as the wall position when tracking back along the reconstructed direction from the reconstructed vertex as shown in Figure 6.1. The parameter  $p_{\text{wall}}$  is categorized according to the wall position (top, bottom and barrel).

Based on the two parameters  $d_{\text{eff}}$  and  $p_{\text{wall}}$ , this cut for 3.5 – 5.0 MeV is determined as follows:

$$\begin{aligned} d_{\text{eff}} &> 1000 \text{ cm, for } p_{\text{wall}} \text{ at top,} \\ d_{\text{eff}} &> 1200 \text{ cm, for } p_{\text{wall}} \text{ at barrel,} \\ d_{\text{eff}} &> 1300 \text{ cm, for } p_{\text{wall}} \text{ at bottom.} \end{aligned} \tag{6.3.8}$$

### 6.3.13 Small hit cluster event cut

When a radioactive event occurs at a PMT glass or a FRP cover and it coincides with a fluctuation of PMT dark noise, the total number of hit PMTs exceeds the trigger threshold.

When such a situation happens, the reconstructed vertex is close to the wall and the hit pattern becomes a small cluster. To characterize small hit clusters, 2 parameters are introduced.

1.  $r02$ : A minimum radius containing more than 20% of hit PMTs within 20 nsec time window.
2.  $N_{20\text{rawT}}$ : A maximum number of hits within a 20 nsec raw timing window without subtracting the time of flight from the reconstructed vertex.

In the case of background events, the number of  $N_{20\text{rawT}}$  divided by the total number of hits,  $N_{20\text{rawT}}/N_{\text{eff}}$ , is expected to be smaller than that of solar neutrino signals.

The left (right) of Figure 6.15 shows the relationship between  $r02$  and  $N_{20\text{rawT}}$  for background (solar neutrino MC). After evaluating the significance, the cut criteria are determined as follows:

$$\begin{aligned} r02 \times (N_{20\text{rawT}}/N_{\text{eff}}) < 75.0, \quad r^2 > 155 \text{ m}^2, \quad z < -7.5 \text{ m}, \quad \text{for } 4.5 - 5.0 \text{ MeV}, \\ r02 \times (N_{20\text{rawT}}/N_{\text{eff}}), \quad r^2 > 120 \text{ m}^2, \quad (z < -3.0 \text{ m or } z > 13.0 \text{ m}), \quad \text{for } 3.5 - 4.5 \text{ MeV}. \end{aligned} \quad (6.3.9)$$

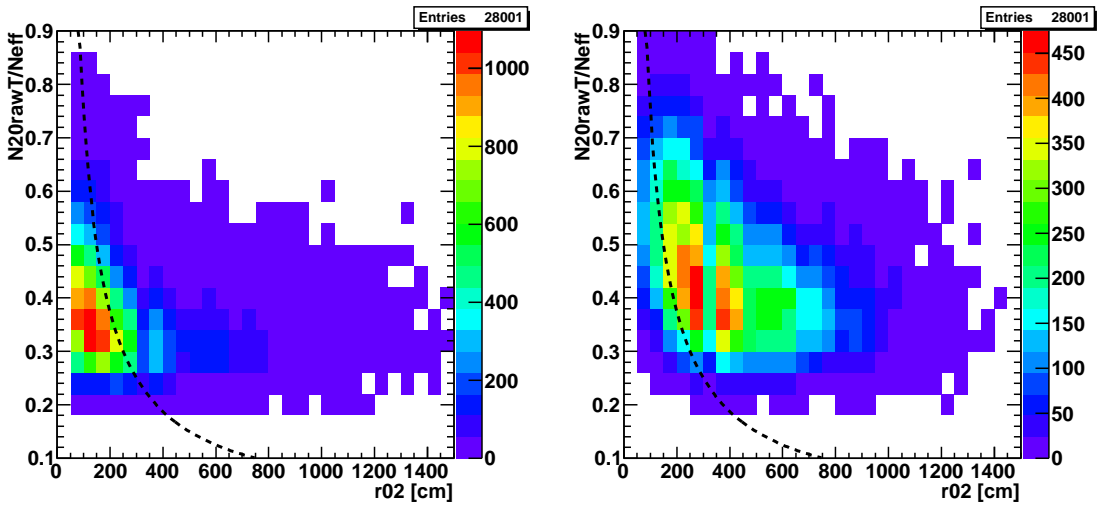


Figure 6.15: Relationship between  $r02$  and  $N_{20\text{rawT}}$  for background (left) and solar neutrino MC (right) after applying radius  $r > 13 \text{ m}$  and  $z > -3 \text{ m}$ . The dashed line illustrated  $(N_{20\text{rawT}}/N_{\text{eff}}) = 75.0/r02$ , and the left side of this line are rejected.

### 6.3.14 Tight fiducial volume cut

Figure 6.16 shows the vertex distribution for the low energy region after all solar neutrino reduction steps. Although all solar neutrino reductions applied to make this sample, background events remains near the wall, especially in the bottom region and near the barrel region. Since the position dependence of the background shape undergoes a large uncertainty in the solar neutrino analysis, it is required to keep uniformity of the vertex distribution. In order to reduce the systematic uncertainty, the additional tighter vertex position cut is developed.

$$z > -7.5 \text{ m, (for } 4.5 - 5.0 \text{ MeV)} \quad (6.3.10)$$

$$(x^2 + y^2) + \left( \frac{150.0}{11.75^4} \times |z - 4.25|^4 \right) < 150.0, \text{ (for } 3.5 - 4.5 \text{ MeV)} \quad (6.3.11)$$

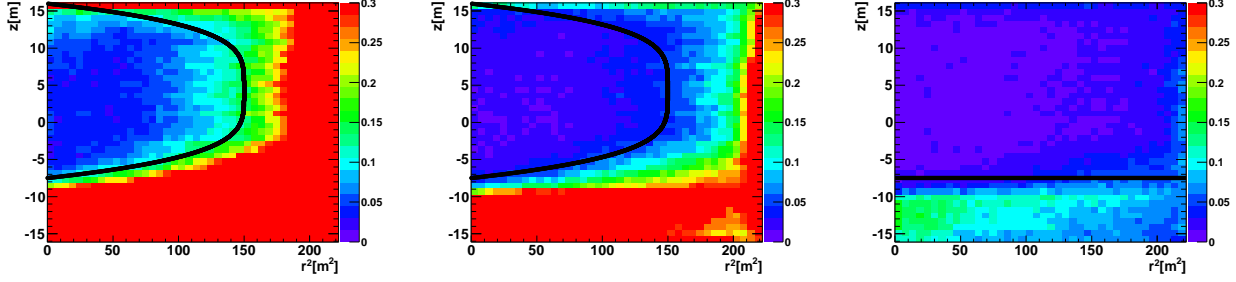


Figure 6.16: The vertex distribution for 3.5–4.0 MeV (left), 4.0–4.5 MeV (middle) and 4.5–5.0 MeV (right) in kinetic energy. The horizontal axis shows  $r^2$  [ $\text{m}^2$ ] and the vertical axis shows  $z$  [m]. The color shows the event rate in unit of event/day/bin. The tighter fiducial volume is illustrated as the region inside of black line (above the black line in the case of 4.5–5.0 MeV).

The tighter fiducial volume is 8.85 kton and 16.45 kton for 3.5–4.5 MeV and 4.5–5.0 MeV, respectively. Above 5.0 MeV, no more additional vertex position cut is required, therefore, the fiducial volume is 22.46 kton.

## 6.4 Summary of the reduction step

Figure 6.17 shows the time variation of the event rate after applying all solar neutrino reduction cuts. A continuous low background level has been kept for the entire period of SK-IV due to the improvements of the water circulation system and optimized cut criteria.

The left of Figure 6.18 shows the energy spectrum in the SK-IV data sample after applying the all solar neutrino reductions compared with that in SK-III. The differences are seen between the final sample of SK-IV and that of SK-III. The reasons why of the differences originate are as follows:

1. 3.5 – 4.5 MeV region: The smaller number of events in SK-IV is caused by the tighter fiducial volume cut. The tight fiducial volume in SK-III is 12.3 kton, while that of SK-IV is 8.85 kton. Since the background events near the wall and the bottom are effectively rejected, the event rate becomes lower.
2. 4.5 – 5.0 MeV region: The smaller number of events in SK-IV is caused by the difference in the event quality cut in this region. It is 0.25 when SK-III, while it is tighter 0.29 in SK-IV.
3. 5.0–6.0 MeV region: The cut criterion of the small hit cluster event is changed. In SK-IV, the cut is removed in this energy region. Due to this, the number of the events in the final sample increases.

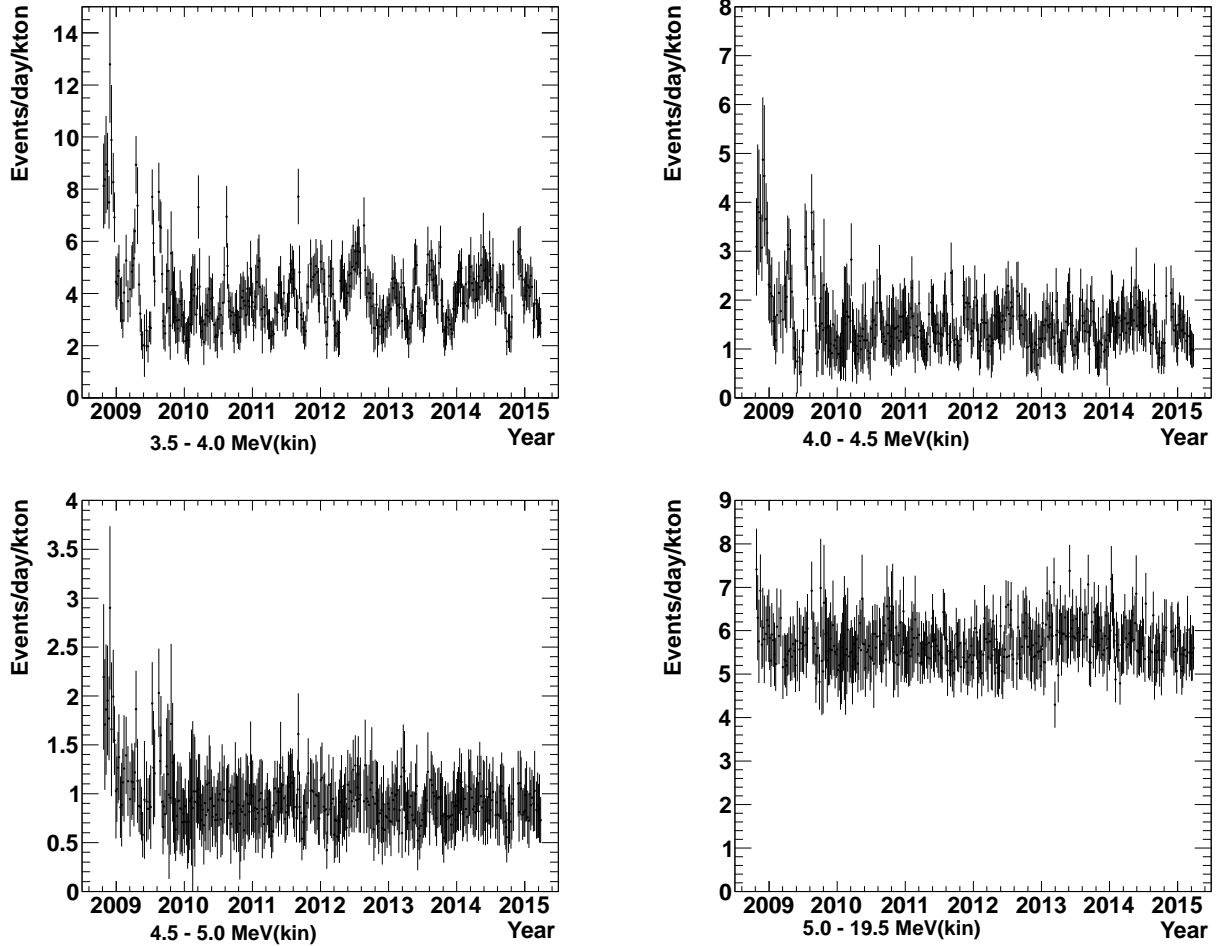


Figure 6.17: Event rate during SK-IV phase. Each plot corresponding to the average of the event rate in 5 days. The horizontal axis shows the date in year and the vertical axis shows the event rate in unit of event/day/kton.

The right of Figure 6.18 shows the reduction efficiency after each reduction step. The reason why there is the difference between the final sample of SK-III and that of SK-IV is the same as in the energy spectrum difference above.

## 6.5 Multiple scattering goodness

After applying the reductions described above, there remain mimic signals, which are mainly caused by the radioactive impurities such as  $^{222}\text{Rn}$  daughters. Especially, the beta decays of  $^{214}\text{Bi}$  whose  $Q$ -value is 3.27 MeV are the source of the background mimic signals. Since the energy resolution in the lower energy region is poor,  $\sim 20\%$  for  $\sim 4.0$  MeV as shown in Figure 10.1, some of these events are reconstructed above the energy threshold 3.5 MeV. The true recoil electron scattered by the solar neutrino moves in a relatively straight way, while the mimic signal multiply scatters by the other electrons or nucleus in the water.

In order to separate the mimic signals from the true  $^8\text{B}$  solar neutrino signal, it is possible to

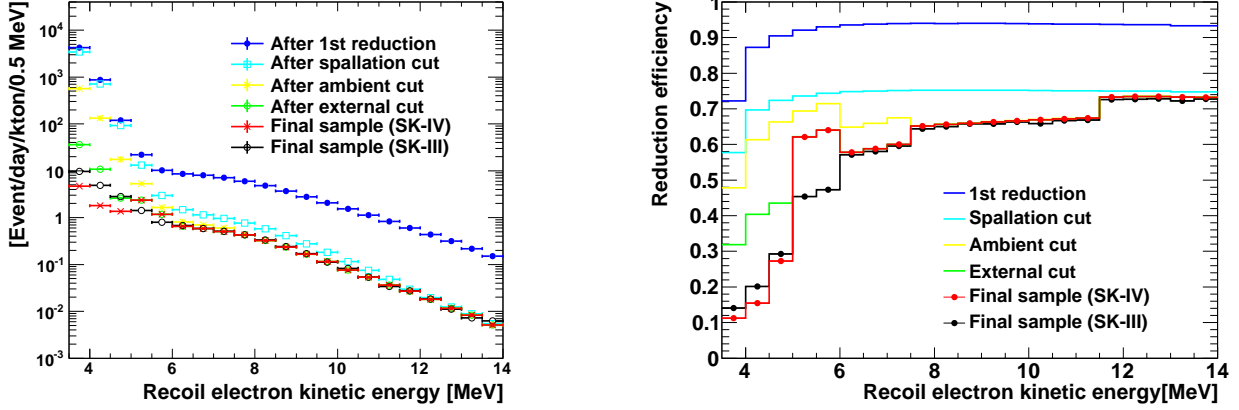


Figure 6.18: Left: Energy spectrum after the each reduction step. The horizontal axis indicates the recoil electron kinetic energy [MeV] and the vertical axis indicates the number of events [event/day/kton]. Right: The reduction efficiency of each reduction step using the MC simulation.

use the hit PMT pattern in the resulting the Cherenkov light cones to reconstruct the multiple scatterings of the electrons. This hit pattern anisotropy is characterized using a “direction fit goodness”. This goodness is called “multiple scattering goodness (MSG)” and is constructed by the following methods;

1. Pairs of the hit PMTs are selected by sliding the 20 nsec time window after subtracting the time of flight. Then the vector  $\vec{r}_i$  whose direction is from the reconstructed vertex position to the  $i$ -th PMT position is obtained.
2. The cones with an opening angle of  $42^\circ$  are projected around each of the vector  $\vec{v}_i$ . The number of the intersection lines between the cones are counted, which becomes either 0, 1 or 2. The left of Figure 6.19 shows the schematic view when the intersection is 2.
3. For the pairs of PMTs which provide the intersection lines from the projection of the cones, the vector from the reconstructed vertex along each of the intersection lines are taken. Then, this newly introduced vector is normalized and defined as “unit vectors”. The unit vectors are found by selecting the all pairs of the hit PMTs within 20 nsec.
4. The cluster of the unit vectors are then found by forming vector sums which are within  $50^\circ$  of a central unit vector. Once the unit vector is used in the formation of the cluster, it is not used as a central one and not used the further forming. The right of Figure 6.19 shows the schematic view of forming the summed vector. Then the longest summed vector is taken as  $\vec{d}_{\text{best}}$ .
5. After repeating the above process, the longest summed vector is finally taken as “best direction vector” as shown in the right of Figure 6.19.
6. The parameter  $MSG$  is calculated as

$$MSG = \frac{\text{Length of best direction vector}}{\text{number of unit vector}}. \quad (6.5.1)$$

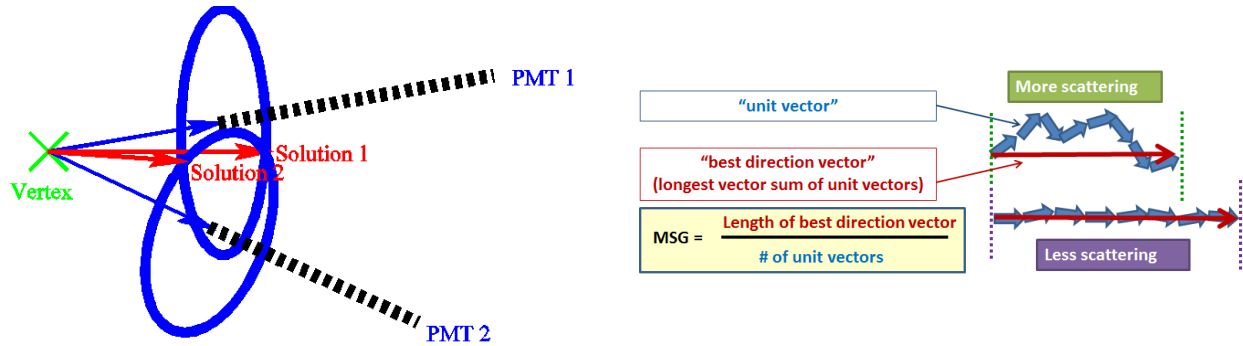


Figure 6.19: Left: The schematic view of selecting the vector  $\vec{v}_i$  (blue) and  $\vec{u}_i$  (red) [108, 110]. Right: The schematic view of the “unite vector”.

The parameter  $MSG$  spans from 0 to 1. The events with more multiple scatterings have lower  $MSG$  value, while these with less multiple scatterings have a higher  $MSG$  value. Figure 6.20 illustrates a typical distribution of  $MSG$  with LINAC calibration data and the MC simulation. When the beam energy becomes higher, the peak position of  $MSG$  shifted to a higher value as expected.

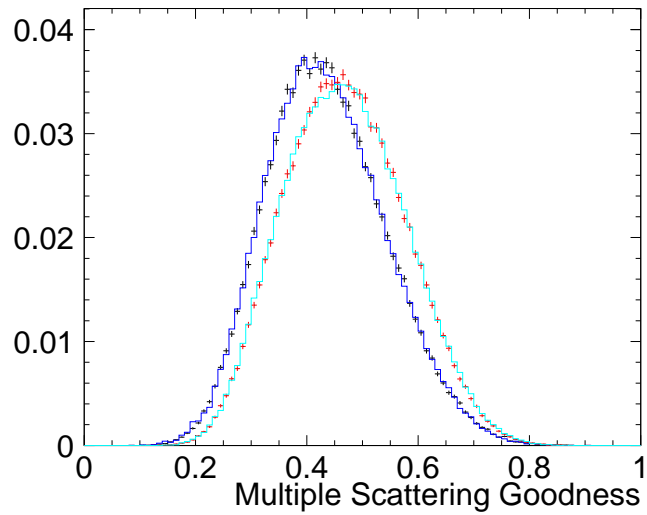


Figure 6.20: The typical distribution of  $MSG$  with the LINCA data (dot) and the MC simulation (hist) [108, 110]. For 4.6 MeV (8.4 MeV), the data point was drawn in black (red) and the MC result was drawn in blue (cyan).

In the solar neutrino analysis, there is no cut using the  $MSG$ , but when the number of the solar neutrino events is subtracted below 7.5 MeV, each energy bins are divided into 3 groups of  $MSG$ , low ( $0.0 \leq MSG < 0.35$ ), middle ( $0.35 \leq MSG < 0.45$ ) and high ( $0.45 \leq MSG \leq 1.0$ ).

# Chapter 7

## Trigger efficiency of low energy event

### 7.1 Motivation and History

In order to understand the MSW effect, it is important to lower the energy threshold as much as possible. For that purpose, understanding the trigger efficiency for low energy events is important.

In the SK-I and SK-III, the trigger efficiency for the low energy region was measured by setting a special trigger in the DT calibration. The trigger threshold was lowered from the usual value of  $-186$  mV to a special value of  $-150$  mV and compared the number of the observed events between the usual trigger and the special trigger [98, 99]. As a result in SK-III, the trigger efficiency for  $3.5 - 4.0$  MeV and  $4.0 - 4.5$  MeV energy bins were  $\sim 88\%$  and more than  $98\%$ , respectively [99].

So far, the energy threshold of the solar neutrino analysis in SK-IV has been set at  $4.0$  MeV in kinetic energy, which is the same as in SK-III [108, 110]. After the installation of the front-end electronics QBEE, the vertex and timing resolutions have been improved compared with the previous phases. So it should be able to lower the analysis threshold down to  $3.5$  MeV. However, the trigger efficiency for the  $3.5 - 4.0$  MeV energy region has not been evaluated precisely in SK-IV.

The trigger efficiency depends on the event position due to the shape of the detector structure, the water transparency and so on. It is also important to evaluate the position dependence of the trigger efficiency. In order to evaluate the trigger efficiency at these low energies, a special Ni calibration is performed to evaluate the detection efficiency.

### 7.2 Special Ni calibration

The method of the special Ni calibration is as:

1. The Ni calibration source is deployed as in the usual operation.
2. The data acquisition hit threshold is changed from 34 (usual) hits to 28 hits.
3. All reduction cuts are applied to the calibration data as described in Chapter 6.

4. Additional timing information cut is applied to the remaining event. For this purpose, a time-of-flight is calculated between the hit PMTs and the Ni calibration source position (not between the hit PMTs and the reconstructed vertex position). The events with the number of hit PMTs within 20 nsec less than 20 are rejected. Applying this cut, background events (non-Ni event) are almost rejected.
5. The number of the events detected with hit threshold 34 is compared with that taken with hit threshold of 28, and evaluated the trigger efficiency. In this study, the trigger efficiency is assumed to be 100.0% for the reference calibration with 28 hit threshold.
6. MC simulation events are prepared under the same conditions of the special Ni calibration, i.e. with threshold of 34 hits and of 28 hits. The same cuts are applied to the MC simulation events and its trigger efficiency is evaluated with the same method.

Figure 7.1 shows the typical vertex and energy distributions of the Ni calibration with the usual hit threshold (left) and the special hit threshold (right).

Even though the additional timing cut is applied, it is found that the events whose vertex is far from the Ni calibration source position are sometimes observed. However, the fraction of such far-position-events is less than  $\sim 10^{-5}\%$  and it is negligible for the evaluation of the trigger efficiency.

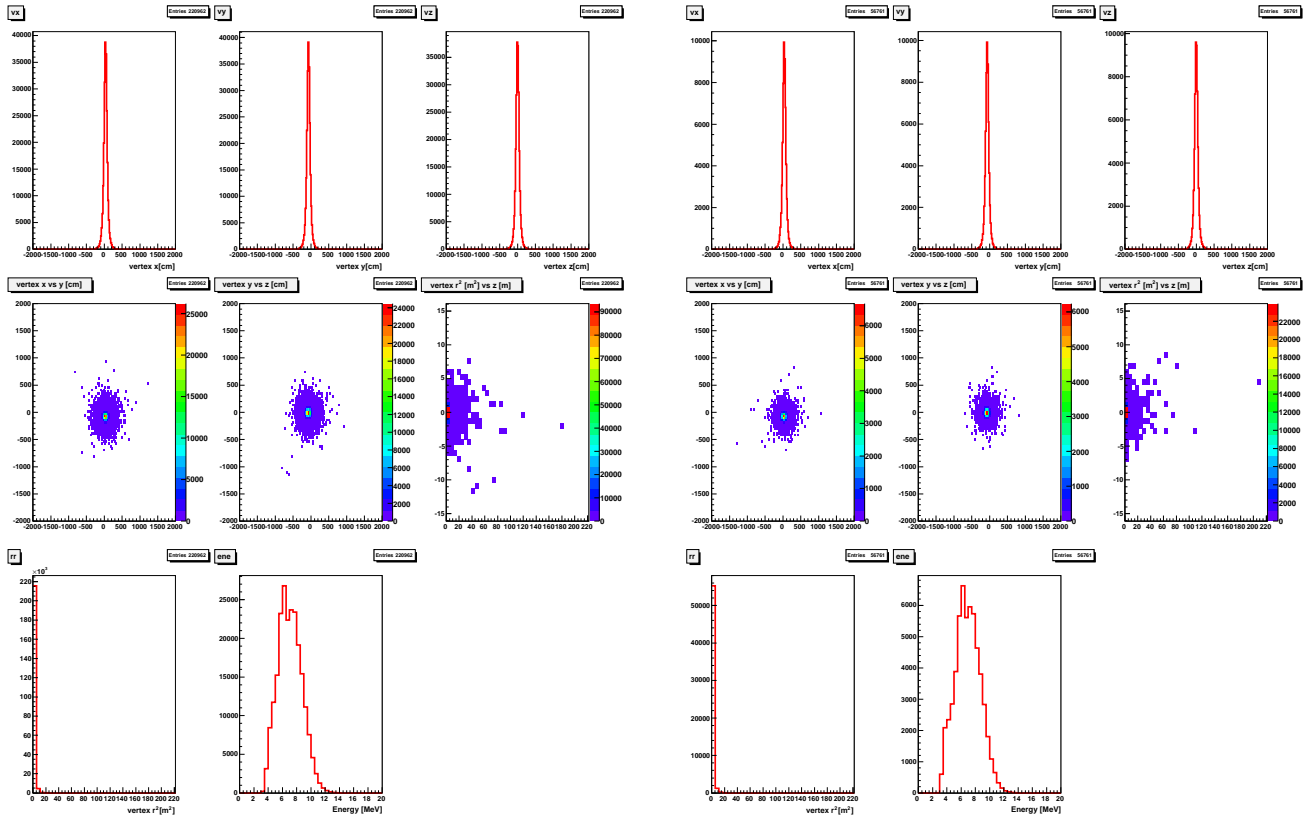


Figure 7.1: The typical vertex distribution of Ni calibration data taken with SLE hit threshold 34 (left) and 28 (right) at the position of  $(x, y, z) = (+0.353, -0.707, \pm 0.0)$  m. The color in the middle row shows event/48sec/bin.

Figure 7.2 shows a typical energy distribution (left) and the trigger efficiency (right) for the calibration data (top) and the MC simulation (bottom) at the position of  $(x, y, z) = (+0.353, -0.707, \pm 0.00)$  m.

It should be noted that the number of detected events is not the same between the 2 calibration data (34 hits and 28 hits). The number of events should be normalized to get the trigger efficiency. The normalization is done by the following method:

1. Since the trigger efficiency above 6.5 MeV is expected to be 100.0%, the total number of events above 6.5 MeV is used for the normalization. The integral number of counts above 6.5 MeV are represented as  $c_{34}$  and  $c_{28}$  in each case.
2. For the energy distribution in the left of Figure 7.2, the entries in each 0.5 MeV interval bins are divided by  $c_{34}$  (or  $c_{28}$ ).
3. For the trigger efficiency in the right of Figure 7.2, the number of the events with 34 hit threshold is scaled by  $c_{28}/c_{34}$ .

### 7.3 Result of the position dependence

The Ni calibration for this study was performed 3 times in 2015. As mentioned in subsection 6.3.14, the tight fiducial volume cut is applied to the data sample in the solar neutrino analysis. Thus, the region within the tight fiducial volume region, i.e.  $r \leq +12.2$  m and  $z \geq -7.0$  m is used for this study. The first and second calibrations were done setting up the Ni calibration ball at  $(x, y) = (+0.353, -0.707)$  m and the third calibration was done setting up the ball at  $(x, y) = (+10.958, -0.707)$  m. The Ni calibration ball was moved from bottom to top in  $z$ -axis direction when the calibration was performed.

The results of the first and second Ni calibration are shown in Figure 7.3. At the highest  $z$  position ( $z = +16$  m), the trigger efficiency is higher than those at the other positions in 3.5–4.0 MeV. This tendency is confirmed in the both calibrations. It is because the Ni calibration ball is close to the wall and the emitted light can reach the PMTs without absorption and scatterings in water. In the lowest energy region, the average of the trigger efficiency is 88.15% and 92.85% for the data and the MC simulation, respectively.

The result of the third Ni calibration is shown in Figure 7.4. The trigger efficiencies are slightly higher than that of the center calibration case. It is caused by the fact that the Ni calibration source in the third calibration is closer to the wall compared with the first and second calibrations. The average of the trigger efficiency at 3.5–4.0 MeV is 90.40% and 92.29% for the data and the MC simulation, respectively.

According to the results, there is a few percent level difference in the trigger efficiency between the data and MC simulation. One of the possible reasons to explain this difference is the spectral shape difference between the Ni calibration data and the MC simulation. A  $^{252}\text{Cf}$  source is used for the Ni calibration and it emits neutrons. Almost all neutrons are captured by the Ni calibration ball, however, roughly 50% of neutrons escape from the Ni ball. Escaping neutrons are mostly captured by free protons in water and then emit 2.2 MeV  $\gamma$ s. Some fraction of these 2.2 MeV  $\gamma$ -rays are observed as events in the energy range of 3.5–4.0 MeV because of the finite energy resolution. In addition,  $\gamma$ -ray emissions from the spontaneous fissions of

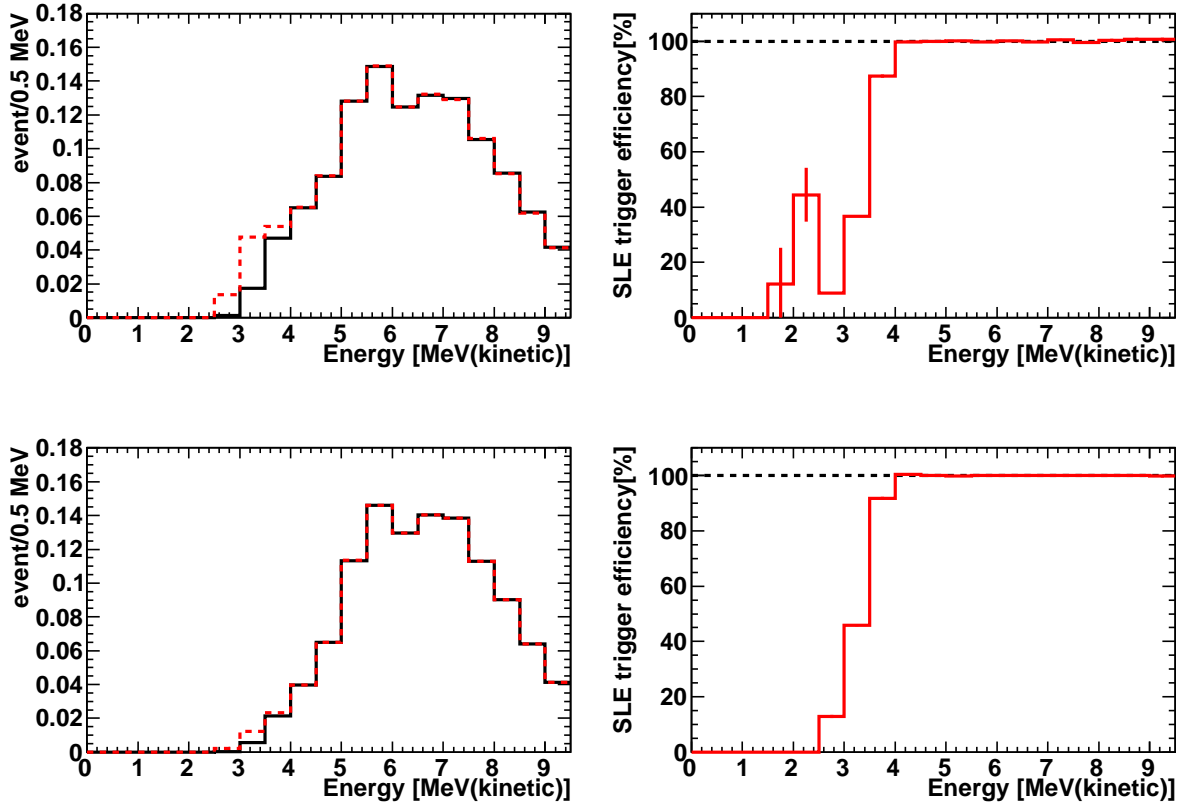


Figure 7.2: The typical energy histogram of the Ni calibration data (top) and the MC simulation (bottom) at the position of  $(x, y, z) = (+0.353, -0.707, \pm 0.0)$  m. The black histogram in the left upper (lower) panel shows the energy histogram of the Ni calibration data with 34 hits threshold and the red histogram shows that with 28 hits. The right upper (lower) panel shows the SLE trigger efficiency for Ni calibration data (MC).

$^{252}\text{Cf}$  may also cause events in this energy bin. In contrast, these processes are not considered in the MC simulation. As a result, because of the different contributions inside an energy bin, systematic difference between the data and MC is observed. In order to demonstrate that a plot of the trigger efficiency with a finer energy bin is shown in Figure 7.5.

## 7.4 The efficiency in the low energy region

In order to take into account the position dependence of the trigger efficiency, the tight fiducial volume is divided into 9 regions as shown in Figure 7.6. Since the special calibrations were taken at  $x = +0.353$  m and  $x = +10.958$  m, the  $(x, y)$  plane is separated by 2 regions, one is  $r^2 \leq 30.02$  m<sup>2</sup> (inside of the yellow circle) and the other is  $r^2 > 30.02$  m<sup>2</sup> (between the red and yellow circles) as shown in the left of Figure 7.6. In the case of  $x = +0.353$  m, there are 5 positions in  $z$  direction coordinate, i.e.  $z = -7$ ,  $z = \pm 0$ ,  $z = +7$ ,  $z = +12$  and  $z = +16$  m. In the case of  $x = +10.958$  m, there are 4 positions in  $z$  coordinate, i.e.  $z = -3$ ,  $z = \pm 0$ ,  $z = +7$

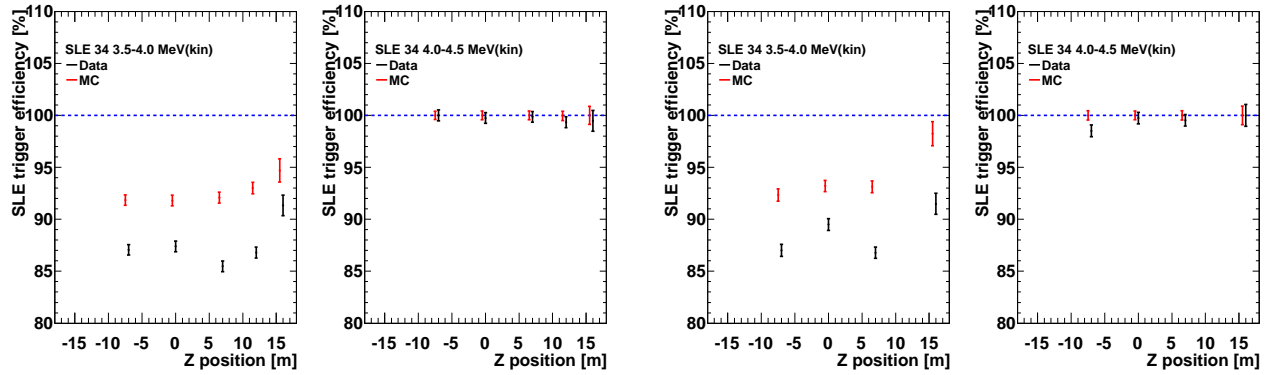


Figure 7.3: The  $z$  direction position dependence of SLE trigger efficiency taken at the center calibration hole on June 18th (left) and July 28th 2015 (right). The black (red) points show the results of data (MC). The left (right) panel show the SLE trigger efficiency for 3.5 – 4.0 MeV (4.0 – 4.5 MeV) region.

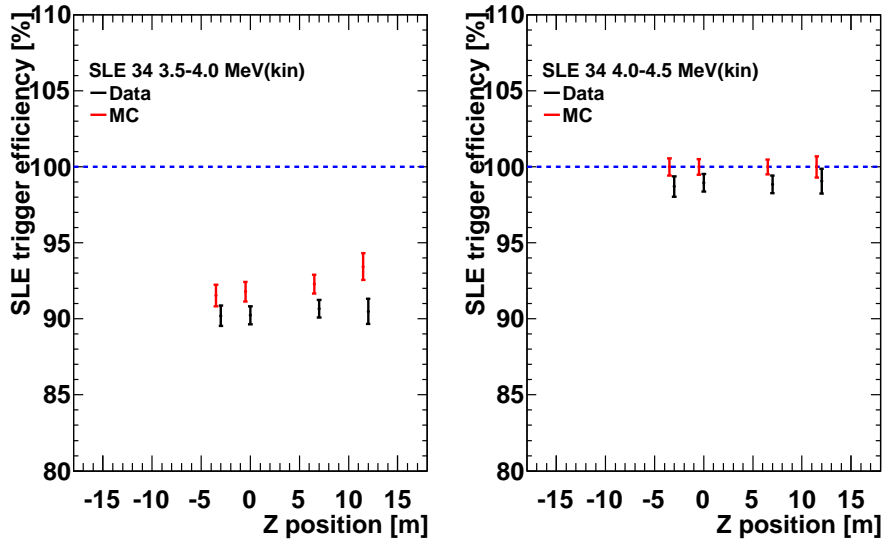


Figure 7.4: The  $z$  direction position dependence of SLE trigger efficiency taken at the calibration hole of  $(x, y) = (+10.958, -0.707)$  m on September 9th 2015. The black (red) points show the results of data (MC). The left (right) panel show the SLE trigger efficiency for 3.5 – 4.0 MeV (4.0 – 4.5 MeV) region.

and  $z = +12$  m. The divided 9 regions are labeled as shown in the right of Figure 7.6. The volumes in the divided regions are calculated and summarized in Table 7.1.

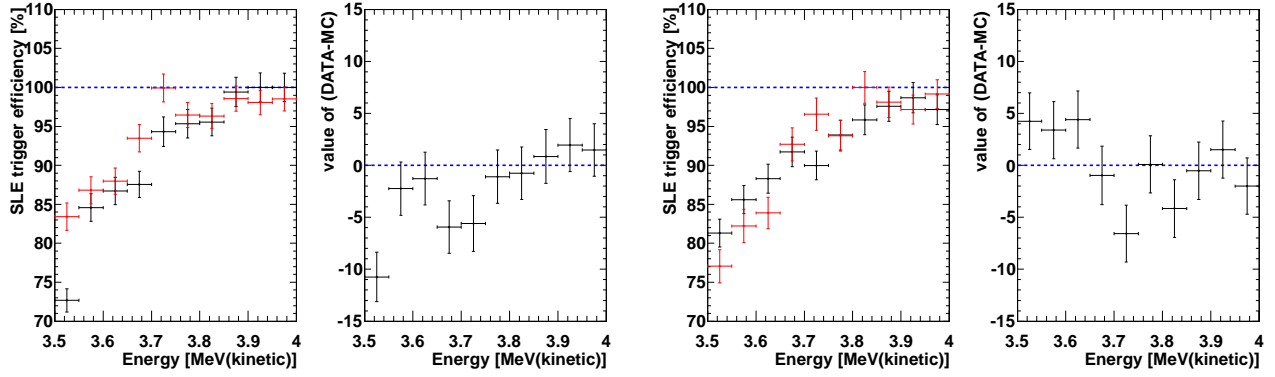


Figure 7.5: Left: A typical plot of the trigger efficiency with a finer energy bin taken at  $(x, y, z) = (+0.353, -0.707, \pm 0.0)$  m on July 28th 2015. The left panel shows the trigger efficiency in 3.5 – 4.0 MeV energy bin divided by 0.05 MeV and the right panel shows the difference between the data and MC simulation. The black (red) points shows the results of the data (MC simulation). Right: A typical plot of the trigger efficiency for a finer energy bin taken at  $(x, y, z) = (+10.958, -0.707, \pm 0.0)$  m on September 9th 2015.

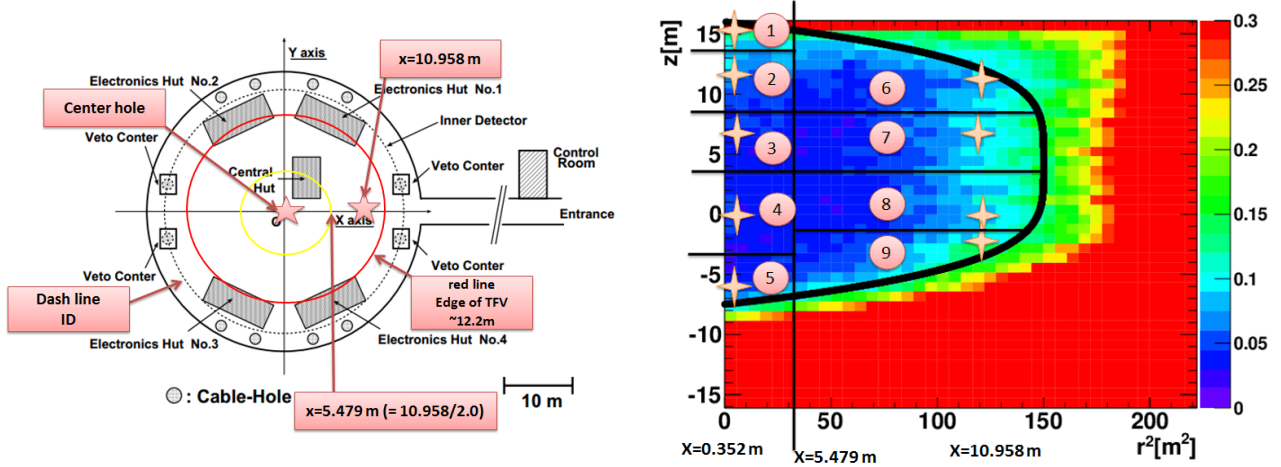


Figure 7.6: Left: The top view of the SK tank, i.e. the  $(x, y)$  plane. The region inside of the yellow circle is represented by the center calibration data and the region between the red and yellow circles is represented by the edge calibration data. Right: The  $z$  vs  $r^2$  in the SK tank. The stars indicate the calibration position. The tight fiducial volume is divided into 9 regions, each of them includes one calibration position. These divided are labeled from 1 to 9.

The trigger efficiency is evaluated as follows:

$$\text{Efficiency} = \frac{\sum e_i V_i}{\sum V_i}, \quad (7.4.1)$$

where  $e_i$  is the trigger efficiency of the  $i$ -th calibration and  $V_i$  is the volume of the  $i$ -th calibration. Finally, the trigger efficiencies for the 3.5 – 4.0 MeV and for the 4.0 – 4.5 MeV energy bins are evaluated as shown in Table 7.2. The trigger efficiencies for the 3.5 – 4.0 MeV

Table 7.1: The definition of each region and volume. The adopted calibration data for each region is marked by open circle.

Region No	$r^2$ [m <sup>2</sup> ] ( $r = +5.479$ m)	$z$ [m]	Volume [m <sup>3</sup> ]	June 18th	July 28th	September 9th
1	$r^2 \leq 30.02$	$z \geq +14.0$	91.09	○	○	—
2	$r^2 < 30.02$	$+9.5 \leq z < +14.0$	424.39	○	—	—
3	$r^2 \leq 30.02$	$+3.5 \leq z < +9.5$	565.85	○	○	—
4	$r^2 \leq 30.02$	$-3.5 \leq z < +3.5$	660.16	○	○	—
5	$r^2 \leq 30.02$	$z < -3.5$	359.63	○	○	—
6	$r^2 > 30.02$	$z \geq +9.5$	1459.88	—	—	○
7	$r^2 > 30.02$	$+3.5 \leq z < +9.5$	2241.86	—	—	○
8	$r^2 > 30.02$	$-1.5 \leq z < +3.5$	1853.56	—	—	○
9	$r^2 > 30.02$	$z < -1.5$	1202.85	—	—	○

energy bin are  $89.36 \pm 0.22\%$  for the calibration data and  $92.42 \pm 0.24\%$  for the MC simulation. Those in the 4.0 – 4.5 MeV energy bin are  $99.18 \pm 0.22\%$  for the data and  $100.00 \pm 0.21\%$  for the MC simulation. In addition, above 4.5 MeV, the trigger efficiency both the calibration data and the MC simulation are evaluated to be 100.0%.

Table 7.2: The detection efficiency evaluated by the special Ni calibration. The difference between the data and the MC simulation is calculated as (DATA-MC)/DATA.

Energy [MeV (kin)]	DATA [%]	MC [%]	Difference [%]
3.5 – 4.0	$89.36 \pm 0.22$	$92.42 \pm 0.24$	$-3.43 \pm 0.37$
4.0 – 4.5	$99.18 \pm 0.22$	$100.00 \pm 0.21$	$-0.86 \pm 0.31$

The differences between the data and the MC simulation are also evaluated to be  $(-3.43 \pm 0.37)\%$  in the 3.5 – 4.0 MeV energy bin and to be  $(-0.86 \pm 0.31)\%$  in the 4.0 – 4.5 MeV energy bin. These differences will be used for the systematic uncertainties in the measurement of the solar neutrino flux which will be described in Chapter 10.

## 7.5 Time variation of the detection efficiency

Since the trigger efficiency evaluation method was developed on 2015, its time variation and stability was not measured before 2015.

As mentioned in the previous section,  $\sim 3\%$  level difference between the Ni calibration data and the MC simulation is seen in the 3.5 – 4.0 MeV energy bin. In order to evaluate the time variation of the detector performance, the trigger efficiency is estimated using the solar neutrino MC simulation regardless of this difference.

Figure 7.7 shows the time variation of the trigger efficiency using the solar neutrino MC simulation. According to Figure 7.7, two tendencies are seen in 3.5 – 4.0 MeV. One is a short ( $\sim$  a year) time variation and another is a long-term increase. The short time variation is strongly correlated with the water transparency variation (left of Figure 5.13) which is input information to the solar neutrino MC simulation. The long-term increase is caused by the

improvement of water transparency and the increase of the dark rate (Figure 4.4) which is also input information to the solar neutrino MC simulation.

As the dark rate of PMTs increases, the accidental hits within the event timing window also increase. The additional accidental hits helps events a little below the hit threshold to reach the hit threshold of the data acquisition system.

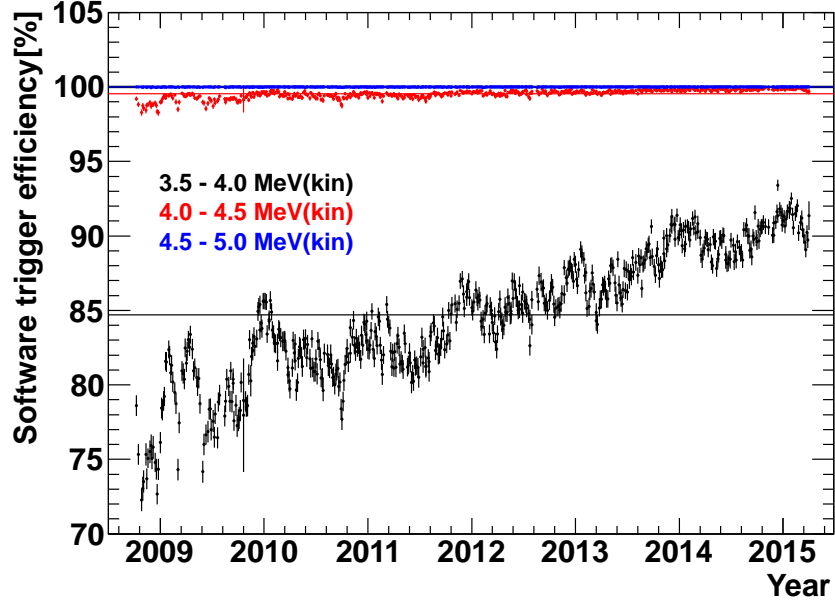


Figure 7.7: The time variation of the software trigger efficiency in lower energy regions. The horizontal axis shows the date in SK-IV and the vertical axis shows the detection efficiency [%]. The black, red and blue plots show the detection efficiency in 3.5 – 4.0 MeV, 4.0 – 4.5 MeV and 4.5 – 5.0 MeV respectively. The lines illustrate the average for the entire period.

## 7.6 Summary of this chapter

The trigger efficiencies in the lower energy region was measured using a Ni-Cf calibration source in 2015. The calibration data were taken at various positions in the detector to evaluate position dependence. It is determined as  $89.36 \pm 0.22\%$  ( $92.42 \pm 0.24\%$ ) for the calibration data (MC simulation) in 3.5 – 4.0 MeV and  $99.18 \pm 0.22\%$  ( $100.00 \pm 0.21\%$ ) in 4.0 – 4.5 MeV, respectively. The differences between the data and the MC simulation are evaluated as  $(-3.43 \pm 0.37)\%$  in 3.5 – 4.0 MeV and  $(-0.86 \pm 0.31)\%$  in 4.0 – 4.5 MeV.

# Chapter 8

## Background study for low energy region

### 8.1 Rn in SK water

#### 8.1.1 Motivation and History

A main physics target of the SK detector is to measure the energy spectrum of the recoil electrons from  ${}^8\text{B}$  and *hep* solar neutrinos. Since its energy spectrum is distributed from 0 MeV to 20 MeV, it is required that the energy threshold for the solar neutrino observation should be lowered as much as possible in order to investigate the mechanism of the solar neutrino oscillation further. However, the data acquisition threshold is limited by the background contamination.

One possibility of the main background in the solar neutrino analysis is  $\beta$  decay of  ${}^{214}\text{Bi}$  whose  $Q$ -value is about 3.27 MeV. The emitted electron from the  $\beta$  decay can not be distinguished from the true solar neutrino signal because the both are detected as events with Cherenkov light.

There are three ways to observe more solar neutrino signals in SK. The first way is to improve the detection efficiency for low energy solar neutrino events. The second way is to enlarge the fiducial volume. The third way is to reduce the background level in the solar neutrino analysis. The main issue in this chapter is to focus on the background events in the solar neutrino analysis in SK.

The solar angle distributions of SK-I, SK-III and SK-IV in 4.5 – 5.0 MeV in kinetic energy region are shown in Figure 8.1. The recoil electrons scattered off by the elastic scattering of solar neutrinos have directional information with respect to the Sun. In order to see the excess of solar neutrino signals above the background, an angle  $\theta_{\text{sun}}$ , which is the angle between the reconstructed event direction and the vector pointing from the Sun, is defined and shown in Figure 8.2. The excess of the solar neutrino signal should be observed at  $\cos\theta_{\text{sun}} = 1.0$ , as shown in Figure 8.1. On the other hand, the events whose  $\cos\theta_{\text{sun}}$  is less than 0 are due to the background events because such events do not have directional correlation with the Sun. According to Figure 8.1, the background level in SK-IV is lower than that in SK-I by a factor of about 4.

The solar angle distributions in the 3.5 – 4.0 MeV region for SK-III and SK-IV are shown in Figure 8.3. A peak toward the Sun direction is not seen clearly in the SK-III. The reasons

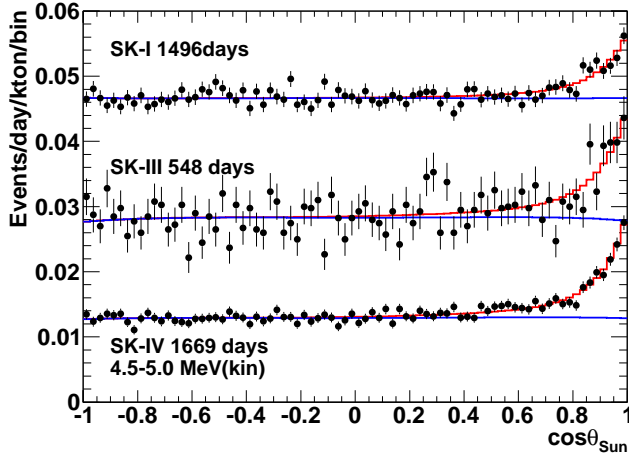


Figure 8.1: The solar angle distributions in SK-I, SK-III and SK-IV. The energy range is 4.5 – 5.0 MeV in kinetic energy. The black points show the data, the red (blue) histograms show the best fit results (background). The top, middle and bottom plots show the distributions in SK-I, SK-III and SK-IV, respectively.

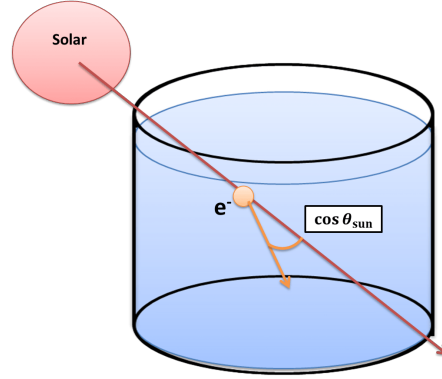


Figure 8.2: The definition of the solar angle  $\theta_{\text{sun}}$ .  $\theta_{\text{sun}}$  is the angle between the reconstructed event direction and the vector pointing from the Sun.

for this are: (1) The total livetime of SK-III is 548 days. However, the data below 6.0 MeV in kinetic energy was taken during only 298.2 days because of the high radioactivity period [99]. It is too short to observe a clear peak of the solar neutrino signal from the solar direction above the background level statistically. The extracted solar neutrino events are  $54^{+81}_{-79}$ (stat.) events in SK-III. (2) The background of the solar neutrino signals is large and its event rate is high compared with that in SK-IV.

On the other hand, a clear peak of events from the Sun direction is observed in SK-IV. In the case of 1669 days data sample, the extracted solar neutrino signals are  $1048^{+132}_{-137}$ (stat.) events, which is about  $7.5\sigma$  level excess.

In order to identify the origin of the background events, the Rn concentration in SK water is measured and its contribution is evaluated .

### 8.1.2 Direct Rn measurements in SK water and their results

Since the Rn concentration in the SK pure water is low, which is estimated less than  $1.0 \text{ mBq/m}^3$ , it is difficult to measure its Rn concentration precisely using commercially available techniques such as liquid scintillator method etc. Therefore, a Rn measurement system for the SK pure water is developed and this system is designed to measure less than  $0.1 \text{ mBq/m}^3$  level of the Rn concentration. The detail of the measurement system is described in Appendix.

The results of the measurement are shown in Figure 8.4. It is confirmed that the Rn concentration in the supply water is higher when it passes through the membrane degasifier system in the water circulation system. After bypassing the membrane system, the Rn concentration in the supply water is reduced from  $9.18 \pm 0.51 \text{ mBq/m}^3$  to  $1.85 \pm 0.31 \text{ mBq/m}^3$ .

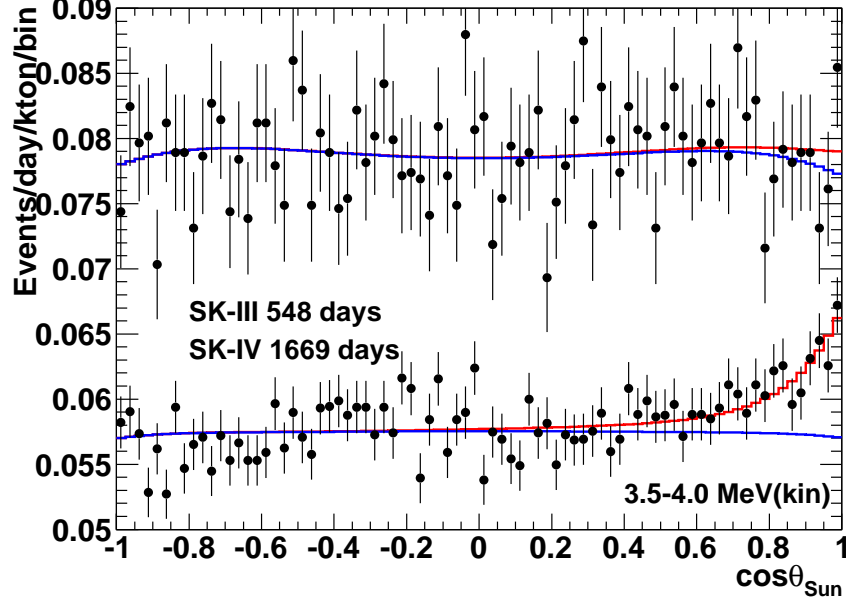


Figure 8.3: The solar angle distributions in SK-III (upper) and SK-IV (lower) in the 3.5 – 4.0 MeV in kinetic energy region. The horizontal axis shows the solar angle  $\cos \theta_{\text{sun}}$  and the vertical axis shows event rate in unit of event/day/kton/bin, where the total number of bins is 80.

Possible reasons for this contamination in the supply water are as follows:

1. Some components of the membrane degasifier emitting Rn from their inner surface and emanated Rn is dissolved into the supply water.
2. Some leak points exist around some joint positions of each component of the membrane degasifier system. The Rn in air dissolves into the supply water from the leak positions.

### 8.1.3 Supply water problem

After bypassing the membrane degasifier system, it is confirmed that not only the Rn concentration in the supply water but also other sampling water such as in the center and bottom regions decreases. This means that the supply water itself is one of the Rn sources in SK.

The inlet positions of the supply water in the SK tank are illustrated in the right of Figure 8.5. The tip position of these inlets are at  $z = -16.5$  m, which is only 50 cm away from the edge of the fiducial volume (2 m from the wall). After applying event selection cuts for the solar neutrino analysis described in Chapter 6, the event vertex distribution is checked by selecting the events in the range of  $-16 \leq z \leq -15$  m as shown in the left of Figure 8.5. There are hot spots in the vertex distribution around the inlet positions. This fact also indicates that Rn in the supply water makes SK water radiochemically dirty.

It is expected that the event rate from the background events should decrease if Rn in the supply water decreases. To check this expectation, the event rate in the bottom region is checked before and after bypassing the membrane system as described in section 8.3. Before checking, a conversion factor from the event rate to the Rn concentration should be evaluated.

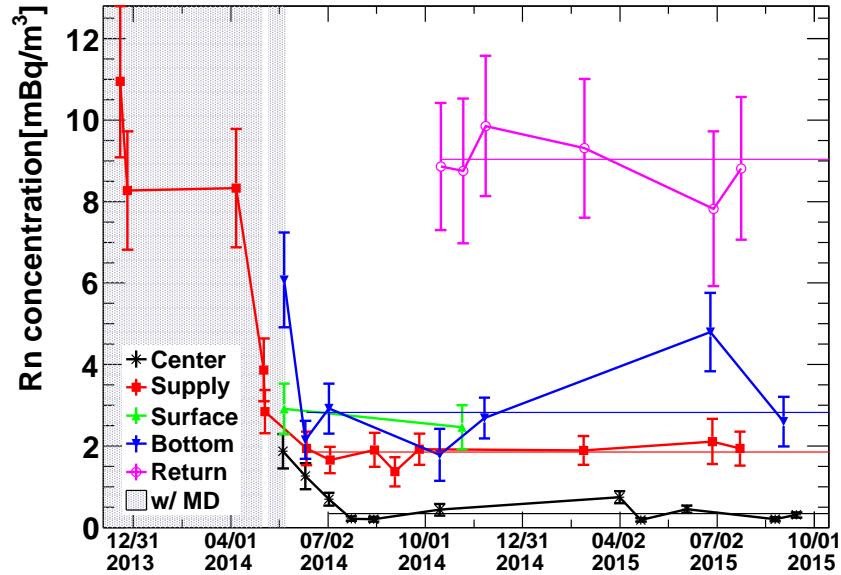


Figure 8.4: The time variation of Rn concentration in SK water. The Rn concentration measurements have been conducted since December 2013. The gray region illustrates the supply water passed through the membrane degasifier system. The Rn concentration decreased after bypassing the membrane system on May 22nd, 2015.

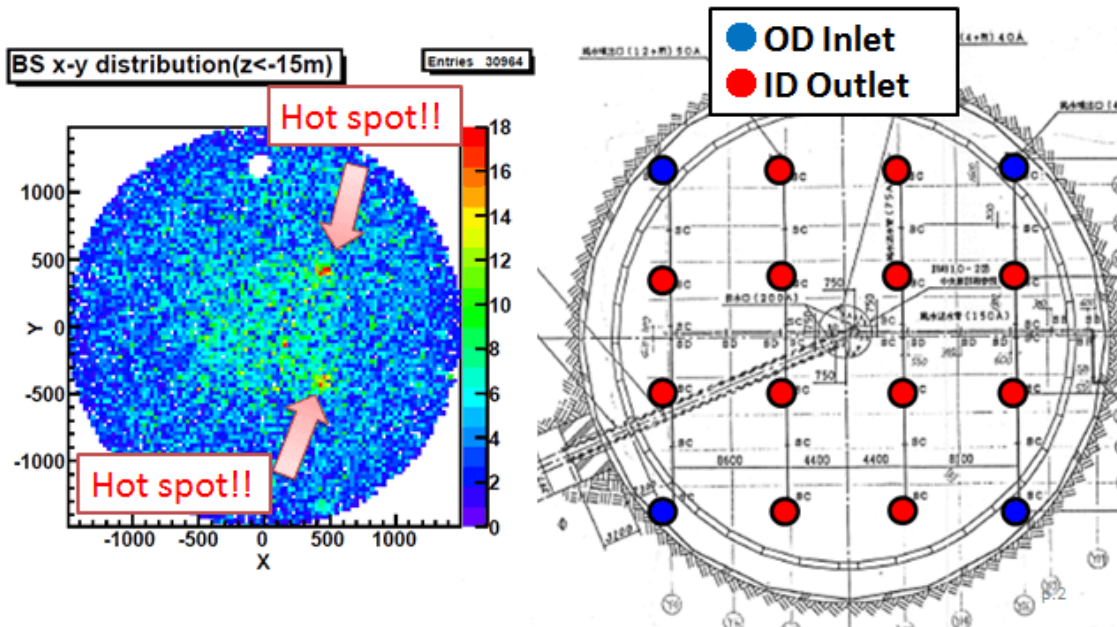


Figure 8.5: The positions of the inlets for supply water in the bottom region. The red (blue) inlets (outlets) are used for the ID (OD) detector.

## 8.2 Rn injection analysis

### 8.2.1 Motivation and history

The easy way to evaluate the background events from the Rn contamination is to inject Rn rich water into SK directly. This idea of the Rn injection was proposed and actually conducted in SK-I [111]. In the SK-I's study, the Rn concentration of the Rn rich water was measured by a liquid scintillation counter<sup>1</sup> and Rn rich water was supplied into the SK tank. 1.2 L of the Rn rich water, which is equivalent to 13 Bq of Rn, was injected into the SK tank. After the injection, a peak was observed in the vertex distribution for 4.5 – 6.0 MeV in kinetic energy [111].

Based on this study, the Rn injection was conducted in SK-IV on October 30th, 2014.

### 8.2.2 Rn rich water production technique

The Rn rich water is produced by the following steps.

1. About 10 L of the supply water to SK is sampled.
2. Using a  $^{226}\text{Ra}$  radioactive source, daughter Rn's are dissolved into the SK pure water under the constant air circulation by a air pump for a few days.
3. 5 L of the Rn rich water is injected into the SK tank. The injected position is  $(x, y, z) = (+0.353, -0.707, +12.5)$  m.
4. After the injection, the rest of the Rn rich water is sampled with three shake flasks soon. Then, its Rn concentration is measured by the liquid scintillation method.

### 8.2.3 Analysis method

The event rate before and after the Rn injection is analyzed as follows:

1. A data sample is selected from September 1st, 2014 to December 31st, 2014. This period covers about 2 months before and after the Rn injection.
2. All solar neutrino reduction cuts are applied and events in the energy range between 3.5 and 5.0 MeV are selected. Samples used in this analysis are from normal runs, i.e. runs for usual physics analysis.
3. Events whose vertex position are  $r \leq 10.0$  m from  $(x, y) = (+0.353, -0.707)$  m and  $10.0 \leq z \leq 15.0$  m are selected. Its volume is 1.57 kton. During this analysis period, the water circulation system was running continuously under the usual operation mode. Since the position dependence of water flow is not understood completely, the selected vertex region is open largely to avoid losing injected Rn events.
4. It is assumed that the excess of the event rate after the Rn injection is due to only the radioactive decay of injected Rn.

---

<sup>1</sup>Packard Tri-Carb Liquid Scintillation Counter

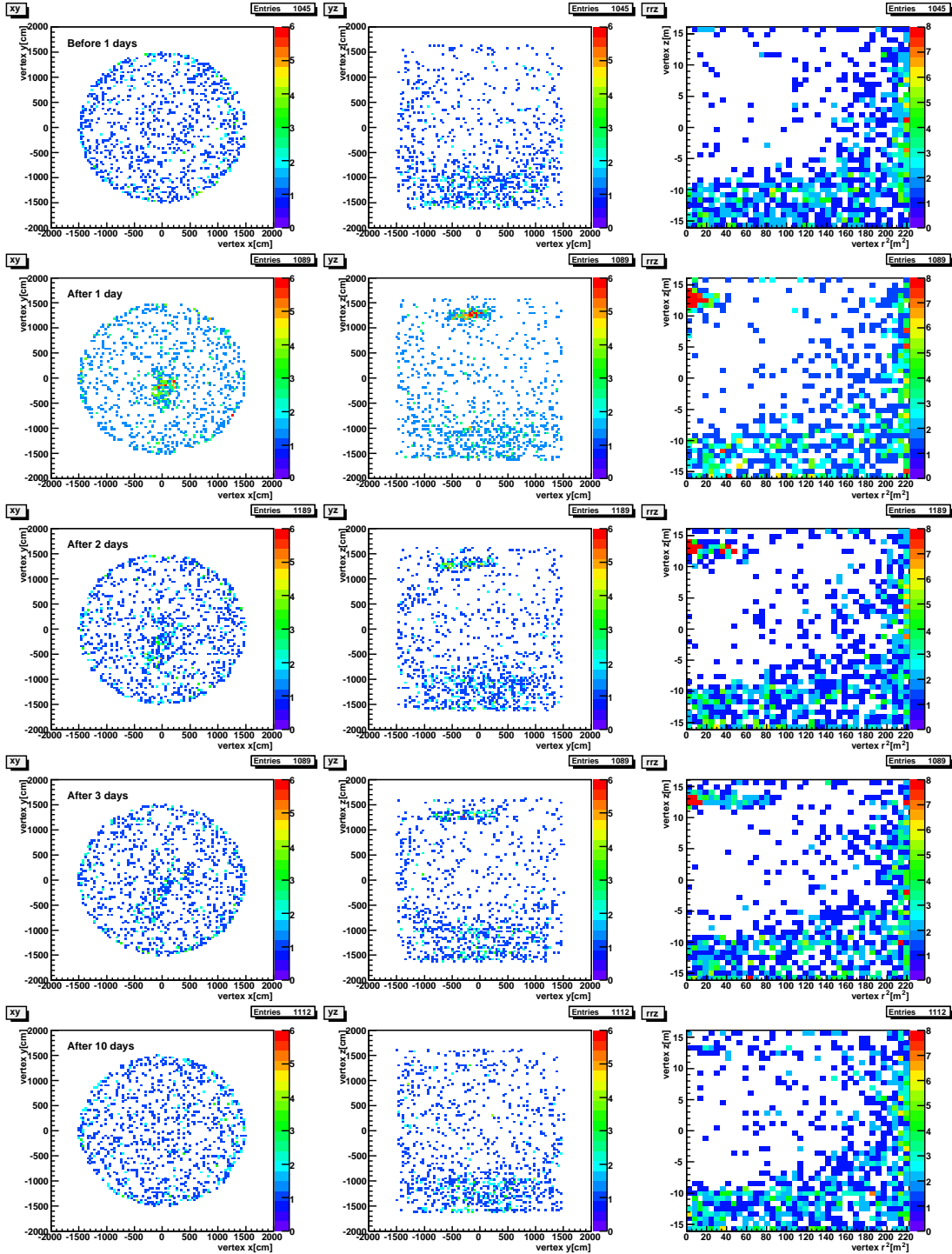


Figure 8.6: The vertex distributions of data sample during the Rn injection period and its time variation. The first through fifth rows show plots for one day before, one, two, three and ten days after the injection, respectively. The first, second and third columns show  $x$  vs.  $y$ ,  $y$  vs.  $z$  and  $r^2$  vs.  $z$  distributions respectively. The energy range is  $3.5 - 5.0$  MeV in kinetic energy. The color of the panels illustrates the event/day/bin. After the injection, the excess events are observed around  $(x, y, z) = (+0.353, -0.707, +12.5)$  m. After 10 days, such a cluster are not observed clearly because of Rn decay and the water circulation. Water flows up from the injected position and injected water finally goes outside the analysis volume.

5. The excess of the event rate after the Rn injection is fitted with a decay function which is defined as

$$F(t) = Ae^{-\lambda t} + B, \quad (8.2.1)$$

where  $\lambda$  ( $= (\ln 2)/3.82$ ) is a decay constant and  $t$  is the time from the Rn injection. The parameter  $A$  means the excess of the event rate caused by the Rn injection and the parameter  $B$  means the constant event rate under the usual operation of SK.

6. The event rate is compared with the Rn concentration in the Rn rich water measured by the liquid scintillation counter.

Figure 8.6 shows the typical vertex distributions in 3.5 – 5.0 MeV in kinetic energy region before and after the Rn injection and its time variation. The cluster of events around  $(x, y, z) = (+0.353, -0.707, +12.5)$  m is observed after the Rn injection. After 10 days, such a cluster are not observed clearly because of Rn decay.

## 8.2.4 Result

The Rn concentration in the Rn rich water measured by the liquid scintillation is  $1.01 \pm 0.05$  Bq/L and the total amount of the supplied Rn rich water is 5.0 L, namely  $5.05 \pm 0.25$  Bq of Rn is injected into the SK tank. Normalized by the volume of the selected region, the additional Rn concentration is  $3.22 \pm 0.16$  mBq/m<sup>3</sup>.

Figure 8.7 shows the event rate before and after the Rn injection. It is obvious that the event rate decreases along with Rn decay time.

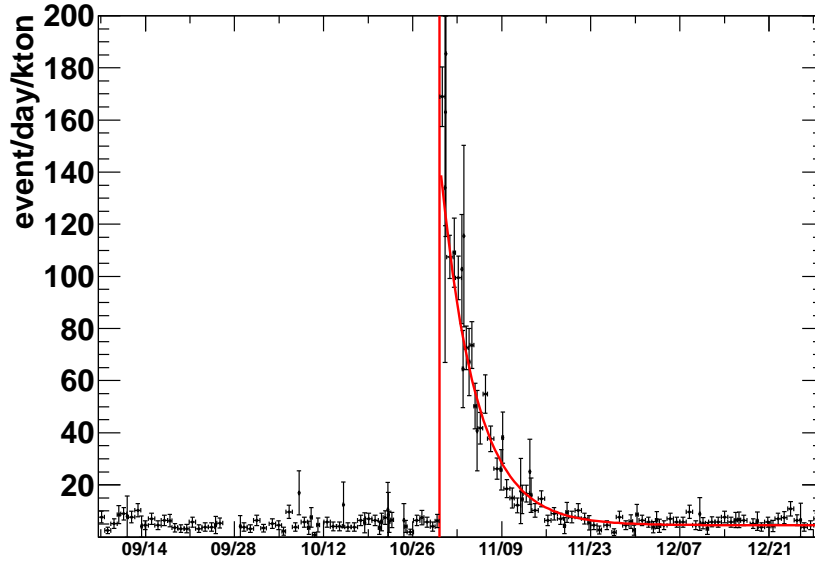


Figure 8.7: The event rate around the Rn injection period. Each black point shows the event rate in unit of event/day/kton for each Normal Run (basically 24 hours). The red curve is the fitting function of Rn decay defined as equation (8.2.1).

The fitting result for the parameters  $A$  and  $B$  is

$$A = 141.84 \pm 5.33, \quad (8.2.2)$$

$$B = 4.53 \pm 0.29. \quad (8.2.3)$$

Then, the conversion factor of the injected position is obtained. The result is

$$10.0 \text{ event/day/kton} = 0.222 \pm 0.008 \text{ mBq/m}^3 \text{ (for } 3.5 - 5.0 \text{ MeV)}. \quad (8.2.4)$$

## 8.3 Event rate analysis

### 8.3.1 Motivation

It is clear that the Rn concentration decreases after bypassing the membrane system as explained in section 8.1.3. To understand the background event from the  $\beta$  decay of Rn daughters, it is needed to compare the event rate before and after bypassing the membrane system.

### 8.3.2 Analysis method

To check the event rate before and after bypassing the membrane system, 2-year data samples are analyzed. The first period is for about 1 year before bypassing and the second period is for about 10 months after bypassing. Table 8.1 summarizes the information on the analysis periods, their livetime and the Rn measurement results in the bottom region.

Before bypassing the membrane system, the Rn concentration measurement in the bottom region was conducted only once. So, the resultant value of the Rn measurement has a large statistical uncertainty.

Table 8.1: The information on the analysis period and the Rn concentration in the bottom region before and after bypassing the membrane system.

Period	Date[YYYY/MM/DD]	Livetime [day]	Rn concentration [mBq/m <sup>3</sup> ]
Before	2013/06/01 – 2014/05/20	322.95	6.08 ± 1.16
After	2014/07/01 – 2015/04/30	255.90	2.79 ± 0.48

To extract the event rate from the background, the event rate is calculated using the following step:

1. All solar neutrino reduction cuts are applied to select events.
2. Select events in 3.5 – 5.0 MeV.
3. To select the events occurring in the bottom region, the vertex position is required to be  $r \leq 10.0$  m from the  $(x, y) = (+0.353, -0.707)$  m and  $-13.5 \leq z \leq -10.5$  m. Its volume is 0.942 kton.

- The events whose  $\cos \theta_{\text{sun}}$  is less than 0 are selected to remove true solar neutrino events. When converting the event rate to the Rn concentration, a factor of 2 due to this cut is corrected as

$$\text{Event Rate} = \frac{2 \times \text{Event}(\cos \theta_{\text{sun}} < 0)}{\text{Livetime} \times \text{Volume}}. \quad (8.3.1)$$

- For the sake of simplicity, it is assumed that the Rn concentration in the above selected region is uniform.

### 8.3.3 Result

The calculated event rates before and after bypassing the membrane system are shown in Figure 8.8. Table 8.2 (Table 8.3) summarizes the event rate for each energy region. It is obvious that the event rate in the bottom region drops after bypassing the membrane system, as shown in Figure 8.8. The measured difference in the event rate between before and after bypassing is  $122.80 \pm 1.14$  event/day/kton.

Table 8.2: The event rate in the bottom region before bypassing.

Energy [MeV(kin)]	Event ( $\cos \theta_{\text{sun}} \geq 0$ )	Event ( $\cos \theta_{\text{sun}} < 0$ )	Total event	Event rate [event/day/kton]
3.5 – 4.0	25373	25873	51246	$170.01 \pm 0.75$
4.0 – 4.5	9032	9110	18142	$59.86 \pm 0.44$
4.5 – 5.0	2220	2235	4455	$14.69 \pm 0.22$
Combined	36625	37218	73843	$244.56 \pm 0.90$

Table 8.3: The event rate in the bottom region after bypassing.

Energy [MeV(kin)]	Event ( $\cos \theta_{\text{sun}} \geq 0$ )	Event ( $\cos \theta_{\text{sun}} < 0$ )	Total event	Event rate [event/day/kton]
3.5 – 4.0	9930	10209	20139	$84.66 \pm 0.59$
4.0 – 4.5	3496	3582	7078	$29.70 \pm 0.35$
4.5 – 5.0	842	892	1734	$7.40 \pm 0.18$
Combined	14268	14683	28951	$121.76 \pm 0.71$

According to the conversion factor (8.2.4) from the Rn injection study, the Rn concentration in the bottom region is estimated as in Table 8.4. The estimated values are consistent with the measured results. Therefore, it is concluded that the background events in the bottom region are mainly due to Rn.

After bypassing the membrane system, the Rn concentration in the supply water is  $1.85 \pm 0.31$  mBq/m<sup>3</sup>, as shown in Figure 8.4. However, the Rn concentration in the bottom region is  $2.79 \pm 0.48$  mBq/m<sup>3</sup>, hence the Rn concentration in the bottom region is larger than that in the supply water. This fact indicates that there are some other Rn sources in the SK tank.

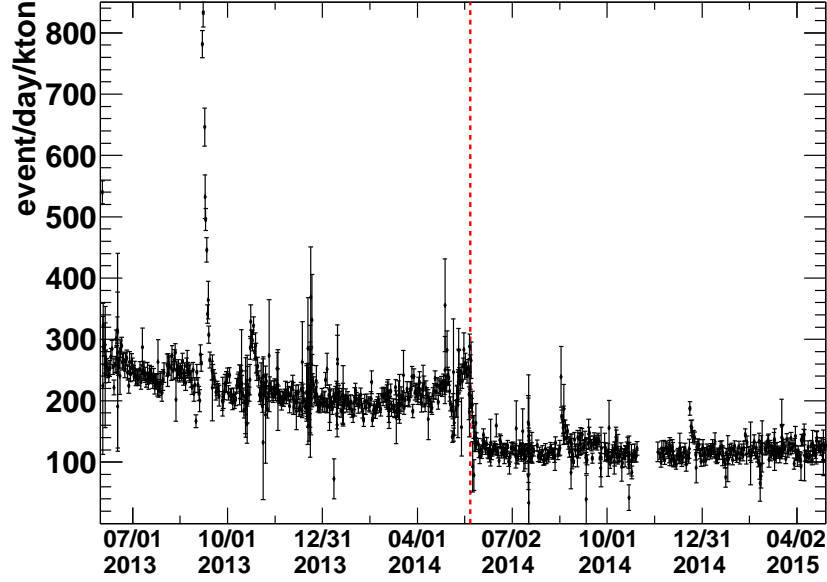


Figure 8.8: The time variation of the event rate in the bottom region from June 1st 2013 to April 30th 2015. The red dashed line shows the date of the bypassing on May 22nd 2014. On September 16th, a power outage happened due to a thunder storm and the water circulation system was down. After that, the event rate in the bottom region became higher than usual. On October 30th 2014, Rn injection study was performed. The data sample taken from October 30th 2014 to November 20th 2014 was removed in this analysis.

Table 8.4: The summary of the estimated Rn concentration in the bottom region before and after bypassing the membrane system.

	Estimated Rn concentration [mBq/m <sup>3</sup> ]	Measurement result [mBq/m <sup>3</sup> ]
Before	$5.43 \pm 0.20$	$6.08 \pm 1.16$
After	$2.71 \pm 0.10$	$2.79 \pm 0.48$

### 8.3.4 Position dependence

In order to evaluate the position dependence of Rn contamination, the event rate and the  $r^2$  distribution are checked. Figure 8.9 shows the those plots using the full SK volume (from  $z = -16$  m to  $z = +16$  m) divided into 8 panels, each of which corresponds to 4 m interval in  $z$ -axis. In addition, Figure 8.10 shows those plots using the bottom half of the SK volume (from  $z = -16$  m to  $z = \pm 0$  m) divided into 8 panels, each of which corresponds to 2 m interval in  $z$ -axis.

In the event rate plots (left of Figure 8.9 and Figure 8.10), the event rate below  $-8$  m decreases after bypassing the membrane system while the event rate above  $-8$  m is unchanged so much. In the  $r^2$  distribution plot (right of Figure 8.9 and Figure 8.10), the distributions

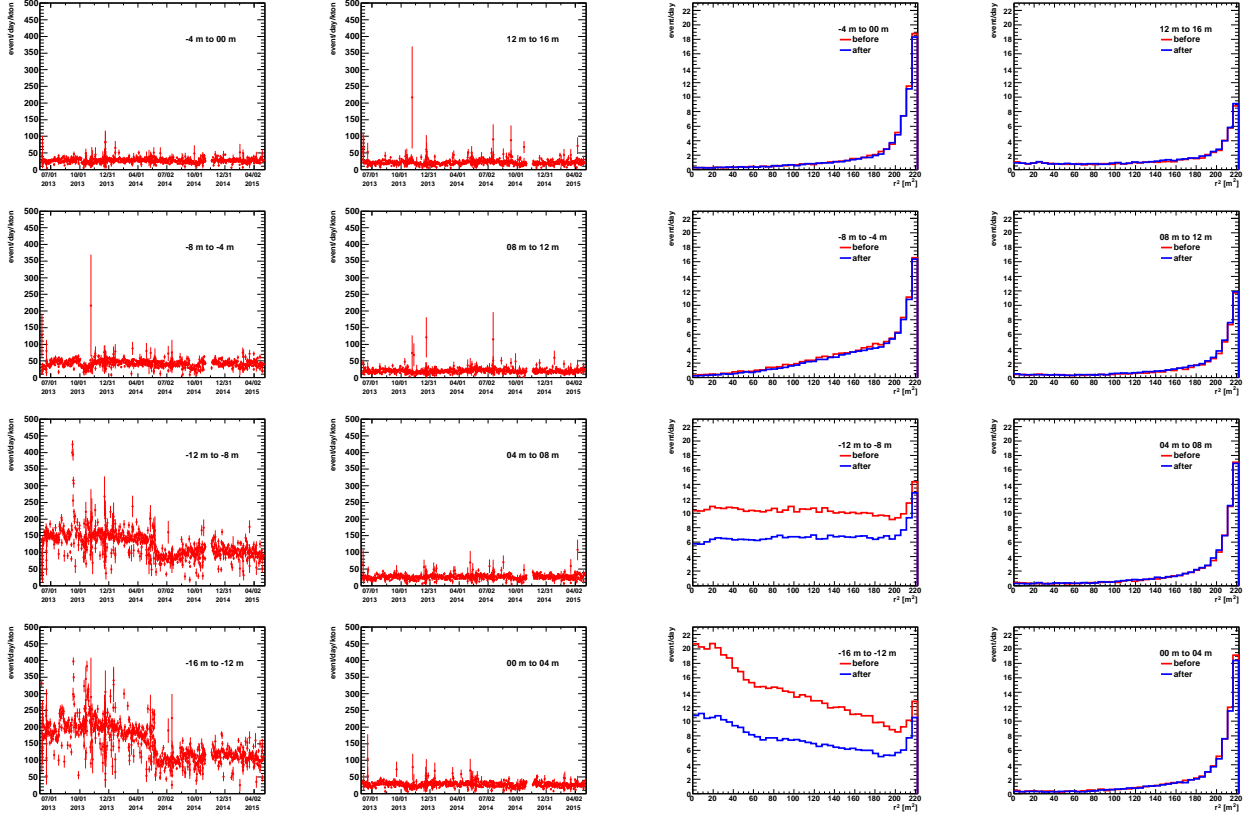


Figure 8.9: Left: time variation of event rate. The SK tank is divided into 8 areas, 4 m in  $z$ -axis. The horizontal axis shows the data from June 1st 2013 to April 30th 2015 and the vertical axis shows the event rate in unit of event/day/kt. Right:  $r^2$  distribution for the 8 divided areas. The horizontal axis shows the  $r^2$  [m] and the vertical axis shows the event rate in unit of event/day. The red (blue) histograms show before (after) bypassing the membrane system.

below  $-8$  m before and after bypassing the membrane system are significantly different. This difference also demonstrates that Rn in the supply water contributes to the background event in the bottom region.

In the  $r^2$  distribution plot, excess at large  $r^2$  position is seen, hence this excess is seen near the wall. These background events are caused by the Rn emanation of the PMT's glass or the FRP cover, external  $\gamma$ -rays and so on.

Below  $-8$  m, excess at small  $r^2$  is also seen. As mentioned in subsection 3.4.1, there is a water convection in the bottom region ( $z < -11$  m) because of the difference in the temperature between the supply water and the bottom water. Due to non-uniformity water in the convection zone, the Rn emitted from the glass of the PMT or the structure of the SK detector and so on is stirred. In consequence, many background events are observed in this convection region as shown in Figure 6.16.

Above results are summarized as follows:

1. After the bypassing the membrane system, the event rate in the bottom region decreases to  $121.76 \pm 0.71$  event/day/kt.

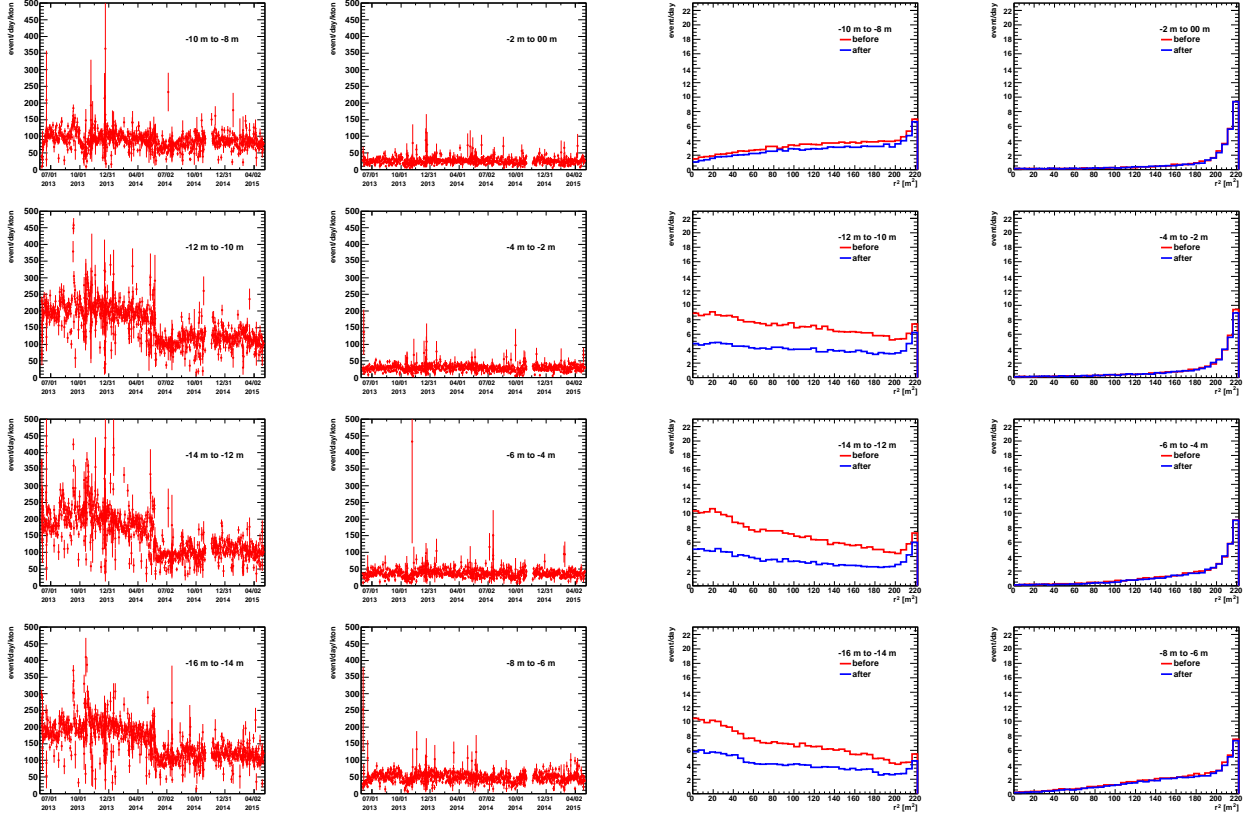


Figure 8.10: Left: time variation of event rate. The SK tank is divided into 8 areas, 2 m in  $z$ -axis. The horizontal axis shows the data from June 1st 2013 to April 30th 2015 and the vertical axis shows the event rate in unit of event/day/ton. Right:  $r^2$  distribution for the 8 divided areas. The horizontal axis shows the  $r^2$  [m] and the vertical axis shows the event rate in unit of event/day. The red (blue) histograms show before (after) bypassing the membrane system.

2. Rn in the supply water contributes to the background events in SK.

## 8.4 Future prospect

### 8.4.1 Solar neutrino observation

After bypassing the membrane system, the event rate in the bottom region decreases. The solar angle  $\cos \theta_{\text{sun}}$  distributions before and after are checked, as shown in Figure 8.11. In order to investigate the radial position dependence, 3 kinds of cuts are applied to select the events:

1. Cut A: Usual solar neutrino reduction cuts are applied to the data and no additional cut is applied. The full fiducial volume  $r \leq 14.9$  m is used. This sample is drawn in black in Figure 8.11
2. Cut B: Usual solar neutrino reduction cuts are applied to the data. Then, in order to remove the background events from the barrel PMTs, the events whose position is

$r \leq 12.2$  m are selected, where 12.2 m is the maximum radius of the tight fiducial volume cut. This sample is drawn in blue in Figure 8.11

- Cut C: Usual solar neutrino reduction cuts are applied to the data. Then, in order to see the most inner region, the events whose position is  $r \leq 10$  m are selected. This sample is drawn in red in Figure 8.11

Below  $-8$  m, the background baseline decreases by a factor of  $\sim 2$ . On the other hand, above  $-8$  m, no significant change is seen in the solar angle distribution. Slight excesses above the background level are seen around  $\cos\theta_{\text{sun}} = 1$ .

When the analysis region is enlarged in  $r$  coordinate, the background baseline becomes high by a factor of  $2 \sim 8$ . This fact indicates that the Rn emanation from the glass of the barrel PMTs contribute to the background events in the solar neutrino analysis. A possible way to reduce these background events is to install an additional acrylic cover in front of the PMTs and to separate the inner physics observation region from PMTs.

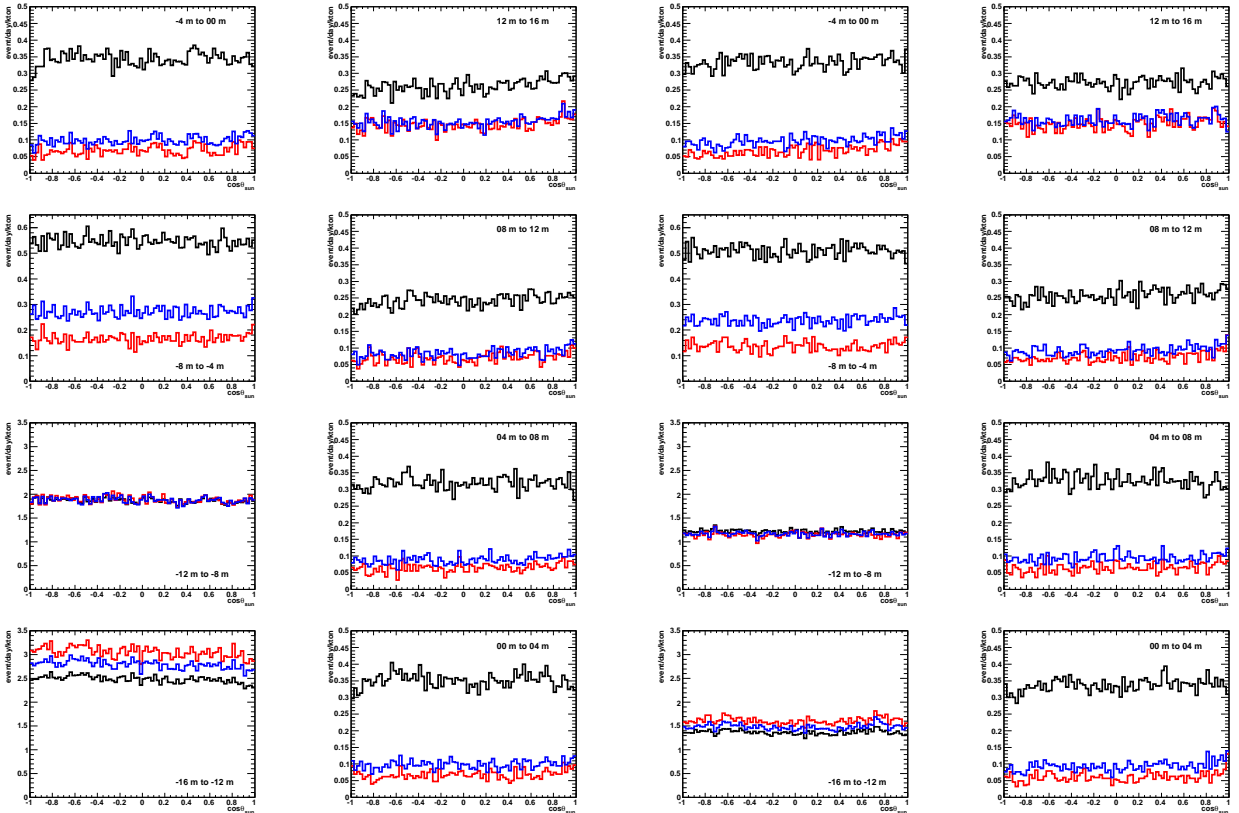


Figure 8.11: The solar angle distributions for divided 8 areas before (left) and after (right) bypassing the membrane system. The SK tank is divided into 8 areas, 4 m in  $z$ -axis. The red, blue black histograms show the events selected by  $r \leq 10$  m,  $r \leq 12.2$  m and  $r \leq 14.9$  m (fiducial volume), respectively.

## 8.4.2 Refurbishment of the membrane degasifier

Based on this study, it is expected that the background level in the bottom region is reduced if the Rn concentration in the supply water is reduced. In order to observe excess of solar neutrino signals below the  $-8$  m region, it is required to reduce the background level by a factor of 10. For this purpose, the membrane degasifier should be refurbished to reduce Rn in the supply water. The Rn removal efficiency of the membrane system was evaluated before the installation in SK-I and it is  $\sim 90\%$  [98]. If the membrane system is recovered, it is expected that the event rate in the bottom region can be reduced and the solar neutrino analysis volume can be enlarged.

In order to refurbish the membrane degasifier system, it is required to identify Rn rich materials used in the system. For this purpose, Rn emanation rate from several materials used in the system is evaluated. Although it is required to measure the Rn emanation rate from materials into the water, it is difficult to measure it due to the technical issues. Therefore, the emanation rate from gaskets to air (not water) is measured in this study.

First of all, EPDM (ethylene propylene diene monomer) gasket which is used to connect the water flow pipe lines is evaluated [112], because 120 sheets of EPDM gasket are used in total. In order to find the low background material, a Butyl and an Urethane type gaskets are also measured. Figure 8.12 shows the gaskets measured in this study.

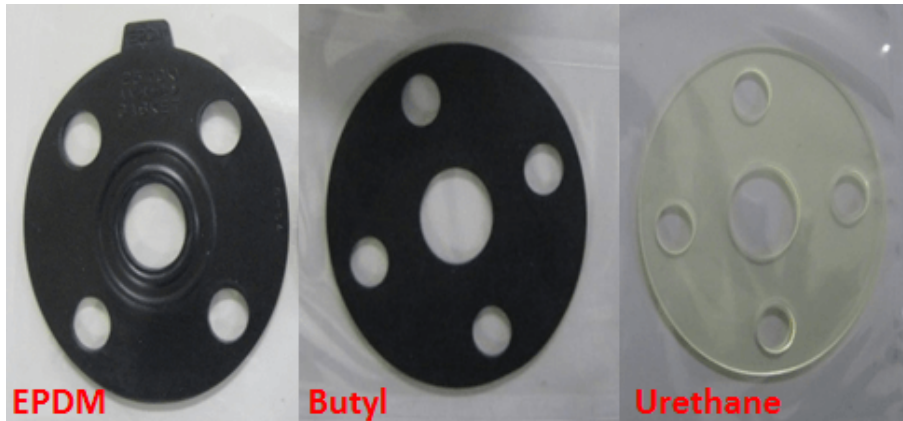


Figure 8.12: Rubber gaskets whose Rn emanation rate is measured. The left gasket is EPDM which used in the membrane degasifier system. The middle (right) gasket is made from Butyl (Urethane).

Table 8.5 summarizes the measured Rn emanation rate. The emanation rate of EPDM gasket is  $1.82 \pm 0.03$  mBq/1gasket, so it is considered that the EPDM gasket is the most suspicious one of the Rn sources in the membrane degasifier system. On the other hand, it is found that the lowest emanation rate among the three gasket types is the Urethane type. Thus, EPDM gasket can be replaced to the alternative low background gasket.

Based on the Rn emanation study, the following things will be expected.

1. If the all EPDM gaskets used in the membrane system are replaced to the Urethane gaskets, it is expected that the Rn concentration in the supply water will be reduced by a factor of 100.

Table 8.5: The summary of the Rn emanation rate from several gaskets used in the membrane degasifier system [112].

Gasket material	Rn emanation [mBq/1gasket]
EPDM	$1.82 \pm 0.03$
Butyl	$3.58 \pm 0.04$
Urethane	$0.013 \pm 0.004$

2. Then, the event rate in the bottom region will be reduced by a factor of more than 10. In addition, it is also expected that background events caused by the Rn decays can be reduced in the tight fiducial volume in the SK tank.
3. The fiducial analysis volume for solar neutrino will be enlarged by a factor of  $\sim 2$  after the refurbishment. This enlargement can help to reduce the statistical fluctuation of the solar neutrino signal in the low energy region and to improve the sensitivity to the “up-turn” of the energy spectrum due to the MSW effect.

## 8.5 Summary of this chapter

The study of background events in the solar neutrino analysis is performed. The measurement system for the Rn concentration in the SK water is newly developed. According to the measurements, it is found that the Rn concentration in the SK water decreases after bypassing the membrane degasifier system.

In order to evaluate the background events from Rn decay, the Rn injection study is performed. The Rn rich water is produced and injected into SK directly. The conversion factor is obtained to be  $10.0 \text{ event/day/kton} = 0.222 \pm 0.008 \text{ mBq/m}^3$  in the 3.5 – 5.0 MeV energy range.

Then, the event rates in the bottom region before and after bypassing the membrane system are checked. The event rate before bypassing is  $244.56 \pm 0.90 \text{ event/day/kton}$  and the event rate after bypassing is  $121.76 \pm 0.71 \text{ event/day/kton}$ . Using this conversion factor, the Rn concentration in the bottom region is estimated. Before bypassing, it is  $5.43 \pm 0.20 \text{ mBq/m}^3$  while it is  $2.71 \pm 0.10 \text{ mBq/m}^3$  after bypassing. These estimated values are consistent with the measurement values of  $6.08 \pm 1.16 \text{ mBq/m}^3$  (before) and  $2.79 \pm 0.48 \text{ mBq/m}^3$  (after). Based on this study, it is concluded that background events in the bottom region are mainly due to Rn.

In addition, the position dependence of the background events is also studied. Background events near the barrel PMTs are seen. It is required to reduce the event rate below  $-8 \text{ m}$  by a factor of 10 to observe the excess of solar neutrino signals.

In order to reduce the event rate in the bottom region, the Rn concentration in the supply water should be reduced. For this purpose, the emanation rate from EPDM gaskets used in the membrane degasifier is measured. It is found that EPDM is one of the possible Rn source in the system. On the other hand, the alternative low background gasket made from Urethane is found. It is expected to refurbish the membrane degasifier system when all the EPDM gaskets are replaced to Urethane type.

If the refurbishment is completed, it is expected that the event rate in the bottom region will be reduced by a factor of  $\sim 10$  and that the analysis fiducial volume will be enlarged by a factor of  $\sim 2$ . Thus, the Rn reduction in the solar neutrino analysis will lead to suppressing the statistical fluctuation of the solar neutrino signal in the low energy region and improve the sensitivity to the “up-turn” of the energy spectrum due to the MSW effect.

# Chapter 9

## Signal extraction method

### 9.1 Extended likelihood function

The direction of the recoil electron is strongly correlated with the direction of the incident neutrino. Therefore, the neutrino events are extracted using the parameter  $\cos \theta_{\text{sun}}$ , as shown in Figure 8.2. In order to precisely determine the number of solar neutrino elastic scattering events, an extended maximum likelihood function fit to the  $\cos \theta_{\text{sun}}$  distribution is used for 3.5 – 19.5 MeV in kinetic energy. This method was developed in SK-I [109] and used in the other phases [113, 114]. The likelihood function is defined as:

$$\mathcal{L} = e^{-(\sum_i B_i + S)} \prod_{i=1}^{N_{\text{bin}}} \prod_{j=1}^{n_i} (B_i \cdot b_{ij} + S \cdot Y_i \cdot s_{ij}). \quad (9.1.1)$$

The variables used in this likelihood function are as follows:

1.  $N_{\text{bin}}$ : The number of energy bins and  $N_{\text{bin}} = 23$  is used in this thesis. The components of  $N_{\text{bin}}$  are, 20 bins with 0.5 MeV width from 3.5 MeV to 13.5 MeV, 2 bins with 1.0 MeV width for 13.5 MeV to 15.5 MeV and one bin spanning from 15.5 MeV to 19.5 MeV.
2.  $n_i$ : The number of observed events in the  $i$ -th energy bin.
3.  $Y_i$ : The fraction of signal events expected in the  $i$ -th energy bin based on the MC solar neutrino simulation. The calculation method will be explained in the next subsection 9.2.
4.  $s_{ij}$ : The signal probability density function calculated from the expected solar neutrino signal. This function consists of three exponential functions plus a Gaussian function as described below:

$$s_{ij} = \sum_{k=0}^2 \exp(p_{i,2k} + p_{i,2k+1} \cos \theta_{\text{sun},j}) + p_{i,6} \exp \left[ -\frac{1}{2} \left( \frac{p_{i,7} - \cos \theta_{\text{sun},j}}{p_{i,8}} \right)^2 \right], \quad (9.1.2)$$

where  $p_{i,0\sim 8}$  are the fitting parameters in the  $i$ -th energy bin. They are obtained from the solar neutrino MC simulation. Figure 9.1 shows the distribution of  $s_{ij}$ .

5.  $b_{ij}$ : The background probability density function calculated from the expected background shape. It is obtained from the detector zenith and azimuthal angular distributions of the real data after all solar neutrino reduction cuts. It is fitted by an eight-order polynomial function and then converted from these coordinates to the  $\cos \theta_{\text{sun}}$  distribution. It is represented as

$$b_{ij} = \left[ \sum_{k=0}^8 a_{i,k} (\cos \theta_{\text{sun},j})^k \right] / a_{i,9}, \quad (9.1.3)$$

where  $a_{i,0\sim 9}$  are the fitting parameters in the  $i$ -th energy bin. Figure 9.2 shows the distribution of  $b_{ij}$ .

6.  $B_i$ : The number of background events in the  $i$ -th energy bin.
7.  $S$ : The total number of solar neutrino events in the entire energy region.

## 9.2 The expected fraction of signal events ( $Y_i$ )

The calculation method for the expected fraction  $Y_i$  is as follows:

1. Based on the  ${}^8\text{B}$  energy spectrum [115], the recoil electron energy distribution by the elastic scattering is calculated. In this calculation, only the electron type neutrino is considered, thus the reaction of  $\nu_e + e^- \rightarrow \nu_e + e^-$ .
2. The expected energy distribution of the recoil electrons is calculated considering the detector response in the MC simulation.
3. Using the above distribution, the expected total number of the elastic scattering events is calculated. According to this calculation, the number of expected events in each energy bin is also calculated.

The concrete treatments are described below.

### 9.2.1 Step 1: Calculation of the recoil electron spectrum

The elastic scattering is simulated based on the theoretical expectation. The cross section of the elastic scattering is described as,

$$\frac{d\sigma}{dT_e} = \frac{G_F^2 m_e}{2\pi} \left[ A_0 + B_0 \left( 1 - \frac{T_e}{E_\nu} \right)^2 + C_0 \frac{m_e T_e}{E_\nu^2} \right]. \quad (9.2.1)$$

The parameters used in this formula are:

1.  $G_F$  : Fermi coupling constant.
2.  $m_e$  : The electron mass.
3.  $E_\nu$  : The energy of the incident neutrino.

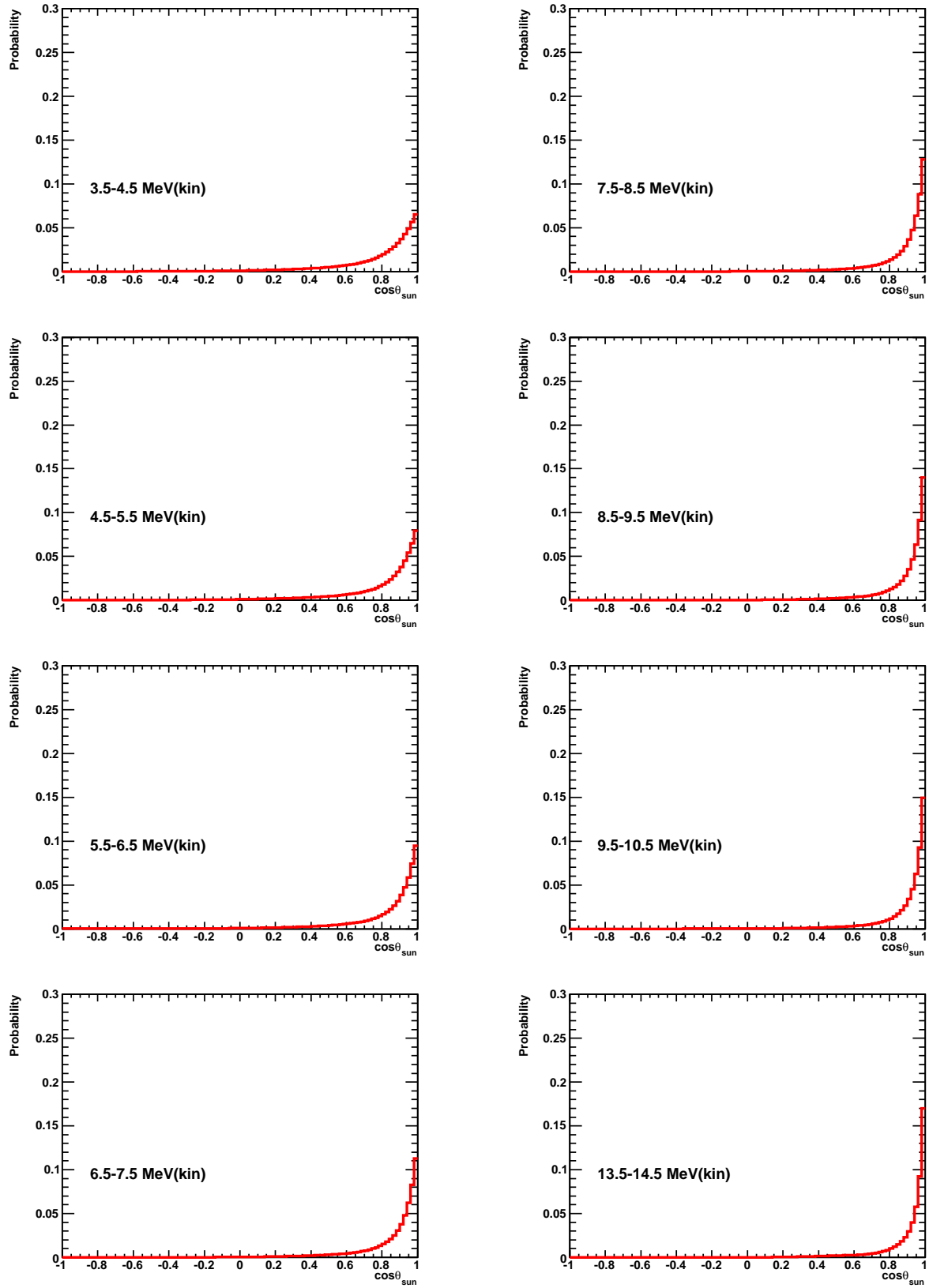


Figure 9.1: The distribution of the probability density function of the signal  $s_{ij}$ .

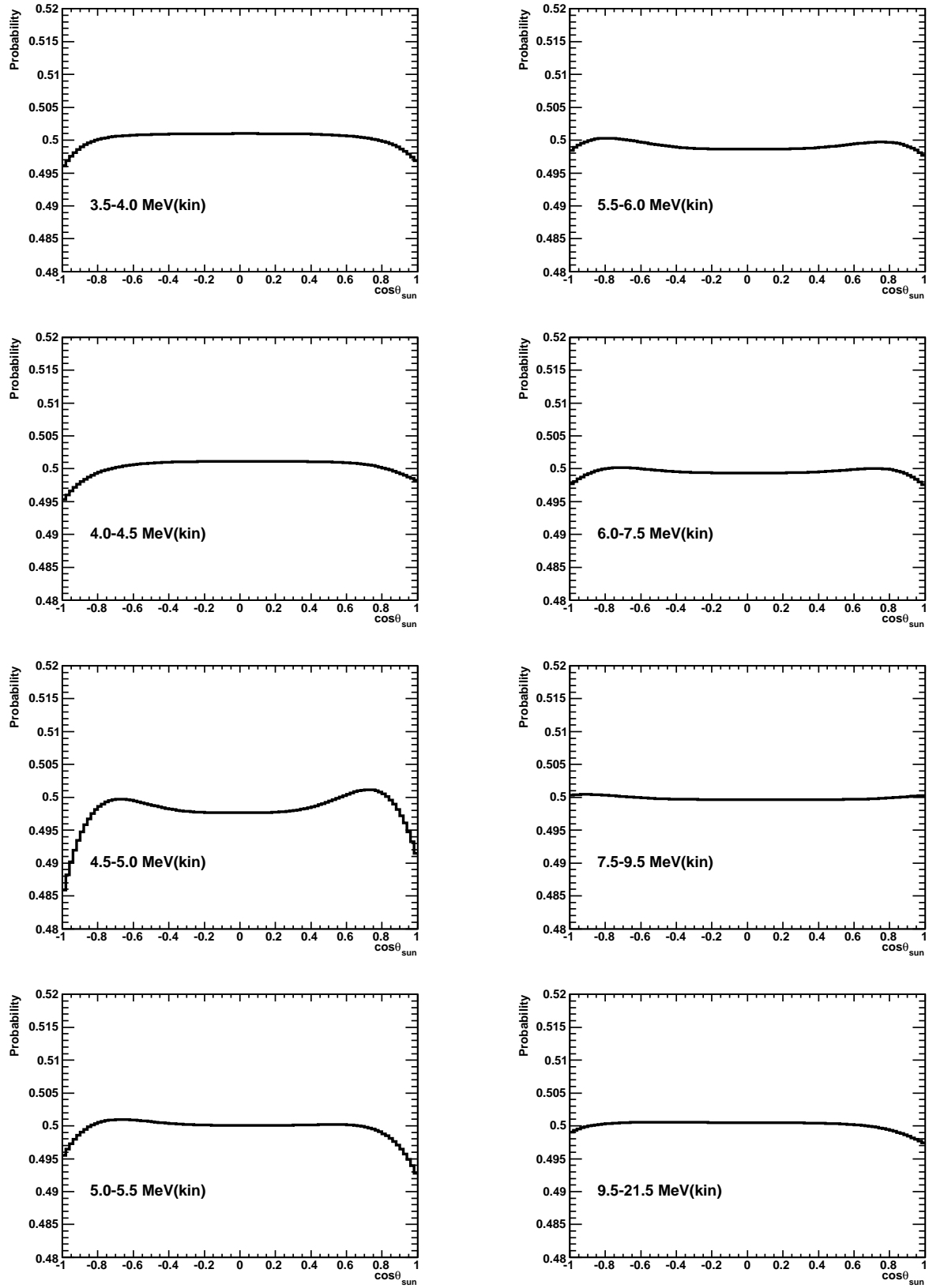


Figure 9.2: The distribution of the probability density function of the background shape  $b_{ij}$ .

4.  $T_e$  : The kinetic energy of the recoil electron. Based on the kinematics, it is described as

$$T_e = \frac{(1 - \cos \theta)E_\nu/m_e}{1 + (1 - \cos \theta)E_\nu/m_e} E_\nu \quad (9.2.2)$$

where  $\theta$  indicates the angle between the direction of the recoil electron and the direction of the incident neutrino<sup>1</sup>. When the  $\theta = \pi$ , the kinetic energy of the recoil electron becomes maximum

$$T_{e,\max} = \frac{E_\nu}{1 + (m_e/2E_\nu)}.$$

5.  $A_0, B_0, C_0$  : These parameters depend on the reaction type of elastic scattering and are represented using alternative parameters of  $g_v = I^3 - 2Q \sin^2 \theta_W$  and  $g_A = I^3$ , where  $I^3$  is the third component of weak isospin of the target particle,  $Q$  is the charge of the target particle and  $\theta_W$  is the Weinberg angle. In the case of electron,  $I^3 = -1/2$ ,  $Q = -1$ ,  $g_v \sim -0.04$  and  $g_A = -1/2$ . Table 9.1 summarizes the parameters  $A_0$ ,  $B_0$  and  $C_0$  for the elastic scattering between a  $\nu_{e,\mu(\tau)}$  and an electron.

Table 9.1: The parameters used in equation (9.2.1).

Reaction	$A_0$	$B_0$	$C_0$
$\nu_e + e^- \rightarrow \nu_e + e^-$	$(g_V + g_A + 2)^2$	$(g_V - g_A)^2$	$-(g_V + 1)^2 + (g_A + 1)^2$
$\bar{\nu}_e + e^- \rightarrow \bar{\nu}_e + e^-$	$(g_V - g_A)^2$	$(g_V + g_A + 2)^2$	$-(g_V + 1)^2 + (g_A + 1)^2$
$\nu_{\mu(\tau)} + e^- \rightarrow \nu_{\mu(\tau)} + e^-$	$(g_V + g_A)^2$	$(g_V - g_A)^2$	$g_A^2 - g_V^2$
$\bar{\nu}_{\mu(\tau)} + e^- \rightarrow \bar{\nu}_{\mu(\tau)} + e^-$	$(g_V - g_A)^2$	$(g_V + g_A)^2$	$g_A^2 - g_V^2$

The left of Figure 9.3 shows the differential cross section of the elastic scattering in the case of incident 11 MeV neutrino and an electron. The total cross section is also obtained by integrating equation (9.2.1) and it is shown in the right of Figure 9.3.

The recoil electron energy distribution is determined as follows:

$$F(T_e)dT_e = \left( \int_0^{E_{\nu,\max}} \frac{d\sigma_{\nu-e}(E_\nu, T_e)}{dT_e} \Phi(E_\nu) dE_\nu \right) dT_e, \quad (9.2.4)$$

where  $\Phi(E_\nu)$  is the solar neutrino flux as a function of neutrino energy. The solar neutrino flux  $\Phi(E_\nu)$  depends on the neutrino energy spectrum shape of  ${}^8\text{B}$  decay. In the solar neutrino analysis of SK-IV, the spectral shape of  ${}^8\text{B}$  neutrinos is taken from the result of the  $\alpha$ -spectrum measurement of  ${}^8\text{B}$  ( ${}^8\text{B} \rightarrow {}^8\text{Be}^* + e^+ + \nu_e$  and  ${}^8\text{Be}^* \rightarrow 2\alpha$ ) by Winter *et al.* [115], which is shown in Figure 9.4.

<sup>1</sup> The angle between the incident neutrino and the recoil electron is determined using the equation (9.2.2)

$$\cos \theta = \frac{1 + (m_e/E_\nu)}{\sqrt{1 + (2m_e/E_\nu)}}. \quad (9.2.3)$$

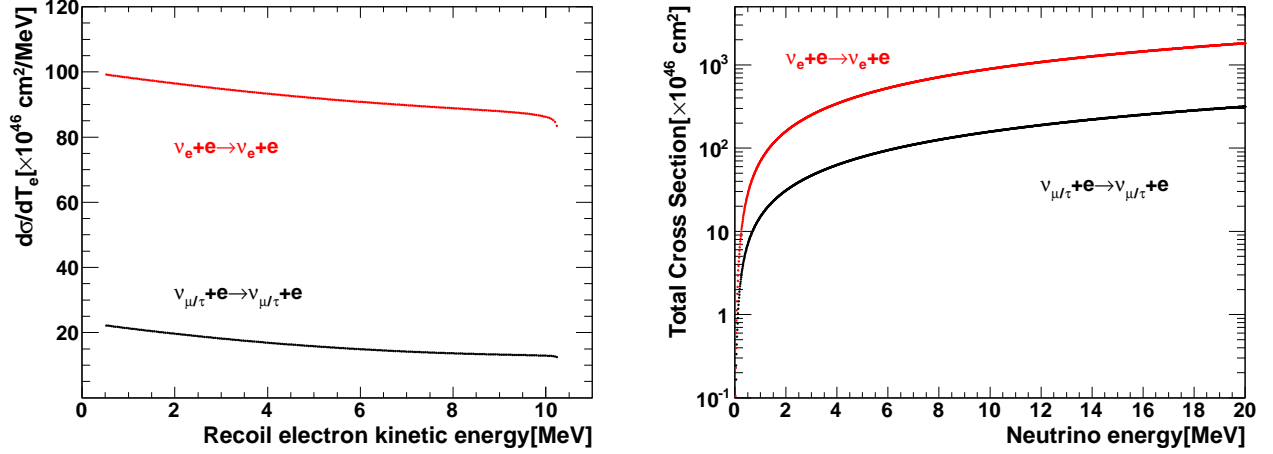


Figure 9.3: Left: The differential cross section when the energy of the incident neutrino is 11 MeV. Right: The total cross section as a function of the kinetic energy of the incident neutrino.

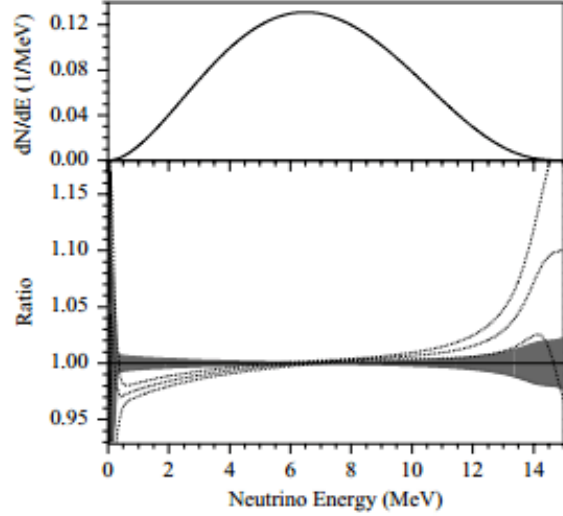


Figure 9.4: The top panel shows the  $^8\text{B}$  neutrino energy spectrum from [115]. The bottom panel shows the ratio between the Winter spectrum [115] and the Oriz spectrum [116]. The gray band shows the  $1\sigma$  experimental uncertainty.

The angular distribution of the recoil electron is described as follows:

$$F(\theta)d\theta = \left( \int_0^{E_\nu, \max} \Phi(E_\nu) \frac{d\sigma}{dT_e} \frac{dT_e}{d\theta} dE_\nu \right) d\theta. \quad (9.2.5)$$

Figure 9.5 shows the calculated angular distribution of solar neutrinos. According to Figure 9.5, the scattered angle is less than  $25^\circ$  if the recoil electron energy is above 3.5 MeV in kinetic. Since  $\cos(25^\circ) = 0.91$ , solar neutrino signals are mostly in the first 4 bins in the solar angle ( $\cos\theta_{\text{sun}}$ ) distribution of Figure 8.1.

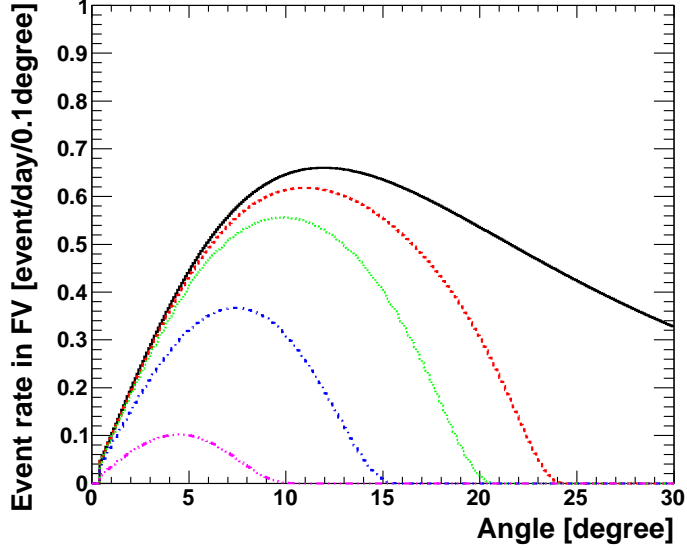


Figure 9.5: The angular distribution of recoil electrons from incident solar neutrinos. The horizontal axis shows the angle of recoil electrons from incident solar neutrinos and the vertical axis shows the event rate in the fiducial volume (22.45 kton). The red, green blue and purple lines illustrate the event rate above 3.5, 4.5, 6.5 and 9.5 MeV, respectively. The black line means the event rate integrated over the full  ${}^8\text{B}$  and *hep* SSM spectrum [45].

### 9.2.2 Step 2 and Step 3: Detector Simulation and the comparison

The solar neutrino MC simulation is carried out in order to take into account the detector response. In the simulation, recoil electrons are uniformly generated in the photosensitive volume (32 ktons) in the detector.

The energy and the scattering angle of the solar neutrino MC event are determined by equation (9.2.1) and equation (9.2.5). Simulation events are generated taking into account the direction with respect to the Sun, in which the detector operation time is precisely reflected. The same methods as in the real data analysis are used to reconstruct the vertex, direction and energy of the generated solar neutrino events.

Then, the all data reduction steps are applied to the MC simulation events and finally the MC simulation events are obtained. Based on this simulation events, the expected fractions  $Y_i$  are obtained. Figure 9.6 shows the expected energy distribution of the MC simulation events.

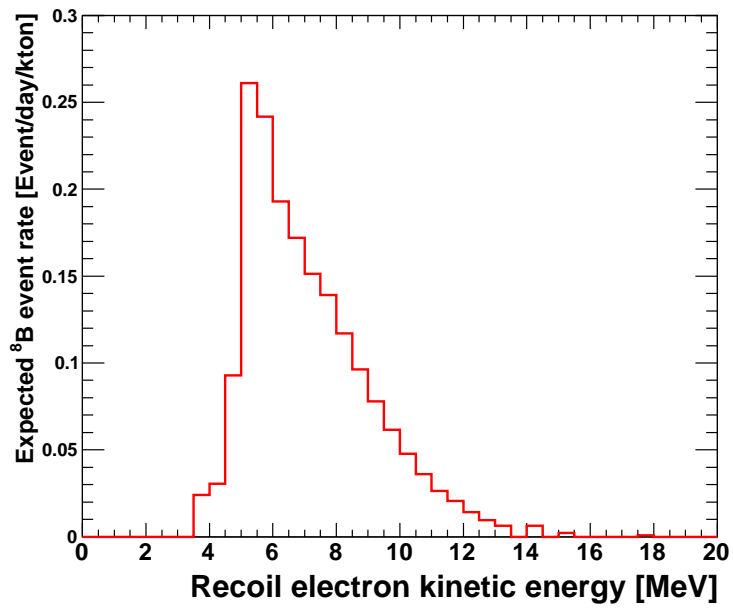


Figure 9.6: The expected  $^8\text{B}$  energy spectrum using the MC simulation. The  $^8\text{B}$  flux from the SNO result [70] and Winter spectrum [115] are used. Since the tight fiducial volume cut applied to the data between 3.5 MeV and 5.0 MeV, the expected event rates between 3.5 MeV and 5.0 MeV are smaller compared with those above 5.0 MeV.

# Chapter 10

## Systematic uncertainty

### 10.1 Systematic uncertainty on the total flux

#### 10.1.1 Energy scale

The systematic uncertainty for the total flux due to the energy scale is estimated by taking into account the systematic uncertainty in the absolute energy scale. Since the systematic uncertainty of the absolute energy scale is estimated to be  $\pm 0.54\%$  as described in subsection 5.3.3, the energy of the MC simulated events is shifted by  $\pm 0.54\%$ . After the shift, new signal fractions  $Y_i^{+\text{scale}}$  and  $Y_i^{-\text{scale}}$  are obtained. Using the shifted signal fractions, the extracted total number of events is changed by  $+1.2\%/ - 1.1\%$ . So, this change is assigned to the systematic uncertainty due to the absolute energy scale.

#### 10.1.2 Energy resolution

The systematic uncertainty due to the energy resolution is estimated using the difference between the LINAC calibration data and its MC simulated data.

#### Detector performance function

A detector performance function  $R(E_e, E_{\text{obs}})$  is defined as:

$$R(E_e, E_{\text{obs}}) = \frac{1}{\sqrt{2\pi}\sigma(E_e)} \exp\left(-\frac{(E_e - E_{\text{obs}})^2}{\sigma(E_e)^2}\right), \quad (10.1.1)$$

where  $E_e$  is the total energy of the recoil electron and  $E_{\text{obs}}$  is the observed energy. To evaluate  $R(E_e, E_{\text{obs}})$ , several MC simulations which generate mono-energetic single electrons are prepared. The top panel of Figure 10.1 illustrates their energy distributions. Fitted by a Gaussian function, their energy resolution is evaluated by calculating  $\Delta\sigma = \sigma(E_e)/E_{\text{obs}}$ , as shown in the bottom panel of Figure 10.1. The energy dependence of the energy resolution is evaluated by fitting to a polynomial function, and the energy resolution as a function of the recoil electron energy is obtained as

$$\sigma(E_e) = \frac{1}{E_e} \left( -0.084 + 0.349\sqrt{E_e} + 0.040E_e \right). \quad (10.1.2)$$

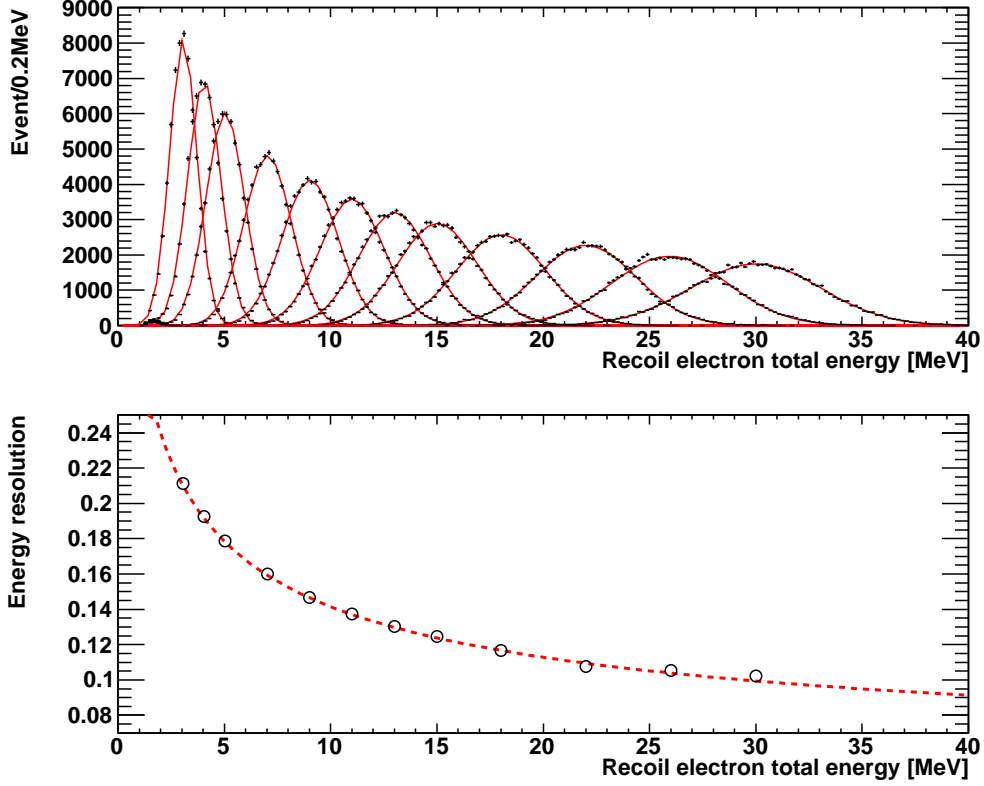


Figure 10.1: The top figure shows the energy distributions of electrons generated by the mono-energetic MC simulations. The black points show the results of the simulation and the red curves show the Gaussian fitting. The lower figure shows the energy resolution as a function of electron total energy. The open circles show the resolution obtained by the Gaussian fitting. The red dotted curve shows a polynomial function fit to the points.

### Energy resolution from the LINAC calibration

Based on the above method, the energy resolution  $\sigma_{\text{LINAC,data(MC)}}$  is obtained using the LINAC calibration data and the MC simulation. The energy distribution (for example, Figure 5.16) is fitted by a Gaussian function and its peak position and standard deviation are checked. The difference between the data and the MC simulation ( $\Delta\sigma_{\text{LINAC}}$ ) is evaluated as below and they are shown in Figure 10.2.

$$\Delta\sigma_{\text{LINAC}} = \begin{cases} 1.00\% & (E < 4.89 \text{ MeV}), \\ 0.60\% & (E > 6.81 \text{ MeV}), \\ \text{interpolation} & (4.89 \text{ MeV} \leq E \leq 6.81 \text{ MeV}). \end{cases} \quad (10.1.3)$$

### Evaluation method

The predicted recoil electron energy spectrum is obtained using equation (9.2.4). The systematic uncertainty in the energy resolution is evaluated taking into account the energy spectrum shape

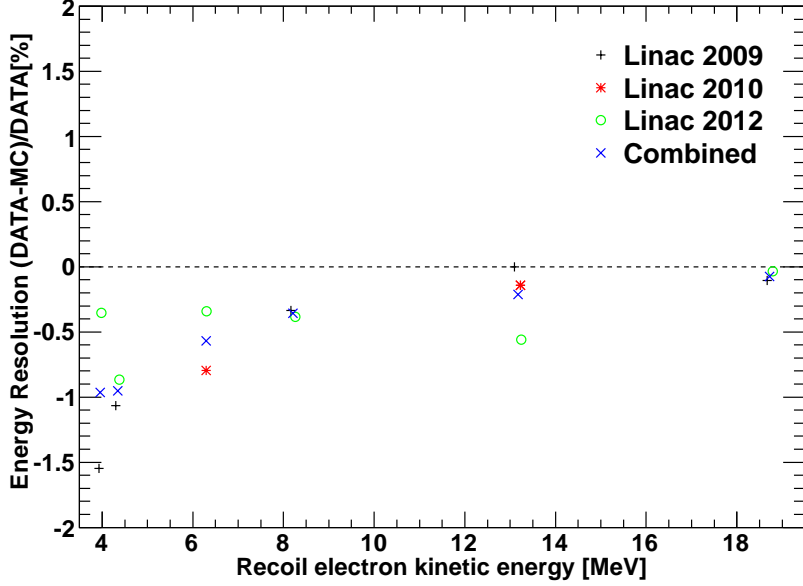


Figure 10.2: The systematic error of energy resolution.

of solar neutrinos. In order to estimate the systematic uncertainty,  $F_{\text{sys}}$  is introduced as

$$F_{\text{sys}}(E_{\text{obs}}) = \int_0^{E_{\text{max}}} F(E_e)R(E_e, E_{\text{obs}})dE_e, \quad (10.1.4)$$

where  $F(E_e)$  is the recoil electron energy spectrum.

In order to be taken into account in the systematic uncertainty, the parameter  $\sigma(E_e)$  in equation (10.1.4) is replaced by  $\sigma^\pm = \sigma(E_e)(1 \pm \Delta\sigma_{\text{LINAC}})$ . Then, the shifted expected spectra  $F_{\text{sys}}^\pm(E_{\text{obs}})$  are obtained. The top-left of Figure 10.3 shows the original expected energy spectrum  $F$  and the shifted energy spectra  $F_{\text{sys}}^\pm$ .

The ratio between the shifted spectra and the original spectrum are evaluated as shown in the top-right of Figure 10.3 and this ratio is used as weighting function for the signal fraction  $Y_i$  in equation (12.3.14). Finally, shifted signal fractions  $Y_i^{E_{\text{res}}^\pm}$  are obtained. The  $^8\text{B}$  solar neutrino flux is calculated using the shifted signal fractions, and the obtained fluxes are changed by  $\pm 0.1\%$  from the original. So, this difference is the estimated systematic uncertainty due to energy resolution.

### 10.1.3 $^8\text{B}$ spectrum

The uncertainty in the shape of the  $^8\text{B}$  solar neutrino spectrum is estimated including both experimental and theoretical uncertainties [109]. To estimate the effect for the extraction of the total solar neutrino flux, the original solar neutrino spectrum  $\Phi(E_\nu)$ , which is used to produce the MC simulation events is distorted according to the uncertainty of  $^8\text{B}$  spectrum shape. Thus, the expected recoil electron spectrum is shifted from  $F(E_{\text{obs}})$  to  $F_{\text{sys}}^{\pm 8\text{B}}(E_{\text{obs}})$ . These new expected recoil electron spectra are shown in the bottom-left of Figure 10.3. The difference between the

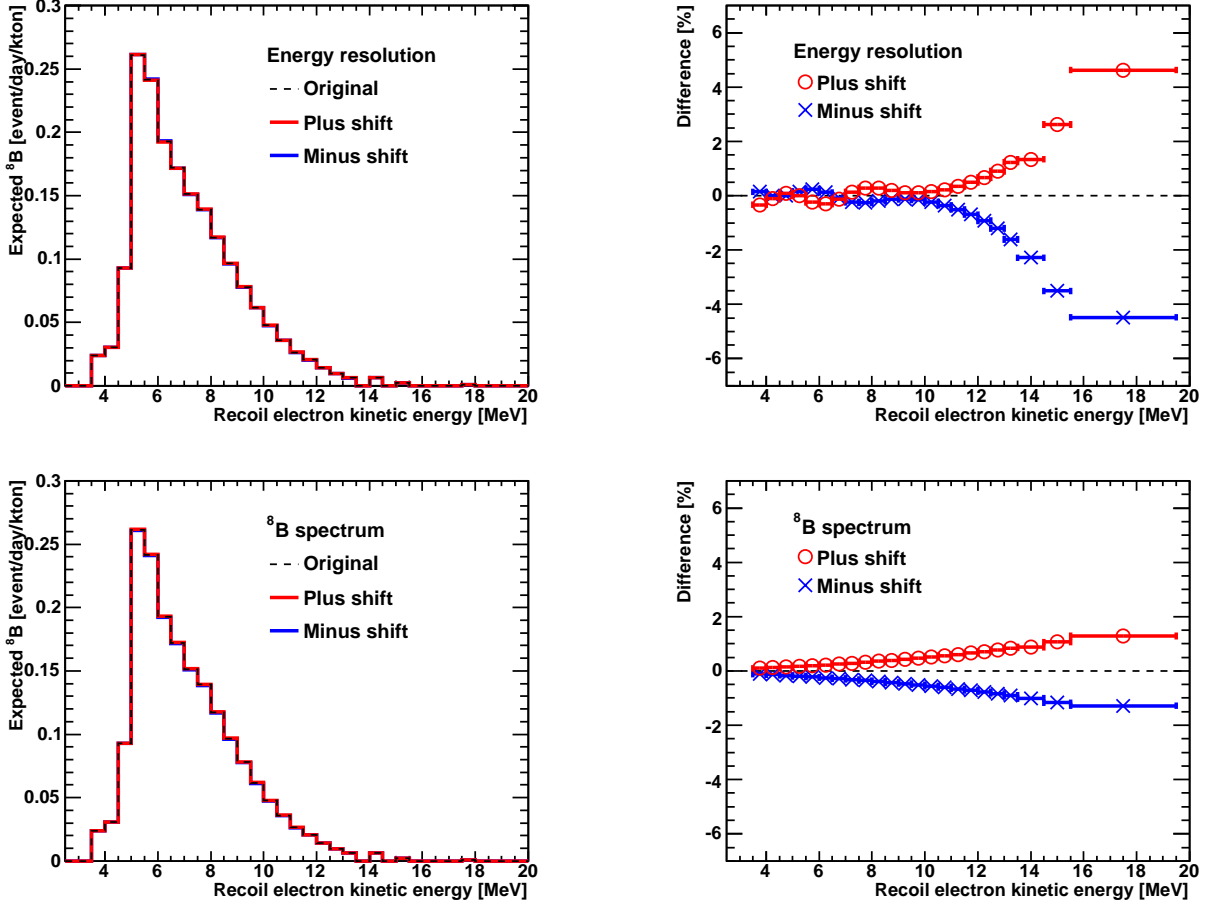


Figure 10.3: Left: The expected recoil electron energy spectrum when shifted the energy resolution ( $^8\text{B}$  spectrum) in top (bottom) panel. The trigger efficiency and reduction efficiency are taken into account in the spectra. Right: The difference between the shifted energy spectra and the original energy spectrum.

original  $F$  and the shifted  $F_{\text{sys}}^{\pm^8\text{B}}$  are shown in the bottom-right of Figure 10.3. They are used to produce the shifted signal fractions  $Y_i^{\pm^8\text{B}}$  in each energy bin, which is used instead of the original  $Y_i$  in the extended likelihood function. By doing so, the systematic uncertainty is estimated to be  $+0.4\% / -0.3\%$ .

### 10.1.4 Background shape

The predicted background shapes  $b_{ij}$  are generated using the detector zenith and azimuthal ( $\phi$ ) angle polynomial fits to the data sample after all solar neutrino reduction cuts. Since the directional dependence is caused by the structure of the detector and possible non-uniform angular distribution of the background, the background shape is not flat as shown in Figure 9.2. In order to evaluate the systematic uncertainty in the background shape, the  $\phi$  distribution is forced to be fit by a flat shape, while still taking into account non-flat zenith angle distribution.

These new background shapes are used to extract the total flux and the resultant systematic uncertainty is estimated to be  $\pm 0.1\%$ .

### 10.1.5 Signal extraction method

The systematic uncertainty in the signal extraction is estimated using a dummy data whose signal and background events are known. After applying the extraction method to the dummy data, the extracted number of events and the true number of events are compared. The difference between them is taken as the uncertainty on the total flux and it is  $\pm 0.7\%$ .

### 10.1.6 Cross section

The uncertainty in the solar neutrino interaction cross section was estimated by J. N. Bahcall *et al.* in 1995 [117]. When masses of the top quark and the higgs particle were measured in 1995, their mass had large uncertainties.

Furthermore, an one loop QCD process also had large uncertainty at that time. Taking into account these uncertainties before 1995, a  $1\sigma$  theoretical uncertainty in the radiative corrections parameters for  $\nu_e - e$  elastic scattering is estimated.

When these radioactive correction parameters are shifted by  $\pm 1\sigma$ , the expected recoil electron spectrum. Using these shifted expected spectra. Then the signal extraction process is performed and the total flux is compared with the original one. Thus, the obtained systematic uncertainty from the cross section is  $\pm 0.5\%$ .

### 10.1.7 Angular resolution

The uncertainty in the angular resolution is evaluated using the LINAC calibration data and its MC simulation. The estimation is done by the following steps:

1. The LINAC beam events are selected by checking the reconstructed direction in  $z$ -axis and the vertex position. The downward events whose vertex position is within 200 cm from the beam injection position are selected.
2. Select events whose energy is between 3.5 MeV and 19.5 MeV.
3. The event quality cut and the external cut are applied to the events, and then count the number of events.
4. Sort the angle between the beam injection direction and the reconstructed direction according to the left of Figure 10.4.
5. Obtain the value of the angle,  $\theta_{\text{diff}}$ , which includes 68% of the selected events.

After getting the value of the angle  $\theta_{\text{diff}}$ , the difference between the LINAC calibration data and the MC simulation is evaluated, as shown in the right of Figure 10.4.

Using the result of the above analysis, the signal shapes  $s_{ij}^{\pm\text{ang}}$  are newly created by shifting the reconstructed direction of the MC simulated solar neutrino event. Then the new signal shapes are used to extract the total flux, and the systematic uncertainty is estimated to be  $+0.2\% / -0.1\%$ .

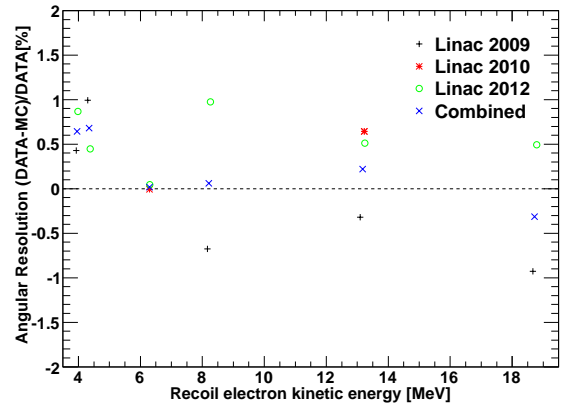
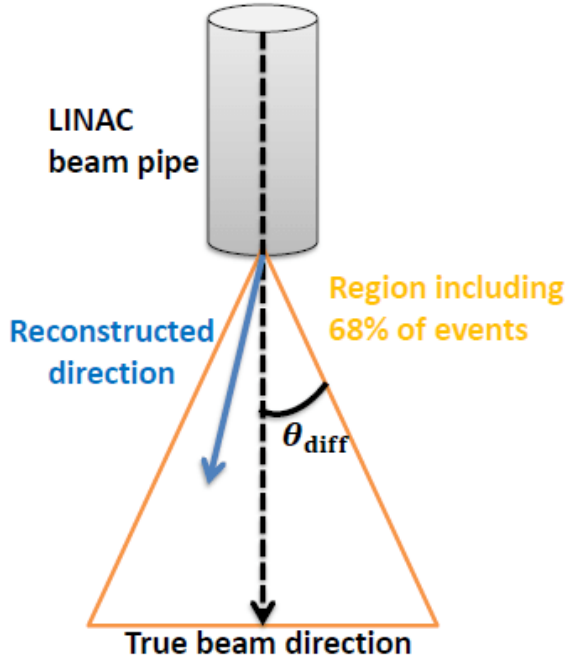


Figure 10.4: Left: The schematic view of the definition of the region including 68% of the LINAC events. Right: The systematic uncertainty in the angular resolution.

### 10.1.8 Vertex shift

Since the quality of the vertex reconstruction for the event occurring near the edge of the fiducial volume is crucial for defining the size of the fiducial volume, the vertex resolution contributes to the systematic error for extracting the solar neutrino signal. To evaluate the systematic error of the vertex reconstruction, the following steps are made.

1. Using the Ni calibration data, the position dependence of the vertex shift is evaluated. It is the difference between the mean values of the reconstructed vertex and the real Ni calibration ball position, as shown in the left of Figure 10.5.
2. Based on the result of vertex shift, the vertex position of the MC simulated solar neutrino event is artificially shifted as follows: (1) If the reconstructed  $z$ -vertex is more than 0 cm (less than 0 cm), the vertex position is shifted by +0.7 cm (-2.7 cm). (2) The radius ( $r^2 = x^2 + y^2$ ) is increased by +1.78 cm<sup>2</sup>.
3. Apply all solar neutrino reduction cuts to the simulated event except for the vertex cut.
4. The (tight) fiducial volume cut is applied to the event and count the number of the surviving events before and after the shift.

The left of Figure 10.5 shows the difference of the selection efficiencies before and the after the artificial shift. The large uncertainties below 5.0 MeV are caused by the tight fiducial volume cut.

The number of selected events is compared between before and after the artificial shift and then the systematic uncertainty in the vertex cut is estimated to be  $\pm 0.2\%$ .

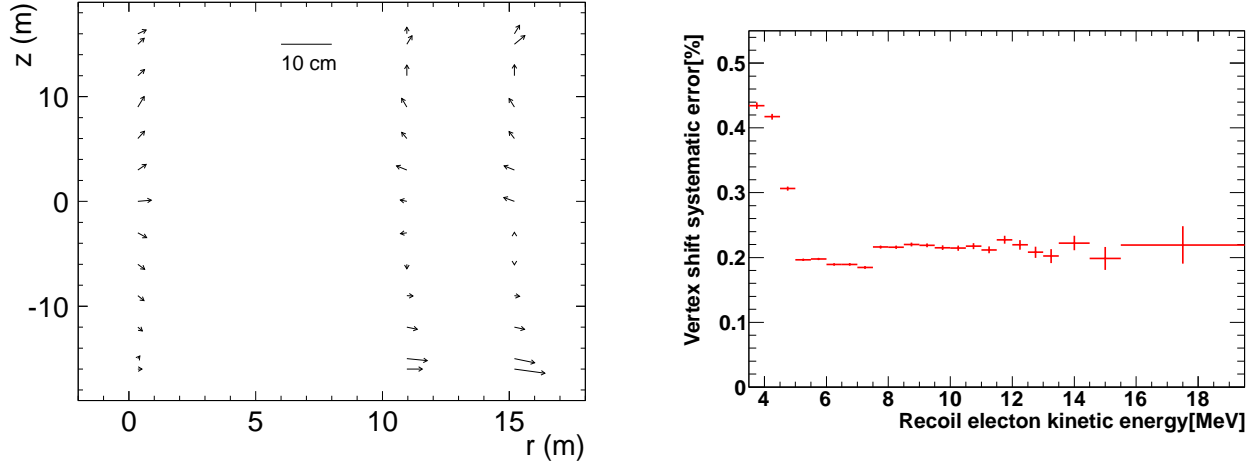


Figure 10.5: Left: The vertex shift based on the Ni calibration. The start of the arrow gives the true Ni source position and the direction indicates the averaged vertex shift at the given position. The length of the arrow indicates the magnitude of the vertex shift. To make the vertex shifts easier to see, the length is scaled by a factor of 20. Right: The systematic uncertainty in the vertex cut.

### 10.1.9 Event quality cut

The uncertainty in the event quality cut is estimated using the LINAC calibration data and MC simulation of LINAC. The estimation is done by the following steps:

1. The LINAC beam events are selected by checking the reconstructed direction and vertex position. The downward events whose vertex position is within 200 cm from the beam injection position are selected.
2. Select events whose energy range is between 3.5 MeV and 19.5 MeV.
3. Count the number of the surviving events.
4. Count the number of events which do not pass the tight event quality cut, i.e.  $g_V^2 - g_A^2 < 0.25$  as described in subsection 6.2.4.

Since the events which does not pass the tight event quality cut are rejected in the solar neutrino reduction steps as described in subsection 6.3.8, the rejected events are used to calculate the inefficiency of the event quality cut. Finally, the systematic uncertainty in the event quality cut is estimated by comparing the inefficiency of the LINAC calibration data and the MC simulation. Figure 10.6 shows the systematic uncertainty in the event quality cut as a function of energy. In the lower energy region, the systematic uncertainty is larger because of the larger uncertainty in the vertex shift. As a result, the uncertainty in the total flux is estimated to be  $\pm 0.1\%$ .

### 10.1.10 Hit pattern cut

The systematic uncertainty is estimated with the same method as used in the event quality cut. The inefficiency of the hit pattern cut is calculated using the LINAC calibration data and its

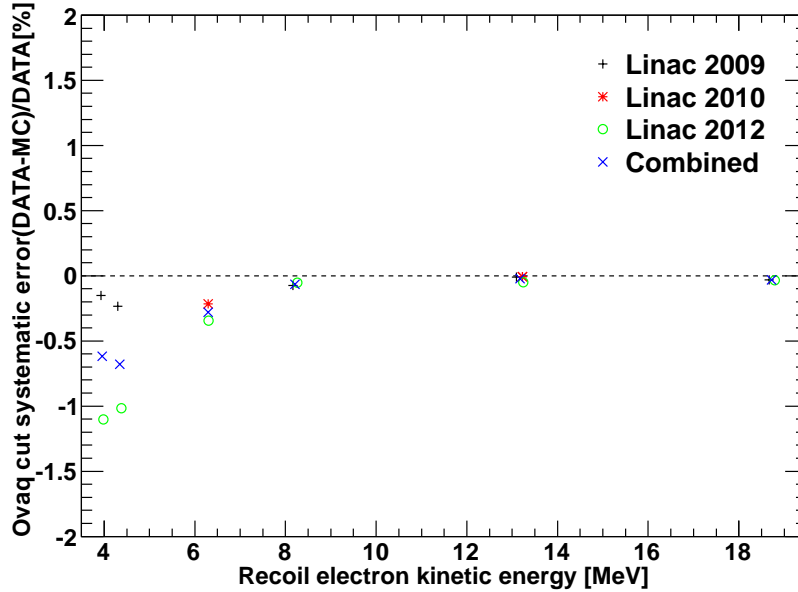


Figure 10.6: The systematic error in the event quality cut.

MC simulation. As mentioned in subsection 6.3.10, this cut is applied to the events with their energy more than 6.0 MeV.

1. The LINAC beam events are selected by checking the reconstructed direction and the vertex position. The downward events whose vertex position is within 200 cm from the beam injection position are selected.
2. Select events whose energy range is between 6.0 MeV and 19.5 MeV.
3. Count the number of the surviving events.
4. Apply the hit pattern cut to the events and then count the rejected events.
5. The inefficiency of the hit pattern cut is evaluated.

Finally, the systematic uncertainty in the hit pattern cut is estimated by comparing the inefficiencies between the calibration data and the MC simulation. Figure 10.7 shows the systematic uncertainty in the hit pattern cut. As a result, the uncertainty in the total flux is estimated to be  $\pm 0.5\%$ .

### 10.1.11 Spallation cut

As already mentioned in subsection 6.3.9, since the dead time caused by the spallation cut is taken into account in the calculation of the expected number of solar neutrino events, the difference in dead time between the random data sample and the MC simulated events is used to estimate the systematic uncertainty in the spallation cut. The dead time depends on the

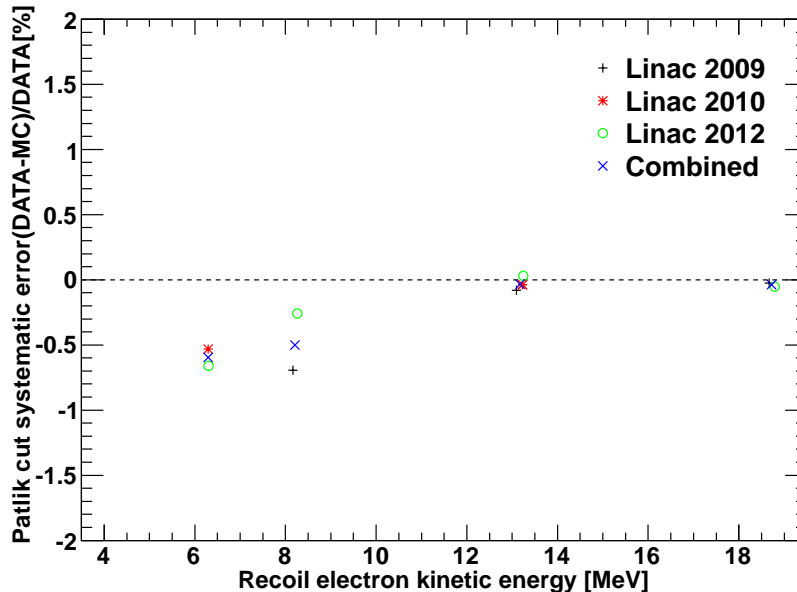


Figure 10.7: The systematic error in the hit pattern cut.

position, as shown in Figure 6.12, because of muon energy, arrival time, direction and so on. According to the right of Figure 6.13, the dead time is stable within 0.3% level during the entire period of SK-IV. Considering this dead time, the systematic uncertainty in the total flux is estimated to be  $\pm 0.2\%$ .

### 10.1.12 External cut

The external cut depends on the vertex position and the reconstructed direction, because the parameter  $d_{\text{eff}}$  is calculated using the information on both the vertex position and direction. In order to estimate the uncertainty in the external cut, the reconstructed vertex and direction are artificially shifted according to the left of Figure 10.8 in the solar neutrino MC simulation. The number of observed events is counted before and after the artificial shift, then the selection efficiency is evaluated. The right of Figure 10.8 shows the difference in selection efficiency before and after the artificial shift in each energy bin. The larger uncertainty below 7.5 MeV is caused by the difference in the cut criteria of the external cut as mentioned in subsection 6.3.12.

The number of selected events are compared between before and after the artificial shift and then the systematic uncertainty of the external cut is estimated to be  $\pm 0.1\%$ .

### 10.1.13 Small hit cluster cut

The systematic uncertainty in the small hit cluster cut is estimated using the DT calibration data and its MC simulation. Since the small hit cluster cut is applied to the events occurring near the wall, the DT calibration is used instead of the LINAC calibration. Using the DT calibration data taken near the wall, an event sample after the external cut is prepared and then the efficiency of the small hit cluster cut is evaluated. Finally, the difference in efficiency

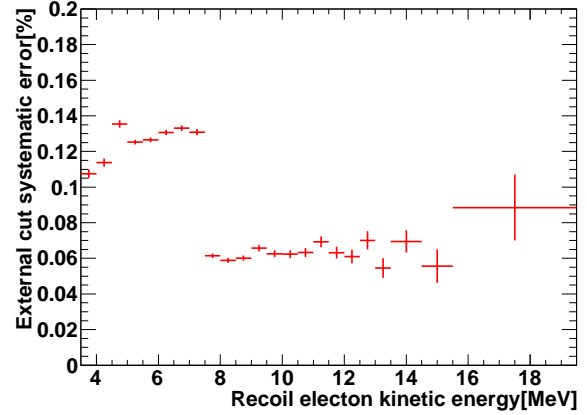
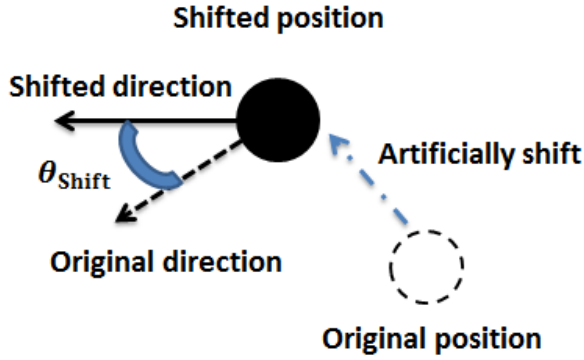


Figure 10.8: Left: Artificially shift of the reconstructed vertex. Right: The systematic uncertainty in the external cut.

between the DT calibration data and the MC simulation is obtained. The systematic uncertainty in the total flux is estimated to be  $\pm 0.4\%$ .

### 10.1.14 Trigger efficiency

The trigger efficiency depends on various things, such as the vertex position, water transparency, the number of the hit PMTs and so on. In order to evaluate the systematic uncertainty in the trigger efficiency, the Ni calibration is used. The detail of the evaluation is described in Chapter 7. The systematic uncertainty on the total flux is estimated to be  $\pm 0.1\%$ .

## 10.2 Summary of systematic uncertainties

Table 10.1 shows the systematic uncertainties in the total flux. Adding these uncertainties in quadrature, the combined systematic uncertainty is calculated to be  $\pm 1.7\%$ .

## 10.3 Spectrum systematic uncertainty

The systematic uncertainty in the spectrum shape is caused by two parts; One is the energy correlated and the other is the energy uncorrelated uncertainty.

### 10.3.1 Energy correlated uncertainty

The energy scale, the energy resolution and the  $^8\text{B}$  solar neutrino spectrum shape cause the energy correlated systematic uncertainty. In order to estimate their uncertainties, their values or parameters are artificially shifted individually using equation (10.1.4). Figure 10.9 shows the results on the energy correlated systematic uncertainty. The largest energy correlated systematic uncertainty is caused by the energy scale.

Table 10.1: The summary of the systematic uncertainties in the total flux in each SK phase.

Phase	SK-I	SK-II	SK-III	SK-IV
Threshold in MeV kinetic	4.5	6.5	4.0	3.5
Trigger efficiency	$\pm 0.4\%$	$\pm 0.5\%$	$\pm 0.5\%$	$\pm 0.1\%$
Angular resolution	$\pm 1.2\%$	$\pm 3.0\%$	$\pm 0.7\%$	$+0.2\%/ -0.1\%$
Event quality	$\pm 1.0\%$	$\pm 3.0\%$	$\pm 0.4\%$	$\pm 0.1\%$
Hit pattern	$\pm 0.8\%$	–	$\pm 0.3\%$	$\pm 0.5\%$
Small Hit cluster	–	–	$\pm 0.5\%$	$\pm 0.4\%$
External Event	$\pm 0.5\%$	$\pm 1.0\%$	$\pm 0.3\%$	$\pm 0.1\%$
Vertex Shift	$\pm 1.3\%$	$\pm 1.1\%$	$\pm 0.5\%$	$\pm 0.2\%$
Second vertex fit	$\pm 1.3\%$	$\pm 1.1\%$	$\pm 0.5\%$	–
Spallation cut	$\pm 0.2\%$	$\pm 0.4\%$	$\pm 0.2\%$	$\pm 0.2\%$
Background shape	$\pm 0.1\%$	$\pm 0.4\%$	$\pm 0.1\%$	$\pm 0.1\%$
Signal extraction	$\pm 0.7\%$	$\pm 0.7\%$	$\pm 0.7\%$	$\pm 0.7\%$
Cross section	$\pm 0.5\%$	$\pm 0.5\%$	$\pm 0.5\%$	$\pm 0.5\%$
Livetime	$\pm 0.1\%$	$\pm 0.1\%$	$\pm 0.1\%$	$\pm 0.1\%$
Energy scale	$+1.7\%/ -1.6\%$	$+4.2\%/ -3.9\%$	$\pm 1.2\%$	$+1.2\%/ -1.1\%$
Energy resolution	$\pm 0.3\%$	$\pm 0.3\%$	$\pm 0.2\%$	$\pm 0.1\%$
$^8\text{B}$ spectrum	$+1.1\%/ -1.0\%$	$\pm 1.9\%$	$\pm 0.4\%$	$+0.4\%/ -0.3\%$
Total	$+3.5\%/ -3.2\%$	$+6.7\%/ -6.4\%$	$\pm 2.2\%$	$\pm 1.7\%$

### 10.3.2 Energy uncorrelated uncertainty

#### Reduction

The energy uncorrelated uncertainties caused by the reduction cuts are estimated by the same method described in section 10.1. The estimated systematic uncertainties are summarized in Table 10.2. The full energy range is divided into 8 ranges, 7 bins with 0.5 MeV width and the last bin from 7.5 to 19.5 MeV, as shown in Table 10.2.

Table 10.2: Energy uncorrelated systematic uncertainty in the spectrum shape.

Energy [MeV]	3.5 – 4.0	4.0 – 4.5	4.5 – 5.0	5.0 – 5.5	5.5 – 6.0	6.0 – 6.5	6.5 – 7.0	7.0 – 7.5	7.5 – 19.5
Trigger efficiency	$+3.6\%$ $-3.3\%$	$\pm 0.8\%$	–	–	–	–	–	–	–
Event quality	$\pm 0.6\%$	$+0.7\%$ $-0.6\%$	$+0.6\%$ $-0.5\%$	$\pm 0.4\%$	$\pm 0.2\%$	$\pm 0.1\%$	$\pm 0.1\%$	$\pm 0.1\%$	$\pm 0.1\%$
Hit pattern	–	–	–	–	–	$\pm 0.6\%$	$\pm 0.6\%$	$\pm 0.6\%$	$\pm 0.4\%$
External	$\pm 0.1\%$	$\pm 0.1\%$	$\pm 0.1\%$	$\pm 0.1\%$	$\pm 0.1\%$	$\pm 0.1\%$	$\pm 0.1\%$	$\pm 0.1\%$	$\pm 0.1\%$
Vertex shift	$\pm 0.4\%$	$\pm 0.4\%$	$\pm 0.2\%$	$\pm 0.2\%$	$\pm 0.2\%$	$\pm 0.2\%$	$\pm 0.2\%$	$\pm 0.2\%$	$\pm 0.2\%$
BG shape	$\pm 2.9\%$	$\pm 1.0\%$	$\pm 0.8\%$	$\pm 0.2\%$	$\pm 0.1\%$	$\pm 0.1\%$	$\pm 0.1\%$	$\pm 0.1\%$	$\pm 0.1\%$
Signal extraction	$\pm 2.1\%$	$\pm 2.1\%$	$\pm 2.1\%$	$\pm 0.7\%$	$\pm 0.7\%$	$\pm 0.7\%$	$\pm 0.7\%$	$\pm 0.7\%$	$\pm 0.7\%$
Cross section	$\pm 0.2\%$	$\pm 0.2\%$	$\pm 0.2\%$	$\pm 0.2\%$	$\pm 0.2\%$	$\pm 0.2\%$	$\pm 0.2\%$	$\pm 0.2\%$	$\pm 0.2\%$
MSG	$\pm 0.4\%$	$\pm 0.4\%$	$\pm 0.3\%$	$\pm 0.3\%$	$\pm 0.3\%$	$\pm 1.7\%$	$\pm 1.7\%$	$\pm 1.7\%$	–
Total	$+5.1\%$ $-4.9\%$	$\pm 2.6\%$	$+2.4\%$ $-2.3\%$	$\pm 0.9\%$	$\pm 0.9\%$	$\pm 2.0\%$	$+2.0\%$ $-1.9\%$	$\pm 1.9\%$	$+0.9\%$ $-0.8\%$

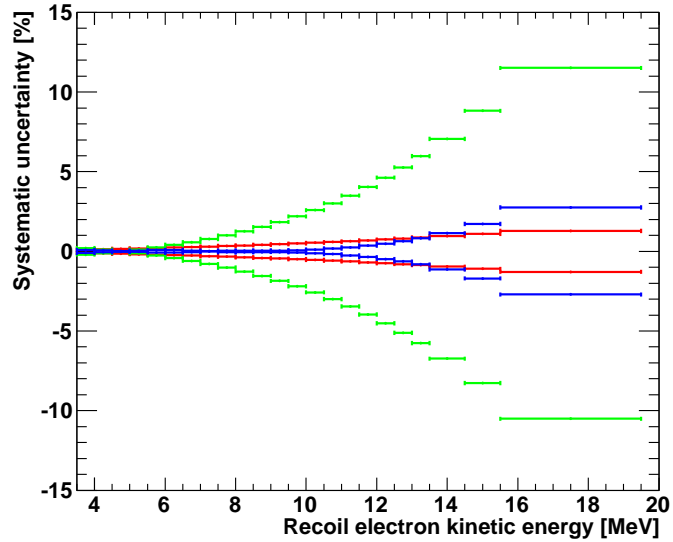


Figure 10.9: The energy correlated systematic uncertainties. The red, blue and green lines show the systematic uncertainties caused by the  $^8\text{B}$  solar neutrino shape, the energy resolution and the energy scale, respectively.

### Multiple scattering goodness

In order to estimate the systematic uncertainty caused by the multiple scattering goodness, the following method is employed:

1. The distributions of the MSG of LINAC calibration data and the MC simulated events are compared. Figure 10.10 shows the ratio of the data over the MC simulation. Scaling functions are obtained by fitting the distributions by a linear function.
2. The scaling functions are applied to the MC simulated events to obtain the distorted functions of signal shape  $s_{ij}$  and the fractions of signal events  $Y_i$  in equation (12.3.14).
3. The difference in the extracted number of events is taken as the systematic uncertainty as summarized in Table 10.2.

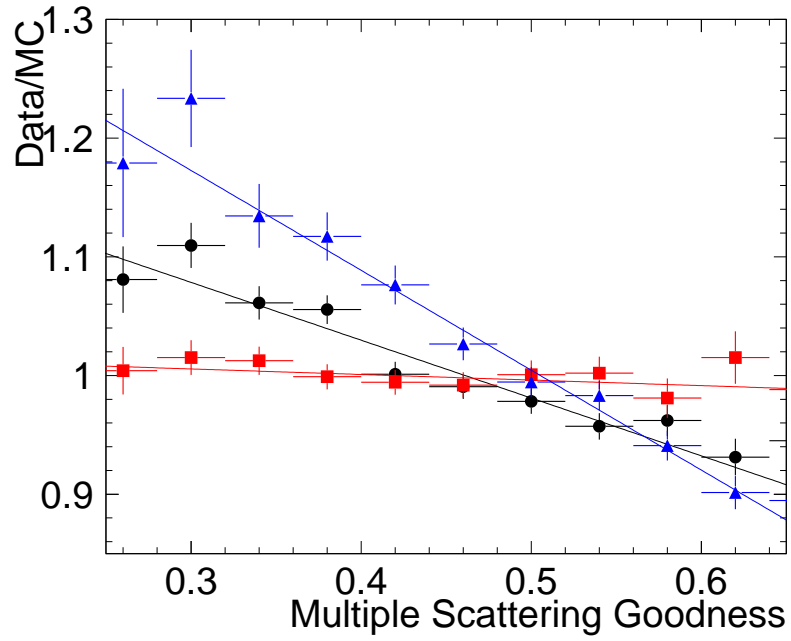


Figure 10.10: The MSG scaling function which is applied to the solar neutrino MC simulated events to estimate the systematic uncertainty in the energy spectrum [110]. The blue, black and red lines correspond to 15.8, 8.36 and 4.59 MeV. The points shows the difference between the LINAC calibration data and its MC simulation. The lines show the fitted results as a function of the MSG value.

# Chapter 11

## Solar neutrino analysis using SK-IV data

### 11.1 $^8\text{B}$ solar neutrino flux measurement

Using the 2055.5-day data in SK-IV, the  $^8\text{B}$  solar neutrino flux measurement is performed. Figure 11.1 shows the solar angle distribution for the data. The energy range is from 3.5 to 19.5 MeV in recoil electron kinetic energy. The extracted number of solar neutrino events is  $39,786_{-315}^{+317}(\text{stat.})_{-674}^{+695}(\text{syst.})$ .

In order to determine the  $^8\text{B}$  solar neutrino flux, the number of the expected signal events is calculated as

$$N_{\text{exp}} = \frac{N_{\text{MC, survival}}}{N_{\text{MC, generated}}} \times T_{\text{Live}} \times R_{\text{exp}} \quad (11.1.1)$$

where  $N_{\text{MC, generate}}$  and  $N_{\text{survival}}$  are the generated events and the surviving events after the all reduction cuts in the solar neutrino MC simulation,  $T_{\text{Live}}$  is the livetime in SK-IV (2055.5 days) and  $R_{\text{exp}}$  is the expected event rate in the ID detector. The expected event rate  $R_{\text{exp}}$  is calculated assuming that the number of electrons in ID is  $1.086 \times 10^{34}$  and using the  $^8\text{B}$  neutrino energy spectrum shape measured by Winter *et al* [115]. Based on the SNO NC result [70],  $\Phi_{^8\text{B}, \text{SNO, NC}} = 5.25 \times 10^6 / \text{cm}^2/\text{sec}$ , the expected event rate in the ID detector is calculated as  $R_{\text{exp}} = 294.75$  event/day/32.5kton. Finally, the expected signal during 2055.5 days is  $N_{\text{exp}} = 90,406$  events.

Comparing the observed signal with the expected signal, the ratio is 0.441, corresponding to a  $^8\text{B}$  solar neutrino flux of

$$\Phi_{^8\text{B}, \text{SK4}} = 2.314 \pm 0.018(\text{stat.}) \pm 0.039(\text{syst.}) \times 10^6 / \text{cm}^2/\text{sec}. \quad (11.1.2)$$

This result is consistent with other phases in SK within the total uncertainty as shown in Figure 11.2. The long-term yearly variation of the  $^8\text{B}$  solar neutrino flux will be shown in section 12.1.

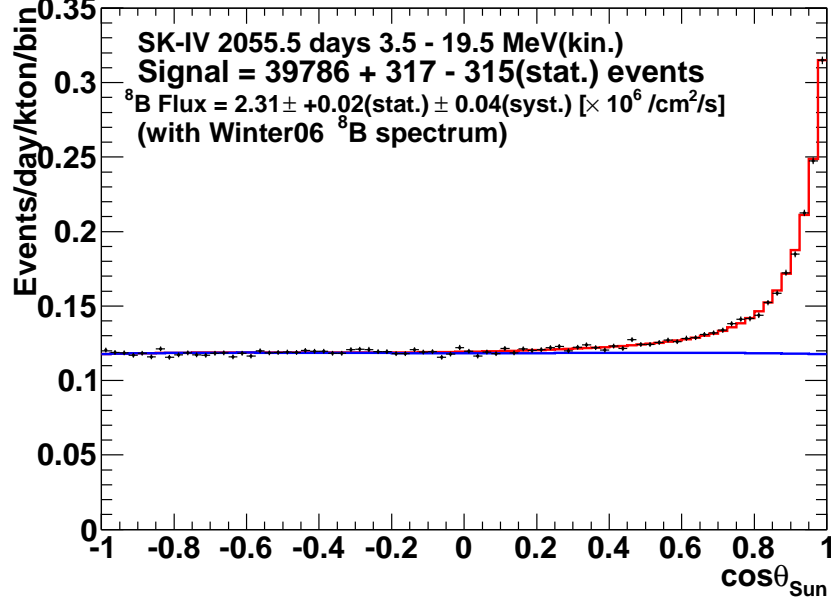


Figure 11.1: The solar angle distribution using 3.5 – 19.5 MeV energy range. The horizontal axis shows the  $\cos \theta_{\text{sun}}$  defined in Figure 8.2 and the vertical axis shows the event rate in unit of event/day/kton/bin where the total number of the bin in horizontal axis is 80. The black marks with error bars show the observed data. The red solid and blue solid histograms show the best fit signal and background shapes, respectively.

## 11.2 Day/Night flux asymmetry

To study the matter effect in the Earth, location of the Sun with respect to the detector coordinate, solar zenith angle  $\theta_z$ , is used. It is defined as the angle between the  $z$ -axis of the detector and the vector from the solar position to the reconstructed vertex position, as shown in the left of Figure 11.3.

The day/night flux asymmetry measurement is measured by extracting the solar neutrino events above 4.5 MeV. Using the information on the solar zenith angle in the SK detector, the daytime and the nighttime are separated as  $\cos \theta_z \leq 0$  and  $> 0$ , respectively. The livetime during daytime and nighttime are calculated for  $\cos \theta_z \leq 0$  and  $\cos \theta_z > 0$ , respectively. They are calculated using the date information of the operation period. For each subrun, the direction of the Sun is calculated. Its accuracy depends on the length of subruns, thus within less than  $\sim 85$  sec as mentioned in chapter 6. The calculated livetime is

$$\begin{aligned} \cos \theta_z \leq 0, \quad T_{\text{Day}} &= 990.7 \text{ days}, \\ \cos \theta_z > 0, \quad T_{\text{Night}} &= 1064.8 \text{ days}. \end{aligned} \quad (11.2.1)$$

The observed  $^8\text{B}$  solar neutrino flux in day and night is calculated individually with the same method as described above. Their results are

$$\begin{aligned} \Phi_{\text{SK4,Day}} &= 2.28 \pm 0.03(\text{stat.}) \pm 0.05(\text{syst.}) \times 10^6 / \text{cm}^2 / \text{sec}, \\ \Phi_{\text{SK4,Night}} &= 2.35 \pm 0.03(\text{stat.}) \pm 0.05(\text{syst.}) \times 10^6 / \text{cm}^2 / \text{sec}. \end{aligned} \quad (11.2.2)$$

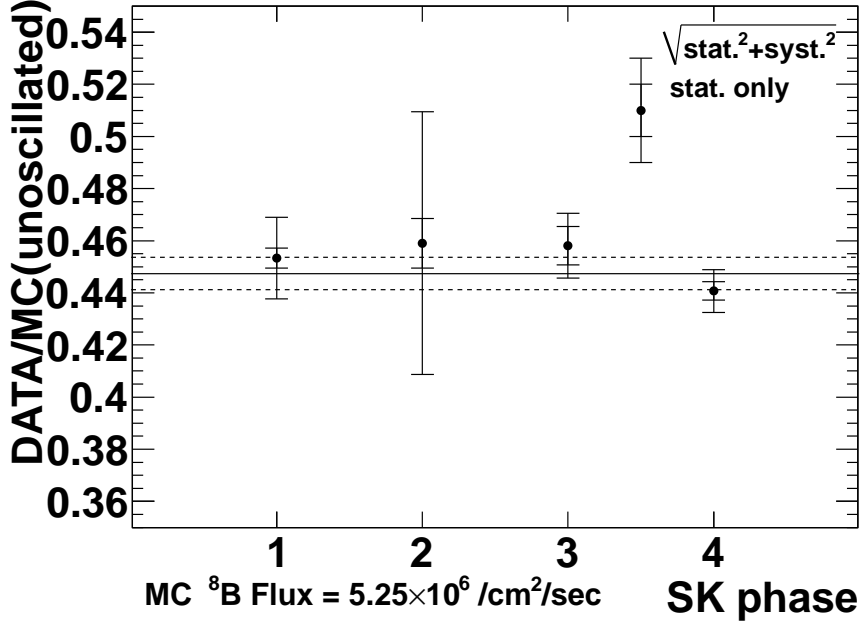


Figure 11.2: The comparison of the solar neutrino fluxes unit of Data/MC (unoscillated) among SK phases. The horizontal axis shows the phase number of SK and the vertical axis shows the ratio of the observed rate to the unoscillated MC simulation (assumed flux of  $5.25 \times 10^6$  /cm<sup>2</sup>/sec). The points illustrate the central value, the inner (outer) error indicates the statistical (statistical+systematic) uncertainty. The large uncertainty in SK-II is due to the half number of PMTs.

The observed day/night flux asymmetry is calculated as

$$\begin{aligned}
 A_{\text{DN,SK4}} &= \frac{\Phi_{\text{SK4,Day}} - \Phi_{\text{SK4,Night}}}{(\Phi_{\text{SK4,Day}} + \Phi_{\text{SK4,Night}})/2} \\
 &= -0.031 \pm 0.016(\text{stat.}) \pm 0.014(\text{syst.}).
 \end{aligned}
 \tag{11.2.3}$$

The day/night flux asymmetry in SK-IV is  $\sim 1.5\sigma$  level away from zero. The combined result will be discussed in subsection 12.1.2.

In addition, the solar zenith angle dependence of the <sup>8</sup>B solar neutrino flux is shown in Figure 11.4.

### 11.3 Energy spectrum

The spectrum of the recoil electrons is measured with the same method as the flux measurement. Namely, the method of the flux measurement is applied to events in each energy bin and the obtained flux is plotted on the spectrum. The energy range from 3.5 to 19.5 is divided into 23 energy bins as described in Chapter 9. In addition, the energy bins below 7.5 MeV are divided into three *MSG* groups. As mentioned in Chapter 6, the event sample with smaller *MSG* value has more background contaminations in the data sample because the background events mainly

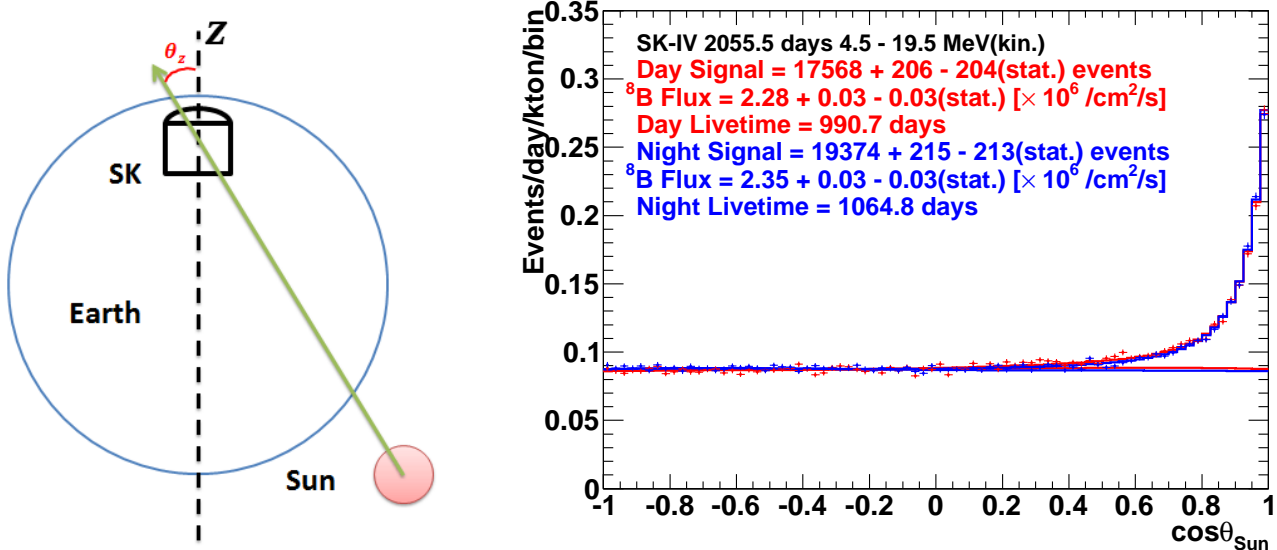


Figure 11.3: Left: The definition of the zenith angle  $\theta_z$ . Right: The solar angle distribution during the day (red) and the night (blue) using events in 4.5 – 19.5 MeV energy range. The horizontal axis shows the  $\cos\theta_{\text{sun}}$  and the vertical axis shows the event rate in unit of event/day/kton/bin where the total number of bin is 80. The data points, best fit signal and the background shape are also shown.

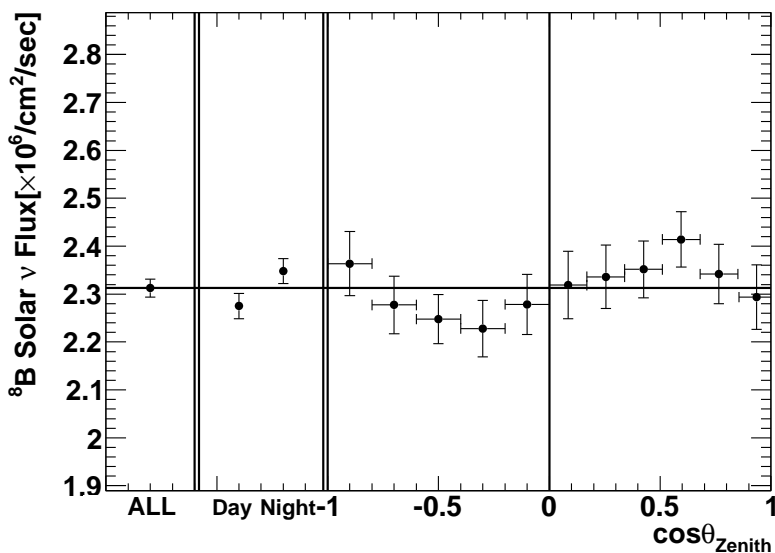


Figure 11.4: The zenith angle dependence of the  ${}^8\text{B}$  solar neutrino flux using events in the 4.5 – 19.5 MeV energy range. The horizontal axis shows ALL, Day, Night and each  $\cos\theta_z$  bin. The full  $\cos\theta_z$  range is divided into 11 bins, 5 bins for daytime plus 6 bins for nighttime. The solar neutrinos pass through the core of the Earth in the most right bin ( $\cos\theta_z > 0.83$ ). The vertical axis shows the observed  ${}^8\text{B}$  solar neutrino flux assuming expected spectrum shape without neutrino oscillations. The error bars indicate the statistical error only.

come from the beta decay of  $^{214}\text{Bi}$ . In contrast, the solar neutrino signal is likely to have a high *MSG* value, because of less multiple scatterings when traveling the water. Hence, more background events exist in the low *MSG* group, while more neutrino signals exist in the high *MSG* groups. Figure 11.5 and Figure 11.6 illustrate the solar angle distributions for the each *MSG* group below 5.5 MeV and below 7.5 MeV, respectively.

For each *MSG* group and each energy bin below 7.5 MeV, the signal probability density  $s_{ij,MSG}$  is obtained from the solar neutrino MC simulation and the background probability density  $b_{ij,MSG}$  is obtained from the final data sample. Then, the signal extraction process is simultaneously performed using new probability densities  $s_{ij,MSG}$  and  $b_{ij,MSG}$  for each *MSG* group. Finally, the results from each *MSG* groups are combined into one. The merit of this method is that the statistical uncertainty can be reduced by about  $\sim 10\%$  [108, 110]. The additional systematic uncertainty caused by this method is relatively small compared to the statistical fluctuation and it is taken into account in the spectrum analysis.

Figure 11.7 shows the solar angle distribution above 7.5 MeV without the MSG method.

Table 11.1 shows the observed and the expected rates in each energy bin.

The observed event rate is also shown in Figure 11.8. The energy spectrum in SK-IV is shown in Figure 11.9.

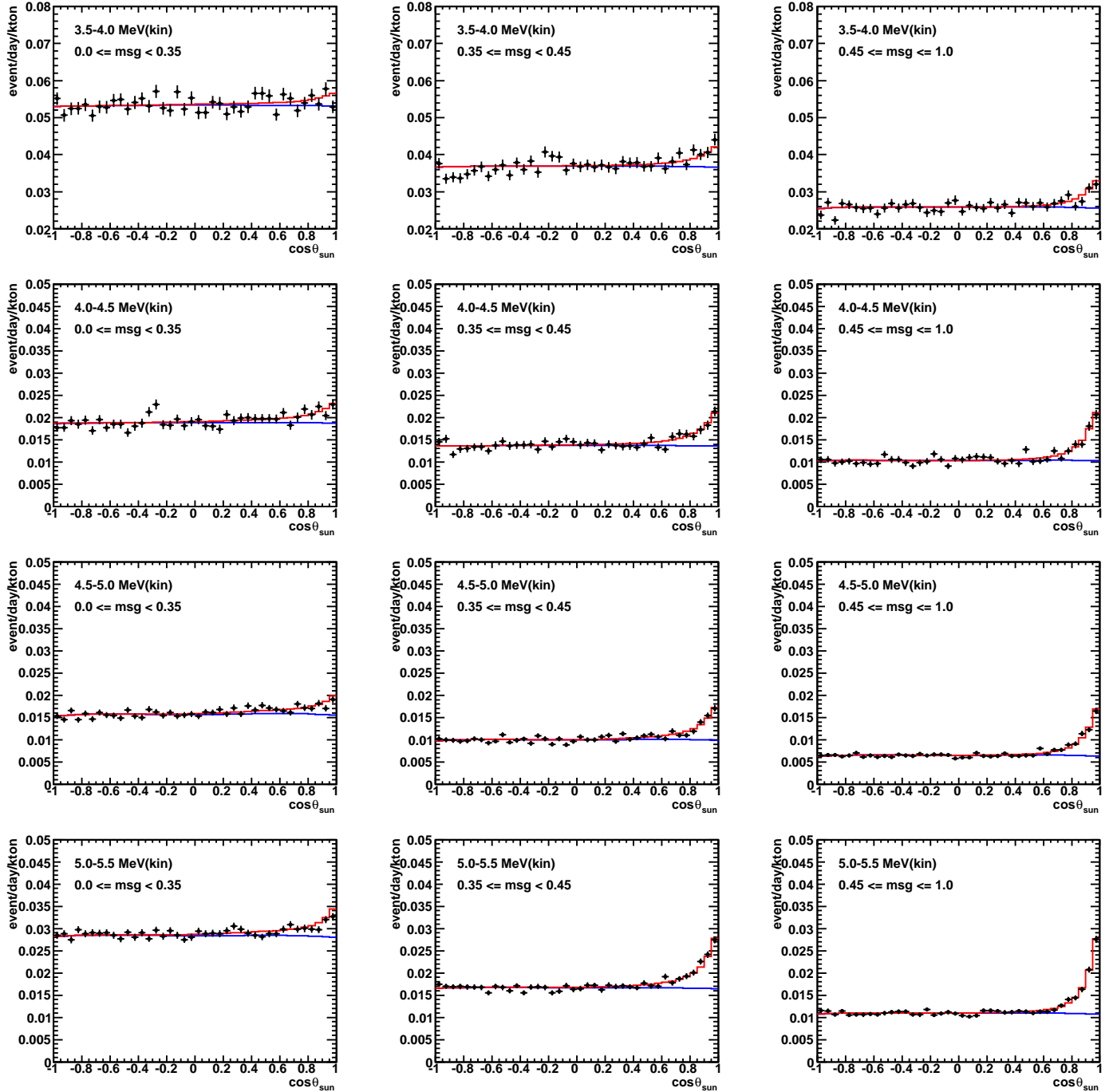


Figure 11.5: The solar angle distributions for the energy bins which use  $MSG$  sub groups. The horizontal axis shows  $\cos\theta_{\text{sun}}$  and the vertical axis shows the event rate in unit of event/day/kton/bin where the total number of bins is 40. The first through the fourth rows show the plots for 3.5 – 4.0, 4.0 – 4.5, 4.5 – 5.0 and 5.0 – 5.5 MeV energy bins, respectively. The first, second and third columns show the plot using  $0 \leq MSG < 0.35$ ,  $0.35 \leq MSG < 0.45$  and  $0.45 \leq MSG \leq 1.0$  respectively.

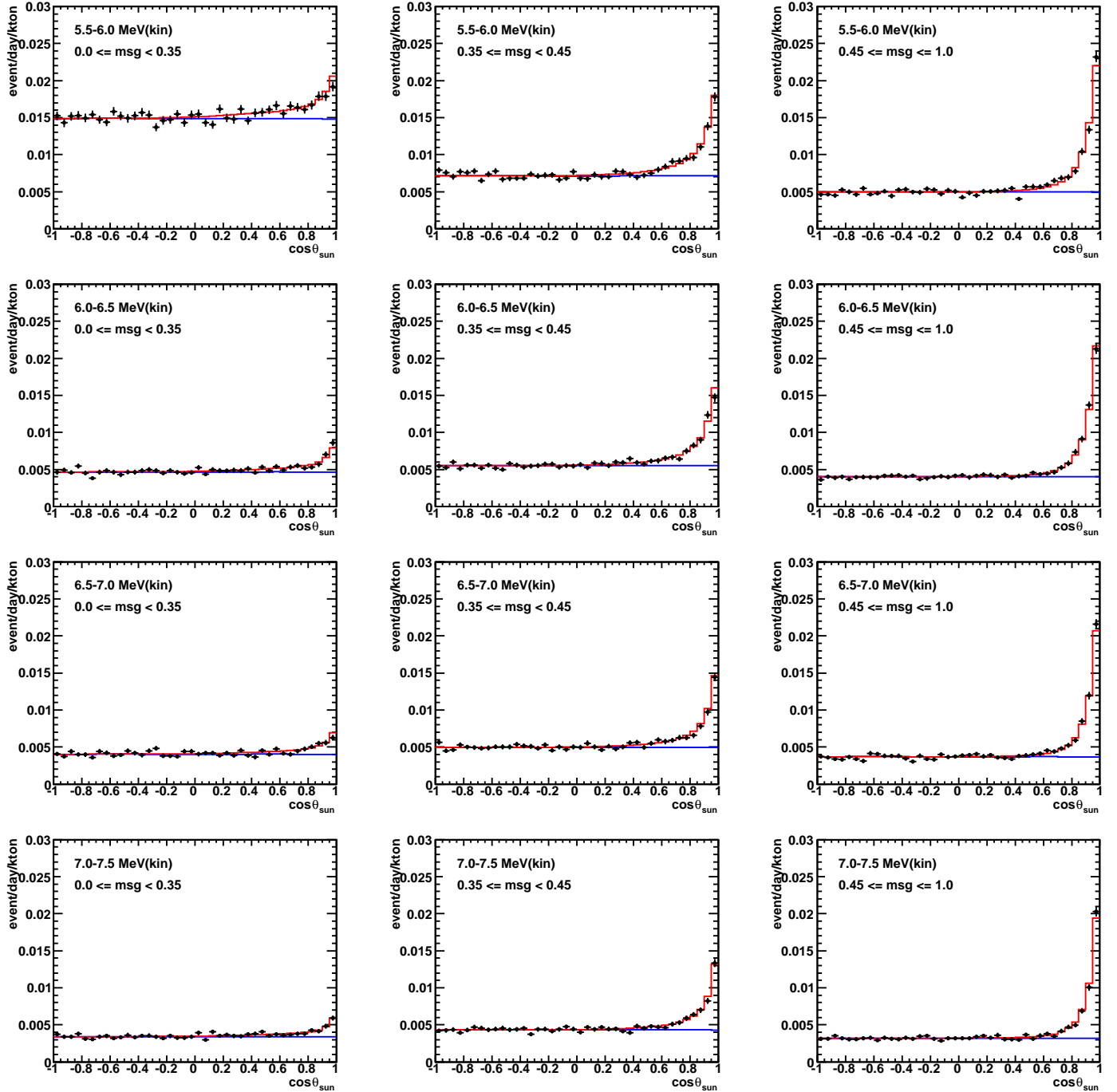


Figure 11.6: The solar angle distributions for the energy bins which use  $MSG$  sub groups. The horizontal axis shows  $\cos\theta_{\text{sun}}$  and the vertical axis shows the event rate in unit of event/day/kton/bin where the total number of bins is 40. The first through the fourth rows show the plots for 5.5 – 6.0, 6.0 – 6.5, 6.5 – 7.0 and 7.0 – 7.5 MeV energy bins, respectively. The first, second and third columns show the plot using  $0 \leq MSG < 0.35$ ,  $0.35 \leq MSG < 0.45$  and  $0.45 \leq MSG \leq 1.0$  respectively.

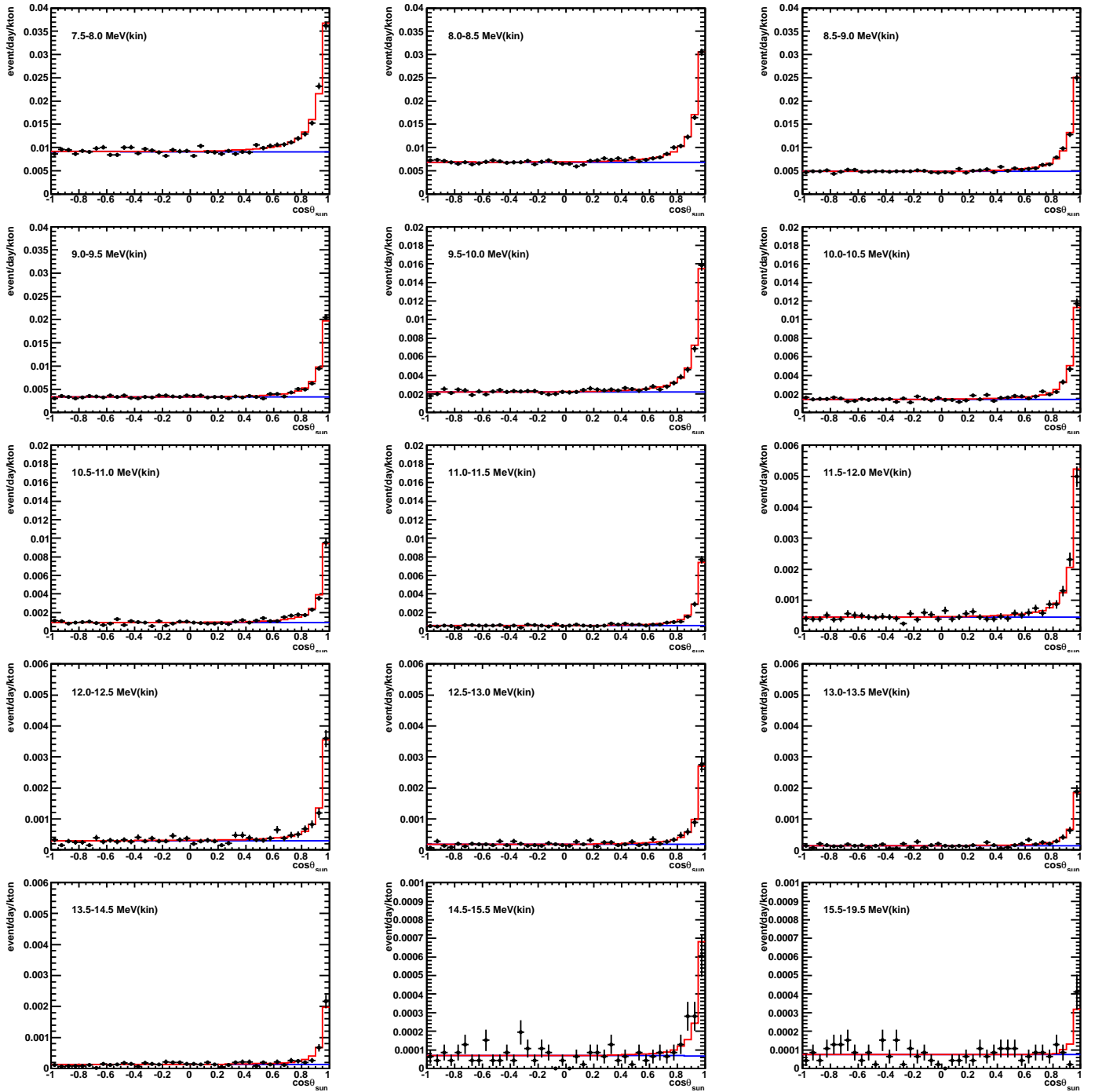


Figure 11.7: The solar angle distributions for the energy bins which do not use *MSG* sub groups. The horizontal axis shows  $\cos \theta_{\text{sun}}$  and the vertical axis shows the event rate in unit of event/day/kton/bin where the total number of bins is 40. The energy ranges are shown in each panel.

Table 11.1: The observed and expected event rates in each energy bin at 1 AU. The errors are statistical errors only. The  $^8\text{B}$  solar neutrino flux is assumed to be  $5.25 \times 10^6$  [/cm<sup>2</sup>/sec].

Energy [MeV(kin)]	Observed rate			Expected rate	
	ALL $-1 \leq \cos \theta_z \leq 1$	DAY $-1 \leq \cos \theta_z \leq 0$	NIGHT $0 < \cos \theta_z \leq 1$	$^8\text{B}$	hep
3.5 – 4.0	90.8 <sup>+10.9</sup> <sub>-10.7</sub>	91.0 <sup>+17.1</sup> <sub>-16.8</sub>	90.5 <sup>+14.0</sup> <sub>-13.8</sub>	196.6	0.347
4.0 – 4.5	82.2 <sup>+5.1</sup> <sub>-5.0</sub>	76.8 <sup>+7.9</sup> <sub>-7.6</sub>	86.5 <sup>+6.8</sup> <sub>-6.6</sub>	182.8	0.335
4.5 – 5.0	75.7 <sup>+3.4</sup> <sub>-3.3</sub>	71.6 <sup>+5.0</sup> <sub>-4.9</sub>	79.0 <sup>+4.6</sup> <sub>-4.5</sub>	167.8	0.323
5.0 – 5.5	64.5 <sup>+2.1</sup> <sub>-2.1</sub>	64.5 <sup>+3.1</sup> <sub>-3.1</sub>	64.5 <sup>+2.9</sup> <sub>-2.9</sub>	153.2	0.312
5.5 – 6.0	58.3 <sup>+1.6</sup> <sub>-1.5</sub>	57.2 <sup>+2.3</sup> <sub>-2.2</sub>	59.3 <sup>+2.2</sup> <sub>-2.1</sub>	137.9	0.298
6.0 – 6.5	55.7 <sup>+1.4</sup> <sub>-1.3</sub>	53.8 <sup>+2.0</sup> <sub>-1.9</sub>	57.5 <sup>+1.9</sup> <sub>-1.9</sub>	121.9	0.282
6.5 – 7.0	47.0 <sup>+1.2</sup> <sub>-1.2</sub>	44.7 <sup>+1.7</sup> <sub>-1.7</sub>	49.2 <sup>+1.7</sup> <sub>-1.7</sub>	106.7	0.266
7.0 – 7.5	41.0 <sup>+1.1</sup> <sub>-1.1</sub>	42.3 <sup>+1.6</sup> <sub>-1.5</sub>	39.7 <sup>+1.5</sup> <sub>-1.5</sub>	92.1	0.249
7.5 – 8.0	35.7 <sup>+0.9</sup> <sub>-0.9</sub>	35.5 <sup>+1.4</sup> <sub>-1.3</sub>	36.0 <sup>+1.3</sup> <sub>-1.3</sub>	78.0	0.232
8.0 – 8.5	29.0 <sup>+0.8</sup> <sub>-0.8</sub>	28.6 <sup>+1.2</sup> <sub>-1.1</sub>	29.5 <sup>+1.2</sup> <sub>-1.1</sub>	65.1	0.215
8.5 – 9.0	23.8 <sup>+0.7</sup> <sub>-0.7</sub>	24.1 <sup>+1.1</sup> <sub>-1.0</sub>	23.5 <sup>+1.0</sup> <sub>-1.0</sub>	53.4	0.197
9.0 – 9.5	18.6 <sup>+0.6</sup> <sub>-0.6</sub>	18.4 <sup>+0.9</sup> <sub>-0.8</sub>	18.8 <sup>+0.9</sup> <sub>-0.8</sub>	42.9	0.180
9.5 – 10.0	14.5 <sup>+0.5</sup> <sub>-0.5</sub>	13.9 <sup>+0.7</sup> <sub>-0.7</sub>	15.2 <sup>+0.8</sup> <sub>-0.7</sub>	33.7	0.162
10.0 – 10.5	10.5 <sup>+0.4</sup> <sub>-0.4</sub>	10.2 <sup>+0.6</sup> <sub>-0.6</sub>	10.8 <sup>+0.6</sup> <sub>-0.6</sub>	26.0	0.144
10.5 – 11.0	8.78 <sup>+0.40</sup> <sub>-0.38</sub>	8.16 <sup>+0.56</sup> <sub>-0.52</sub>	9.37 <sup>+0.57</sup> <sub>-0.54</sub>	19.52	0.128
11.0 – 11.5	6.90 <sup>+0.34</sup> <sub>-0.32</sub>	7.03 <sup>+0.49</sup> <sub>-0.46</sub>	6.77 <sup>+0.48</sup> <sub>-0.44</sub>	14.30	0.112
11.5 – 12.0	4.45 <sup>+0.27</sup> <sub>-0.25</sub>	4.10 <sup>+0.38</sup> <sub>-0.35</sub>	4.79 <sup>+0.39</sup> <sub>-0.36</sub>	10.23	0.097
12.0 – 12.5	2.99 <sup>+0.22</sup> <sub>-0.21</sub>	3.08 <sup>+0.32</sup> <sub>-0.29</sub>	2.90 <sup>+0.32</sup> <sub>-0.29</sub>	7.08	0.083
12.5 – 13.0	2.29 <sup>+0.19</sup> <sub>-0.17</sub>	2.36 <sup>+0.27</sup> <sub>-0.24</sub>	2.22 <sup>+0.27</sup> <sub>-0.24</sub>	4.78	0.071
13.0 – 13.5	1.55 <sup>+0.16</sup> <sub>-0.14</sub>	1.62 <sup>+0.23</sup> <sub>-0.20</sub>	1.47 <sup>+0.23</sup> <sub>-0.19</sub>	3.09	0.059
13.5 – 14.5	1.62 <sup>+0.16</sup> <sub>-0.14</sub>	1.59 <sup>+0.23</sup> <sub>-0.20</sub>	1.65 <sup>+0.23</sup> <sub>-0.20</sub>	3.16	0.088
14.5 – 15.5	0.534 <sup>+0.099</sup> <sub>-0.083</sub>	0.559 <sup>+0.144</sup> <sub>-0.112</sub>	0.504 <sup>+0.147</sup> <sub>-0.114</sub>	1.116	0.056
15.5 – 19.5	0.198 <sup>+0.067</sup> <sub>-0.050</sub>	0.120 <sup>+0.089</sup> <sub>-0.055</sub>	0.271 <sup>+0.108</sup> <sub>-0.075</sub>	0.456	0.064

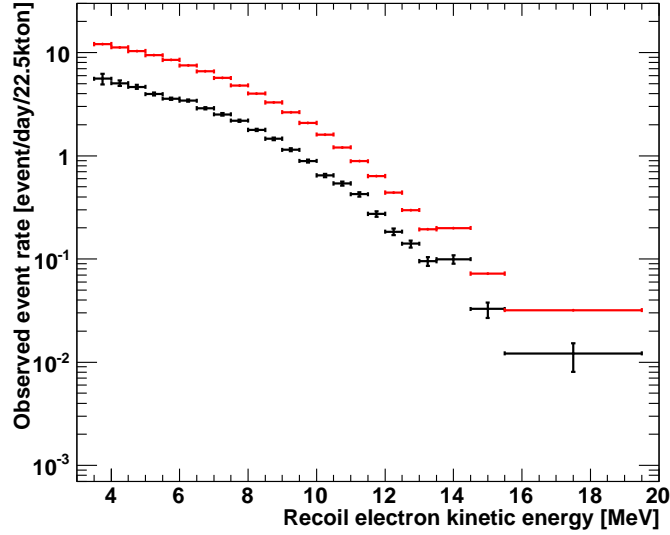


Figure 11.8: The observed  $^8\text{B}$  solar neutrino event rate. The horizontal axis shows the recoil electron kinetic energy [MeV] and the vertical axis shows the event rate [event/day/22.5kton]. The black (red) points show the observed solar neutrino event in data (MC). The reduction efficiencies for each reduction cut are corrected.

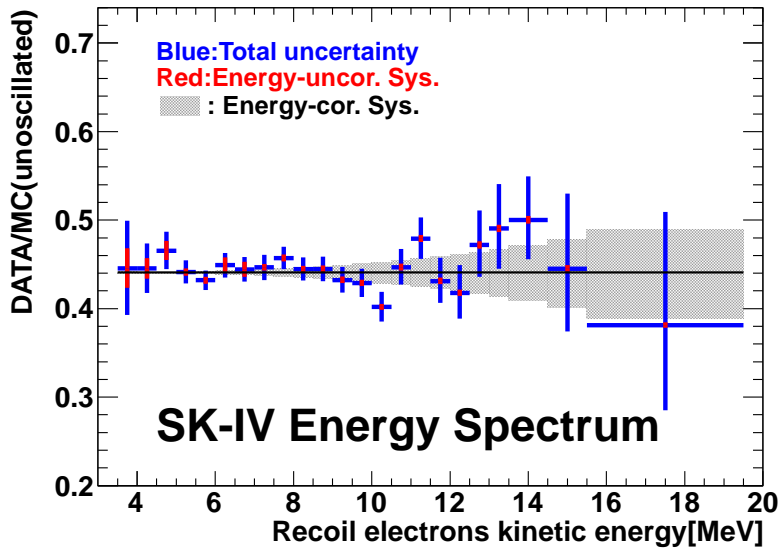


Figure 11.9: The energy spectrum of  $^8\text{B}$  solar neutrino in SK-IV. The horizontal axis shows the recoil electron kinetic energy [MeV] and the vertical axis shows the ratio of the measured rate to the unoscillated solar neutrino MC simulation rate. The MC simulation assumes a total flux of  $5.25 \times 10^6 / \text{cm}^2/\text{sec}$ . Below the 7.5 MeV region, the signal extraction is performed taking into account the MSG groups.

## 11.4 Low energy region

After the improvement of the water circulation system, optimization of the data reduction cuts, the detection efficiency calibration study and the background study, the energy threshold of the analysis is lowered down to 3.5 MeV from 4.0 MeV. The solar angle distributions in 3.5 – 4.0 MeV and 4.0 – 4.5 MeV energy ranges are shown in Figure 11.10. For the first time, the clear solar neutrino signal is extracted in the 3.5 – 4.0 MeV energy range. The number of extracted events,  $N_{3.5-4.0}$  is:

$$N_{3.5-4.0} = 1299_{-154}^{+156}(\text{stat.})_{-64}^{+66}(\text{syst.}) \text{ events.} \quad (11.4.1)$$

So this number is  $7.8\sigma$  away from 0. It gives the most precise (statistically significant) measurement in the 3.5 – 4.0 MeV region among the all solar neutrino experiments.

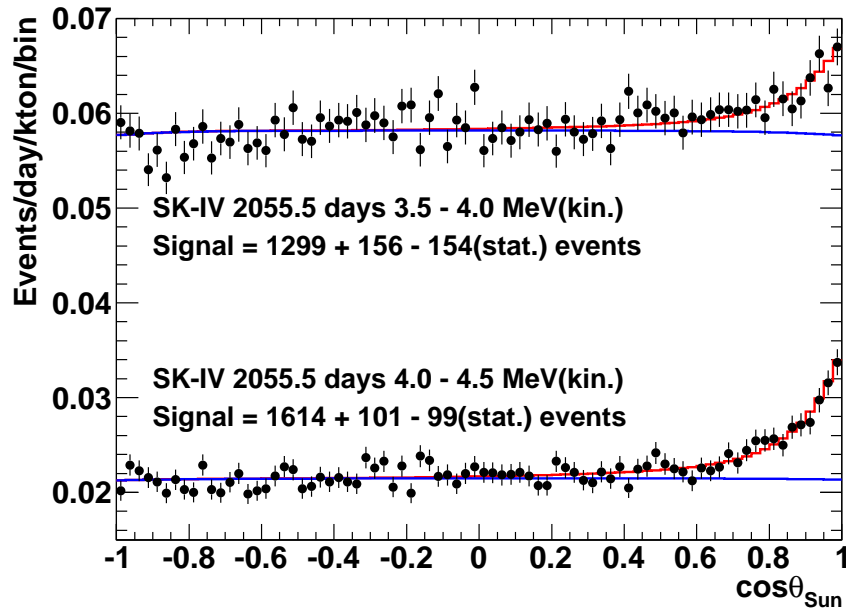


Figure 11.10: The solar angle distribution for the first lowest energy bin (3.5 – 4.0 MeV) and the second lowest energy bin (4.0 – 4.5 MeV). The horizontal axis shows the  $\cos\theta_{\text{sun}}$  and the vertical axis shows the event rate in unit of event/day/kton/bin where the total number of bins is 80. The black dots show the observed data. The red solid line and blue solid line show the best fit signal and background shapes, respectively

# Chapter 12

## Combined analysis result

### 12.1 $^8\text{B}$ solar neutrino flux measurement

#### 12.1.1 Extracted signal

Figure 12.1 shows the solar angle distributions through all SK phases. Since SK-IV has the longest observation time and the lowest energy threshold, the solar neutrino signal peak around  $\cos \theta_{\text{sun}} = 1$  is the largest among all SK phases. Since the livetime of daytime and nighttime is different, the primary difference in height of the distribution is due to the livetime.

Figure 12.2 shows the solar angle distribution for the combined data of SK-I through SK-IV. The extracted solar neutrino signal exceeds 77,000 events in 4890 days.

#### 12.1.2 Combined result of $^8\text{B}$ solar neutrino flux measurement

Table 12.1 summarizes the flux measurements with SK. As shown in Figure 11.2, the flux measurements among the SK phases are consistent within the total uncertainties which is the quadratic sum of statistical and systematic errors.

In order to calculate the combined flux value, a special treatment is done as follows: (1) The statistical uncertainty and the total flux systematic uncertainties except for cross section, neutrino spectrum shape, signal extraction and spallation are combined, which is represented as  $es_p$ , then, the weight factor is obtained for each SK phase. (2) Take the average of the flux value using weight factors. (3) For the remaining above 4 uncertainties above, take the average using the weight factors, then, merge into one by adding in quadrature, which is represented as  $eu_p$ . (4) The total combined uncertainty is calculated by adding  $es_p$  and  $eu_p$  in quadrature. Finally, the obtained combined total flux of all SK data is

$$\Phi_{\text{sB,SK}} = 2.341 \pm 0.044(\text{stat.} + \text{syst.}) \times 10^6 / \text{cm}^2 / \text{sec}. \quad (12.1.1)$$

Figure 12.3 shows the zenith angle distribution in each SK phase. The left of Figure 12.4 shows the combined zenith angle distribution. When considering the solar neutrino flux during daytime and nighttime, the day/night asymmetry can be calculated as

$$A_{\text{DN}} = \frac{\Phi_{\text{Day}} - \Phi_{\text{Night}}}{(\Phi_{\text{Day}} + \Phi_{\text{Night}})/2}. \quad (12.1.2)$$

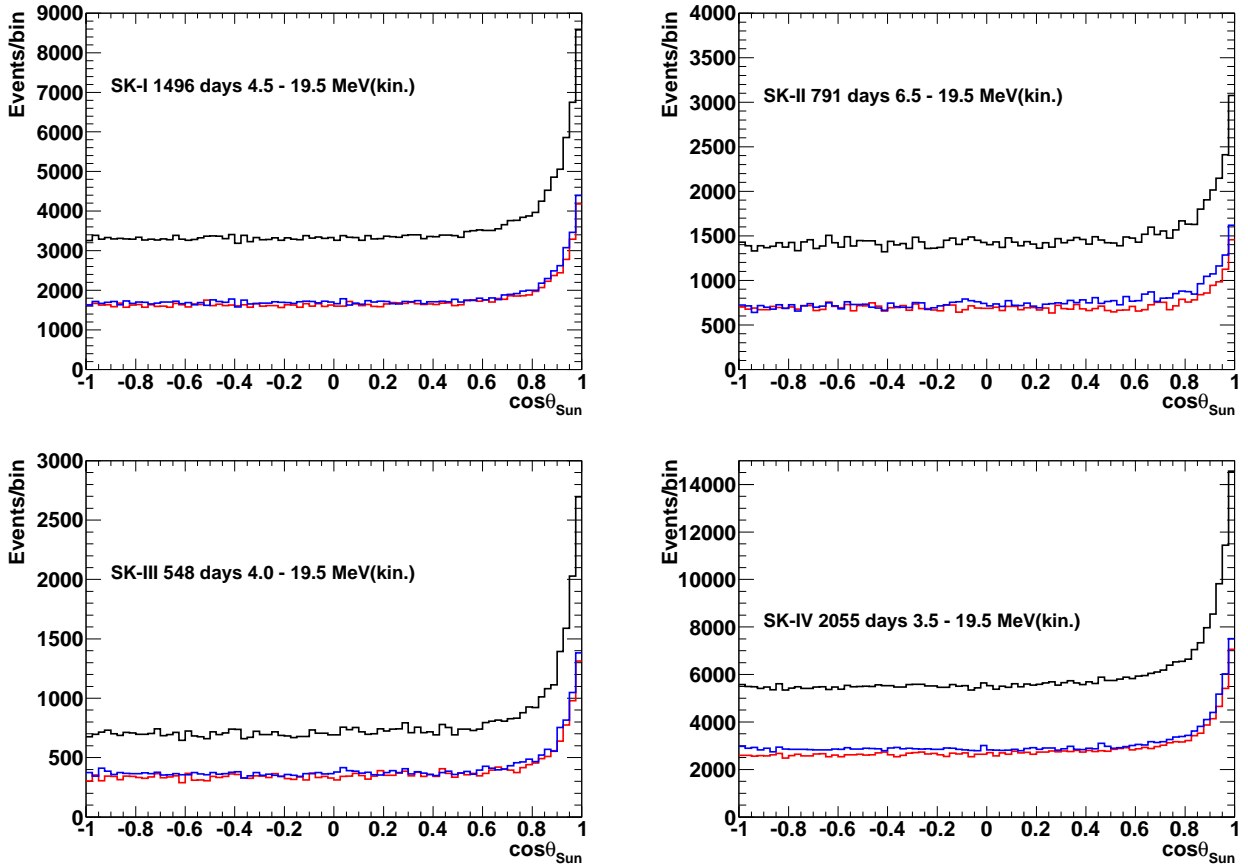


Figure 12.1: Solar angle distributions of each SK phase. The horizontal axis shows the solar angle  $\cos\theta_{\text{sun}}$  and the vertical axis shows the number of events in each bin, where total number of bins is 80. The black histograms are the solar angle distribution during all livetime, the red histograms and the blue histograms are the solar angle distribution during daytime and nighttime, respectively. Since the livetime between daytime and nighttime is different, the primary difference in height of the distribution is due to the livetime.

Table 12.1: Summary of the flux measurement results of SK.

	Live time [days]	Energy [MeV]	Extracted signal	Flux [ $\times 10^6/\text{cm}^2/\text{sec}$ ]	Ref.
SK-I	1496	4.5 – 19.5	$22,443^{+227}_{-225}(\text{stat.})^{+786}_{-718}(\text{syst.})$	$2.38 \pm 0.02(\text{stat.}) \pm 0.08(\text{syst.})$	[109]
SK-II	791	6.5 – 19.5	$7,210^{+153}_{-151}(\text{stat.})^{+483}_{-461}(\text{syst.})$	$2.41 \pm 0.05(\text{stat.})^{+0.16}_{-0.15}(\text{syst.})$	[113]
SK-III	548	4.0 – 19.5	$8,148^{+133}_{-131}(\text{stat.}) \pm 176(\text{syst.})$	$2.40 \pm 0.04(\text{stat.}) \pm 0.05(\text{syst.})$	[114]
SK-IV	2055	3.5 – 19.5	$39,786^{+317}_{-315}(\text{stat.})^{+695}_{-674}(\text{syst.})$	$2.31 \pm 0.02(\text{stat.}) \pm 0.04(\text{syst.})$	This work
Combined	4890	-	more than 77,000	$2.341 \pm 0.044(\text{stat.} + \text{syst.})$	This work

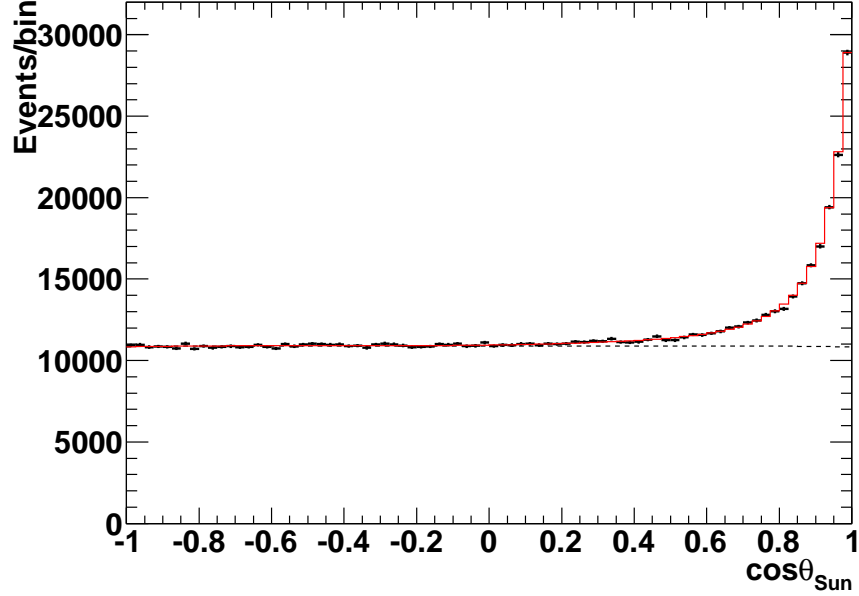


Figure 12.2: Combined solar angle distribution for SK-I through SK-IV, the total live time is 4840 days. The horizontal axis shows the solar angle  $\cos \theta_{\text{sun}}$  and the vertical axis shows the number of events, where the number of bins is 80. The back points show the data, the red histograms are the best fit result and the black dashed line shows the background shape, respectively.

Table 12.2: Summary of day/night asymmetry for each SK phase.

Phase	$A_{\text{DN}} \pm (\text{stat.}) \pm (\text{syst.}) [\%]$
SK-I	$-2.1 \pm 2.0 \pm 1.3$
SK-II	$-5.5 \pm 4.2 \pm 3.7$
SK-III	$-5.9 \pm 3.2 \pm 1.3$
SK-IV	$-3.1 \pm 1.6 \pm 1.4$
Combined	$-3.3 \pm 1.1 \pm 0.8$

The Table 12.2 shows the measurements of  $A_{\text{DN}}$  for each phase. The SK combined day/night flux asymmetry is obtained as

$$A_{\text{DN},\text{SK}} = (-3.3 \pm 1.1(\text{stat.}) \pm 0.8(\text{syst.})) \%, \quad (12.1.3)$$

where it is  $2.4\sigma$  away from zero. The negative sign indicates that the night flux is larger than that of the day flux.

The right of Figure 12.4 shows the values of day/night asymmetry in each SK phase as well as the combined result.

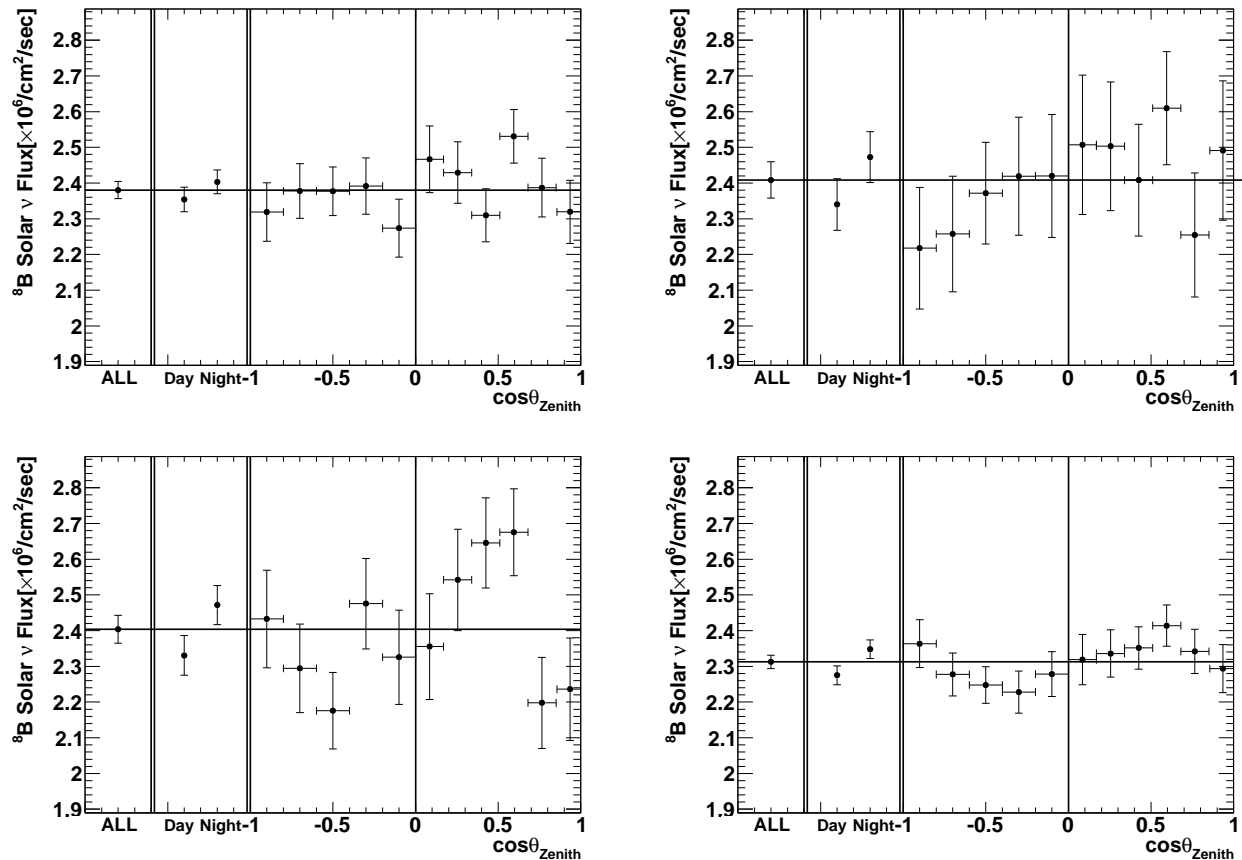


Figure 12.3: The day and night flux values and the its zenith angle distributions. The horizontal axis shows the ALL, Day, Night and the  $\cos\theta_z$  respectively. The full  $\cos\theta_z$  range is divided into 11 bins, 5 bins for the day time and 6 bins for the night time. The solar neutrinos passing through the core of the Earth in the most right bin. The vertical axis shows the observed  ${}^8\text{B}$  solar neutrino flux, assuming  $5.25 \times 10^6 / \text{cm}^2/\text{sec}$ . The left-top, right-top, left-bottom, right-bottom show the plots for SK-I, SK-II, SK-III and SK-IV, respectively. The error bars are only statistical errors.

### 12.1.3 Yearly variation of the ${}^8\text{B}$ solar neutrino flux

As explained in subsection 2.1.4, the solar activity changes with the 11-year cycle. SK observed solar neutrinos for 18 years, which corresponds to about 1.5 solar activity cycle. So, it is possible to discuss whether the solar neutrino flux is correlated with the solar activity or not.

To check the stability of the  ${}^8\text{B}$  solar neutrino flux, the yearly flux values are calculated with the same signal extraction method as described in section 11.1. The data above 4.5 MeV (6.5 MeV for SK-II) is used, because the events above 4.5 MeV can be detected with the efficiency of 100% among all SK phases. Although the data set used in this thesis includes a half of 2015 (Table 3.1), the data taken in 2015 is not used in this analysis, because it is not the complete one year measurement. In addition, the data in 2002 is not used, because SK-II started in October and the total livetime in 2002 is less than 3 months. It is noted that the yearly flux in 2008 is divided into two, one is during SK-III and the other is during SK-IV.

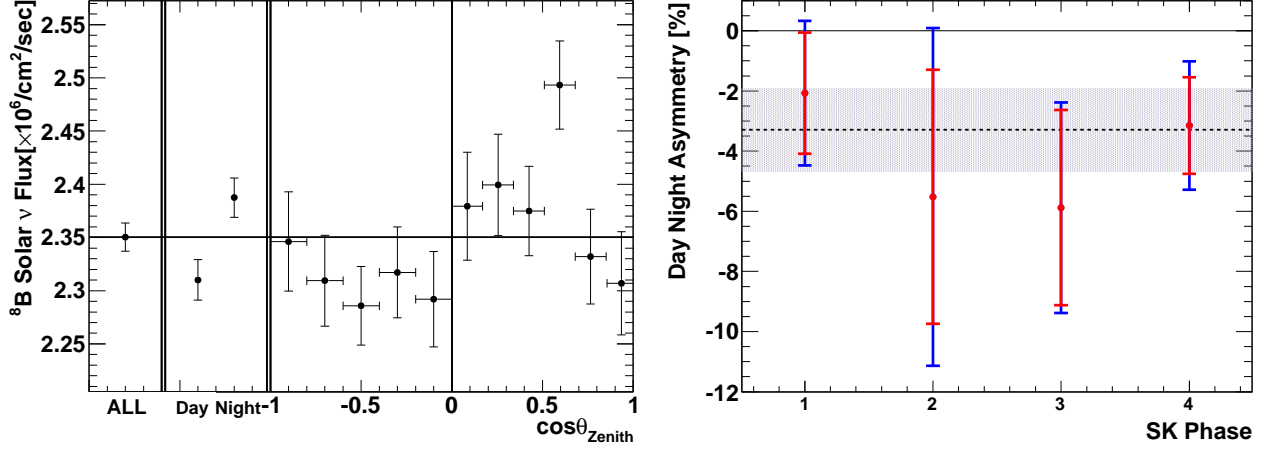


Figure 12.4: Left: The combined zenith angle dependence of the solar neutrino flux. The error bars are only statistical errors. The horizontal axis shows the ALL, Day, Night and the  $\cos\theta_z$  respectively. The  $\cos\theta_z$  region is divided into 11 bins, 5 bins are used for the day time and 6 bins are used for the night time. The solar neutrino passed through the core of the Earth in the most right bin. The vertical axis shows the observed  ${}^8\text{B}$  solar neutrino flux assuming  $5.25 \times 10^6 / \text{cm}^2/\text{sec}$ . Right: The day/night asymmetry for each SK phase. The horizontal axis illustrates the phase of SK and the vertical axis shows the value of  $A_{\text{DN}}$ . The red points show the measurement results of each SK phase, where the inner error shows the statistical error only and the outer (blue) error shows the total (stat.+syst.) error. The gray band shows the combined value (stat.+syst.).

The right of Figure 12.5 shows the SK yearly solar neutrino flux measured throughout the different phases in SK together with the corresponding sunspot number. The yearly variation of the measured flux is fully consistent with a constant solar neutrino flux emitted by the Sun.

In order to test the correlation between the yearly fluxes and the sunspot numbers, the  $\chi^2$  between the average flux value and the yearly flux values is defined as:

$$\chi^2 = \text{Min} \left[ \sum_{p=1}^{N_{\text{SK}}} \sum_{t=1}^{n_p} \left( \frac{r - (d_{p,t} + \alpha_p)}{\sigma_{p,t}} \right)^2 + \left( \frac{\alpha_p}{\tau_p} \right)^2 \right], \quad (12.1.4)$$

where  $p$  is a SK phase,  $t$  is the year in a SK phase,  $r$  is the combined SK average flux,  $d_{p,t}$  is the yearly flux corresponding to the SK phase  $p$  and the year  $t$ ,  $\sigma_{p,t}$  is the statistical uncertainty of  $d_{p,t}$ ,  $\tau_p$  is the systematic uncertainty of SK phase  $p$  and  $\alpha_p$  is the nuisance parameter describing systematic shift of phase  $p$ . The  $\chi^2$  is calculated with the total experimental error as,

$$\chi^2 = 12.86/18 \text{ d.o.f}, \quad (12.1.5)$$

which corresponds to probability of 80.0%.

In addition, to evaluate the correlation between observed  ${}^8\text{B}$  solar neutrino flux and the sunspot number, the following function is defined as

$$f(s_y) = a_0 \times s_y + c_0, \quad (12.1.6)$$

where  $s_y$  is an average value of sunspot number in each year,  $a_0$  and  $c_0$  are the fitting parameters. The right of Figure 12.5 shows the yearly variation of the measurement flux as a function of sunspot number as well as the best fit result, where best fit parameters are

$$a_0 = (0.53 \pm 1.05) \times 10^{-4}, \quad (12.1.7)$$

$$c_0 = 0.443 \pm 0.006. \quad (12.1.8)$$

According to the fitting result, the slope of the function is consistent with 0. No significant correlation with the solar activity is seen.

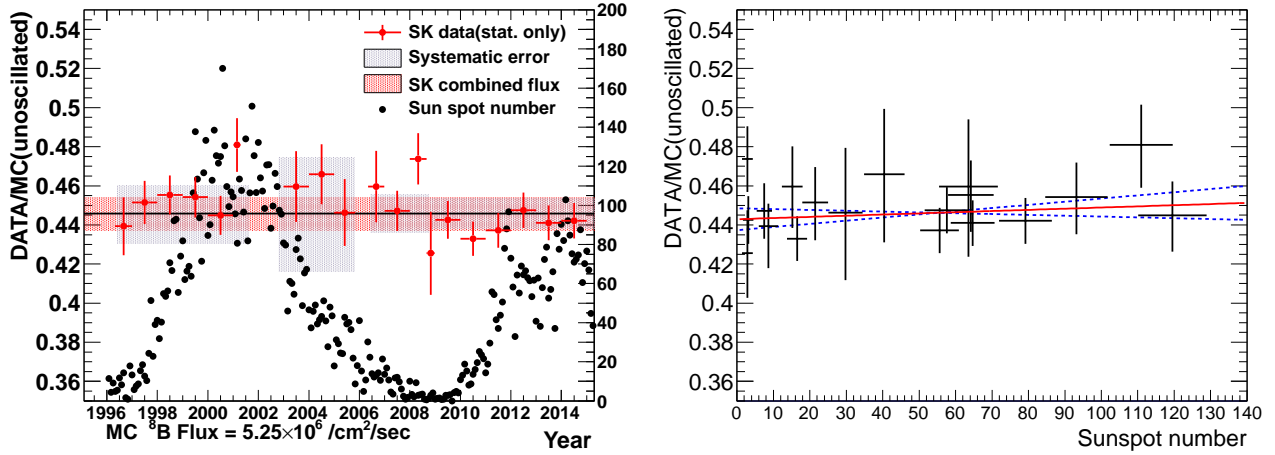


Figure 12.5: Left: The yearly variation of the  $^8\text{B}$  solar neutrino flux measured by SK. The horizontal axis shows the data in year and the left (right) horizontal axis shows the measured solar neutrino flux normalized to the unoscillated MC prediction using  $5.25 \times 10^6 / \text{cm}^2/\text{sec}$  (sunspot number). The red points show the yearly flux measured by SK (statistical error only), the gray bands show the systematic uncertainty in each SK phase, the red band shows the error on the combined solar neutrino flux and the black points show the sun spot number taken from [49]. Right: The yearly flux as a function of sunspot number. The black points show the yearly flux with the total uncertainty (stat.+syst.), the red line shows the best fit result and the blue dashed lines show the  $1\sigma$  band.

## 12.2 Energy spectrum

Figure 12.6 shows the energy spectrum with the total uncertainty in each SK phase. As mentioned before, the energy threshold is lowered to 3.5 MeV in SK-IV while the lowest energy is 4.0 MeV in SK-I and SK-III. In addition, the SK-IV data gives the most precise result among all SK phases because of the longest operation time and the smallest systematic uncertainties. The combined energy spectrum will be shown after the oscillation analysis.

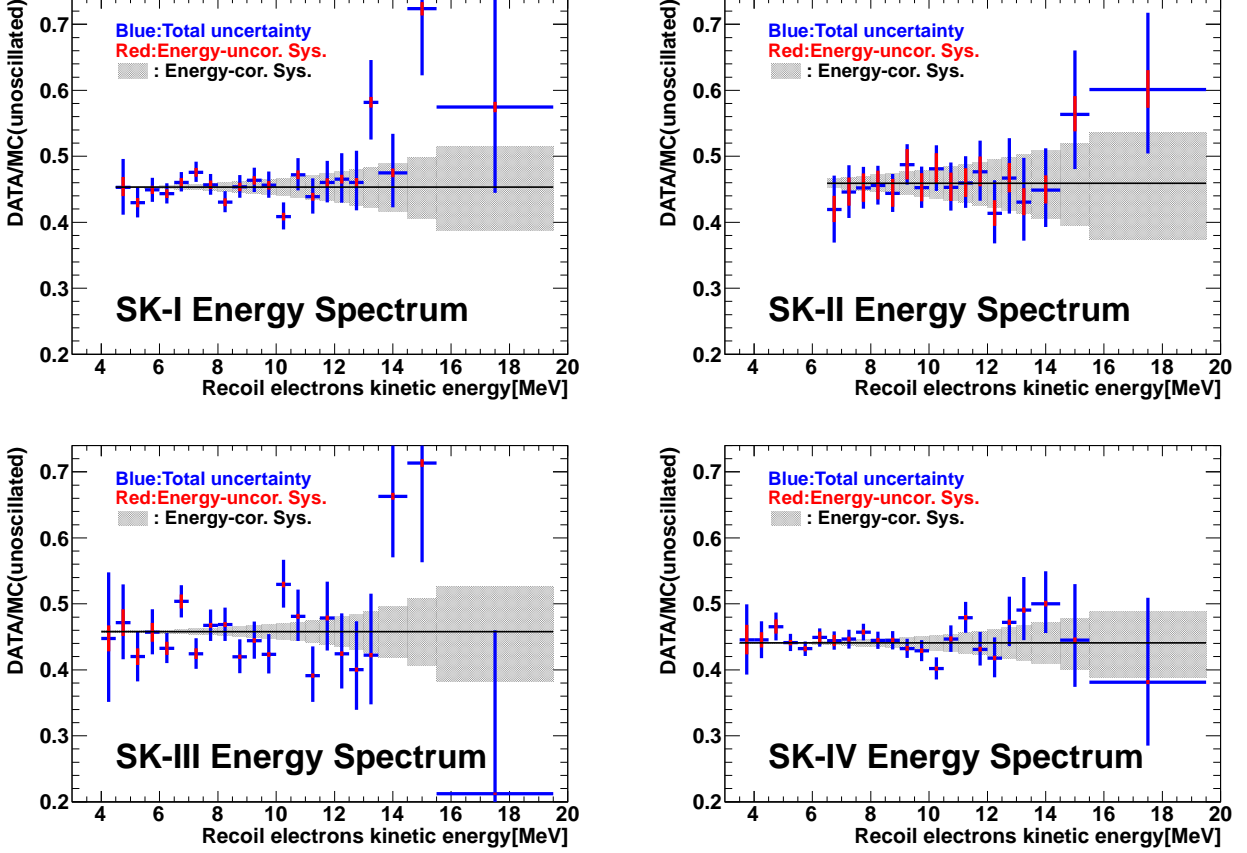


Figure 12.6: The energy spectrum in each SK phase. The horizontal axis shows the recoil electron kinetic energy [MeV] and the vertical axis shows the ratio of the measured flux to the unoscillated solar neutrino MC simulation flux. The total flux of  $5.25 \times 10^6$  /cm<sup>2</sup>/sec is assumed in the MC simulation. The SK-IV result has already been shown in Figure 11.9, however, it is put here again for comparison.

## 12.3 Oscillation Analysis

### 12.3.1 Spectrum shape prediction

The expected energy spectrum of the recoil electrons is calculated by taking into account neutrino oscillations. The survival probability of electron type neutrino is weighted by a factor  $p_e$ , survival probability of an electron neutrino, and by a factor of  $(1 - p_e)$  and a cross section ratio of  $\nu_{\mu/\tau}$  and  $\nu_e$  ( $\sigma_{\nu_{\mu/\tau}}/\sigma_{\nu_e}$ ).

Since solar neutrinos are produced at the core of the Sun, their neutrino oscillations are affected by the matter effect. Then, after going out from the surface of the Sun, neutrinos travel in vacuum. In addition, neutrinos travel through the Earth during nighttime and matter effect of the Earth must be taken into account. Thus, the predicted survival probability is calculated by taking into account the following things: (1) From the production location to the surface of the Sun, (2) From the surface of the Sun to the surface of the Earth, (3) From the surface of the Earth to the SK detector.

It is known that the traveling length from the Sun to the Earth is much longer than the vacuum oscillation length, when the current oscillation parameters are assumed. Thus, in the case (2), it is assumed that  $\nu_1$  and  $\nu_2$  of the mass eigenstates are incoherent. Under this condition, the survival probability can be expressed as

$$p_e = p_1 \times p_{1e} + p_2 \times p_{2e} = 2p_1p_{1e} + 1 - p_1 - p_{1e}, \quad (12.3.1)$$

where  $p_i$  means that  $\nu_e$  produced at the core of the Sun appears as  $\nu_i$  and  $p_{ie}$  means that  $\nu_i$  at the surface of the Earth appears as  $\nu_e$  in the SK detector [118]. In the MC simulation, the production location distribution is based on the SSM model, as shown in the right of Figure 2.5. Since the path of the observed solar neutrinos in the Sun is not identified, the expected value of  $p_1$  is obtained by averaging over the production location. On the other hand, the path through the Earth is uniquely determined when the time of the event, namely the position of the Sun, is given. Since the matter effect in the Earth also depends on the oscillation parameters ( $\Delta m^2, \theta$ ),  $p_{1e}$  is obtained as a function of both the energy and the zenith angle with various oscillation parameters, thus  $p_{ie}$  is described as  $p_{ie}(E_\nu, \Delta m^2, \theta, \cos \theta_z)$ .

Since the signal extraction is performed by using  $N_{\text{bin}} = 23$  in SK-IV, the predicted rate of the solar neutrino interaction in the  $i$ -th bin in the observed energy range from  $E_{\text{low},i}$  to  $E_{\text{high},i}$  is defined as

$$r_i = \int_{E_{\text{low},i}}^{E_{\text{high},i}} dE \int_{E_\nu} dE_\nu \Phi(E_\nu) dE_e R(E_e, E) \left( p_e \frac{d\sigma_{\nu_e}}{dE_e} + (1 - p_e) \frac{d\sigma_{\nu_\mu/\tau}}{dE_e} \right), \quad (12.3.2)$$

where  $R(E_e, E)$  is the detector response function defined as equation (10.1.1),  $d\sigma_{\nu_x}/dE_e$  is the differential cross section of the elastic scattering for  $\nu_x$ .

In the analysis, the bin of  $\cos \theta_z$  in the daytime is 1 while the bin of  $\cos \theta_z$  in the nighttime is divided into 1000. By means of this binning, the predicted event rate for  ${}^8\text{B}$  and  ${}^{\text{hep}}$  solar neutrinos in the  $i$ -th energy bin is represented as

$$B_i^{\text{osc}} = \sum_{cz=1}^{1001} \frac{\tau(cz)}{\tau_{\text{tot}}} \times r_i^{{}^8\text{B}}(cz), \quad (12.3.3)$$

$$H_i^{\text{osc}} = \sum_{cz=1}^{1001} \frac{\tau(cz)}{\tau_{\text{tot}}} \times r_i^{\text{hep}}(cz), \quad (12.3.4)$$

where  $\tau(cz)$  is the livetime of the  $cz = (\cos \theta_z)$  bin, which is obtained from the run profile corresponding to the real operation data, and  $\tau_{\text{tot}}$  is the total livetime. Figure 12.7 shows the distribution of the livetime fraction  $\tau(cz)/\tau_{\text{tot}}$ .

### 12.3.2 $\chi^2$ definition for the spectrum shape

The definition of  $\chi^2$  is

$$\chi^2 = \sum_{i=1}^{N_{\text{bin}}} \frac{[d_i - (\beta b_i + \eta h_i) \times f(E_i, \delta_B, \delta_S, \delta_R)]^2}{\sigma_i^2} + \delta_B^2 + \delta_S^2 + \delta_R^2. \quad (12.3.5)$$

The parameters used in this equation are as follows:

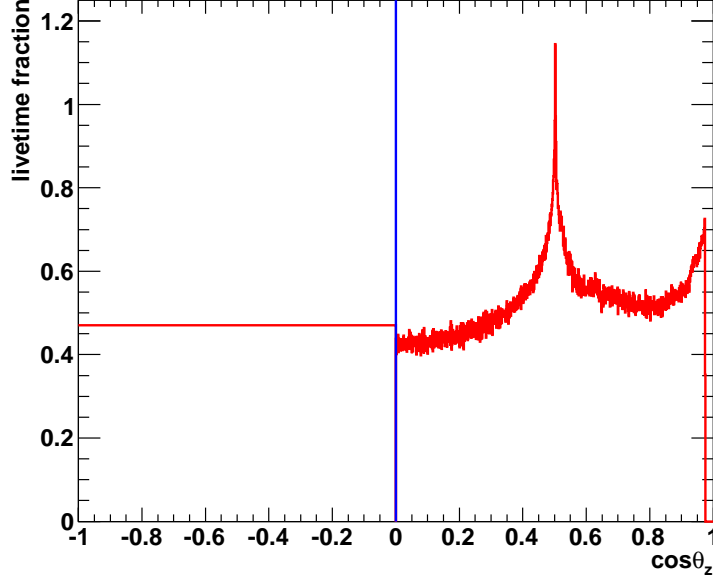


Figure 12.7: The livetime fraction as a function of  $cz(= \cos \theta_z)$ .

1.  $i$ : The  $i$ -th energy bin defined in section 9.1.
2.  $d_i$ ,  $b_i$  and  $h_i$ : Ratios of the data and the oscillated MC  $^8\text{B}$  solar neutrino event rate to the unoscillated SSM MC  $^8\text{B}$  solar neutrino event rate, which defined as:

$$d_i = \frac{D_i}{B_i + H_i},$$

$$b_i = \frac{B_i^{\text{osc}}}{B_i + H_i},$$

$$h_i = \frac{H_i^{\text{osc}}}{B_i + H_i},$$

where  $D_i$  is the observed solar neutrino event rate,  $B_i$  and  $H_i$  are the expected event rates without oscillations, which are summarized in Table 11.1.

3.  $\beta$  and  $\eta$ : The free parameters to allow the arbitrary fit of the total neutrino fluxes.
4.  $f(E_i, \delta_B, \delta_S, \delta_R)$ : The energy spectrum shape factor due to systematic uncertainties. They are defined as:

$$f(E_i, \delta_B, \delta_S, \delta_R) = f_B(E_i, \delta_B) \times f_S(E_i, \delta_S) \times f_R(E_i, \delta_R), \quad (12.3.6)$$

where  $B$  is the  $^8\text{B}$  neutrino spectrum,  $S$  is the energy scale and  $R$  is the energy resolution in the systematic errors. The function  $f_x(E_i, \delta_x)(x = B, S, R)$  is defined as:

$$f_x(E_i, \delta_x) = \frac{1}{1 + \delta_x \varepsilon_x^\pm(E_i)}, \quad (12.3.7)$$

where  $\delta_x$  is the dimensionless parameter to scale the energy correlated uncertainty and  $\varepsilon$  is the energy correlated systematic error on the spectrum shape shown in Figure 10.9.

5.  $\sigma_i$ : The combined uncertainty of statistical and energy uncorrelated systematic uncertainties in quadrature with these errors.

$\delta_x$  varies until  $\chi^2$  becomes minimum with  $\beta_{\min}$  and  $\eta_{\min}$ , where  $\beta_{\min}$  and  $\eta_{\min}$  are calculated analytically by setting the partial first derivative of  $\chi^2$  with respect to  $\beta$  and  $\eta$  to zero. When  $\beta_{\min}$  and  $\eta_{\min}$  are minimum,  $\chi^2$  is denoted by  $\chi_{\min}^2$ .

In equation (12.3.5), the uncertainty  $\sigma_i$  is calculated, taking into account the energy uncorrelated systematic uncertainty on the total flux. For this purpose, Taylor expansion of  $\chi^2$  is calculated around minimum of  $\chi_{\min}^2$ .

$$\chi^2(\beta, \eta) = \chi_{\min}^2(\beta_{\min}, \eta_{\min}) + \begin{pmatrix} \beta - \beta_{\min} \\ \eta - \eta_{\min} \end{pmatrix}^T C_0 \begin{pmatrix} \beta - \beta_{\min} \\ \eta - \eta_{\min} \end{pmatrix}, \quad (12.3.8)$$

where

$$C_0 = \sum_{i=1}^{N_{\text{bin}}} \begin{pmatrix} b_i^2/\sigma_i^2 & b_i h_i/\sigma_i^2 \\ b_i h_i/\sigma_i^2 & h_i^2/\sigma_i^2 \end{pmatrix}. \quad (12.3.9)$$

$C_0$  is scaled by a new factor  $\alpha_{\text{sys}}$  to add the total energy uncorrelated systematic uncertainty  $\sigma_{\text{sys}}$ .  $\alpha_{\text{sys}}$  is defined as

$$\alpha_{\text{sys}} = \frac{\sigma_0}{\sigma_0^2 + \sigma_{\text{sys}}^2}, \quad (12.3.10)$$

where the statistical uncertainty  $\sigma_0^2$  is also defined as

$$\sigma_0^2 = \sum_{i=1}^{N_{\text{bin}}} \frac{1}{(\sigma_{\text{stat},i})^2}. \quad (12.3.11)$$

Using  $\alpha_{\text{sys}}$ ,  $\chi^2$  is scaled as

$$\chi_{\alpha_{\text{sys}}}^2(\beta, \eta) = \chi_{\min}^2(\beta_{\min}, \eta_{\min}) + \begin{pmatrix} \beta - \beta_{\min} \\ \eta - \eta_{\min} \end{pmatrix}^T \alpha_{\text{sys}} C_0 \begin{pmatrix} \beta - \beta_{\min} \\ \eta - \eta_{\min} \end{pmatrix} \quad (12.3.12)$$

Finally,  $\chi^2$  for the energy spectrum is represented as

$$\chi_{\text{spec}}^2(\beta, \eta) = \text{Min} \left[ \chi_{\alpha_{\text{sys}}}^2(\beta, \eta, \delta_B, \delta_S, \delta_R) + \delta_B^2 + \delta_S^2 + \delta_R^2 \right] \quad (12.3.13)$$

with five fitting parameters;  $\beta, \eta, \delta_x$  ( $x = B, S, R$ ).

### 12.3.3 Time variation analysis

The time variation analysis is performed taking into account the matter effect in the Earth. The probability density of the signal  $s_{ij}$  in equation (12.3.14) is scaled by a scaling function in order to take into account the matter effect. The scaling function is defined as,  $r_i(cz)/r_i^{\text{ave}}$  where  $r_i(cz)$  is the predicted solar neutrino event rate as a function of  $\cos \theta_z$  in the  $i$ -th energy bin and  $r_i^{\text{ave}}$  is the average of the oscillated event rate over  $\cos \theta_z$ .

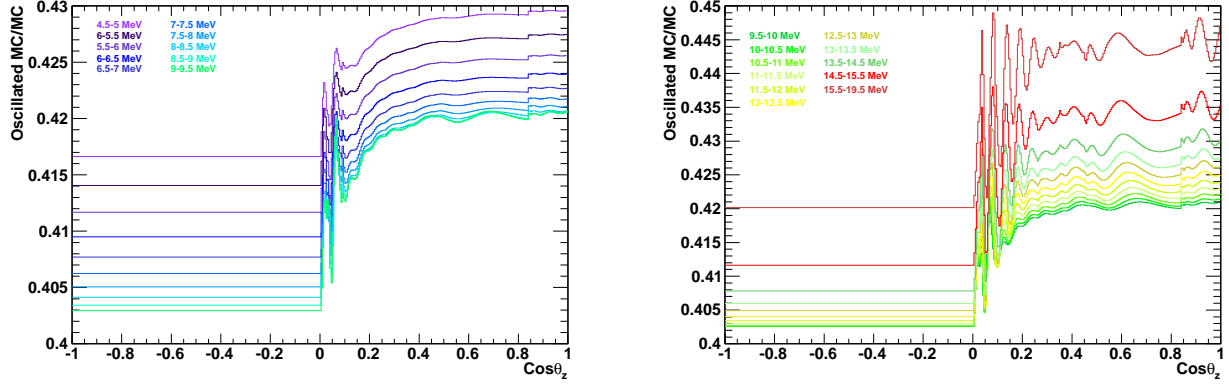


Figure 12.8: The predicted zenith angle dependence of the solar neutrino event rate. The horizontal axis shows  $\cos \theta_z$  and the vertical axis shows the ratio of the oscillated MC event rate to the unoscillated event.

The  $\cos \theta_z$  dependence of the predicted solar neutrino rate is shown in Figure 12.8 with  $\Delta m_{21}^2 = 4.84 \times 10^{-5} \text{ eV}^2$  and  $\sin^2 \theta_{12} = 0.314$ .

According to the above modification, the likelihood function is rewritten as

$$\mathcal{L}_{\text{time}} = e^{-(\sum_i B_i + S)} \prod_{i=1}^{N_{\text{bin}}} \prod_{j=1}^{n_i} (B_i \cdot b_{ij} + S \cdot Y_i \cdot s_{ij} \cdot r_i(cz) / r_i^{\text{ave}}). \quad (12.3.14)$$

Then, in order to test the matter effect in the Earth, the difference between the original  $\mathcal{L}$  and the  $\mathcal{L}_{\text{time}}$  is considered. The  $\Delta \chi_{\text{time}}^2$  is obtained as

$$\Delta \chi_{\text{time}}^2 = -2(\log \mathcal{L} - \log \mathcal{L}_{\text{time}}). \quad (12.3.15)$$

Finally, the  $\chi^2$  is defined as

$$\chi^2 = \chi_{\text{spec}}^2 + \Delta \chi_{\text{time}}^2. \quad (12.3.16)$$

Since SK has four different phases,  $\chi^2$  in each SK phase should be summed up as

$$\begin{aligned} \chi_{\text{SK,full}}^2 &= \sum_{p=0}^4 \chi_p^2 \\ &= \sum_{p=0}^4 \left( \text{Min} \left[ \chi_{\alpha_{\text{sys},p}}^2(\beta, \eta, \delta_{B,p}, \delta_{S,p}, \delta_{R,p}) + \delta_{B,p}^2 + \delta_{S,p}^2 + \delta_{R,p}^2 \right] + \Delta \chi_{\text{time},p}^2 \right). \end{aligned} \quad (12.3.17)$$

### 12.3.4 Flux constraint

When the formalization of  $\chi_{\text{spec}}^2$ , free parameters  $\beta$  and  $\eta$  are introduced. In order to minimize the difference between the data and the MC simulation prediction,  $\beta$  and  $\eta$  are allowed to have any values. For the flux constraint fit, the flux factor  $\beta$  and  $\eta$  are constrained to the total rate of the solar active neutrinos measured by SNO, hence the NC flux is used [71].

To take into account this constraint, new two terms are added to  $\chi_{\text{SK,full}}^2$  as

$$\chi_{\text{SK,full}}^2 = \sum_{p=0}^4 \chi_p^2 + \frac{(\beta - 1)^2}{\sigma_{\Phi_{8\text{B}}}} + \frac{(\eta - 1)^2}{\sigma_{\Phi_{\text{hep}}}}. \quad (12.3.18)$$

where  $\sigma_{\Phi_{8\text{B}}} (= 0.04)$  is the uncertainties from the SNO NC measurement and  $\sigma_{\Phi_{\text{hep}}} (= 2.0)$  is the uncertainty from the limit of the SSM prediction.

### 12.3.5 Oscillation analysis result

Using the flux constrained  $\chi^2$  method, an allowed region of the solar neutrino oscillation parameters is obtained. Figure 12.9 shows the allowed region of  $\tan^2 \theta_{12}$  vs  $\Delta m_{21}^2$  (left) and  $\sin^2 \theta_{12}$  vs  $\Delta m_{21}^2$  (right). The best fit parameters are

$$\sin^2 \theta_{12,\text{SK}} = 0.339_{-0.023}^{+0.027}, \quad (12.3.19)$$

$$\Delta m_{21,\text{SK}}^2 = (4.73_{-0.81}^{+1.42}) \times 10^{-5} \text{ eV}^2. \quad (12.3.20)$$

The SK measurement strongly constrains neutrino oscillation parameters. The SK measurement uniquely selects the Large Mixing Angle (LMA) solution at  $\sim 3\sigma$  level. When comparing the obtained values with those with KamLAND, they agree well in  $\sin^2 \theta_{12}$ , while there is a  $2\sigma$  tension in  $\Delta m_{21}^2$ .

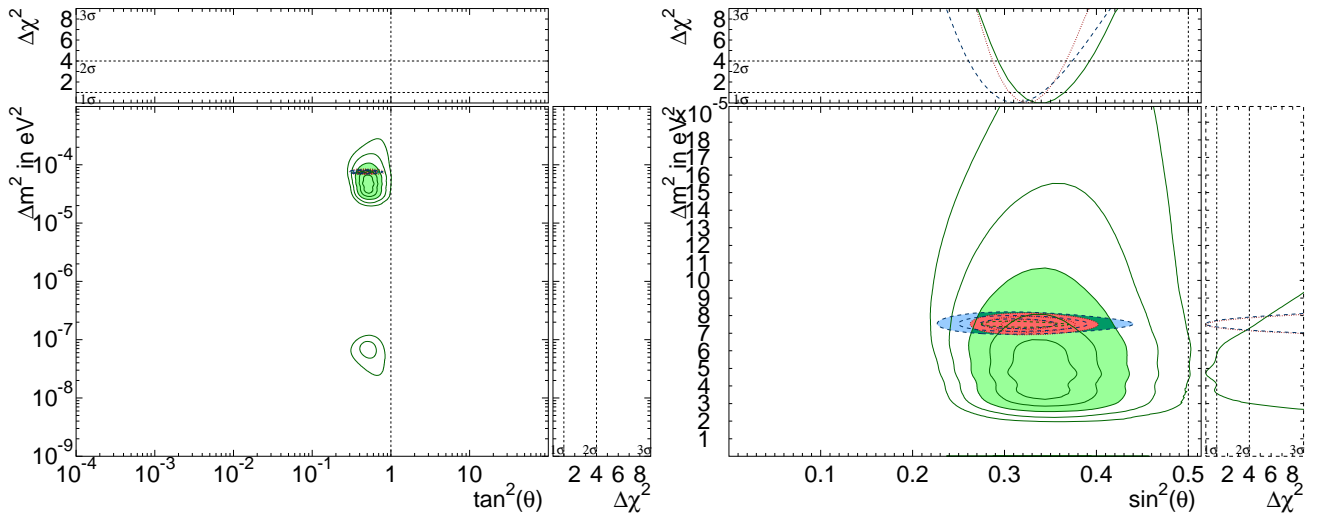


Figure 12.9: Left: The allowed region (green) from the SK combined analysis with KamLAND allowed region (light blue). The combined region is drawn in red. The horizontal axis shows  $\tan^2\theta_{12}$  and the vertical axis shows  $\Delta m_{21}^2$ . Right: The allowed region (green) from the SK combined analysis with KamLAND allowed region (light blue). The combined region is drawn in red. The horizontal axis shows  $\sin^2\theta_{12}$  and the vertical axis shows  $\Delta m_{21}^2$ .

# Chapter 13

## Discussion

### 13.1 Comparison with other solar neutrino experiments

Since both SK and SNO can observe  ${}^8\text{B}$  solar neutrinos in a similar energy range, it is better to compare them. In order to combine the SK result with the SNO result, the SNO's  $\chi^2$  is prepared [110]. It is added into the SK's  $\chi^2$  and it is used as the fifth phase of SK. Figure 13.1 shows the allowed region from the SK and SNO combined analysis. SK result is consistent with SNO result. When both results are combined, the best fit neutrino oscillation parameters are

$$\sin^2 \theta_{12,\text{SK+SNO}} = 0.321 \pm 0.013, \quad (13.1.1)$$

$$\Delta m_{21,\text{SK+SNO}}^2 = (4.78_{-0.67}^{+1.21}) \times 10^{-5} \text{ eV}^2. \quad (13.1.2)$$

The result from the radiochemical experiments, Homestake, SAGE and Gallex/GNO, and the Borexino experiment ( ${}^7\text{Be}$  only) are added into the calculation of  $\chi^2$  with SK plus SNO. The definition of  $\chi^2$  from [119] is

$$\chi_{\text{other}}^2 = \sum_{n=1, m=1}^{N=3} \left[ (R_n^{\text{Obs}} - R_n^{\text{Theor}}) (\sigma_{nm}^2)^{-1} (R_m^{\text{Obs}} - R_m^{\text{Theor}}) \right], \quad (13.1.3)$$

where the  $N = 3$  represent the number of experiments (Gallium experiments are merged),  $R_{n/m}^{\text{Obs}}$  is the observed solar neutrino rate for the  $n/m$ -th experiment,  $R_{n/m}^{\text{Theor}}$  is the predicted solar neutrino event rate based on the SSM and  $\sigma_{nm}^2$  is a matrix of squared uncertainty, which is the sum of the correlated uncertainties.

After adding the  $\chi_{\text{other}}^2$  into  $\chi^2$  of both SK and SNO, the allowed region is scanned as shown in Figure 13.2. The best fit oscillation parameters are obtained as

$$\sin^2 \theta_{12,\text{solar}} = 0.315 \pm 0.014, \quad (13.1.4)$$
$$\Delta m_{21,\text{solar}}^2 = (4.82_{-0.63}^{+1.26}) \times 10^{-5} \text{ eV}^2.$$

Then, by adding the results from KamLAND, the best fit oscillation parameters are

$$\sin^2 \theta_{12,\text{solar+KamLAND}} = 0.311 \pm 0.013, \quad (13.1.5)$$
$$\Delta m_{21,\text{solar+KamLAND}}^2 = (7.48_{-0.17}^{+0.19}) \times 10^{-5} \text{ eV}^2.$$

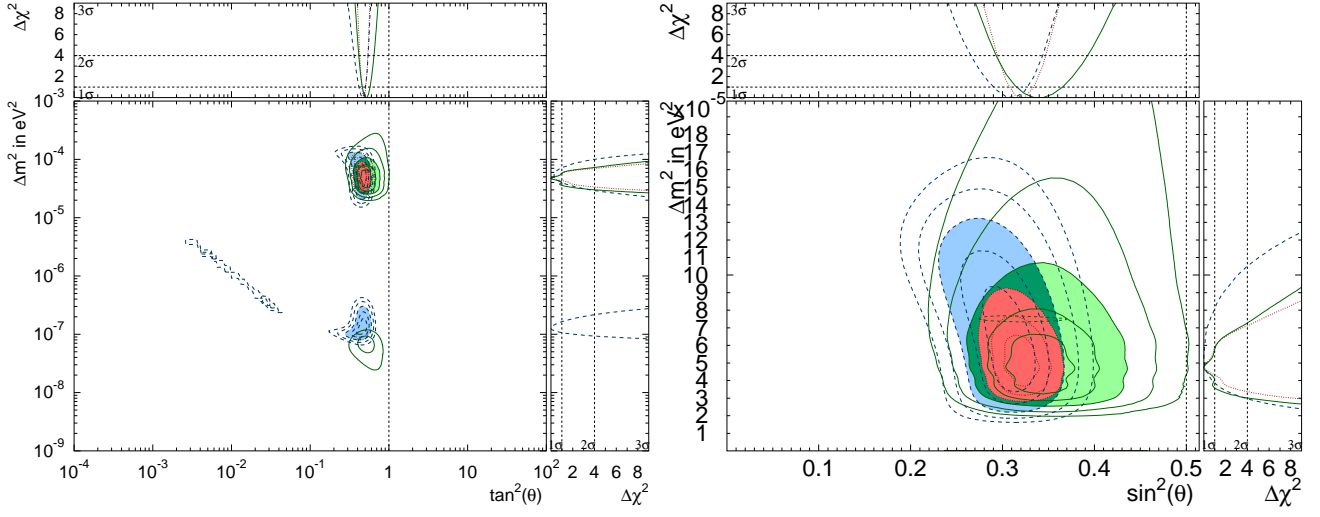


Figure 13.1: Left: The allowed region (green) from the SK combined analysis with the SNO allowed region (light blue). The combined region is drawn in red. The horizontal axis shows  $\tan^2 \theta_{12}$  and the vertical axis shows  $\Delta m_{21}^2$ . Right: The allowed region (green) from the SK combined analysis with the SNO allowed region (light blue). The combined region is drawn in red. The horizontal axis shows  $\sin^2 \theta_{12}$  and the vertical axis shows  $\Delta m_{21}^2$ .

After combining the results from the all solar experiments, a  $2\sigma$  level tension is still seen in  $\Delta m_{21}^2$  between the KamLAND result. As mentioned in chapter 1, the neutrino and anti-neutrino disappearances are governed by the same oscillation pattern assuming the CPT invariance. It is noted that this tension is not caused by the result from the SK, hence the center values from the all solar neutrino experiments are slightly smaller than the result from KamLAND.

It is also possible to obtain the mixing angle  $\theta_{13}$ , when the constraining term of  $\chi^2$  for SK plus SNO is removed. Figure 13.3 shows the allowed region in the  $\sin^2 \theta_{12}$  vs.  $\sin^2 \theta_{13}$  plane. The solar neutrino global fit is drawn in green and the best fit neutrino oscillation parameters are

$$\begin{aligned} \sin^2 \theta_{12,\text{solar}} &= 0.310_{-0.017}^{+0.022}, \\ \sin^2 \theta_{13,\text{solar}} &= 0.027_{-0.027}^{+0.024}. \end{aligned} \quad (13.1.6)$$

Then, by adding the result from the KamLAND, which is drawn in light blue, the best fit neutrino oscillation parameters are

$$\begin{aligned} \sin^2 \theta_{12,\text{solar+KamLAND}} &= 0.309_{-0.013}^{+0.014}, \\ \sin^2 \theta_{13,\text{solar+KamLAND}} &= 0.027 \pm 0.015, \end{aligned} \quad (13.1.7)$$

which gives  $\sim 2\sigma$  significance for a non-zero  $\theta_{13}$ . This result is consistent with the results from T2K and the short baseline reactor experiments [34, 37, 38].

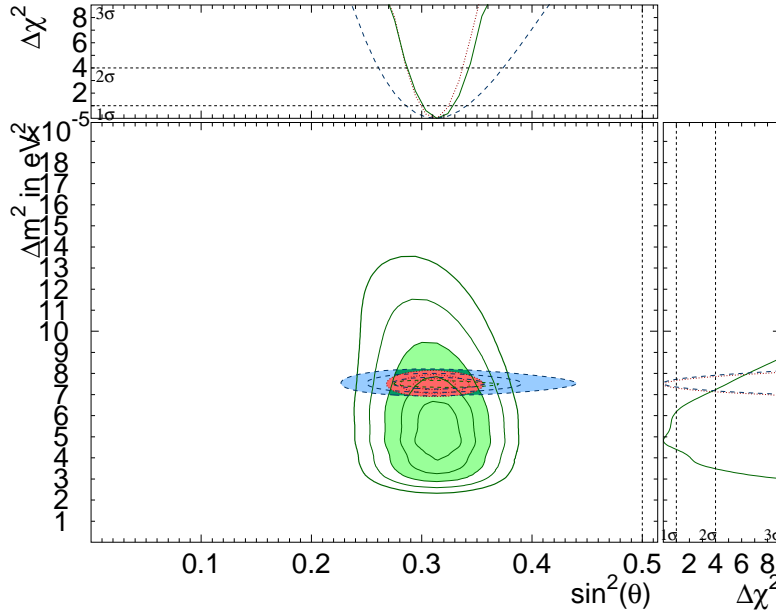


Figure 13.2: The allowed region (green) from the all solar combined analysis with the KamLAND allowed region (light blue). The combined region is drawn in red. The horizontal axis shows  $\sin^2 \theta_{12}$  and the vertical axis shows  $\Delta m_{21}^2$ .

## 13.2 Combined energy spectrum

In order to test the MSW effect, it is convenient to calculate the prediction of the energy spectrum with the measured oscillation parameters. Based on the oscillation analysis, the two sets of the oscillation parameters are used, i.e. the result from solar neutrino global (13.1.4) and solar plus KamLAND (13.1.5). In addition, the  ${}^8\text{B}$  solar neutrino flux is constrained based on the SNO NC result [71], i.e.  $5.25 \times 10^6 / \text{cm}^2 / \text{sec}$ . The numbers of bins in the energy spectrum are, 21 for SK-I, 17 for SK-II, 22 for SK-III and 23 for SK-IV, respectively. Thus the total number of bins becomes 83. Since the three parameters are constrained in the prediction, the degree of freedom is 80 in total. It is noted that this spectrum analysis is independent of the oscillation analysis, in other words, the combined spectrum shape is not used for the oscillation analysis as described in section 12.3.2.

The  $\chi^2$  between the measured energy spectrum and the prediction is calculated for each SK phase because their systematic uncertainties are not the same. Then, four  $\chi^2$ s are merged into one. Since the best fit  ${}^8\text{B}$  and *hep* solar neutrino fluxes for each phase are changed into one value in the merge-process, the value of  $\chi^2$  becomes worse. In addition, the systematic uncertainty in neutrino spectrum is also considered in the merge-process. This systematic uncertainty also contributes to the value of  $\chi^2$ . The best fit results are shown in Table 13.1.

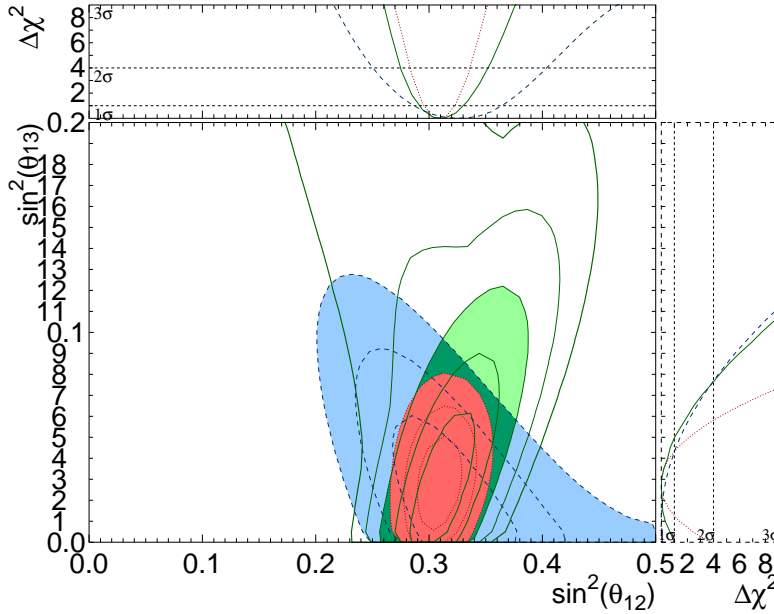


Figure 13.3: The allowed region (green) from the all solar combined analysis with the KamLAND allowed region (light blue). The combined region is drawn in red. The horizontal axis shows  $\sin^2 \theta_{12}$  and the vertical axis shows  $\sin^2 \theta_{13}$ .

On the other hand, the ratio of the measured flux to the predicted flux provides with information on the energy dependence of  $\nu_e$  solar neutrino survival probability  $P_{ee}$ . In order to discuss the survival probability of  $\nu_e$  flavor in solar neutrinos, a generic function is introduced by SNO [71] as:

$$P_{ee}(E_\nu) = c_0 + c_1 \left( \frac{E_\nu}{\text{MeV}} - 10 \right) + c_2 \left( \frac{E_\nu}{\text{MeV}} - 10 \right)^2. \quad (13.2.1)$$

This quadratic function is also used in the spectrum study. Based on the SNO analysis, the three parameters are determined from the energy spectrum measurement. The  $\chi^2$  is also listed in Table 13.1.

In addition, in order to obtain the flat shape of the energy spectrum, the parameter  $p_e$  used in equation (12.3.1) is fixed at 0.317. Under this assumption, the “up-turn” in the transition region can be suppressed. In consequence, the flat-like energy spectrum shape is obtained in the transition region. It is noted that the flat-like shape is not completely flat due to the energy dependence of the differential cross section between  $\nu_e$  and  $\nu_{\mu/\tau}$ .

Comparing the  $\chi^2$  values of four different assumptions, the flat shape prediction is preferred to the MSW predictions by 1.0 – 1.9 $\sigma$  level. The left Figure 13.4 shows the combined energy spectrum as well as the predicted energy spectra. Since the systematic uncertainties for each

phase are not the same, it is not adequate to statistically merge the energy spectra into one plot. For this reason, Figure 13.4 is used only for demonstration purposes. In addition, the survival probability is obtained from the parameters in the quadratic function. The right of Figure 13.4 shows the  $1\sigma$  allowed band of the survival probability as a function of neutrino energy.

Table 13.1: Comparison of  $\chi^2$  fitting results.

$\sin^2 \theta_{12} = 0.315, \Delta m_{21}^2 = 4.82 \times 10^{-5} \text{ eV}^2$			
Phase	$^8\text{B}$ flux [ $\times 10^6/\text{cm}^2/\text{sec}$ ]	<i>hep</i> flux [ $\times 10^3/\text{cm}^2/\text{sec}$ ]	$\chi^2$
SK-I	5.47	56.3	5.35
SK-II	5.41	40.8	19.07
SK-III	5.49	14.6	28.36
SK-IV	5.37	16.2	17.51
Combined	5.43	14.6	72.47
$\sin^2 \theta_{12} = 0.311, \Delta m_{21}^2 = 7.48 \times 10^{-5} \text{ eV}^2$			
Phase	$^8\text{B}$ flux [ $\times 10^6/\text{cm}^2/\text{sec}$ ]	<i>hep</i> flux [ $\times 10^3/\text{cm}^2/\text{sec}$ ]	$\chi^2$
SK-I	5.29	54.6	5.38
SK-II	5.27	39.4	19.56
SK-III	5.30	15.5	28.92
SK-IV	5.17	16.0	18.43
Combined	5.23	15.0	74.79
quadratic fit $(c_0, c_1, c_2) = (0.3355, 0.0014, 0.0008)$			
Phase	$^8\text{B}$ flux [ $\times 10^6/\text{cm}^2/\text{sec}$ ]	<i>hep</i> flux [ $\times 10^3/\text{cm}^2/\text{sec}$ ]	$\chi^2$
SK-I	5.26	50.3	5.39
SK-II	5.21	36.0	18.94
SK-III	5.28	10.5	27.95
SK-IV	5.17	13.0	17.21
Combined	5.22	12.9	71.25
flat shape			
Phase	$^8\text{B}$ flux [ $\times 10^6/\text{cm}^2/\text{sec}$ ]	<i>hep</i> flux [ $\times 10^3/\text{cm}^2/\text{sec}$ ]	$\chi^2$
SK-I	5.52	58.5	5.26
SK-II	5.47	42.6	18.81
SK-III	5.55	13.4	27.97
SK-IV	5.45	16.6	17.67
Combined	5.50	14.1	71.42

## 13.3 Future prospect

### 13.3.1 “Up-turn” observation

Although it is not statistically significant, the spectrum shape of combined spectrum might show a hint of the upturn observation. To observe the “up-turn” of the energy spectrum due

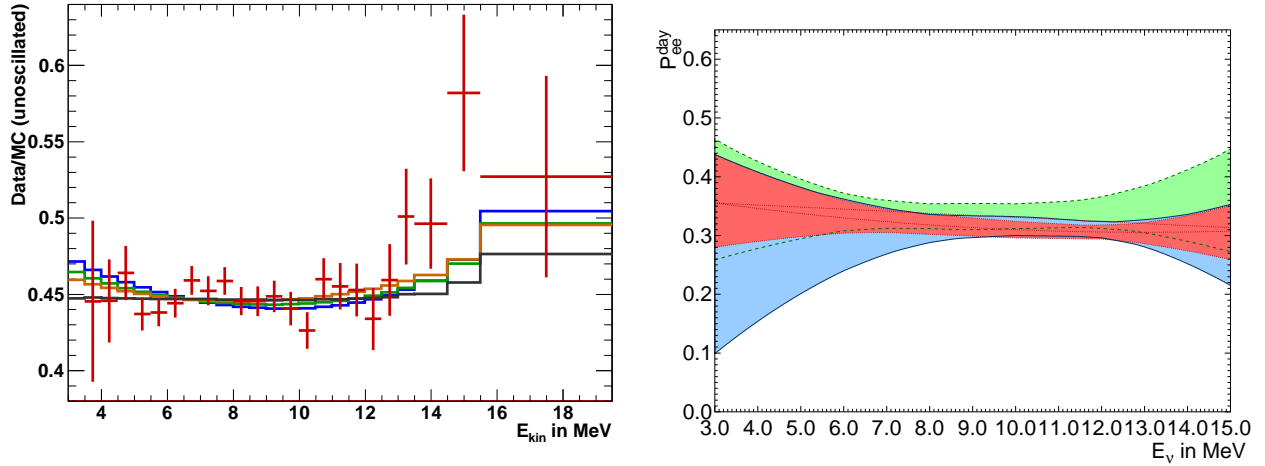


Figure 13.4: Left: SK combined energy spectrum together with the MSW prediction curves. The horizontal axis shows the recoil electron kinetic energy [MeV] and the vertical axis shows the observed event rate normalized by the unoscillation prediction,  $5.25 \times 10^6$  /cm<sup>2</sup>/sec. The red points show the data, the green curve shows the predicted distorted shape with  $(\sin^2 \theta_{12}, \Delta m_{12}^2) = (0.315, 4.82 \times 10^{-5})$  from solar neutrino global and the blue curve shows the predicted distorted shape with  $(\sin^2 \theta_{12}, \Delta m_{12}^2) = (0.311, 7.48 \times 10^{-5})$  from solar plus KamLAND. The orange curve shows the quadratic fit, where  $(c_0, c_1, c_2) = (0.3355, 0.0014, 0.0008)$  and the black curve shows the flat shape prediction. Right: The survival probability. The horizontal axis shows the neutrino kinetic energy in MeV and the vertical axis shows the survival probability. The green and blue contour show the allowed region obtained from the SK and the SNO [71]. The red contour shows the SK plus SNO combined allowed region.

to the MSW effect, it is required to improve the detector sensitivity to the lower energy solar neutrino. Some possible ways to improve the sensitivity is discussed in this section. Related with works presented in this thesis, the following topics are considered.

1. Background level in the solar neutrino analysis.
2. Trigger (Detection) efficiency for the lower energy region.

## Background level

As described in section 8.4, the background level should be reduced by a factor of 10 to observe the solar neutrino in the bottom region in the SK tank. Since it is found that EPDM gaskets used in the membrane degasifier system emanate Rn, they should be replaced to the low background Urethane type gaskets to reduce the Rn concentration in the supply water. If the refurbishment is completed, it is expected that the Rn concentration in the supply water will be reduced. Therefore, it is expected that the background events in the solar analysis will be reduced.

Currently, the dominant uncertainty in the 3.5 – 4.0 MeV (kin) region is statistical uncertainty as described in equation (11.4.1). If the Rn background reduction above is completed,

the analysis fiducial volume is expected to be enlarged by a factor of  $\sim 2$  (8.85 kton  $\rightarrow$  22.45 kton). The enlargement of the analysis volume can help to reduce statistical uncertainty.

In addition, the analysis energy threshold can be lowered below the current 3.5 MeV, when the low background level is achieved. The lowered energy threshold can improve the sensitivity to the “up-turn” of the energy spectrum caused by the MSW effect as described in subsection 2.3.1.

### Trigger (detection) efficiency

As mentioned in Table 3.6, the hit threshold of SLE trigger was changed from 34 to 31 in May 2015. It allows to detect the low energy event more efficiently. Figure 13.5 shows the energy dependence of the SLE trigger efficiency when the hit threshold is 31 or 34. As expected, the detection efficiency is improved in the low energy region when the hit threshold is lowered. For example, in 3.5 – 4.0 MeV region, the trigger efficiency changes from  $\sim 88\%$  to  $\sim 99\%$ .

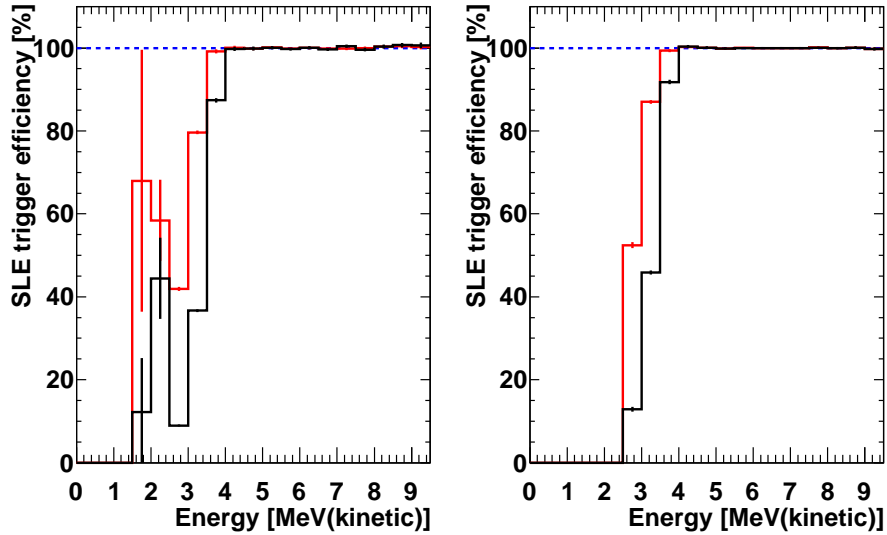


Figure 13.5: The comparison of the trigger efficiency when the trigger hit threshold is 31 vs. 34. This data is taken at the center calibration hole  $(x, y, z) = (+0.353, -0.707, 0.0)$  m. The left (right) panel shows the calibration data (MC simulation). The red (black) hist shows the trigger efficiency when the hit threshold is 31 (34) hit. The horizontal axis shows the reconstructed energy [MeV] and the vertical axis shows the trigger efficiency [%].

The largest systematic uncertainty in the 3.5 – 4.0 MeV region is related with the trigger efficiency, where it is  $+3.6/ - 3.3\%$ , as shown in Table 10.2. This systematic uncertainty is caused by the difference in the data and the solar neutrino MC simulation as described in Chapter 7. Under the condition where the hit threshold is 31, the difference in the data and the MC simulation is expected to be  $< \pm 1.0\%$  in the 3.5 – 4.0 MeV region. Thus, the systematic uncertainty in the 3.5 – 4.0 MeV region can be reduced by lowering the hit threshold.

## Estimation of the sensitivity to the “up-turn”

Assuming the following conditions will be satisfied, the sensitivity to the “up-turn” of the energy spectrum is estimated.

1. The detection efficiency in the lower energy region is  $\sim 100\%$ .
2. Background level is lowered by a factor of 1.5 – 2 in the tight fiducial volume. The current event rate in the (tight) fiducial volume is shown in Figure 6.17. For example, the event rate in the 3.5 – 4.0 MeV region should be lowered from 3 – 5 event/day/kton to 1 – 3 event/day/kton.
3. The (energy correlated) systematic uncertainty is half of the current evaluation.

The first and second conditions above are (expected to be) achieved based on the works presented in this thesis. The first condition has been already achieved when the hit threshold of the data acquisition is lowered from 34 to 31 as described above.

The second condition will be achieved, when the refurbishment of the membrane degasifier system is completed as described in section 8.4.

The third condition, the systematic uncertainty, should be studied after the refurbishment of the membrane degasifier system in the future.

Under the conditions above, the significance for “up-turn” is estimated, as in Figure 13.6. It is expected that roughly  $3\sigma$  observation will be achieved within approximately 6 years.

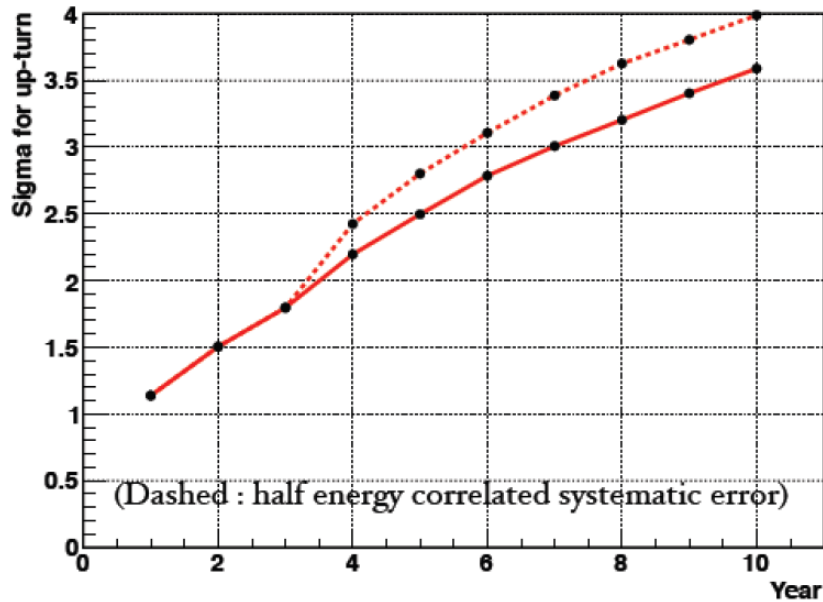


Figure 13.6: Sensitivity to the MSW effect (upturn) in future. The horizontal axis shows the operation period and the vertical axis shows the significant for the upturn measurement. The assumption in the text is considered. The solid line assumes that the background level is lowered by a factor of  $\sim 2$ . The dashed line assumes that the background level is lowered by a factor of  $\sim 2$  and the energy correlated systematic uncertainty is half 3 years later.

### 13.3.2 Day/Night flux asymmetry

Since the day/night flux asymmetry measurement is statistically limited, it is required to take more data. For 5- to 10-year observation, the significance of the day/night flux asymmetry will achieve  $\sim 3\sigma$  level.

# Chapter 14

## Conclusion

The solar neutrino analysis using the fourth phase of the Super-Kamiokande, SK-IV, is carried out to observe the MSW effect. In order to improve the sensitivity to the MSW effect, the analysis energy threshold is lowered to 3.5 MeV in kinetic energy. For this purpose, the detection efficiency, which includes the trigger efficiency and the data reduction, is precisely evaluated, using calibration sources. In addition, a study of background at lower energy region is performed and it is found that main background source is identified as radon in the tank water.

The flux of  $^8\text{B}$  solar neutrinos is revised, using all observed solar neutrino events above 3.5 MeV. In this thesis, systematic uncertainties of various reduction cuts are precisely re-evaluated also for higher energy solar neutrino events. Finally, the total systematic uncertainty on the  $^8\text{B}$  solar neutrino flux is estimated to be  $\pm 1.7\%$ , which is the lowest among all SK phases.

Using 2055.5 day's data sample taken in SK-IV, the observed  $^8\text{B}$  solar neutrino flux is

$$\Phi_{s\text{B},\text{SK4}} = 2.314 \pm 0.018(\text{stat.}) \pm 0.039(\text{syst.}) \times 10^6/\text{cm}^2/\text{sec},$$

which is consistent with SK-I through SK-III results. In the 3.5 – 4.0 MeV region, the number of the extracted solar neutrino signal is

$$1299_{-154}^{+156}(\text{stat.})_{-64}^{+66}(\text{syst.}) \text{ events},$$

which is the most precise (statistically significant) measurement among the all solar neutrino experiments.

Combining the results in all SK phases, the  $^8\text{B}$  solar neutrino flux is

$$\Phi_{s\text{B},\text{SK}} = 2.341 \pm 0.044(\text{stat.} + \text{syst.}) \times 10^6/\text{cm}^2/\text{sec}.$$

The day/night asymmetry is expected from the matter effect of the Earth. The flux is measured separately for daytime and nighttime and their asymmetry is

$$\begin{aligned} A_{\text{DN},\text{SK}} &= \frac{\Phi_{\text{Day}} - \Phi_{\text{Night}}}{(\Phi_{\text{Day}} + \Phi_{\text{Night}})/2} \\ &= (-3.3 \pm 1.1(\text{stat.}) \pm 0.8(\text{syst.})) \%, \end{aligned}$$

where it is  $2.4\sigma$  away from zero. The SK data shows  $2.4\sigma$  level asymmetry of the day/night difference.

The correlation between  $^8\text{B}$  solar neutrino fluxes observed by SK and the solar activity is yearly evaluated. First of all, the  $\chi^2$  assuming a constant flux is calculated to be  $\chi^2 = 12.86/18$  d.o.f, which corresponds to 80%. The fit taking into account the linear correlation with sunspot number is given. No significant correlation is seen.

The neutrino oscillation analysis combing all SK phases is performed. Obtained oscillation parameters are

$$\begin{aligned}\sin^2 \theta_{12,\text{SK}} &= 0.339_{-0.023}^{+0.027}, \\ \Delta m_{21,\text{SK}}^2 &= 4.73_{-0.81}^{+1.42} \times 10^{-5} \text{ eV}^2.\end{aligned}$$

In addition, the oscillation analysis including all solar neutrino experiments (SK, Chlorine, Gallium, SNO and Borexino) is performed and obtained oscillation parameters are

$$\begin{aligned}\sin^2 \theta_{12,\text{solar}} &= 0.315 \pm 0.014, \\ \Delta m_{21,\text{solar}}^2 &= 4.82_{-0.63}^{+1.26} \times 10^{-5} \text{ eV}^2.\end{aligned}$$

The value of  $\sin^2 \theta_{12}$  is consistent with the KamLAND  $\bar{\nu}_e$  measurement ( $\sin^2 \theta_{12,\text{KamLAND}} = 0.312_{-0.025}^{+0.033}$ ). However,  $\sim 2\sigma$  level tension is seen in  $\Delta m_{21}^2$  compared with the value in KamLAND ( $\Delta m_{21,\text{KamLAND}}^2 = 7.54_{-0.18}^{+0.19} \times 10^{-5} \text{ eV}^2$ ). Combining the solar neutrino global result and the KamLAND result, the oscillation parameters are obtained as

$$\begin{aligned}\sin^2 \theta_{12,\text{solar+KamLAND}} &= 0.311 \pm 0.013, \\ \Delta m_{21,\text{solar+KamLAND}}^2 &= 7.48_{-0.17}^{+0.19} \times 10^{-5} \text{ eV}^2.\end{aligned}$$

The 3-flavor oscillation analysis is also performed. When combining all SK phases and other solar neutrino experiments, the best fit parameters are given as

$$\begin{aligned}\sin^2 \theta_{12,\text{solar}} &= 0.310_{-0.017}^{+0.022}, \\ \sin^2 \theta_{13,\text{solar}} &= 0.027_{-0.027}^{+0.024}.\end{aligned}$$

Then, by adding the result from KamLAND experiment, the best fit parameters are

$$\begin{aligned}\sin^2 \theta_{12,\text{solar+KamLAND}} &= 0.309_{-0.013}^{+0.014}, \\ \sin^2 \theta_{13,\text{solar+KamLAND}} &= 0.027 \pm 0.015.\end{aligned}$$

which is consistent with the results from the T2K and the short baseline reactor experiments.

In summary, the SK solar neutrino data is consistent with the global oscillation analysis of solar plus KamLAND. However, there is a  $2\sigma$  level tension between solar neutrino global and KamLAND  $\Delta m_{21}^2$ . The main reason for the tension is the larger value of the day/night asymmetry and small distortion of the energy spectrum.

Because of the MSW effect, the ‘‘up-turn’’ of the energy spectrum should be observed. Using the low threshold SK-IV data combined with SK-I, II and III, the spectrum shape is discussed. The  $\chi^2$  of the observed spectrum with respect to general quadratic fit, flat shape, the solar neutrino global best fit oscillation parameters and solar plus KamLAND best fit oscillation parameters are 71.25, 71.42, 72.47 and 74.79, respectively. The flat shape is favored by  $1.1 - 1.9\sigma$  level compared with the MSW prediction with best fit oscillation parameters.

Based on the study of the detection efficiency and the background, the future prospect for the observation to the “up-turn” of the energy spectrum is discussed. With the improvements of the detection efficiency and the reducing the radon background in the solar analysis, the “up-turn” of the energy spectrum due to the MSW effect is expected to be observed at  $\sim 3\sigma$  level within about 6 years.

# Appendix A

## Rn measurement system

In order to understand the origin of the background events in SK, it is required to measure the Rn concentration in ultra pure water. For this purpose, a Rn measurement system is developed. However, it is difficult to measure  $\sim 0.1$  mBq/m<sup>3</sup> level of the Rn concentration in purified water. Therefore, firstly new low BG 80 L Rn detector had been developed [102]. In order to increase the sensitivity of the Rn detector, increasing the volume of the detector is the straight forward way. However, it costs high and it is necessary to calibrate the detector, which takes long time. Hence, it is chosen to measure Rn concentration using activated charcoal.

The strategy for direct measurement of the Rn concentration in purified water is follows:

1. Degas Rn from purified water with a Rn extraction mixer which is newly developed.
2. Absorb Rn into the cooled activated charcoal.
3. Degas Rn from the activated charcoal.
4. Measure the Rn concentration with the Rn detector.

### A.1 Development of Rn extraction system

#### A.1.1 Mechanical structure

Figure A.1 shows a schematic diagram of Rn extraction system from water to air, as it mixes water with air. It is called “mixer” hereafter. This mixer consists of 12 wing units, an inlet part and an outlet part for water and air, and a water buffer tank.

The inside of the wing unit is welded with 4 wings which direct downward. Its height is 60.0 mm, its inner diameter is 41.6 mm and its outer diameter is 48.6 mm. The 6 right-turn wing units and 6 left-turn wing units are prepared, then they are welded with each others alternately. Each wing has many holes as described in Figure A.1. The surface of the inside is electro-polished including holes.

The sampled water is supplied from the inlet at the top while pure air is also supplied to the mixer from the inlet at the bottom. As water falls down through the mixer and hits against the wings, water becomes mist-like and is mixed with pure air. During this process, Rn is degassed from the sampled water and degassed to the air. The mixed air is sampled from the outlet at the top of the mixer.

Degassed water after mixing is stored in the water tank under the mixer. The water tank is made of PVC and it has three layers to prevent Rn outside from coming into the mixer.

### A.1.2 Extraction efficiency

Total radioactivity of Rn in water and air is the same before and after they are mixed

$$C_{w,0}F_w\Delta t + C_{a,0}F_a\Delta t = C_wF_w\Delta t + C_aF_a\Delta t, \quad (\text{A.1.1})$$

where  $C_{w,0}$  ( $C_{a,0}$ ) is the Rn concentration in water (air) before mixing,  $C_w$  ( $C_a$ ) is the Rn concentration of water (air) after mixing,  $F_w$  ( $F_a$ ) is the flow rate of water (air) through this mixer and  $\Delta t$  is small unit time.

The equation (A.1.1) is re-written as follows

$$1 = \frac{C_w}{C_{w,0}} + \frac{C_a - C_{a,0}}{C_{w,0}} \times \frac{F_a}{F_w}. \quad (\text{A.1.2})$$

The first term is the ratio of the Rn concentration in purified water before mixing and after mixing. The second term is the ratio between the sampled water before mixer and mixed air after mixer. The second term in equation (A.1.2) is the efficiency of Rn extraction in this system

Thus, the Rn extraction efficiency can be determined by measuring the Rn concentration in both air and water. For the Rn concentration in air, the Rn detector which has been developed is used [120, 102]. For the Rn concentration in water, the liquid scintillator method which is defined as a standard Rn concentration measurement method for hot spring water is adopted. For this purpose, Liquid Scintillator Counter system (LSC) is used.

### A.1.3 Calibration setup

To obtain the Rn extraction efficiency, a calibration system is constructed. Figure A.2 shows a schematic diagram of the calibration system.

The system consists of a 70 L Rn detector [120], an air flow meter, two pressure gauges for monitoring the pressure inside of the mixer, a mass flow meter, an electrical dehumidifier for removing water in degassed air, an air pump and an ionization chamber.

The electrical dehumidifier is installed just after the mixer to remove water in the air because the ionization chamber is sensitive to humidity.

The calibration data are taken under the atmospheric pressure because it is doubted that the Rn extraction efficiency is sensitive to the pressure.

In this calibration system, the water flow rate is set at  $F_w = 4.0$  L/min.

### A.1.4 Calibration method

This calibration is performed by the following steps.

**Step I** Set water flow rate and air flow rate. After setting, keep running for over 12 hours.

**Step II** Sample input water and output water into shake flasks.

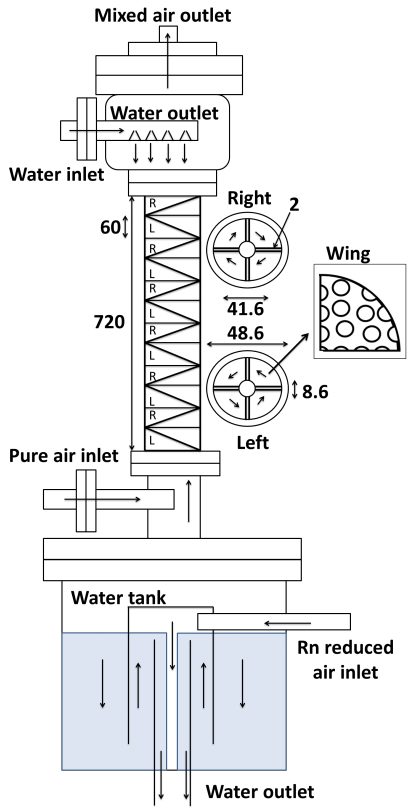


Figure A.1: A schematic diagram of Rn extraction system. The length described in this figure as in unit of mm. Arrows in each mixer unit explain the direction of the wings from top to bottom of these units.

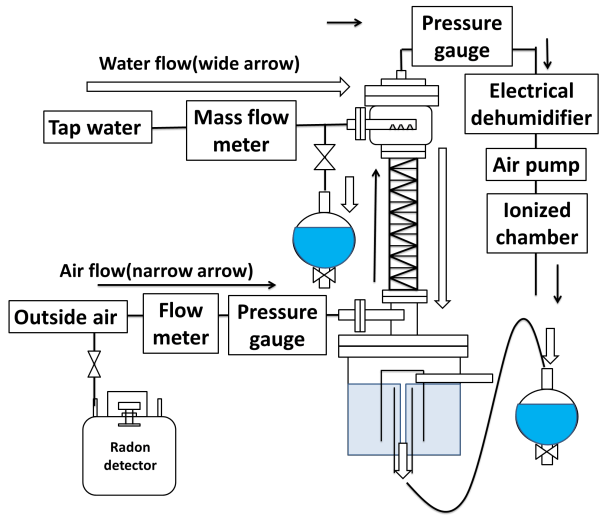


Figure A.2: A schematic diagram of the calibration setup.

**Step III** Measure the Rn concentration of outside air ( $C_{a,0}$ ) with the high sensitivity 70 L Rn detector, and measure that of output air ( $C_a$ ) with the ionization chamber.

**Step IV** Measure the Rn concentration in the input water ( $C_{w,0}$ ) and the output water ( $C_w$ ) with the LSC system.

**Step IV** Substitute these measured values for the corresponding variables in equation (A.1.2).

### A.1.5 Systematic uncertainties

The systematic uncertainties in the Rn extraction efficiency in the calibration are follows:

- The accuracy of the Rn concentration measurement with the ionization chamber  $\pm 5\%$ .
- The accuracy of the Rn concentration measurement with 70 L Rn detector  $\pm 1\%$ . Originally the 70 L Rn detector has  $\pm 10\%$  uncertainty but the contribution of this uncertainty is quite small because the Rn concentration in input-outside air ( $C_{a,0}$ ) is less than 0.01 Bq/L, while those from other sources are more than 2.5 Bq/L.
- The accuracy of the LSC system  $\pm 10\%$ .
- The stability of the water flow controlled by the mass flow meter  $\pm 2\%$ .

According to these uncertainties, the total systematic uncertainty is estimated as  $\pm 11.4\%$ .

### A.1.6 Calibration result

Figure A.3 shows the result of the calibration in the case of  $F_w = 4.0$  L/min and  $F_a = 2.0$  L/min. The ratio of the flow rate is  $F_a/F_w = 0.508 \pm 0.004$ , the terms in equation (A.1.2) are

$$\frac{C_w}{C_{w,0}} = 0.344 \pm 0.040(\text{stat.} + \text{syst.}), \quad (\text{A.1.3})$$

$$\frac{C_a - C_{a,0}}{C_w} \times \frac{F_a}{F_w} = 0.654 \pm 0.084(\text{stat.} + \text{syst.}). \quad (\text{A.1.4})$$

By adding (A.1.3) and (A.1.4), the obtained result is  $0.998 \pm 0.093(\text{stat.} + \text{syst.})$ . It is confirmed that the total radio activity before and after mixing is conserved within the total uncertainty.

## A.2 Measurement system and method

### A.2.1 Absorption and desorption with activated charcoal

Activated charcoal is an effective absorbent for various impurities by physical absorption. Activated charcoal completely absorbs Rn in purified air, when it is cooled under  $-60\text{ }^\circ\text{C}$  and desorbs, when it is heated over  $120\text{ }^\circ\text{C}$  [101]. So, a simple Rn trap is constructed in order to absorb or desorb Rn in purified air. The Rn trap is a 1/2-inch stainless U-tube which contains 12.5 g activated charcoal. This U-tube can be put into liquid ethanol in a dewar vessel and chilled with a refrigerator, while it is heated by a band heater when needed.

A commercial activated charcoal, DIASORB G4-8 produced by Calgon Carbon Japan KK, is used for the Rn trap. The typical size of this activated charcoal is between  $2.4 \sim 4.8$  mm in diameter. The average of its pore diameter is  $19\text{ \AA}$  and its pore volume is less than  $300\text{ \AA}$  ( $0.46\text{ mL/g}$ ). Its specific surface is  $980\text{ m}^2$ .

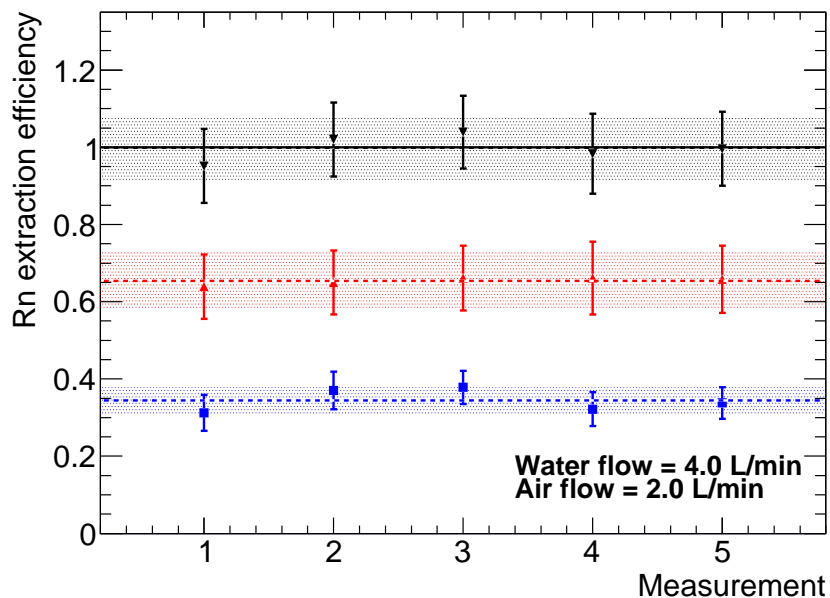


Figure A.3: Efficiency of Rn extraction with the mixer. 5-times calibrations are performed when the water flow rate is set at 4.0 L/min and the air flow rate is set at 2.0 L/min. The blue plots show the first term, and the red plots show the second term in equation (A.1.2). In addition, the black plots show the sum of these terms and they are corresponding to 1.0 within the total uncertainty.

## A.2.2 Measurement setup

Figure A.4 (Figure A.5) shows a schematic diagram of this measurement system when an absorption (desorption) process. The SK water is sampled from the SK tank or the water flowing lines by a water circulation pump. Then, the sampled water is supplied into the mixer and it is mixed with purified air.

The mixer is connected with an electrical dehumidifier, two cooled copper wool traps, the cooled activated charcoal trap, a dewpoint meter, a mass flow meter, an air circulation pump and a 80 L Rn detector. The cooled copper wool traps and the cooled activated charcoal trap are put into stainless steel 3/4 and 1/2 inch U-tubes respectively and they are put into chilled liquid ethanol with the refrigerator.

## A.2.3 Measurement method

There are two steps to measure the Rn concentration in purify water. The first step is an absorption process to absorb Rn into cooled activated charcoal. The second step is a desorption process to extract Rn from activated charcoal with a band heater.

First one is performed in the following steps.

**Step 1** Before stating this measurement, the inside of the piping line except for the mixer and the activated charcoal trap, is evacuated with a vacuum pump at less than  $1.0 \times 10^{-4}$  Pa level.

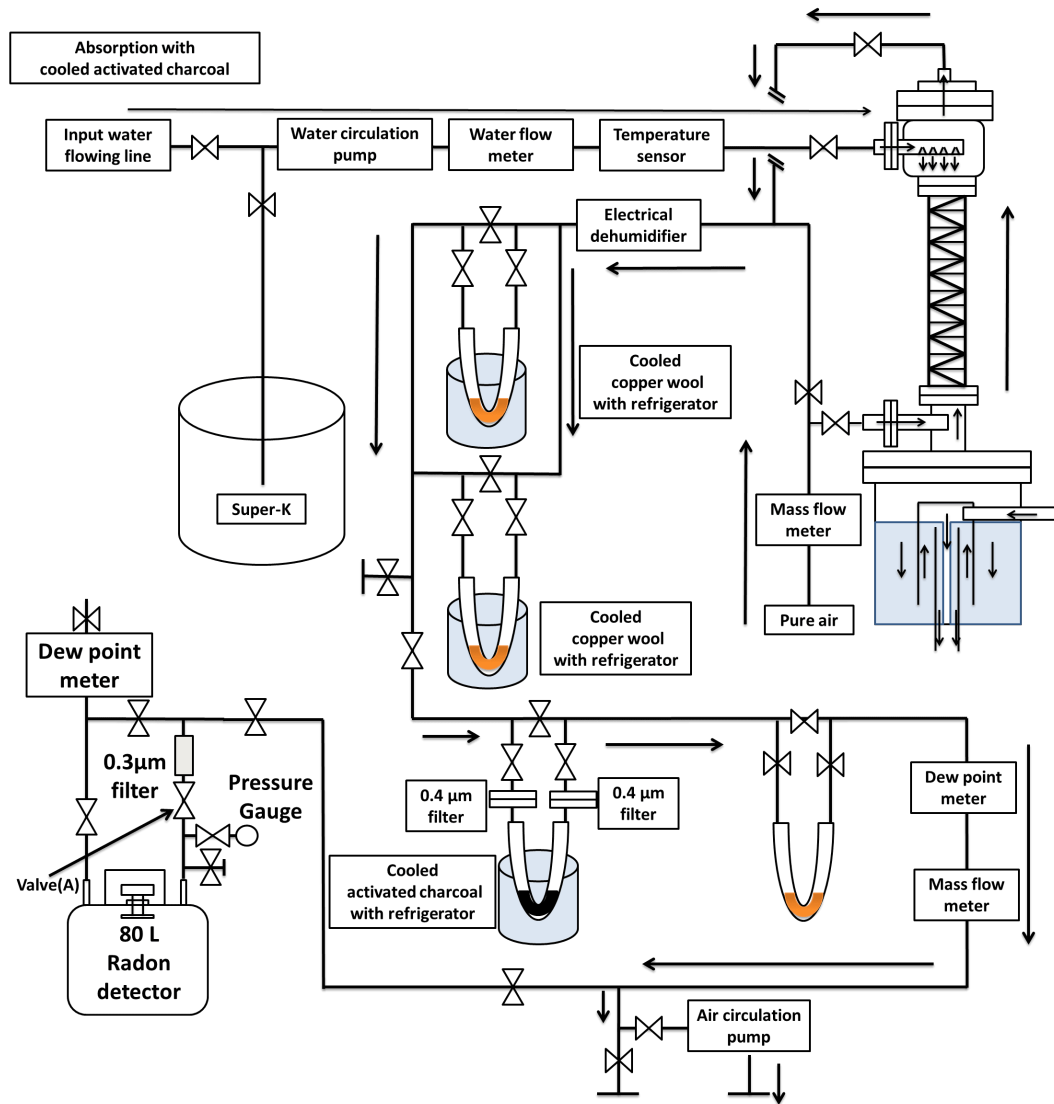


Figure A.4: A schematic diagram of the measurement system when the absorption process.

- Step 2** Then, close all valves and open the Rn trap. Heat the trap with a 230 °C band heater.
- Step 3** Keep this state for over 1.5 hours with the inside of the Rn trap in vacuum.
- Step 4** After the heating, close the valves of the the Rn trap and remove the band heater. Then, cool down the Rn trap with the dewar vessel filled with  $-90\text{ }^{\circ}\text{C}$  ethanol.
- Step 5** Purge Rn extraction mixer with pure air for over 1 hours.
- Step 6** After the purge, set air flow rate at 2.0 L/min. Then, sample the SK water with the water circulation pump at 4.0 L/min. Open the valves as in Figure.A.4.
- Step 7** Keep this state for several hours.
- Step 8** During this absorption step, make the inside of the Rn detector evacuated at less than  $4.0 \times 10^{-4}$  Pa.

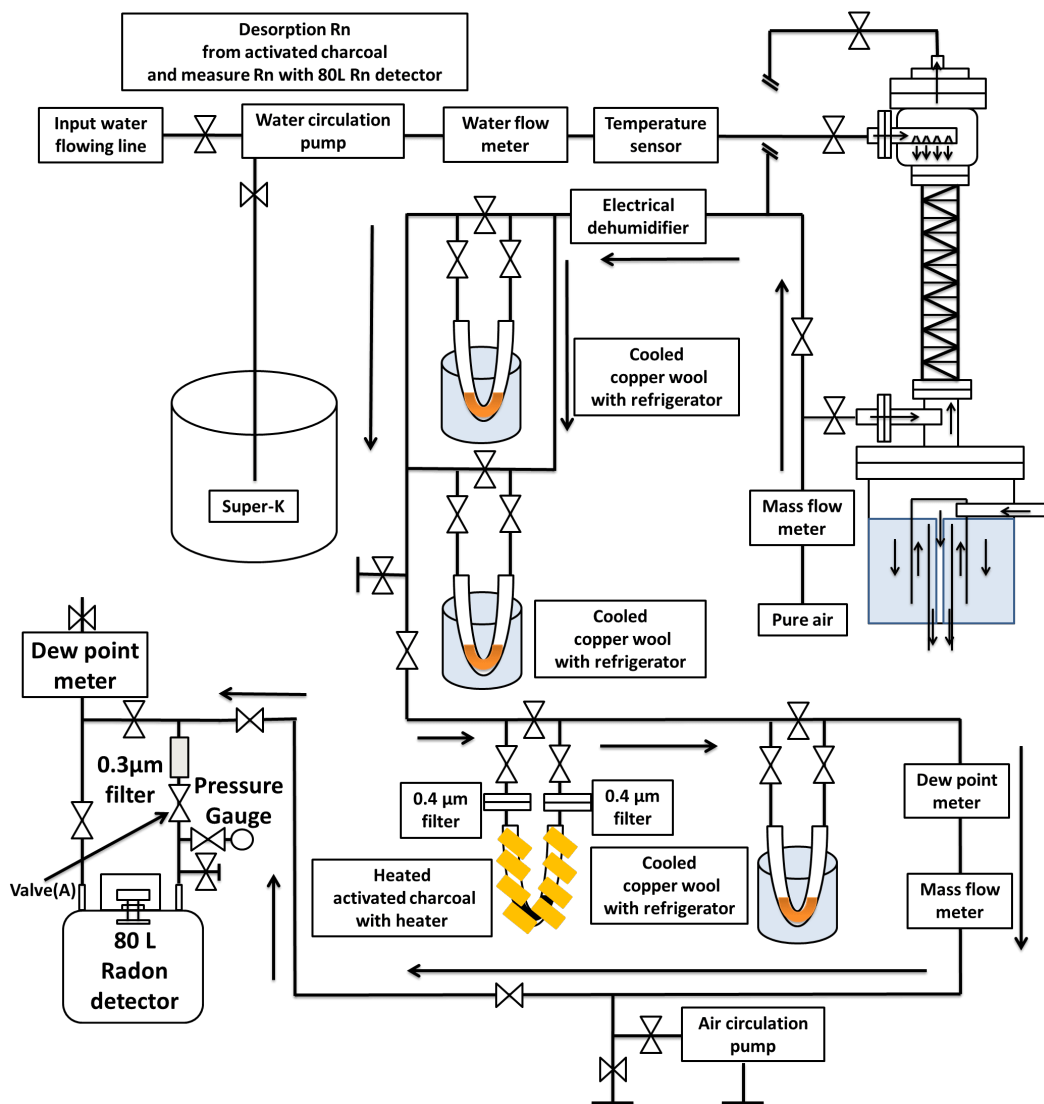


Figure A.5: A schematic diagram of the measurement system when the desorption process.

After the absorption process above, shift to the second step. Second one is performed in the following steps.

**Step A** Close the valves of the activated charcoal trap. Remove the dewar vessel and wipe the surface of the outside of the U-tube.

**Step B** Wrap the band heater around the U-tube of the trap. Set its temperature at 230 °C.

**Step C** Set the air flow rate at 1.0 L/min.

**Step D** Open or close the valves as shown in Figure A.5 and fill air degassed from heated activated charcoal into the evacuated 80 L Rn detector.

**Step E** Keep this state until the inside of the Rn detector becomes at atmospheric pressure.

**Step F** Closed the valve (A) described in Figure A.5.

**Step G** Set the supplied high voltage to the Rn detector to  $-2.0$  kV.

**Step H** Start measurement for the Rn concentration with the 80 L Rn detector for about 20 days to obtain a decay curve.

The decay curve obtained by the Step H is fitted to the following exponential function

$$C(t) = C(0)e^{-(\ln 2.0/3.82)t} + C_{BG}, \quad (\text{A.2.1})$$

where  $t$ ,  $C(t)$ ,  $C(0)$  and  $C_{BG}$  are the elapsed time since start to measure the Rn concentration with the 80 L Rn detector, the Rn concentration at time  $t$ , the Rn concentration at the start time of the Rn concentration measurement, background from the 80 L Rn detector itself, respectively. For every measurement, these parameters are obtained. Figure A.6 shows a typical result on the Rn concentration measurement with the 80 L Rn detector.

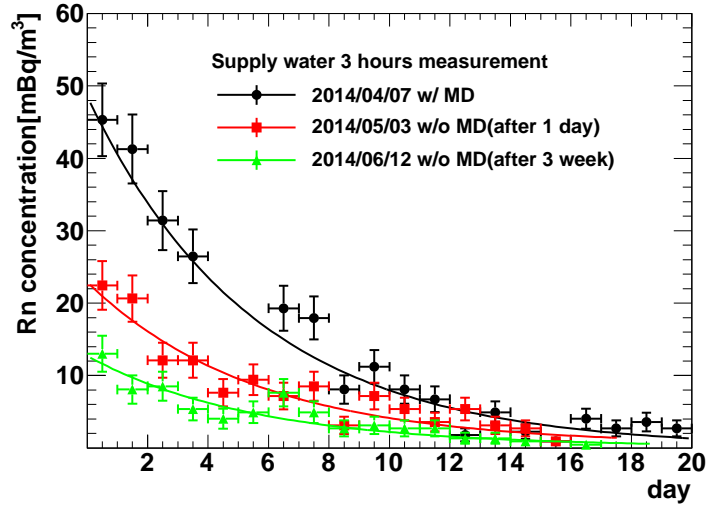


Figure A.6: A typical result on the Rn concentration measurement in the supply water. Similar measurements are performed during 3-hour absorption process. The fitting curves are defined by equation A.2.1. The horizontal axis shows the date in day and the vertical axis shows the Rn concentration measured by the 80 L Rn detector.

## A.2.4 Analysis method

After the measurements described in the previous subsection, the Rn concentration in the sampled water is calculated using the following procedures.

1. The Rn concentration in the mixed air is calculated. First of all, the total Rn radioactivity in the 80 L Rn detector should be obtained. It is described as  $C(0) \times 0.080$ , where  $0.080$  [ $\text{m}^3$ ] is the volume of the 80 L Rn detector. Then, the total Rn radioactivity in the mixed air is described as  $C_a V_a$ , where  $V_a = F_a \times t_{\text{abs}}$  [ $\text{m}^3$ ] is the total volume of mixed air through activated charcoal. These two total Rn radioactivities should be the same. Therefore, the Rn concentration in the mixed air is obtained as  $C_a = C(0) \times (0.080/V_a)$ .

2. The efficiency of absorption with activated charcoal is taken account. The efficiency, described as  $F_{\text{abs}}$ , is 99 % in this calculation, when activated charcoal is cooled under  $-80$  °C.
3. The efficiency of desorption with activated charcoal is also taken account. The efficiency, described as  $F_{\text{des}}$ , is 99 % in this calculation, when activated charcoal is heated above 200 °C.
4. Rn decays during the absorption and the desorption steps. So, a time correction factor  $F_t = \exp\{(\ln 2/3.82)t_c\}$  is defined, where  $t_c = t_{\text{abs}} + t_{\text{des}}$  is the total time during the absorption and the desorption steps. Concretely, the start time is Step 6 and the end time is Step G.
5. The Rn concentration in the sampled water ( $C_{w,0}$ ) is obtained, using the Rn extraction efficiency ( $F_{\text{mixer}}$ ). It is calculated as  $C_{w,0} = C_a/F_{\text{mixer}}$ .

Finally, the Rn concentration in the sampled water is calculated as

$$C_{w,0} = \frac{C_a F_t}{F_{\text{abs}} F_{\text{des}} F_{\text{eff}}}. \quad (\text{A.2.2})$$

# List of Figures

1.1	The neutrino mass eigenstates in matter. . . . .	7
1.2	The experimental results of the generation of light neutrino. . . . .	8
2.1	The schematic view of the pp-chain and the CNO cycle . . . . .	10
2.2	The distribution of the luminosity and the pressure as a function of $R/R_{\odot}$ . . . . .	10
2.3	The distribution of the chemical abundance of each isotope and the mass fraction as a function of $R/R_{\odot}$ . . . . .	11
2.4	The distribution of the electron density and the temperature as a function of $R/R_{\odot}$ . . . . .	11
2.5	The solar neutrino energy spectrum and the local production rate of solar neutrinos. . . . .	13
2.6	The time variation of sun spot number. . . . .	14
2.7	The time variation of sunspot number and the magnetic fields. . . . .	15
2.8	The $^{37}\text{Ar}$ production rate as a function of time. . . . .	16
2.9	The experimental results from Kamiokande experiment. . . . .	17
2.10	The $^8\text{B}$ solar neutrino flux measured by Kamiokande vs the sunspot number. . . . .	18
2.11	The capture rate of the solar neutrino measured by SAGE and GALLEX plus GNO experiments. . . . .	19
2.12	The experimental results from SNO experiment. . . . .	21
2.13	The experimental results from the Borexino experiment. . . . .	22
2.14	The experimental results from the KamLAND experiment. . . . .	23
2.15	The solar neutrino flux prediction vs the experimental results. . . . .	24
2.16	The expected survival probability of solar neutrinos. . . . .	25
2.17	The visual explanations of the day/night flux asymmetry and the profile of the mass density of the Earth. . . . .	27
2.18	The expectation of the value of the day/night flux asymmetry. . . . .	27
3.1	The Super Kamiokande detector. . . . .	31
3.2	Basic variable definitions used in our analysis. . . . .	32
3.3	The schematic view of one unit of the PMT support structure. . . . .	32
3.4	The schematic view of the 20-inch PMT and the picture of the FRP and the acrylic case. . . . .	33
3.5	The properties of the PMT. . . . .	34
3.6	The schematic view of Helmholtz coils. . . . .	34
3.7	The layout of the ID DAQ used in SK-I through SK-III. . . . .	36
3.8	The schematic view of the input and output channel of the ATM module. . . . .	37
3.9	The timing chart for the signal and the generation of the global trigger. . . . .	37
3.10	The schematic view of the DAQ system used in SK-IV. . . . .	38

3.11	Left: The picture of the new front end electronics QBEE. Right: The block diagram of the signal processing in the QBEE. . . . .	39
3.12	The schematic view of the water circulation system. . . . .	40
3.13	The water pipes and the water temperature in the water tank. . . . .	42
3.14	The schematic view of the Rn free air system. . . . .	43
3.15	The schematic view of the Rn concentration monitoring system for Rn water. . .	44
3.16	The time variation of the Rn concentration in the SK area. . . . .	44
3.17	A position dependence of the PMT hit rate. . . . .	46
3.18	The schematic view of the PMT response in the simulation. . . . .	48
4.1	The probability density function of the timing residuals used for the vertex reconstruction maximum likelihood fit. . . . .	50
4.2	The vertex resolutions for SK-I, SK-III and SK-IV. . . . .	50
4.3	The energy dependence of the angular likelihood function used in the direction reconstruction. . . . .	52
4.4	The time variation of the average of the dark rate of PMTs. . . . .	53
4.5	The definition of the angle $(\theta_i, \phi_i)$ and the effective PMT photo-cathode coverage correction factor. . . . .	54
4.6	The relationship between $N_{\text{eff}}$ and the generated electron total energy. . . . .	55
5.1	The typical charge distribution of the single photoelectron. . . . .	57
5.2	The relative gain measured using the laser calibration data. . . . .	59
5.3	A typical hit timing distribution of the Ni calibration. . . . .	59
5.4	The incident angle dependence of the PMT acceptance. . . . .	60
5.5	A position dependence of the normalized hit probability. . . . .	62
5.6	The visual explanation of the time-walk effect. . . . .	63
5.7	The USHO laser calibration system and the diffuser ball. . . . .	63
5.8	Typical scatter plot for the timing and charge distribution and the timing resolution among SK phases. . . . .	64
5.9	The laser injection system for water parameter measurement and the typical hit rate distribution. . . . .	65
5.10	Typical observed coefficients of water parameters and the time variation of the coefficients. . . . .	66
5.11	The typical hist of $\ln(\bar{Q}(r))$ vs $r$ . . . . .	67
5.12	The time variation of water transparency with decay electrons samples. . . . .	68
5.13	The time variation of the effective hit before and after the water transparency correction. . . . .	68
5.14	The monitoring result of the top-bottom asymmetry. . . . .	69
5.15	The linearity of the germanium detector and its deviation. . . . .	71
5.16	The typical distribution of Linac calibration data. . . . .	72
5.17	The LINAC calibration position and the difference of the peak position of the $N_{\text{eff}}$ distribution. . . . .	73
5.18	The schematic view of DT calibration method . . . . .	74
5.19	The position and angular dependences of the difference of effective hit. . . . .	75
5.20	The stability of energy scale obtained by the DT calibrations during the SK-IV phase. . . . .	75

6.1	The definition of $d_{\text{eff}}$ , $p_{\text{wall}}$ , $f_{\text{wall}}$ and $\theta_{\text{PMT}}$ .	79
6.2	Correlation of $g_V^2$ and $g_A^2$ .	80
6.3	The time variation of bad channel of ID.	81
6.4	The time variation of bad channel of OD.	81
6.5	An example of an increase in number of bad channels.	82
6.6	The rate of the OD trigger rate.	82
6.7	The typical scatter plot for max charge vs the number of hit PMTs surrounding PMT with max charge.	84
6.8	The typical distribution of the time difference to previous low energy triggered event	85
6.9	The distribution of the variables using in spallation cut.	87
6.10	The distribution of the variables using in spallation cut.	87
6.11	The distribution of spalogle like for Random samples and spallation like samples.	88
6.12	The position dependence of the dead time resulting from the spallation cut.	89
6.13	The distribution of spallation dead time and its time variation during SK-IV.	89
6.14	The distribution of $L_{\text{pattern}}$ .	90
6.15	Relationship between $r02$ and $N_{20\text{rawT}}$ for background and solar neutrino MC.	92
6.16	The vertex distribution in the lowest energy region.	93
6.17	Event rate during SK-IV phase.	94
6.18	The energy spectrum after each reduction step and the reduction efficiency of each cuts.	95
6.19	The visual explanation for multiple scattering goodness.	96
6.20	The typical distribution of MSG.	96
7.1	The typical vertex distribution of Ni calibration data taken at the center position.	98
7.2	The typical energy histogram of Ni calibration data and MC and the its detection efficiency.	100
7.3	The $z$ direction position dependence of SLE trigger efficiency taken on June 18th and July 28th 2015.	101
7.4	The $z$ direction position dependence of SLE trigger efficiency taken on September 9th 2015.	101
7.5	A typical plot of the trigger efficiency with a finer energy bin.	102
7.6	9 divided area for the Ni calibration.	102
7.7	The time variation of the software trigger efficiency in lower energy regions.	104
8.1	The solar angle distributions in SK-I, SK-III and SK-IV in 4.5 – 5.0 MeV.	106
8.2	The definition of the solar angle $\theta_{\text{sun}}$ .	106
8.3	The solar angle distributions in SK-III and SK-IV in the 3.5 – 4.0 MeV in kinetic energy region.	107
8.4	The time variation of Rn concentration in SK water.	108
8.5	The positions of the inlet for supply water.	108
8.6	The typical vertex distribution after the Rn injection.	110
8.7	The event rate around Rn injection.	111
8.8	The time variation of the event rate in the bottom region.	114
8.9	The time variation of event rate and $r^2$ distributions divided by 4 m interval in $z$ -axis.	115

8.10	The time variation of event rate and $r^2$ distributions divided by 2 m interval in $z$ -axis. . . . .	116
8.11	The solar angle distributions before and after bypassing the membrane system. . . . .	117
8.12	Rubber gaskets. . . . .	118
9.1	The distribution of the probability density function of the signal $s_{ij}$ . . . . .	123
9.2	The distribution of the probability density function of the background shape $b_{ij}$ . . . . .	124
9.3	The differential cross section and the total cross section. . . . .	126
9.4	The $^8\text{B}$ neutrino energy spectrum. . . . .	126
9.5	The angular distribution of recoil electrons from incident solar neutrinos. . . . .	127
9.6	The expected $^8\text{B}$ energy spectrum using the MC simulation. . . . .	128
10.1	The energy distributions of electrons generated by the mono-energetic MC simulations. . . . .	130
10.2	The systematic error of energy resolution. . . . .	131
10.3	The expected recoil electron energy spectrum and the difference between the shifted energy spectra and the original energy spectrum. . . . .	132
10.4	The systematic uncertainty in the angular resolution. . . . .	134
10.5	The systematic uncertainty in the vertex cut. . . . .	135
10.6	The systematic error in the event quality cut. . . . .	136
10.7	The systematic error in the hit pattern cut. . . . .	137
10.8	The systematic uncertainty in the external cut. . . . .	138
10.9	The energy correlated systematic uncertainties. . . . .	140
10.10	The MSG scaling function. . . . .	141
11.1	The solar angle distribution using 3.5 – 19.5 MeV energy range. . . . .	143
11.2	The comparison of the solar neutrino fluxes. . . . .	144
11.3	The solar angle distribution during the day and the night. . . . .	145
11.4	The zenith angle dependence of the $^8\text{B}$ solar neutrino flux. . . . .	145
11.5	The solar angle distributions below 5.5 MeV. . . . .	147
11.6	The solar angle distributions below 7.5 MeV. . . . .	148
11.7	The solar angle distributions above 7.5 MeV. . . . .	149
11.8	The observed $^8\text{B}$ solar neutrino event rate. . . . .	151
11.9	The energy spectrum of $^8\text{B}$ solar neutrino in SK-IV. . . . .	151
11.10	The solar angle distribution for the first lowest energy bin. . . . .	152
12.1	Solar angle distributions of each SK phase. . . . .	154
12.2	Combined solar angle distribution for SK-I through SK-IV. . . . .	155
12.3	Zenith angle distribution for each SK phases. . . . .	156
12.4	The combined zenith angle dependence . . . . .	157
12.5	Yearly data plot vs sun spot number. . . . .	158
12.6	The energy spectrum in each SK phase. . . . .	159
12.7	The livetime fraction as a function of $cz(= \cos \theta_z)$ . . . . .	161
12.8	The predicted zenith angle dependence of the solar neutrino rate. . . . .	163
12.9	The allowed region from the SK measurement. . . . .	165
13.1	The allowed region from the SK combined analysis with the SNO. . . . .	167

13.2	The allowed region from the all solar combined analysis with the KamLAND allowed region. . . . .	168
13.3	The allowed region from the all solar combined analysis with the KamLAND allowed region. . . . .	169
13.4	SK combined energy spectrum together with the MSW prediction curves and the survival probability. . . . .	171
13.5	The comparison of the trigger efficiency when the trigger hit threshold is 31 vs. 34.	172
13.6	Sensitivity to the MSW effect (upturn) in future. . . . .	173
A.1	A schematic diagram of Rn extraction system. . . . .	180
A.2	A schematic diagram of the calibration setup. . . . .	180
A.3	The efficiency of Rn extraction. . . . .	182
A.4	A schematic diagram of the measurement system when the absorption process. .	183
A.5	A schematic diagram of the measurement system when the desorption process. .	184
A.6	A typical result om the Rn concentration measurement in the supply water. . .	185

# List of Tables

1.1	The typical traveling length and the energy of neutrino for various neutrino sources.	4
1.2	The best fit values after Neutrino 2014. . . . .	8
2.1	The predicted solar neutrino fluxes. . . . .	12
3.1	The summary of characteristics of each SK phase. . . . .	30
3.2	The characteristic of 20-inch PMT. . . . .	33
3.3	The values of the current for each Helmholtz coil. . . . .	33
3.4	The global trigger threshold in each SK phase. . . . .	38
3.5	The characteristics of each input channel. . . . .	39
3.6	The threshold for each trigger and its event time width. . . . .	40
3.7	Threshold of the Cherenkov radiation for typical charged particles. . . . .	45
5.1	The values of the absolute gain for each SK phase. . . . .	58
5.2	The summary of the typical water parameters. . . . .	65
5.3	The summary of the LINAC calibration position and the target energy. . . . .	70
5.4	The summary of the average for the difference between the data and MC simulation. . . . .	73
6.1	The example for the reduction efficiency after pre-reduction. . . . .	80
6.2	The calibration sources and those positions. . . . .	83
6.3	The list of Spallation production. . . . .	86
7.1	The definition of each region. . . . .	103
7.2	The detection efficiency evaluated by the special Ni calibration. . . . .	103
8.1	The information on the analysis periods and the Rn concentration. . . . .	112
8.2	The event rate in the bottom region before bypassing. . . . .	113
8.3	The event rate in the bottom region after bypassing. . . . .	113
8.4	The summary of the estimated Rn concentration in the bottom region. . . . .	114
8.5	The summary of the Rn emanation rate. . . . .	119
9.1	The parameters used in equation (9.2.1). . . . .	125
10.1	The summary of the systematic uncertainties in the total flux in each SK phase. . . . .	139
10.2	Energy uncorrelated systematic uncertainty in the spectrum shape. . . . .	139
11.1	The observed and expected event rates. . . . .	150
12.1	Summary of the flux measurement results of SK. . . . .	154

12.2 Summary of day/night asymmetry for each SK phase. . . . .	155
13.1 Comparison of $\chi^2$ fitting results. . . . .	170

# Bibliography

- [1] W. Pauli, Phys. Today **31N9**, 27 (1978).
- [2] F. Reines and C. L. Cowan, Nature **178**, 446 (1956).
- [3] C. L. Cowan *et al.*, Science **124**, 103 (1956).
- [4] G. Danby *et al.*, Phys. Rev. Lett. **9**, 36 (1962).
- [5] K. Kodama *et al.*, Phys. Lett. **B504**, 218 (2001).
- [6] M. Goldhaber *et al.*, Phys. Rev. **109**, 1015 (1958).
- [7] R. Davis *et al.*, Phys. Rev. Lett. **20**, 1205 (1968).
- [8] K. Hirata *et al.*, Phys. Rev. Lett. **63**, 16 (1989).
- [9] K. Hirata *et al.*, Phys. Lett. **B205**, 416 (1988).
- [10] R. Becker Szendy *et al.*, Phys. Rev. **D46**, 3720 (1992).
- [11] Y. Fukuda *et al.*, Phys. Rev. Lett. **81**, 1562 (1998).
- [12] S. Fukuda *et al.*, Phys. Rev. Lett. **86**, 5651 (2001).
- [13] Q. Ahmad *et al.*, Phys. Rev. Lett. **89**, 011301 (2002).
- [14] B. Pontecorvo, Zh. Eksp. Teor. Fiz. **33**, 549 (1957).
- [15] B. Pontecorvo, Zh. Eksp. Teor. Fiz. **34**, 247 (1958).
- [16] Z. Maki *et al.*, Prog. Theor. Phys. **28**, 870 (1962).
- [17] L. Wolfenstein, Phys. Rev. **D17**, 2369 (1978).
- [18] L. Wolfenstein, Phys. Rev. **D20**, 2634 (1979).
- [19] S. Mikheyev and A. Smirnov, Sov. J. Nucl. Phys. **42**, 913 (1985).
- [20] H. A. Bethe, Phys. Rev. Lett. **56**, 1305 (1986).
- [21] The ALEPH Collaboration, The DELPHI Collaboration, The L3 Collaboration, The OPAL Collaboration, The SLD Collaboration, The LEP Electroweak Working Group, The SLD Electroweak and Heavy Flavour Groups, Phys. Rept. **427** 257-454 (2006).

- [22] P.A.R. Ade *et al.*, *A&A* **A16**, 571 (2014).
- [23] K. Eguchi *et al.*, *Phys. Rev. Lett.* **90**, 021802 (2003).
- [24] T. Araki *et al.*, *Phys. Rev. Lett.* **94**, 081801 (2005).
- [25] Y. Ashie *et al.*, *Phys. Rev. Lett.* **93**, 101801 (2004).
- [26] M. H. Ahn *et al.*, *Phys. Rev.* **D74**, 072003 (2006).
- [27] D. G. Michael *et al.*, *Phys. Rev. Lett.* **97**, 072003 (2006).
- [28] D. G. Michael *et al.*, *Phys. Rev. Lett.* **97**, 191801 (2006).
- [29] P. Adamson *et al.*, *Phys. Rev. Lett.* **101**, 031802 (2008).
- [30] P. Adamson *et al.*, *Phys. Rev. Lett.* **106**, 181801 (2011).
- [31] K. Abe *et al.*, *Phys. Rev.* **D85**, 031103 (2012).
- [32] K. Abe *et al.*, *Phys. Rev. Lett.* **111**, 211803 (2013).
- [33] K. Abe *et al.*, *Phys. Rev. Lett.* **107**, 041801 (2011).
- [34] F. P. An *et al.*, *Phys. Rev. Lett.* **108**, 171803 (2012).
- [35] F. P. An *et al.*, *Chinese Phys.* **C37**, 011001 (2013).
- [36] F. P. An *et al.*, *Phys. Rev. Lett.* **112**, 061801 (2014).
- [37] J. K. Ahn *et al.*, *Phys. Rev. Lett.* **108**, 191802 (2012).
- [38] Y. Abe *et al.*, *Phys. Rev. Lett.* **108**, 131801 (2012).
- [39] Y. Abe *et al.*, *Phys. Rev.* **D86**, 052008 (2012).
- [40] K. Abe *et al.*, *Phys. Rev.* **D91**, 072010 (2015).
- [41] D. V. Forero *et al.*, *Phys. Rev.* **D90**, 093006 (2014).
- [42] J. N. Bahcall *et al.*, *Rev. Mod. Phys.* **54**, 767 (1982).
- [43] J. N. Bahcall *et al.*, *Phys. Lett.* **B433**, 1 (1998).
- [44] J. N. Bahcall *et al.*, *Astrophys. J.* **555**, 990 (2001).
- [45] J. N. Bahcall *et al.*, *Phys. Rev. Lett.* **92**, 121301 (2004).
- [46] J. N. Bahcall *et al.*, *Astrophys. J.* **621**, 85 (2005).
- [47] <http://www.sns.ias.edu/~jnb/SNdata/solarmodels.html>.
- [48] R. Wolf, *Mittheli. Zurich* **2**, 3 (1859).

- [49] [http://solarscience.msfc.nasa.gov/greenwch/spot\\_num.txt](http://solarscience.msfc.nasa.gov/greenwch/spot_num.txt).
- [50] [http://wso.stanford.edu/meanfld/MF\\_timeseries.txt](http://wso.stanford.edu/meanfld/MF_timeseries.txt).
- [51] <http://wso.stanford.edu/Polar.html>.
- [52] B. Cleveland *et al.*, *Astrophys. J.* **496**, 505 (1998).
- [53] R. Davis *et al.*, *Prog. Nucl. Part. Phys.* **32**, 13 (1994).
- [54] J. N. Bahcall *et al.*, *Astrophys. J.* **320**, 69 (1987).
- [55] K. Arisaka *et al.*, *J. Phys. Soc. Jap.* **54**, 3213 (1985).
- [56] T. Kajita *et al.*, *J. Phys. Soc. Jap.* **54**, 4065 (1985).
- [57] Y. Fukuda *et al.*, *Phys. Rev. Lett.* **77**, 1683 (1996).
- [58] S. Fukuda *et al.*, *Nucl. Instrum. Meth.* **A501**, 418 (2003).
- [59] A. I. Abazov *et al.*, *Phys. Rev. Lett.* **67**, 3332 (1991).
- [60] P. Anselmann *et al.*, *Phys. Lett.* **B285**, 376 (1992).
- [61] M. Altmann *et al.*, *Phys. Lett.* **B490**, 16 (2000).
- [62] J. N. Abdurashitov *et al.*, *J. Exp. Theor. Phys.* **95**, 181 (2002).
- [63] M. Altmann *et al.*, *Phys. Lett.* **B616**, 174 (2005).
- [64] N. Abdurashitov *et al.*, *Phys. Rev.* **C80**, 015807 (2009).
- [65] J. Boger *et al.*, *Nucl. Instrum. Meth.* **A449**, 172 (2000).
- [66] Q. Ahmad *et al.*, *Phys. Rev. Lett.* **87**, 071301 (2001).
- [67] S. Ahmed *et al.*, *Phys. Rev. Lett.* **92**, 181301 (2004).
- [68] B. Aharmin *et al.*, *Phys. Rev.* **C72**, 055502 (2005).
- [69] B. Aharmin *et al.*, *Phys. Rev. Lett.* **101**, 111301 (2008).
- [70] B. Aharmin *et al.*, *Phys. Rev.* **C87**, 015502 (2013).
- [71] B. Aharmin *et al.*, *Phys. Rev.* **C88**, 025501 (2013).
- [72] G. Alimonti *et al.*, *Astropart. Phys.* **16**, 205 (2002).
- [73] C. Arpesella *et al.*, *Phys. Rev. Lett.* **101**, 091302 (2008).
- [74] C. Arpesella *et al.*, *Phys. Lett.* **B658**, 101 (2008).
- [75] G. Bellini *et al.*, *Phys. Rev. Lett.* **107**, 141302 (2011).

- [76] G. Bellini *et al.*, Phys.Rev. **D89**, (2014) 112007.
- [77] G. Bellini *et al.*, Phys. Rev. **D82**, 033006 (2010).
- [78] G. Bellini *et al.*, Phys. Rev. Lett. **108**, 051302 (2012).
- [79] G. Bellini *et al.*, Nature **512**, 383 (2014).
- [80] S. Abe *et al.*, Phys. Rev. Lett. **100**, 21803 (2008).
- [81] <http://www.sns.ias.edu/jnb/SNviewgraphs/Nobel04/colortheoryvsexp.pdf>.  
J. N. Bahcall, Phys. Scripta T121 (2005) 46-50.
- [82] J. Arafune *et al.*, Phys. Rev. **D55**, 1653 (1997).
- [83] J. Arafune *et al.*, Phys. Rev. **D56**, 3093 (1997).
- [84] D. L. Anderson, "Theory of the Earth", Blackwell scientific publication (1989).  
<http://authors.library.caltech.edu/25018/1/TheoryoftheEarth.pdf>.
- [85] A. Renshaw *et al.*, Phys. Rev. Lett. **112**, 091805 (2014).
- [86] A. Cisneros, Astrophys. Space. Sci **10**, 87 (1971).
- [87] L. B. Okun *et al.*, Sov. J. Nucl. Phys. **44**, 440 (1986).
- [88] A. G. Beda *et al.*, Adv. High Energy Phys. **2012**, 350150 (2012).
- [89] S. Yamada *et al.*, Nucl. Instrum. Meth. **A458**, 638 (2001).
- [90] H. Kume *et al.*, Nucl. Instrum. Meth. **205**, 433 (1983).
- [91] A. Suzuki *et al.*, Nucl. Instrum. Meth. **A329** 299 (1993).
- [92] T. Yamaguchi, Ph.D thesis, Osaka University, 1998,  
[http://www-sk.icrr.u-tokyo.ac.jp/sk/\\_pdf/articles/guchi.pdf](http://www-sk.icrr.u-tokyo.ac.jp/sk/_pdf/articles/guchi.pdf).
- [93] K. Abe *et al.*, Nucl. Instrum. Meth. A **737**, 153 (2014).
- [94] T. Tanimori *et al.*, IEEE Trans. Nucl. Sci. NS-**36**, 497 (1989).
- [95] H. Ikeda *et al.*, Nucl. Instrum. Meth. **A320**, 310 (1992).
- [96] T. K. Ohsuka *et al.*, KEK Report 85-10 (1985).
- [97] S. Yamada *et al.*, IEEE Trans. Nucl. Sci. **57**, 428 (2010).
- [98] C. Mitsuda, Ph.D. thesis, Niigata University, 2004,  
[http://www-sk.icrr.u-tokyo.ac.jp/sk/\\_pdf/articles/mitsuda-doctor2.pdf](http://www-sk.icrr.u-tokyo.ac.jp/sk/_pdf/articles/mitsuda-doctor2.pdf).
- [99] M. Ikeda, Ph.D. thesis, University of Tokyo, 2010,  
[http://www-sk.icrr.u-tokyo.ac.jp/sk/\\_pdf/articles/ikeda-dron.pdf](http://www-sk.icrr.u-tokyo.ac.jp/sk/_pdf/articles/ikeda-dron.pdf).

- [100] H. Nishino *et al.*, Nucl. Instrum. Meth. **A610** 710 (2009).
- [101] M. Shimo *et al.*, J. At. Energy Soc. Jpn. **25**, 562 (1983).
- [102] K. Hosokawa *et al.*, Prog. Theor. Exp. Phys. (2015) 033H01.
- [103] I. Thormahlen, J. Straub and U. Grigull, J. Phys. Chem. Ref. Data **14**, 933 (1985).
- [104] R. M. Pope and E. S. Fry. Appl. Opt. **36**, 8710 (1997).
- [105] M. Smy. Proc. of the 30th ICRC, **5**, 1279 (2007).
- [106] M. Nakahata *et al.*, Nucl. Instrum. Meth. **A421**, 113 (1999).
- [107] E. Blaufuss *et al.*, Nucl. Instrum. Meth. **A458**, 638 (2001).
- [108] T. Yokozawa, Ph.D. thesis, University of Tokyo, 2013,  
[http://www-sk.icrr.u-tokyo.ac.jp/sk/\\_pdf/articles/yokozawa\\_thesis.pdf](http://www-sk.icrr.u-tokyo.ac.jp/sk/_pdf/articles/yokozawa_thesis.pdf).
- [109] J. Hosaka *et al.*, Phys. Rev. **D73**, 112001 (2006).
- [110] A. Renshaw, Ph.D. thesis, University of California, Irvine., 2013,  
[http://www-sk.icrr.u-tokyo.ac.jp/sk/\\_pdf/articles/Renshaw\\_Doctoral\\_Thesis.pdf](http://www-sk.icrr.u-tokyo.ac.jp/sk/_pdf/articles/Renshaw_Doctoral_Thesis.pdf).
- [111] Y. Takeuchi *et al.*, Phys. Lett. **B452**, 418 (1999).
- [112] H. Sekiya, Talk at Low Radioactivity Techniques workshop, Seattle (2015)
- [113] J. P. Cravens *et al.*, Phys. Rev. **D78**, 032002 (2008).
- [114] K. Abe *et al.*, Phys. Rev. **D83**, 052010 (2011).
- [115] W. T. Winter *et al.*, Phys. Rev. **C73**, 025503 (2006).
- [116] C. E. Ortiz *et al.*, Phys. Rev. Lett. **85**, 2909 (2000).
- [117] J. N. Bahcall *et al.*, Phys. Rev. **D51**, 6416 (1995).
- [118] G. L. Fogli *et al.*, Phys.Rev. **D62**, 113004 (2000).
- [119] G. L. Fogli *et al.*, Phys.Rev. **D66**, 053010 (2002).
- [120] Y. Takeuchi *et al.*, Nucl. Instrum. Meth. **A421**, 334 (1999).